UNIVERSITAT POLITÈCNICA DE VALÈNCIA

INSTITUTO INTERUNIVERSITARIO DE INVESTIGACIÓN DE RECONOCIMIENTO MOLECULAR Y DESARROLLO TECNOLÓGICO

" Nanotechnology and supramolecular chemistry in controlled release and molecular recognition processes for biomedical applications "

PhD. THESIS

Submitted by

Cristina de la Torre Paredes

PhD. Supervisors:

Prof. Ramón Martínez Máñez
Dr. Félix Sancenón Galarza

València, November 2017

RAMÓN MARTÍNEZ MÁÑEZ, PhD in Chemistry and Professor at the *Universitat Politècnica de València* and FÉLIX SANCENON GALARZA PhD in Chemistry and Lecturer at the *Universitat Politècnica de València*,

CERTIFY:

That the work *"Nanotechnology and supramolecular chemistry in controlled release and molecular recognition processes for biomedical applications*" has been developed by Cristina de la Torre Paredes under their supervision in the Instituto Interuniversitario de Investigación de Reconocimiento Molecular y Desarrollo Tecnológico de la Universitat Politècnica de València, as a thesis Project in order to obtain the degree of PhD in Chemistry at the *Universitat Politècnica de València.*

València, September 2017.

Prof. Ramón Martínez Máñez Dr. Félix Sancenón Galarza

“La vida es todo lo que nos sucede mientras perseguimos nuestros sueños y metas”

“Ningú aconsegueix la meta amb un sol intent. Ni perfecciona la vida amb una sola rectificació, ni arriba a prendre altura amb un sol vol. Ningú camina per la vida sense haver trepitjat en fals moltes vegades”

Agradecimientos

Como en cualquier carrera de fondo, lo importante de llegar a meta es todo lo que aprendes en el camino. Llegados a este punto, donde me encuentro en la recta final para cruzar la línea de meta, es importante echar la vista atrás y agradecer a todas esas personas que dia a dia te ayudan a continuar caminando, a no detenerte y a afrontar los distintos obstáculos que te encuentras.

En primer lugar, agradecer a mi director, el Profesor Ramón Matinez Mañez por darme la oportunidad de realizar la tesis doctoral en su grupo de investigación. Gracias por confiar en mi desde el primer momento, siempre recordaré la entrevista en la que me comentabas que realizaría ensayos en células porque la doctora que se ocupa de ellos se marchaba en breve y yo te contesté, con total sinceridad, que no tenía ningún conocimiento de cultivos celulares pero que aprendería sin problemas (en ese momento en mi cabeza pensaba : “y yo que estudié dibujo técnico en lugar de biología en Bachillerato…mare meua!”). Gracias por darme la oportunidad de crecer “químicamente”, por la libertad e independencia que me has dado durante este periodo ya que gracias a ello he aprendido a superar los obstáculos y problemas que surgen, a “buscarme las castañas”.

Como no, agradecer a Félix Sancenón por ser mi segundo director, por ser el filtro de todos los papers, la persona que siempre está disponible para responder tus dudas experimentales, para corregirte lo que necesites y siempre con una eficiencia difícil de mejorar. Considero que todo el trabajo realizado ha sido posible gracias a tu ayuda y a tus consejos y positividad. Haces las cosas mucho más fáciles, al principio, durante y ahora en la recta final, ayudándome con todos los trámites de la tesis.

También agradecer la ayuda prestada a Loles, Jose Vicente, Jose Ramón Murguía y Luis Villaescusa (y sus clases y conversaciones en la sala del Rayos X).

Agradecimientos

Gracias a Quique y Eva, por todos los trámites que nos facilitais, por solucionar los lios de compras en los que nos metemos a veces y por vuestra eficiencia.

Muchisimas gracias a Mar Orzaez y Enrique Pérez Payá, por todo lo que me habéis enseñado y por la paciencia que tuvisteis conmigo en los inicios de la tesis. Gracias por aceptarme en vuestro laboratorio y hacer que fuera una más en él. Gracias a Maria José Alcaraz y a su laboratorio, en especial a Carmen Terencio. Gracias por lo que me has enseñado, por como me has tratado, de tú a tú y por la confianza que has puesto en mi. Gracias a Reynaldo por las colaboraciones que hemos realizado y el trabajo en equipo que tan bien organiza.

Inifinitas gracias a Eduardo Ruiz, por recibirme con los brazos abiertos en su laboratorio de Dublin. "*Una actitud positiva causa una reacción en cadena de pensamientos, sucesos y resultados positivos*". Esta frase te define a la perfección. Durante el tiempo que estuvimos trabajando juntos destaco tu positividad ante los resultados obtenidos en el laboratorio, tu interés por conocer mi opinión y mis propuestas, tu disponibidlidad para ayudar en cualquier momento y tu actitud creativa y curiosa. Eres un profesor muy motivante. Creo que todas estas cosas hacen que la estancia en tu laboratorio fuera una experiencia que disfruté gratamente y de la que aprendí mucho. Espero que en tiempos futuros podamos seguir trabajando juntos.

Gracias, a las doctoras que han estado ahí para ayudar a los predoc y guiarnos. Gracias Carmen, Elena y Andrea por vuestra ayuda durante la tesis y por todo lo que me habéis enseñado.

Son muchas las personas que han compartido el camino conmigo y me han enseñado que si te tropiezas y caes no significa que no estés en la senda correcta, sino que las cosas no son siempre fáciles y por ello, no hay que abandonar. Durante todo este tiempo tienes días positivos donde un mal resultado no te derrota, pero también hay muchos otros donde las cosas no salen, o salen justo al contrario de lo que esperas y te desesperas y desmotivas. Siempre ha habido

alguien que me ha escuchado o me ha hecho ver que hay días malos de los que también se puede aprender. Como cualquier actividad nueva que comienzas a realizar, necesitas un tiempo de adaptación, de entrenamiento y después de continua mejora. Necesitas invertir tiempo y también a alguien que te guie. En este punto, he de darte las gracias, Laura Mondragón, por todo lo que me enseñaste en los diez días que tuvimos. Fueron unos días intensos y un poco caóticos, pero hiciste todo lo posible por enseñarme conceptos y ensayos en cultivos celulares. Empezar de 0 y tener que aprender en tan poco tiempo fue una tarea difícil para ambas, pero lo logramos.

Gracias a los compañeros del laboratorio de Mar en el CIPF, porque ellos también tuvieron que ayudarme en numerosas ocasiones y compartimos muy buenos momentos fuera del lab (Andy, Tatiana, Fede, Vicente, Pablo, Ally y Guille).

También me he encontrado con personas que son de admirar. Alessandro, el italiano del grupo, estaba para todo y todos, inteligente y buen compañero. Sameh, la persona más trabajadora que conozco, humilde y sencillo. Édgar, porque siempre ha sido la persona más carismática del lab, con la agenda siempre llena de eventos, trabajando a deshoras y comiendo rosquilletas o gominolas de un sitio a otro. Toni, trabajador y con una mente y capacidad de aprendizaje muy grande (aunque nuestros inicios no fueron muy buenos, jajaja). ¡Te sales y lo que te queda! ¡Sois un ejemplo!

Como en cualquier carrera, hay mucha gente por delante de ti y por detrás, gente con la que coincides poco tiempo, compartes momentos al principio, pero después tomais distintos ritmos y otras que van a tu lado y con las que compartes gran parte del camino o momentos especiales durante él. Esas son las personas que te motivan a ir cada dia al laboratorio, con las que tienes momentos de risas donde terminas llorando, conversaciones y debates sobre la lengua valenciana, sobre las parejas, manias, el azúcar, la hipertensión o las ampollas de los pies.

Elisa, mi “amigui” de Cuenca, gracias por tu ayuda, tus críticas, tus riñas, tu orden que hace que intente mejorar un poco el mio, y tu forma de ser. Has sido

un pilar importante durante los últimos años. Sabes que en realidad nos parecemos más de lo que parece.

Lluis, porque has hecho que me lo pase muy bien esta última etapa dentro y fuera del laboratorio. Porque eres una persona que *pixes alt i fas clotet…* pero trabajador y en realidad molas. Tienes carisma y te haces querer. Pero tengo que decir que…pobre Lorena!

Campitos, ¡¡como te echo de menos!! Durante un tiempo fuimos compañeras y vecinas… ahora, una amiga. ¡Eres única! Gracias por estar ahí, dentro y fuera.

Gracias a toda la gente que forma el laboratorio o ha pasado por él durante estos años. Grandes compañeros/as como Estela, Núria, Mar, Cristina Giménez, Roman, Cristina Marin, Inma Candel, Carol, Maria o Lluis. Estela, una crack donde las haya, con un curriculum de miedo; Núria, carismatica, valencianeta a tope y el alma de la fiesta además de buena cocinera jeje; Mar que empezamos estudiando la licenciatura juntas, coincidimos en el máster (muy poco jeje) y acabamos realizando la tesis en el mismo instituto; Cristina Giménez, la dulzura personificada, entregada, amable y sencilla como ella misma; Román que junto con Campos son los dos amigos electrónicos, con los que comparto la manera de ver muchas cosas de la vida y Lluis, el xiquet que nunca pierde la sonrisa y con una personalidad auténtica. A los que están a mitad camino y a los que les deseo lo mejor para lo que les queda: Angela, Irene, Bea, Bea de Luis, Ismael, Hazem, Santi, Adrián, Sara, Amelia, Lorena, Alba, Mª Elena, Xente, Iris, Tania, Andy, Damián, Eva... y seguramente me deje a alguien. También mucha fuerza para las últimas incorporaciones de doctores, Mari Carmen, Borja y Maria. Esos superhéroes! Un placer conoceros a cada uno de vosotros y poder haber compartido momentos juntos!

Gracias a la oportunidad de realizar la tesis en un entorno como este (y gracias a Carol que me lió de qué manera…), decidí empezar a hacer deporte. Unos años después me he convertido en un friki del mismo, si, lo reconozco. Me ha aportado mucho, aprendes valores que puedes trasladar a la vida diaria y al trabajo. El

deporte me ha hecho crecer durante esta etapa y también en parte gracias a la gente que he conocido practicándolo. Gracias al equipo de triatlón y al equipo de atletismo de la Universidad Politécnica de Valencia, gracias por los valores que transmitis y los buenos momentos que he vivido con vosotros. Gracias Toni y Juanjo y gracias a todos los compañeros de equipo.

Por último, agradecer a mi familia y amigos el apoyo y sobretodo, por soportar mi mal humor en algunos momentos sin saber bien porque, por no preguntar muchas veces, por confiar en mi y por hacer que cuando estuve en Dublin no os sintiera lejos. Gracias Marta por tu amistad, Isa, Marta M, Fredman, Xavi, Cristian y Saioa**..** Al comboi que vino de visita a Dublin, ¡como me alegró teneros allí! Mi amiga Marieta, mi rubia y Roldán, hay que organizar otro viaje pronto, no?

Al equipo de "novios de los amigos" (mi segundo hermano Bellvis, cuánto me aguantas! y lo que te queda!, Ana y Rober, Samu y sus sabios consejos, Rafa y nuestras conversaciones montados sobre ruedas acerca de la vida) y al equipo de "Globers".

A Belinda y Bea, dos amigas que conocí durante la estancia, gracias a vosotras disfruté tanto! Gracias por los vinos, las comidas fuera de casa, conciertos y sobretodo las fajitas! Jajajaja. Gracias también al equipo de Piranhas!! Una decisión de la que jamás me arrepentiré!

Gracias a l@s alcoian@s, que hacen que Alcoi ya sea mi segunda casa. Mi amigo Ricky, cuanto te quiero tio!, Paula, Saray, Santi, Sergio, Guty y Mar. Mil gracias a Nacho Olcina, por su gran ayuda con la porta de la tesis!! Eres un crack!!

Mari Leo y Toni, que me cuidan como una hija más.

Gracias papa, mama, tete y Bruno! Porque dais todo sin pedir nada a cambio, por educarme como lo habéis hecho.

Por último, gracias Àlex por aguantarme, por ayudarme y entenderme. Gracias por hacerme mejor persona y por compartir la vida juntos. Sea como sea y donde sea.

Es de bien nacido ser agradecido asi que…

Gracias a tod@s!!

Abstract

This PhD thesis entitled “Nanotechnology and supramolecular chemistry in controlled release and molecular recognition processes for biomedical applications”, is focused on two important subjects: molecular recognition and controlled delivery processes.

This PhD thesis is structured in four chapters.

The first chapter introduces the concept of organic-inorganic hybrid materials containing switchable “gate-like” ensembles and their biomedical applications as nanomaterials for targeting and control drug delivery. Furthermore, is introduced a short review about chromo-fluorogenic chemosensors based on basic principles of supramolecular chemistry, particulary in molecular recognition processes.

In particular, in chapter 2 is focus on the development of enzymatic-driven nanodevices. These hybrid materials are composed of two main units: an inorganic silica based mesoporous scaffold, able to store organic molecules and an organic compound anchored on the external surface of the inorganic mesoporous support than acts as molecular gate. All the systems proposed use peptidic gates that respond to temperature or enzimatic stimulis. A short review about peptides in nanomedicine and their multiple applications as targeting ligands, proteases substrates and molecular gates is reported.

The first example was based on the design, synthesis and characterization of mesoporous silica nanoparticles using peptides as molecular gates in which the release of the cargo entrapped inside the pores was achieved by a progressive α-helix-to-disordered transformation when temperature increased.

A second example was focused on the design, synthesis, characterizations and applications of a new protease-responsive nanodevice for intracelular-controlled release. The system consists of MCM-41 nanoparticulated mesoporous scaffold loaded and capped with a peptidic sequence designed to be selectively hydrolysed

by cathepsin B enzyme overexpressed in several cancer cells. Viability and internalization studies in HeLa cells and controlled delivery studies of a chemotherapeutic agent have been carried out. In the same way, the fourth example describes a system based on mesoporous silica support capped with a peptide with the objective of release a therapeutic for decreasing unwanted cell death. We have focused on caspase 3 enzyme and developed a peptide containing a target sequence for this enzyme. We report the preparation of gated MSNs capable of selectively deliver their cargo in the presence of activated caspase 3 enzyme in cells, once apoptosis has been induced. The next example describes a new targeted delivery systems using mesoporous silica nanoparticles (MSNs) capped with a peptide with great affinity to a receptor which is overexpressed in lymphoma cells. The results show that peptide is able to gide the nanoparticles to lymphoma cells to facilitate MSNs uptake *via receptor*. The last example of this chapter is centered on the development of a protease-responsive nanodevice as carrier for peptide delivery inside cells. Herein, the material has been based on the use of MCM-41 mesoporous silica nanoparticles capped with the polymer ε-poly-L-lysine that could be degradated by lysosomal enzymes inside cells. It is known that peptide used (C9h) disrupt the interaction between caspase-9 and PP2Acα interaction with subsequent apoptosis induction. The nanoparticles provided peptide protection from degradation additionally allowing a dose reduction of up to ten times to observe an apoptotic effect when compared with the peptide alone or in combination with a cell-penetrating peptide.

The second part of this PhD thesis is focused on the design and development of a new chemical compound capable of detecting carbon monoxide in vivo. The probe is based on a ruthenium(II) vinyl complex suitable for use in aqueous systems bearing a 5-(3-thienyl)-2,1,3-benzothiadiazole (TBTD) ligand as a signalling unit. It is a coloured complex and in presence of CO, the TBTD is displaced and a concomitant colour change is observed. The results have shown that the probe is capable of selectively detecting carbon monoxide in cells

(treated with CORM-3 or hemin) and *in vivo* using mice with a subcutaneous air pouch as a model for inflammation.

In summary, for all the results above mentioned we can say that this PhD thesis constitutes an original scientific contribution to the development of supramolecular chemistry. Its results derived from the studies presented leaves open routes to continue the study and development of new hybrid materials and more efficient chemical sensors with biomedical and therapeutic applications.

Resumen

La presente tesis doctoral, titulada "*Nanotecnología y química supramolecular en procesos de liberación controlada y reconocimiento molecular para aplicaciones biomédicas",* se centra en dos temas importantes: el reconocimiento molecular y los procesos de liberación controlada.

Esta tesis doctoral está estructurada en cuatro capítulos.

El primer capítulo introduce el concepto de materiales híbridos orgánicos-inorgánicos funcionalizados con puertas moleculares y sus aplicaciones biomédicas como nanomateriales para dirigir y controlar la liberación controlada de fármacos. Además se introduce una breve descripción sobre sensors colorimétricos basados en la base de la quimica supramolecular, particularmente en los procesos de reconocimiento molecular.

En particular, el capítulo 2 describe la preparacion de cinco nanodispositivos que responden a enzimas. Estos materiales híbridos se componen de dos unidades principales: un soporte mesoporoso basado en sílice inorgánica, capaz de encapsular moléculas orgánicas y un compuesto orgánico anclado en la superficie externa del soporte mesoporoso inorgánico que actúa como puerta molecular. Todos los sistemas propuestos utilizan puertas moleculares peptídicas que responden a temperatura o enzimas como estímulo. Se ha descrito una breve reseña sobre péptidos en nanomedicina y sus múltiples aplicaciones como ligandos diana, sustratos de proteasas y como puertas moleculares. El primer ejemplo descrito se ha diseñado, síntetizado y caracterizado un sistema basado en nanopartículas de sílice mesoporosa de tipo MCM-41 y utilizando péptidos como puertas moleculares en las que la liberación de la molécula encapsulada dentro de los poros se logró mediante una transformación progresiva de la estructura del peptide de alfa-hélice a "*random*" como consecuencia de un aumento de la temperatura. El segundo ejemplo descritó se centra en el diseño, síntesis, caracterización y aplicaciones de un nuevo nanodispositivo que responde a

proteasas para la lograr una liberación controlada intracelular. El sistema consta de nanoparticulas de tipo MCM-41 cargadas y funcionalizadas con una secuencia peptídica diseñada para ser selectivamente hidrolizaza por la enzima “Catepsina B” en células tuorales. Se ha llevado a cabo estudios de viabilidad e internalización en células HeLa y estudios de liberación controlada de un agente quimioterapéutico. Del mismo modo, el cuarto ejemplo describe un sistema basado en un soporte de sílice mesoporoso funcionalizado con un péptido con el objetivo de liberar un fármaco para disminuir la muerte celular no deseada. En este caso, nos centramon en la enzima ”Caspasa 3” y se desarrolló un péptido que contiene una secuencia diana para esta enzima. Se describe la preparacion de MSN capaz de liberar selectivamente su carga en presencia de la enzima Caspasa 3 activada en el interior de las célualas, una vez que se ha inducido la apoptosis. El siguiente ejemplo describe un nuevo sistema de liberación controlada dirigida usando MCM-41 funcionalizadas con un peptide (derivado del peptide T22) con gran afinidad a un receptor (CXCR4) que se encuentra sobreexpresado en células de linfoma. Los resultados muestran que el peptide (T22) es capaz de dirigir a las nanopartículas a las células de linfoma que incorporar en receptor CXCR4 y facilitar la entrada al interior de la célula. El último ejemplo de este capítulo se centra en el desarrollo de un nanodispositivo sensible a proteasas como posible vehículo para la liberación controlada de fármacos en el interior de la célula. En este caso, las nanoparticulas se funcionalizaron con el polímero ε-poli-L-lisina que es degradabale en presenia de enzimas lisosómales en el interior cellular. El péptido utilizado (C9h) es capaz de impedir que se produzca la interacción entre caspasa-9 y PP2Ac α dando lugar a la inducción de la apoptosis. Las nanopartículas proporcionan protección a los péptidos contra la degradación y además permiten una reducción de dosis de hasta diez veces para observar un efecto apoptótico en comparación con la administración del péptido libre o en combinación con un péptido penetrante.

La segunda parte de esta tesis doctoral se centra en el diseño y desarrollo de un nuevo compuesto químico capaz de detectar monóxido de carbono *in vivo*. La

sonda se basa en un complejo de vinilo de rutenio (II) apto para uso en sistemas acuosos que lleva un ligando de 5- (3-tienil) -2,1,3-benzotiadiazol (TBTD) como unidad de señalización. Es un complejo coloreado y en presencia de CO, el TBTD se desplaza y se observa un cambio de color simultáneo. Los resultados demuestran que la sonda es capaz de detectar selectivamente monóxido de carbono en células (tratadas con CORM-3 o hemina) e *in vivo* utilizando ratones con una bolsa de aire subcutánea como modelo para la inflamación.

En resumen, para todos los resultados antes mencionados podemos decir que esta tesis doctoral constituye una contribución científica original al desarrollo de la química supramolecular. Sus resultados derivados de los estudios presentados dejan rutas abiertas para continuar el estudio y el desarrollo de nuevos materiales híbridos y sensors químicos más eficientes para aplicaciones biomédicas y terapeuticas.

Resum

La present tesi doctoral, titulada "Nanotecnologia i química supramolecular en processos d'alliberament controlat i reconeixement molecular per a aplicacions biomèdiques", es centra en dos temes importants de la química: el reconeixement molecular i els processos d'alliberament controlat.

Aquesta tesi doctoral està estructurada en quatre capítols.

El primer capítol introdueix el concepte de materials híbrids orgànics-inorgànics funcionalitzats amb portes moleculars i les seves aplicacions biomèdiques com nanomaterials per dirigir i controlar l'alliberament controlat de fàrmacs. A més s'introdueix una breu descripció sobre sensors colorimètrics fonamentats en la base de la química supramolecular, particularment en els processos de reconeixement molecular.

En particular, el capítol 2 descriu la preparació de cinc nanodispositius que responen a enzims. Aquests materials híbrids es componen de dues unitats principals: un suport mesoporos basat en sílice inorgànica, capaç d'encapsular molècules orgàniques i un compost orgànic ancorat a la superfície externa del suport mesoporós inorgànic que actua com a porta molecular. Tots els sistemes proposats utilitzen portes moleculars peptídiques que responen a temperatura o a enzims com a estímul. S'ha descrit una breu ressenya sobre pèptids en nanomedicina i les seves múltiples aplicacions com lligands diana, substrats de proteases i com a portes moleculars. En el primer exemple descrit s'ha dissenyat, sintetitzat i caracteritzat un sistema basat en nanopartícules de sílice mesoporosa de tipus MCM-41 i s'ha utilitzat pèptids com portes moleculars en les que l'alliberament de les molècules encapsulades dins dels porus s'aconsegueix mitjançant una transformació progressiva de l'estructura del peptide d'alfa-hèlix a "random" com a conseqüència d'un augment de la temperatura. El segon exemple descrit es centra en el disseny, síntesi, caracterització i aplicacions d'un nou

nanodispositiu que respon a proteases per a la aconseguir un alliberament controlat intracel·lular. El sistema consta de nanoparticules de tipus MCM-41 carregades i funcionalitzades amb una seqüència peptídica dissenyada per ser selectivament hidrolitzada per l'enzim "catepsina B" en cèl·lules tumorales. S'ha dut a terme estudis de viabilitat i internalització en cèl·lules HeLa i estudis d'alliberament controlat d'un agent quimioterapèutic. De la mateixa manera, el quart exemple descriu un sistema basat en el mateix tipus de suport funcionalitzat amb un pèptid amb l'objectiu d'alliberar un fàrmac per disminuir la mort cel·lular no desitjada. En aquest cas, ens vam centrar en l'enzim "Caspasa 3" i es va desenvolupar un pèptid que conté una seqüència diana per aquest enzim. Es descriu la preparació de MCM-41 capaç d'alliberar selectivament la seva càrrega en presència de l'enzim Caspasa 3 activat a l'interior de les cèl·lules, una vegada que s'ha induït l'apoptosi. El següent exemple descriu un nou sistema d'alliberament controlat dirigit usant MCM-41 funcionalitzades amb un peptid (derivat del peptid T22) amb gran afinitat a un receptor (CXCR4) que es troba sobreexpressat en cèl·lules de limfoma. Els resultats mostren que aquest peptid és capaç de dirigir a les nanopartícules a les cèl·lules de limfoma que expressen el receptor CXCR4 i facilitar l'entrada a l'interior de la cèl·lula via receptor. L'últim exemple d'aquest capítol es centra en el desenvolupament d'un nanodispositiu sensible a proteases com a possible vehicle per a l'alliberament controlat de fàrmacs a l'interior de la cèl·lula. En aquest cas, les nanoparticules es funcionalitzaren amb el polímer ε-poli-L-lisina que és degradable en presencia d'enzims lisosomals a l'interior cel·lular. El pèptid utilitzat (C9h) és capaç d'impedir que es produeixi la interacció entre caspasa-9 i el domini PP2Ac α donant lloc a la inducció de l'apoptosi. La finalitat de les nanopartícules en aquest treball es proporcionar protecció al pèptids contra la seva degradació i a més permetre una reducció de la seua dosis de fins a deu vegades per tal de observar un efecte apoptòtic en comparació amb l'administració del pèptid lliure o en combinació amb un pèptid penetrant.

La segona part d'aquesta tesi doctoral es centra en el disseny i desenvolupaent d'un nou compost químic capaç de detectar monòxid de carboni in vivo. La sonda

es basa en un complex de vinil de ruteni (II) apte per a ús en sistemes aquosos i un lligant de 5- (3-tienil) -2,1,3-benzotiadiazol (TBTD) com a unitat de senyalització. És un complex coloreat i en presència de CO, la molécula de TBTD es desplaça i s'observa un canvi de color simultani. Els resultats demostren que la sonda és capaç de detectar selectivament monòxid de carboni en cèl·lules (tractades amb CORM- 3 o hemina) i in vivo utilitzant ratolins amb una bossa d'aire subcutània com a model de inflamació.

En resum, per a tots els resultats abans mencionats podem dir que esta tesi doctoral constituïx una contribució científica original al desenvolupament de la química supramolecular. Els seus resultats derivats dels estudis presentats deixen rutes obertes per a continuar l'estudi i el desenvolupament de nous materials hibrids i sensors químics més eficients per a aplicacions biomèdiques i terapeutiques.

Abbreviation and Acronyms

A

AB. Azobencene.

AD. Alzheimer's disease.

AP. 3-aminopropyl.

AR. Aspect-ratio.

ATP. Adenosine triphosphate**.**

AUC. Area Under Concentration.

B

B-CD. β-cyclodextrin.

BET. Brunauer, Emmett and Teller Model.

BHJ. Barrett, Joyner and Halenda Model.

BN. Mammalian Bombesin.

BRS3. Bombesin Receptor Subtype 3.

BSA. Bovine Serum Albumin.

C

CAPs. Cancer associated proteases.

CD. Cyclodextrin.

CD.GOx. Cyclodextrin modified-glucose oxidase.

CdS. Cadminum sulfide**.**

CBPQT^{4+}. Cyclobis (paraquat-p-phenylene**).**

CLSM. Confocal Laser Scanning Microscopy.

CMC. Critical Micelle Concentration.

CPT. Camptothecin

CQ. Clioquinol.

CRT. Control Release technology.

CTAB. Hexadecyltrimethylammonium Bromide.

CytC. Cytocrome C.

D

DDS. Drug Delivery System.

DHLA. Dihydrolopoic acid.

DLS. Dynamic light scattering.

D-MEM. Dulbecco's Modified Eagle's Medium.

DMF. Dimethylformamide.

DIEA. Diisopropylehylamine.

DMHA. N,N- Dimethylhexadecylamine.

DNA. Deoxyribonucleic acid**.**

DOTA. 1,4,7,10- tetraazacyclododecane-1,4,7,10- tetraacetic acid.

DOX. Doxorubicin.

DTPA. Diethylenetriaminopentaacetic acid.

DTT. Dithiothreitol.

E

ECM. Extra cellular matrix

EPR. Enhanced permeability and retention.

ε-PL. ε-poly-L-lysine.

F

FA. Folic acid.

FAP. N-folate-3-aminopropyl.

FDA. Food and drug administration.

FITC. Fluoescein isothiocyanate.

FMNPs. Ferrocene-based Mechanized nanoparticles.

FMOC. Fluorenylmethyloxycarbonyl.

G

GCPRs. G protein-coupled receptors.

GOS. Galacto-oligosaccharide.

GP. Guanidinopropyl.

Gr. Human granzyme.

GRPR. Gastrin-releasing peptide receptors.

GSH. Glutathione.

H

HA. Hyaluronic acid.

HE. Hematoxylin and eosin.

HIFU. High intensity focused ultrasound.

HPLC. High Performance Liquid Cromatography.

I

IB. Ibuprofen.

ICP. Intrinsically conducting polymers.

IgC. Inverse gas chromatography.

IR. Infra Red.

IUPAC. International Union of Pure and Applied Chemistry.

L

LAMP1. Lysosomal-associated membrane protein 1.

LDLr. Low-density lipoprotein receptor.

LEUS. Low energy ultrasound.

LHRH. Luteinizing hormone releasing hormone.

LRET. Luminiscence resonance energy transfer.

M

MCM. Mobile Crystalline Material.

MMP. Matrix metalloproteinases.

MRI. Magnetic Resonance Imaging.

MSN. Mesoporous Silica Nanoparticles.

MTX. Methotrexate.

N

NE. Neuroendocrine cells.

NK. Natural killer cells.

NLO. Non linear optical.

NMBR. Neuromedin B receptor.

NPS. Nanoparticles.

NSPS. Neutrophil serine proteases

P

PA. Peptide amphiphile.
PAH. Poly (allylamine hydrochloride).
PBA. Phenylboronic acid.
PBS. Phosphate-Buffered Saline.
PCI. Photochemical internalization.
PDC. Peptide based drug conjugated.
PDSM. Poly(dimethylsiloxane).
PEG. Polyethylene glycol.
PEI. Polyethylenimine.
PEM. Polyelectrolyte multilayers.
PLGA. Poly (glutamic acid).
PNIPAm. Poly(N-isopropylacrylamide).
PR3. Proteinase 3.
PS. Photosensitizers.
PVP. Poly(2-vinylpyridine).
PXRD. Powder X-Ray diffraction.

Q

QD. Quantum dots.

R

RGD. Arninine-Glycine-Aspartic acid.
RITC. Rhodamine B isothiocyanate.
RNA. Ribonucleic acid.

ROS. Reactive Oxygen Species.

RGD. Arginine-Glycine-Aspartic acid**.**

Ru(bipy)$^{2+}$. Tris(2,2'bipytidyl)Ruthenium(II).

S

SA-β-Gal. Senescence associated β-Galactosidase.

SBA. Santa Barbara Amorphous Material.

SCE. Saturated Calomel Electrode.

SEM. Scanning Electron Microscopy.

SMCC. Succinimidyl 4-Nmalemidomethyl cyclohexane-1-crboxylate.

T

T2DM. Type 2 diabetes mellitus.

TAT. The trans-activator of transcription.

TDD. Targeted drug delivery.

TEM. Transmission Electron Microscopy.

TEOS. Tetraethoxysilane.

Tf. Transferrin.

TFA. Trifluoroacetic acid.

TGA. Thermogravimetric analysis.

TMB. 1,3,5- Trymethylbenzene.

TMOS. Tetramethoxysilane.

TUNEL. Terminal deoxynucleotidyl transferase dUTP nick end labeling.

T2DM. Type 2 diabetes mellitus.

U

UCNP. Upconversion nanoparticle.

UPA. Urokinase plasminogen activator.

UV. Ultraviolet.

UVM. Universidad Valencia Material.

W

WST-1. 4-[3-(4-iodophenyl)-2-(4-nitro-phenyl)-2H-5-tetrazolo]-1,3-benzenedisulfonate (reagent for cell proliferation assasys).

X

XRD. X-Ray diffraction

Table of Contents

*1.*General introduction

1.1 Nanotechnology

Nanotechnology is a theoretical and experimental field of applied science and technology. It is an engineering of functional systems at the molecular level, covers a broad range of topics and is focused on controlling and exploiting the structure of matter on a scale below 100 nanometers. The word 'Nano' derives from the Greek word 'Nanos', which means dwarf or extremely small. Nanotechnology is sometimes referred to as a *general-purpose technology*. That's because in its advanced form it will have significant impact on almost all industries and all areas of society. It will offer better built, longer lasting, cleaner, safer, and smarter products for the home, for communications, for medicine, for transportation, for agriculture, and for industry in general.

As is the case with many other disciplines, applications of nanotechnology (for example, in making steel and creating paintings) were in use centuries before the field was formally defined. Early contributors to the field include James Clark Maxwell (Scottish physicist and mathematician, 1831-1879) and Richard Adolf Zsigmondy (Austrian-German chemist, 1865-1929). Zsigmondy studied *colloids* (chemical mixtures where one substance is dispersed evenly throughout another) and looked at gold sols and other nanomaterials. Other important contributors in the first half of the 20th century include Irvin Langmuir (American chemist and physicist, 1881-1957) and Katherine B. Blodgett (American physicist, 1898-1979), the first woman to get a Ph.D. studying Physics at the University of Cambridge.

The earliest systematic discussion of nanotechnology is considered to be a speech given by Richard Feynman (American physicist, 1918-1988) in 1959. It was titled: "There's Plenty of Room at the Bottom." In this speech Feynman discussed the importance "of manipulating and controlling things on a small scale" and how they could "tell us much of great interest about the strange phenomena that occur in complex situations." He described how physical phenomena change their

manifestation depending on scale, and posed two challenges: the creation of Nanotechnology is a theoretical and experimental field of applied science and technology.

The term 'nanotechnology' was used first by the Japanese scientists Norio Taniguchi (1912-1999) in a 1974 paper on production technology that creates objects and features on the order of a nanometer. The American engineer K. Eric Drexler (b. 1955) is credited with the development of molecular nanotechnology, leading to nanosystems machinery manufacturing.

The invention of scanning tunneling microscope in the 1980s by IBM Zurich scientists and then the atomic force microscope allowed scientists to see materials at an unprecedented atomic level. The availability of more and more powerful computers around this time enabled large scale simulations of material systems. These studies provided insight into nanoscale material structures and their properties. The complementary activities of modeling and simulation, atomic scale visualization and characterization, and experimental synthesis fueled nanoscale research tasks in the 1980s.

Tailoring the properties of materials on a molecular level offers the potential for improvement in device performance for applications across the entire range of human activity: from medicine to cosmetics and food, from information and communication to entertainment, from earth-bound transport to aerospace, from future energy concepts to environment and climate change, from security to cultural heritage. Nanomaterials will lead to a radically new approach to manufacturing materials and devices. Faster computers, advanced pharmaceuticals, controlled drug delivery, biocompatible materials, nerve and tissue repair, crackproof surface coatings, better skin care and protection, more efficient catalysts, better and smaller sensors, even more efficient telecommunications, these are just some areas where nanomaterials will have a major impact. In summary, nanomaterials have been increasingly incorporated into consumer products, although research is still ongoing on their potential

effects to the environment and human health. This research will continue long into the future. Nowadays nanotechnology has potential applications in many sectors and in addition, presents new opportunities to improve how we measure, monitor and manage. Nanotechnology has emerged as a growing and rapidly changing field. [1,2]

1.2. Organic-inorganic hybrid nanomateriales

In the past twenty years, sol-gel science and technology have undergone remarkable development. The several stages of the sol-gel processes have been scrutinized in considerable detail and established a strong basis for technological development. A turning point was reached with the emergence of organic-inorganic nanocomposites, synthesized through sol-gel processes, which opened gateway to whole classes of new materials.

In 1985, Wilkes and co-workers described the preparation of new organic-inorganic hybrid materials by reacting metal alkoxides with end-functionalized condensational polymeric/oligomeric species through a sol-gel process. At this respect, the authors incorporated poly(dimethylsiloxane) (PDMS) oligomers into one silica matrix.[3] Later, in 1990, Wei and co-workers were able to synthesize hybrid materials based on several metal oxides functionalized with certain vinyl-based polymers.[4] An important landmark in the sol-gel science was the work published by Kresge and co-workers in 1992. The authors prepared ordered mesoporous silica oxides by templating silica species with surfactant molecules.[5] These new materials, known under the group name M41S (with the hexagonal MCM-41 being the most prominent member), dramatically expanded the range of pore sizes accessible in the form of an ordered porous system. Then, research in this area has been extended to the preparation of porous metal oxides and also to the functionalization of the inorganic support with selected (bio)organic moieties (either on the external surface, inside the pores wall, or entrapped within the channels).

Organic-inorganic hybrid composites are one of the most important classes of synthetic engineered materials. A nanocomposite is an interacting mixture of two phases, one of which is in the nanometer size range, typically, 1-20 nm in at least one dimension.[6] Thus, a composite is a material formed by two or more physically distinct components, mixed with the intention of achieve better properties than that of a single homogeneous material. Aside from the intrinsic physical properties of the components, composite materials can also display new features as a result of the nature and degree of interfacial interaction between the two species. One of the frontiers in composites engineering is the development of viable methods for the efficient design and synthesis of organic-inorganic hybrids with nanometer scale architectures.

Organic and inorganic materials are usually quite different from each other in their properties. Inorganic materials, such as glass and ceramics, are hard but not impact resistant, that is, they are brittle, whereas organic polymer/oligomers are resilient. However, organic polymers generally suffer several inherent drawbacks such as instability to heat and tendency of natural degradation upon aging. In general, inorganic species usually have good mechanical and thermal stability as well as optical properties. On the other hand, organic moieties would provide flexibility, toughness, hydrophobicity and new electronic or optical properties. The properties of organic-inorganic hybrid materials are not only the sum of the individual contributions of both phases, but the role of their inner interfaces could be predominant.

Due to the new features of these nanocomposite materials, that are non-present in the traditional macroscale composites, the preparation, characterization, and applications of these organic/inorganic hybrids have become a fast expanding area of research in materials science. However, since the traditional processing conditions for inorganic materials usually involve high temperature, the survival of organic compounds is completely impossible. Thus,

the mild-conditions of sol-gel processes slowly gained popularity for the synthesis of organic- inorganic hybrid materials.

The sol-gel process, which is mainly based on inorganic polymerization reactions, is a chemical synthesis method initially used for the preparation of inorganic materials such as glasses and ceramics. Their unique low temperature synthesis condition allows it to be well adopted for the preparation of organic-inorganic hybrid materials and have proven to be effective. It brings both inorganic and organic components into intimate mixing that lead to new morphologies and unique properties. Several different methods can be used in the preparation of these hybrid materials.

The scope of research and applications of these hybrid materials have ranged from inorganically modified organic polymers to inorganic glasses modified by organic compounds. Potential applications for these materials include: scratch and abrasive resistant coatings,[7] electrical and nonlinear optical (NLO) properties,[8] adhesives and contact lens materials,[9] reinforcement of elastomers and plastics,[10] catalyst and porous supports,[11] adsorbents,[12] hybrid solid-state dye laser and chemical/biomedical sensory materials,[13] and photochromic hybrid materials.[14] These multifunctional materials constitute a golden gate giving access to a large variety of tunable systems and devices. Moreover, the combination of supramolecular chemistry, inorganic solids, and nanotechnology has already led to significant advances in many areas such as sensing, controlled motion, and delivery.

1.2.1. Mesoporous materials as inorganic scaffolds

In the last century, porous materials with large specific surface areas have been attracted considerable research attention due to their potential applications in areas such as adsorption,[15] separation,[16] catalysis,[17] gas storage [18] and sensor technology[19]. According to their pore sizes, porous materials are classified by the International Union of Pure and Applied Chemistry (IUPAC) as microporous

(pore size < 2 nm), mesoporous (pore size in the 2–50 nm range) and macroporous (pores size > 50 nm) materials. The properties of these materials and thus, their suitability for different applications depend, to a large extent, on the characteristics of the porous system. Therefore, the development of new methodologies for the synthesis of materials with specific porosity architectures has been extensively explored.

In 1992, researchers at Mobil Corporation discovered the M41S family of silicate/aluminosilicate mesoporous molecular sieves with exceptionally large uniform pore structures and later they were produced at Mobil Corporation Laboratories.[20-22] The synthesis of this family of mesoporous materials is based on the combination of sol-gel processes and templating features of surfactants. The template agent used is no longer a single, solvated organic molecule or metal ion, but rather a self-assembled surfactant molecular array. Three different mesophases in this family have been identified, i.e., lamellar (MCM-50), hexagonal (MCM-41), and cubic (MCM-48) phases. These new silicate materials possess extremely high surface areas and narrow pore size distributions.[23] Rather than an individual molecular directing agent participating in the ordering of the reagents forming the porous materials, assemblies of molecules, dictated by solution energetics, are responsible for the formation of these porous systems. This supramolecular directing concept has led to a family of materials whose structure, composition, and pore size can be tailored during synthesis by variation of the reactant stoichiometry, the nature of the surfactant molecule, the auxiliary chemicals, the reaction conditions, or by post-synthesis functionalization techniques. These materials present an orderly arrangement of pores, with a very homogeneous pore size, whose average value falls within the 2-10 nm range. Moreover, they have a high pore volume, in the order of 1 $cm^3\ g^{-1}$ and a specific surface area between 500 and 1000 $m^2\ g^{-1}$. Those M41S materials are featured by high chemical inertness and thermal stability. Last but not least, the material synthetic procedure is well described and requires inexpensive and nonhazardous precursors. The peculiarity of presenting all this whole range of properties makes

these materials ideal supports for adsorption processes of small molecules**. Figure 1.1** shows the different structures of the M41S family components.

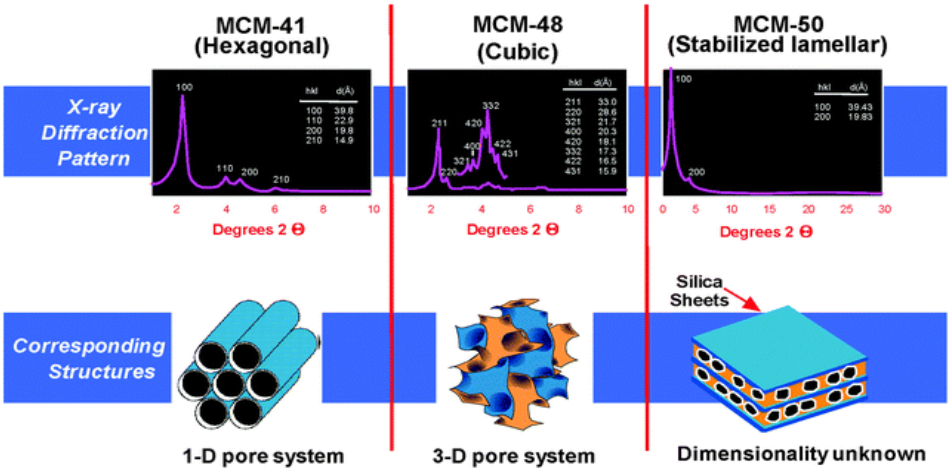

Figure 1.1. Structures of mesoporous silica materials: MCM-41 (hexagonal), MCM-48 (cubic) and MCM-50 (lamellar) and its X-ray diffraction patterns. *(Reprinted with the permission from C.T. Kresge and W.J.Roth, Chem. Soc. Rev., 2013 ,42, 3663-3670. Copyright © 2013 The Royal Society of Chemistry*).

Inside the M41S family, the hexagonal mesophase, denoted as MCM-41, possesses highly regular arrays of uniform-sized channels whose diameters are in the range of 15–100 Å depending on the templates used, the addition of auxiliary organic compounds, and the reaction parameters. The pores of this material are nearly as regular as zeolites, however, they are considerably larger than those present in crystalline materials thus offering new opportunities for applications in catalysis, chemical separation, adsorption, and advanced composite materials.

MCM-41 has been investigated extensively because the other members in this family are either thermally unstable or difficult to obtain.[24] In 1998 another siliceous material with a hexagonal array of pores namely Santa Barbara Amorphous nº 15 (SBA-15) was prepared.[25] This SBA-15 mesoporous material has not only larger pores (from 4.6 to 30 nm) than that of MCM-41, but also thermal,

mechanical and chemical resistance features and that makes it a preferable choice for use as a catalyst (see **Figure 1.2**). The formation of ordered uniform pores up to 30 nm was accomplished using amphiphilic triblock copolymers in strong acidic media.[26]

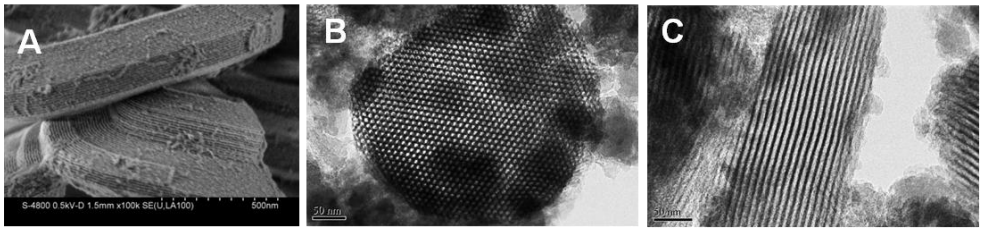

Figure 1.2. SEM image (A) and TEM images (B and C) of Mesoporous Silica Molecular SBA-15 from ACS Material Advanced Chemical Supplier.

Porous materials created by nature or by synthetic design have found great utility in all aspects of human activities. Since the discovery of these ordered mesoporous materials, formed by the self-cooperative assembly of inorganic species and organic surfactants, researchers have aimed to understand and improve their structures to obtain forms suitable for different applications. Mesoporous silica, in its many forms, adsorbs a wide range of compounds. Due to their highly organized porosity, high surface area, high pore volume, tailorable pore size, wall thickness, chemical nature and morphology these are attractive materials for applications in catalysis, filtration and separation, gas adsorption and storage, chemical/biochemical sensing, enzyme immobilization, biomedical tissue regeneration and drug delivery.[27]

1.2.2. Synthesis of mesoporous materials

The structural phase of mesoporous materials is based on the fact that surfactant molecules are active components with variable supramolecular structures that changed with its concentration.[28] At low concentrations, the surfactants energetically exist as single molecules. With increasing concentration,

surfactant molecules combine together to form micelles in order to decrease the system entropy.[29] The critical micelle concentration (CMC) is defined as the concentration of surfactant above which the single molecules aggregate to form isotropic micelles. In the micelle core, which is essentially liquid hydrocarbon, there is greater freedom for movement and so the entropy associated with the hydrocarbon tails also increase. The next step in the process is the coalescence of the adjacent, mutually parallel cylinders to produce the lamellar phase. In some cases, the cubic phase also appears prior to the lamellar one. The cubic phase is generally believed to consist of complex, interwoven networks of rod-shaped aggregates.[27[

The formation of a particular phase in a surfactant aqueous solution depends not only on the concentration but also on the nature of the surfactant. At this respect the length of the hydrophobic carbon chain, the hydrophilic head group, and the counter ion (in the case of ionic surfactants) are also important factors. Moreover, also depends on environmental parameters, such as pH, temperature, ionic strength, solvent, and other additives (*i.e.*, organic compounds). Generally, the CMC decreases with the increase of the surfactant chain length due to the enhancement of the negative free energy of micellisation. Increasing the ionic strength in the solution and the valence of the counter ions lead also to a reduction in the CMC. On the other hand, the CMC increases with the growing of counter ion radius, pH, and temperature. Also, it is known that non-ionic surfactants generally exhibit lower CMC than its ionic counterparts.

It is important to note that a high surfactant concentration, high pH, low temperature, and low degree of silicate polymerization always support the formation of cylindrical micelles as well as the hexagonal mesophases. The mesophases are formed by interaction of the organic parts with inorganic species, and thus both components play a crucial role in the assembly. The possible types of interactions between the organic and the inorganic parts that drive the formation of the mesophases depend on the charge on the surfactant (S^+ or S^-), on the inorganic species (I^+ or I^-), and on the presence of mediating ions, (*i.e.*, X^-

or M^+). All permutations enabling Coulombic attraction are possible, *i.e.*, S^+I^-, S^-I^+, $S^+X^-I^+$ or $S^-M^+I^-$.

Sol-gel reactions are those which convert an aqueous metal alkoxide [$Mn^+(OR)_n$] solution into an inorganic network. The sol-gel method is also capable of producing homogeneous, high purity inorganic oxide glasses at room temperature, much lower than the high temperatures required by the conventional glass manufacturing process. For example, silica can be obtained from melt processing glass, but the sol-gel method is more effective for the production of amorphous silica. Another advantage of the sol-gel procedure is its ability to produce silica in different forms such as molded gels,[30] spun fibers,[31] thin films,[32] molecular cages,[33] aerogels and xerogels,[34] and mesoporous materials.[35,36] Therefore, changing the conditions of sol-gel polymerization and processing is helpful for controlling the bulk properties of silica. The sol-gel process involves transformation of a "sol" to a "gel". A "sol" is defined as a colloid of small particles that are dispersed into a liquid. A "gel", on the other hand, is a rigid non-fluid mass and is usually a substance made up of a continuous network including a continuous liquid phase.[37]

Therefore, sol-gel reactions involve hydrolysis and condensation reactions of inorganic alkoxide monomers in order to obtain colloidal particles ("sol") and consequently convert them into a network ("gel"). A metal or metalloid element bound to various reactive ligands represents the precursor used to synthesize the colloids. Metal alkoxides are the reagents most used for this purpose due to their ease of hydrolysis in the presence of water. Alkoxysilanes, such as tetramethoxysilane (TMOS) and tetraethoxysilane (TEOS), are extensively used for the production of silica gels. Aluminates, titanates, and zirconates, however, are usually used for the synthesis of alumina, titania, and zirconia gels, respectively.

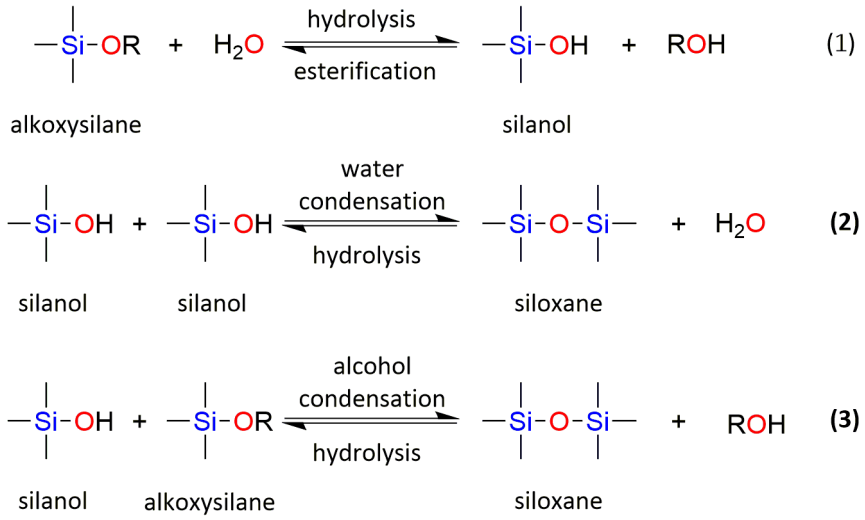

Scheme 1.1. Sol-gel general reaction mechanism.[*Materials* **2012**, *5]*.

Scheme 1.1 displays the involved hydrolysis and condensation reactions of an alkoxysilane. The hydrolysis step takes place by the addition of water to the alkoxysilane solution under neutral, acidic, or basic conditions. The hydrolysis step, equation 1 in **Scheme 1.1**, leads to the generation of a silanol group (Si–OH). The mechanism of hydrolysis is catalyst dependent while its rate depends on the pH value, the water-alkoxide ratio, and the solvent used. Since alkoxysilanes are not water-soluble, an organic co-solvent is required to facilitate the hydrolysis step. [37]

In the second step, the silanol group condenses with either an alkoxide or another silanol group (reactions in equations 2 and 3 in **Scheme 1.1**) to build a strong siloxane linkage (Si–O–Si) with the loss of either an alcohol (ROH) or a water molecule. As the number of Si–O–Si bridges increases, the siloxane particles can aggregate into a “sol”, which disperses in the solution into small silicate clusters. Condensation of the latter silicate clusters leads to the formation of a network (a “gel”), trapping the water and the alcohol by-products. The rates and mechanisms of hydrolysis and condensation reactions are strongly affected by the identity of the catalyst.

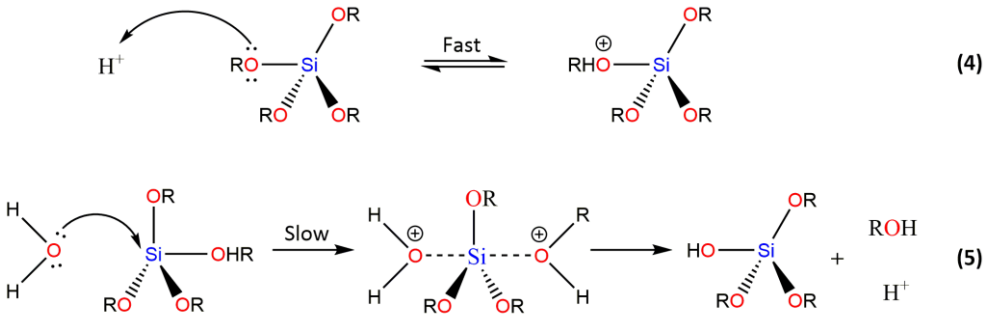

Scheme 1.2. Hydrolisis mechanism of an alkoxysilane using acidic catalyst.

In acid catalysis (**Scheme 1.2**), the first step in hydrolysis (**Equation 4**) is electrophilic attack of the proton on an alkoxide oxygen atom, leading to the development of a positive charge on it. The rate-controlling step in acid hydrolysis (**Equation 5**) is an SN_2 nucleophilic attack of water oxygen on the silicon from the backside. This latter nucleophilic attack results in the formation of a penta-coordinate transition state in which the silicon center is partially bonded to both –OH_2 and –OHR. It was found that the hydrolysis reaction was first-order with respect to water concentration under acidic conditions.

In the condensation mechanism in acid catalysis (**Scheme 1.3**), the first step is the fast step and is an electrophilic attack of the proton on the oxygen of the silanol group (**Equation 6**). This attack results in the silanol oygen becoming positively charged. The second step (**Equation 7**) is the formation of a siloxane bridge via the loss ofa hydronium cation (the catalyst) as a result of the condensation between a protonated silanol groups with an unprotonated one. The mechanism of condensation under acidic conditions is depited in **Scheme 1.3.**

When a base catalyst is used for the formation of silica, the hydroxide ion serves as a nucleophile that attacks the silicon atom center of the tetraalkoxysilane in an SN_2 hydrolysis step (see **Scheme 1.4**).[39] The result of this step is a silanol and an alkoxide ion (**Equation 8**). Abstraction of the silanol proton by the hydroxide ion is the first step in the condensation process (**Equation 9**),

leading to the formation of siloxide ion and water. A siloxane linkage is then formed through the SN_2 attack of the latter ion on the silicon center of silanol (**Equation 10**).

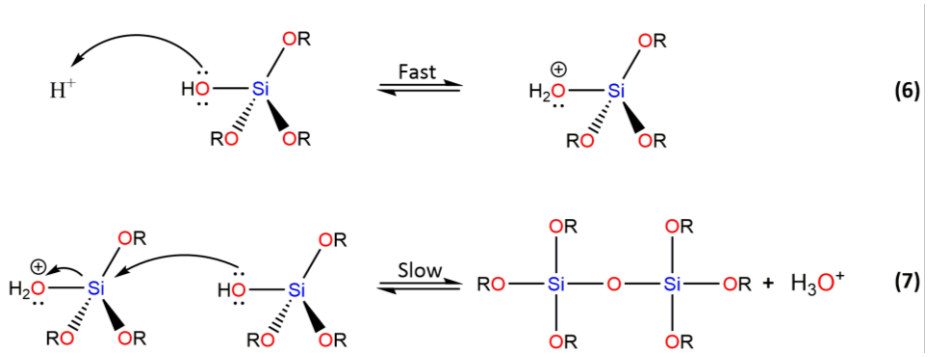

Scheme 1.3. Condensation mechanism of an alkoxysilane using acidic catalyst.

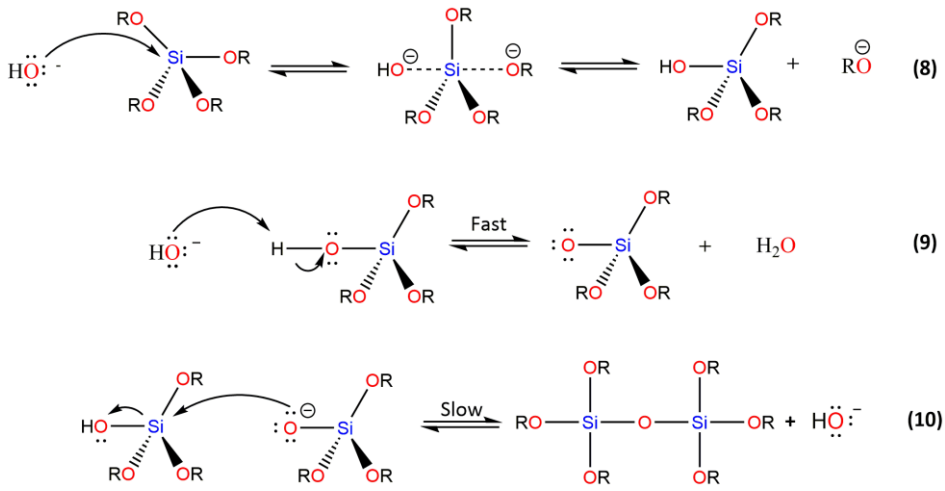

Scheme 1.4. Hydrolysis mechanism and condensation mechanism of an alkoxysialne using basic catalyst.

One of the most used procedures to obtain colloidal mesoporous silica is the Stöber method.[40-43] This method used several bases (KOH, NaOH, ammonia,

triethanolamine) and a silica source (tetraetylortosilicate, TEOS) to prepare mesoporous silica nanoparticles with diameters in the 20-150 nm interval. Besides, cetyltrimethylammonium bromide (CTAB) is used as structure directing agent (template) for the preparation of MCM-41 based nanoparticles. Although the pore size of mesoporous silica nanoparticles could be controlled somewhat by varying the alkyl chain length of homologs of quaternary ammonium surfactants, the range is rather limited (1.8 to 2.3 nm). To further expand the pore size of the nanoparticles *N*,*N*-dimethylhexadecylamine (DMHA) and 1,3,5-trimethylbenzene (TMB) as swelling agents were used to synthesize pore-expanded materials.[44,45]

Once the final templated material is prepared, CTAB was removed from the silicate lattice by calcination or by solvent extration. ***Calcination*** is the burning out of the template under conditions which do not greatly affect the integrity of silicate structure. This has the advantage of ensuring the removal of all carbonaceous material, but also causes a significant shrinkage in the MCM-41 lattice parameter. The temperature used for calcination does not appear to affect the quality of the product greatly. Shrinkage of up to 25% in the lattice constant has been observed after calcination, although pore collapse occurs only after heating to temperatures of 900^{o}C in dry air. Other effective technique for structure directing agent removal is ***washing*** out the template by boiling in HCl/ethanol mixtures. It causes less lattice shrinkage than the calcination method. Template removal by washing in acidic ethanol has been shown to be more successful in mesoporous silicates made via neutral templating routes than by ionic templating. There is however, debate as to whether some template remains in the structure after such treatments.

The MCM-41 synthesis is schematically represented in **Figure 1.3**. As explained before, the synthesis consists of the polymerization of TEOS around supra-micellar-template previously formed in basic water solution. Then, the subsequent removal of the surfactant gives the final mesoporous inorganic scaffold with cylindrical unidirectional empty channels arranged in a hexagonal distribution.

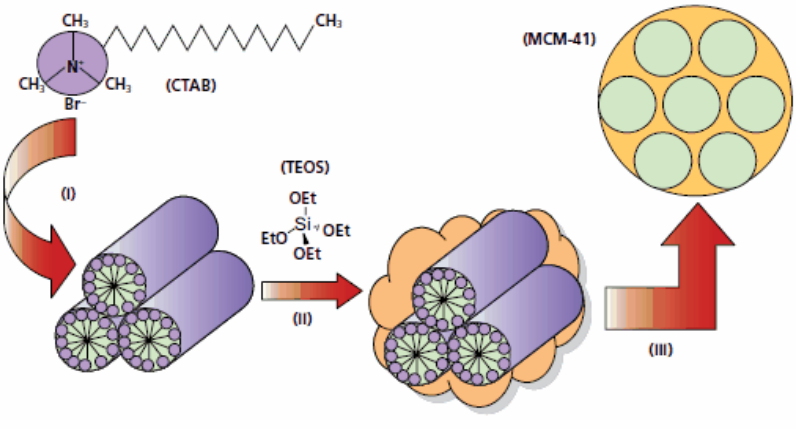

Figure 1.3. Schematic of the classical mesoporous silica (MCM-41) synthesis route. **(i)** Surfactant, e.g. cetyltrimethylammonium bromide is used to form liquid crystalline micelles in water. **(ii)** Sol-gel precursor, e.g. tetraethylorthosilicate (TEOS) is added to this micellar solution to make, upon hydrolyses and condensation, a silica network around the micelles. **(iii)** Removal of the organic template by thermal treatment (calcination) or solvent extraction yields a mesoporous material, in this case hexagonally ordered MCM-41 silica framework.

1.2.3. Functionalization of mesoporous materials

One important way of modifying the physical and chemical properties of mesoporous silica materials is the incorporation of organic, supramolecular or biological components, either on the external or internal surface of the inorganic support or entrapped within the channels.

Anchoring organic groups in mesoporous materials (functionalization) allows the tuning of surface properties (such as hydrophilicity, hydrophobicity, acidity, basicity and binding behavior with certain molecules), alteration of the surface reactivity, protection of the surface from chemical attack, and modification of the bulk properties of the materials while at the same time stabilizing them towards

hydrolysis. Surface functionalized mesoporous materials are of great interest because of their potential applications in various areas such as catalysis, adsorption, chromatography, nanotechnology, metal ion extraction, and molecular recognition. For example, mesoporous silica functionalized with thiol groups in the inner pore surface showed high adsorption efficiency for heavy metals such as Hg(II), Ag(I), and Cd(II).[46-49] Besides, sulfonic acid moieties grafted onto mesoporous materials exhibited high catalytic activity for selective formation of bulky organic molecules.[50,51]

Mesoporous materials are interesting supports for organic functional groups due to their high surface area, large and uniform pore size, and narrow pore size distribution. While the silica framework provides thermal and mechanical stability, the surface organic moieties provide control of interfacial and bulk material features. There are several methods for functionalizing mesoporous solids (such as MCM-41) with organic moieties but the most used are ***grafting*** and ***co-condensation***.

1.2.3.1. Grafting

In post-synthesis grafting method the pore wall surface of the pre-fabricated inorganic mesoporous scaffold is modified with alkoxysilane derivatives after the surfactant removal. In the process of grafting mesoporous supports, the surface silanol groups (Si-OH), which can be present in high concentration, act as convenient anchoring points for organic functionalization. (See **Figure 1.4**)

Surface functionalization with organic groups by grafting is most commonly carried out by silylation, which is accomplished by one of the three reactions (**equations 11 to 13**). Silylation occurs on free (≡Si-OH) and geminal silanol ($=Si(OH)_2$) groups, but hydrogen bonded silanol groups are less accessible to modification because they form hydrophilic networks among themselves. The original structure of the mesoporous support is generally maintained after grafting.

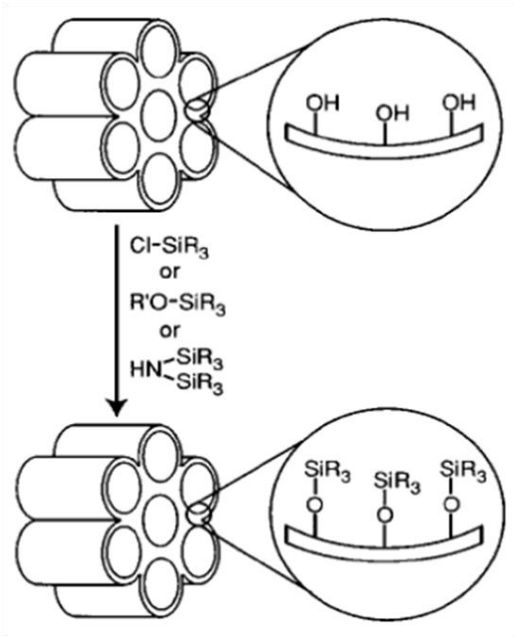

Figure 1.4. Functionalization of a previously prepared mesoporous support by grafting procedure. Reproduced from A. Stein, B.J. Melde, R.C. Schroden*, Adv. Mater*. 2000, 12, 1403-1419, with permission from The Royal Society of Chemistry.

$$\equiv Si-OH + Cl-SiR_3 \longrightarrow \equiv Si-OSiR_3 + HCl\cdot base \quad \textbf{(11)}$$

$$\equiv Si-OH + R'O-SiR_3 \longrightarrow \equiv Si-OSiR_3 + HOR' \quad \textbf{(12)}$$

$$2 \equiv Si-OH + HN(SiR_3)_2 \longrightarrow 2 \equiv Si-OSiH_2R_3 + NH_3 \quad \textbf{(13)}$$

Scheme 1.5. The silylation reaction for the modification of the surface of mesoporous silica .

Mesoporous supports present two different surfaces (the inner and the outer of the mesopores) and both types can be functionalized. In the grafting protocol the external surface is more accessible and is functionalized predominantly over

the internal mesopore surface. The functional groups on the external surface are also more accessible in subsequent reactions, leading to reduced selectivities in processes that benefit from pore confinement. Controlled dual functionalization has been achieved by two different site-selective grafting strategies (**Figure1.5**).

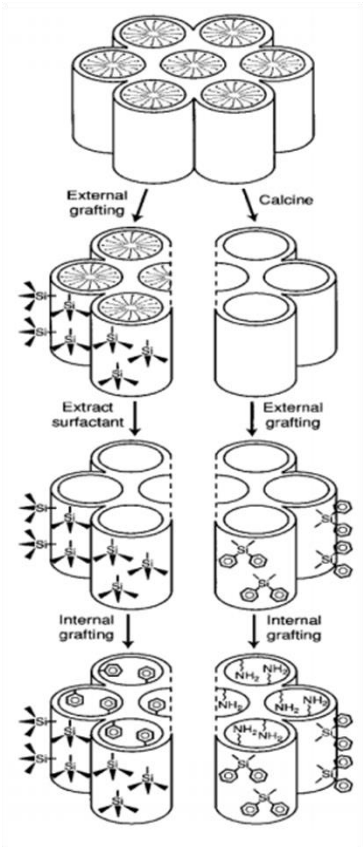

Figure 1.5. Methods of selective grafting on external and internal surfaces of mesoporous silicates. Reproduced from A. Stein, B.J. Melde, R.C. Schroden, Adv. Mater. 2000, 12, 1403-1419, with permission from The Royal Society of Chemistry.

In the ***first strategy*** the external surface of an "as synthesized" inorganic scaffold (whose pores are still filled with the surfactant template) is passivated using a selected organoalkoxysilane derivative. In this step, the organic moieties are grafted only in the external surface of the scaffold because the pores are fully loaded with surfactant molecules. Then, the surfactant was extracted from the

pores and a second functionalization step, with other organoalkoxysilane derivative, is carried out. The second organic functionalization is grafted exclusively in the inner of the mesopores due to the passivation of the external surface. The ***second strategy*** is based in the assumption that silanol groups on the external surface of a calcined mesoporous support are kinetically more accessible for functionalization. After this first grafting step, another functionalization process is carried out. In this case the organic moieties are anchored in the inner pore walls.

1.2.3.2. Co-condensation

This method is based on the co-condensation of a tetraalkoxysilane (siloxane) and one or more organoalkoxysilane precursors with Si–C bonds through a sol-gel process. Siloxane precursors work as the main framework of the mesoporous materials while the organoalkoxysilane precursors contribute to the building of the framework and work as functional groups on the surface. The direct synthesis has an advantage over the grafting method, it produces mesoporous materials with high loading of the functional groups.[52]

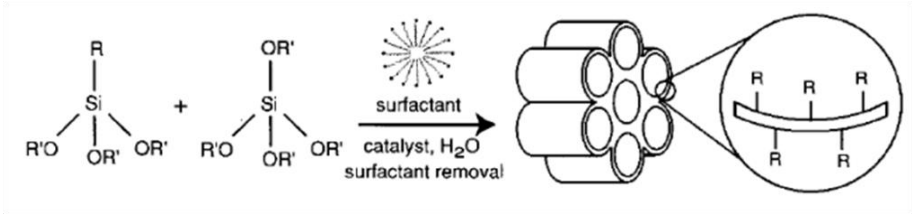

Figure 1.6. Co-condensation between tetraalkoxysilane and organoalkoxysilanes with Si-C bonds to synthesize hybrid inorganic-organic mesoporous silicates. Reproduced from A. Stein, B.J. Melde, R.C. Schroden, Adv. Mater. 2000, 12, 1403-1419, with permission from The Royal Society of Chemistry.

Compared with the grafting method in which the distribution of functional groups often tends to be inhomogeneous, the co-condensation is able to give homogeneously distributed organic groups on the entire inner pore surfaces and

no pore-blockage or shrinkage problems have been reported. Even though bulky organoalkoxysilane precursors often perturb the original textural properties of the systems, several methods to decorate the surface wall efficiently while maintaining the mesoporous structure are described. Another advantage of co-condensation over post-synthesis grafting is the possibility to control the particle morphology of final mesoporous support.

Using this method the removal of the organic template has to be by solvent extraction, calcination is not possible due to the presence of organic groups in the nanoparticles.

1.2.4. Characterization of mesoporous materials

Mesoporous supports are characterized using standard techniques of materials chemistry. These techniques includes scanning electron microscopy (SEM), transmission electron microscopy (TEM), powder X-ray diffraction (PXRD), N_2 adsorption-desorption measurements, thermogravimetric analysis (TGA) and dynamic light scattering (DLS). The particle morphology is typically studied by SEM, while the ordered arrangement of pores can be detected by TEM. PXRD can be used to determine the periodic-ordered structure of the material. N_2 adsorption-desorption measurements are used to determine surface area, pore volume, and pore size distributions. DLS is used to measure the hydrodynamic radius of the particles and to assess its possible suspension in water and in organic solvents. On the other hand, TGA is used to measure the amount of organic compounds grafted on the particle surface.

1.2.4.1. Electron microscopy

The electron microscope uses a beam of electrons to create an image of the sample. It operates according to the same basic principles as the light microscope but uses electrons instead of light. It is capable of much higher magnifications and has a greater resolving power than a light microscope, allowing it to visualize

smaller objects in detail. TEM involves the use of a high voltage electron beam (generated by an electron gun) focused into a small, thin, coherent beam by condenser lens. The electron beam is restricted by the condenser aperture to remove high angle electrons before it reaches the sample. It is important that the sample is thin enough to allow some electrons to transmit through the specimen. Electrons that are transmitted through the specimen carry information about is structure. TEM provides a 'shadow image' of the specimen with its different parts displayed in varied darkness according to the atom density in the sample. Heavy atoms, having high electron density, resulted in more interactions between the electrons in the primary beam and those in the sample, which in turn provides a higher contrast in the resultant image.

The successful imaging of nanoparticles using TEM relies on the contrast of the sample relative to the background. Samples are prepared for imaging by drying nanoparticles on a copper grid. Materials which have electron densities significantly higher than amorphous carbon are easy to image. TEM allows gathering information about particle size, shape, and surface coating. TEM was also used to verify the presence and arrangement of the pores.

Figure 1.7 shown TEM images of MSNs of different particle size obtained on a JEOL 100CX microscope with a CeB6 filament and an accelerating voltage of 100 kV.

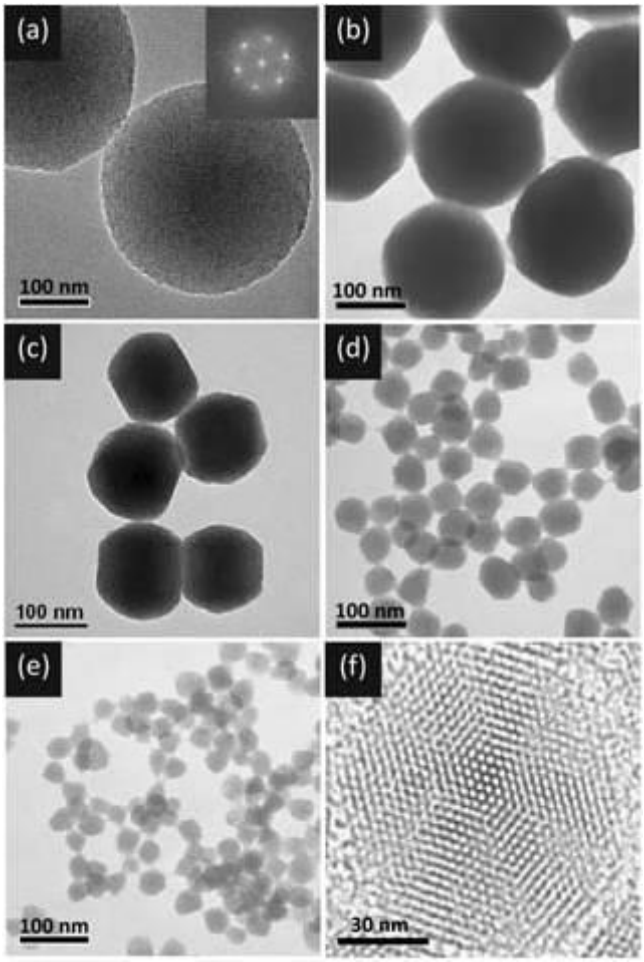

Figure 1.7. Images of mesoporous silica with different average sizes: (a) 280 nm; inset: Fast Fourier Transform (FFT) analysis of the TEM image; (b) 170 nm, (c) 110 nm , (d) 50 nm, (e) 30 nm. (f) High resolution TEM image of a single particle in (c). Reproduced with permission from *Small* **2009**, 5, 1408, Copyright © 2009 Wiley-VCH Verlag GmbH & Co. KGaA, Weinheim.

1.2.4.2. N_2 adsorption-desorption analysis

N_2 adsorption-desorption measurements are of crucial importance for the characterization of mesoporous materials, as specific surface area, specific pore volume, pore size and its distribution can be determined using this technique. N_2 physisorption process is described quantitatively by an adsorption/desorption

isotherm, representing the amount of adsorbed/desorbed gas at a fixed temperature as a function of its partial pressure. The amount of N_2 adsorbed by the mass of solid is dependent on the equilibrium pressure, the temperature, and the nature of the gas-solid system. These relationships are represented in the adsorption-desorption isotherm. The adsorption-desorption isotherms are displayed in graphical form with the N_2 amount adsorbed plotted against the equilibrium relative pressure (P/P_0). In the 1985 IUPAC recommendations physisorption isotherms were grouped into six types. [53] However, over the past 30 years various new characteristic types of isotherms have been identified and shown to be closely related to particular pore structures. Therefore, the proposed updated classification of physisorption isotherms is shown in **Figure 1.8**. The shape of these isotherms is based on the strength of the adsorbent–adsorbate interactions and the type of porosity (or porosities) of the adsorbent.

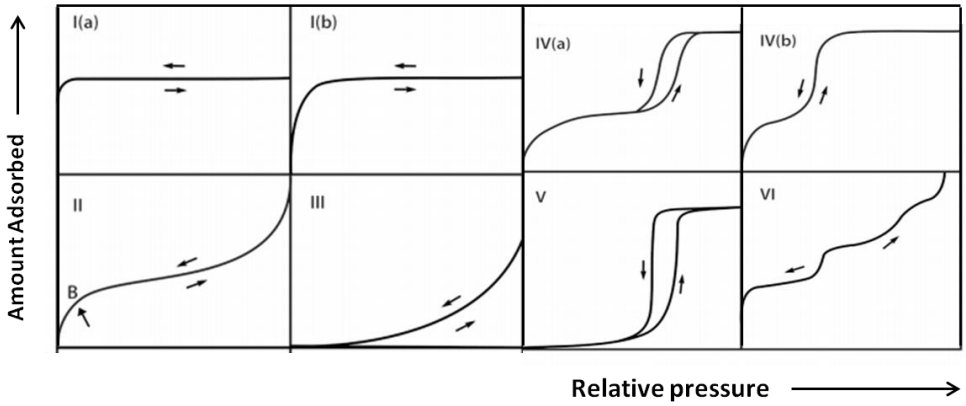

Figure 1.8. IUPAC classification of physisorption isotherms of porous solids. Reprinted with permission from M. Thommes, K. Kaneko, A.V. Neimark, J.P. Olivier, F. Rodriguez-Reinoso, J. Rouquerol, K.S.W.Sing, *Pure & Appl. Chem.* **2009**, *57*, 603, Copyright © **2009** IUPAC.

MCM-41 mesoporous materials presented typical ***type IV*** isotherms. A characteristic feature of ***type IV*** isotherms is the presence of a hysteresis loop, the lower branch of which represents measurements obtained by progressive N_2 addition and the upper branch by progressive withdrawal of gas from the solid.

The shape of the hysteresis loop is associated with the filling and emptying of mesopores by capillary condensation, which reveals additional information about the pore structure. This specific hysteresis loop is of H1 type and is caused by a narrow distribution of uniform pores.

The Brunauer-Emmett-Teller (BET) gas adsorption model is the most widely employed procedure for the determination of the specific surface area of finely divided and porous materials using the physisorption isotherm data.[54,55] This model is based on the assumption that only monomolecular adsorption takes place, adsorption is localized onto surface sites and the energy of adsorption is independent of the surface coverage.

On the other hand, pore size can be determined from either the adsorption or the desorption branch of the N_2 isotherm. The Kelvin equation (**Equation 14**) with a correction for the multilayer thickness in the pore walls can be used to evaluate the pore width, or more precisely the pore size distribution, from the pore filling pressure.

$$\ln (p/p_0) = 9\text{-}2\gamma V_L / rRT \qquad (14)$$

where p/p_0 is the relative pressure, r is the mean radius of curvature of liquid in a pore, γ is the surface tension of the liquid, V_L is the molar volume of the liquid, R is the gas constant and T is the absolute temperature.

The most common model for pore size distribution analysis is the Barrett-Joyner-Halenda (BJH), which is based on the Kelvin equation.[56]

1.2.4.3. Powder X-ray diffraction

This technique is based on diffraction of X-rays by the electron clouds of the atoms. In the absence of absorption effects, the intensity of the scattered radiation is directly proportional to the electron density differences in the system.

When an x-ray beam with wavelength λ strikes a material with periodic long-range order, characteristic reflections of intensity for planes will be observed in a diffractogram as a result of the constructive interference when the scattering angle (θ) satisfies Bragg's law (**Equation 15).**

$$n\lambda = 2d \cdot sen\theta \qquad (15)$$

where n is an integer number of wavelengths (order of diffraction), λ is the wavelength, d is the repeating distance between reflecting planes and θ is the scattering angle. Bragg's law shows the relationship between crystal lattices (d) and the observed scattering angle. In Bragg's law, the scattered intensity is measured as a function of scattering angle. In a crystal, a set of crystallographic planes hkl can be defined as the set of parallel equidistant planes and the spacing between diffracting planes is called the d-spacing. MCM-41 has a hexagonally ordered pore structure. As illustrated in **Figure 1.9**, the unit cell size, a, can be calculated from the first Bragg peak position.

$$a = \frac{2}{\sqrt{3}} d_{100}. \qquad (16)$$

For crystalline materials the lattice planes are often in the order of a couple of Å which gives a scattering angle of ~20˚ if CuKα radiation (λ = 1.54 Å) is used and scans between 20-80˚ are common for characterization of the atomic structure of the material. For amorphous materials, such as mesoporous silica, there are no periodic atomic planes but the technique is still useful for characterization of the ordered pore structure. Compounds with different cells units have different assemblies of lattice spacings and hence will lead to different diffraction patterns. Thus, the combination of d-spacings and intensities are characteristic for each structure.

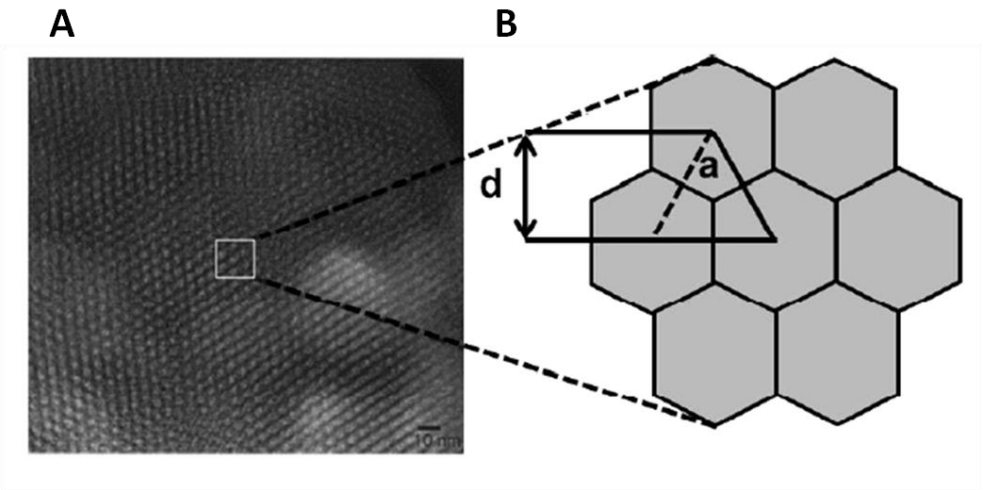

Figure 1.9. (A) TEM image of MCM-41, (B) illustration of the 2D hexagonally-ordered lattice with d_{100} spacing and unit cell parameter a. Reproduced with permission from Handbook of Heterogeneous Catalysis (Wiley-VCH, 1997).

Consequently, analyzing the positions of the reflected beams information about the size and symmetry of the lattice dimensions can be obtained. In MCM-41, there is no repeat unit in the "c" axis and so only reflections from the hk planes, in two dimensions, are seen. MCM-41 can be indexed to a hexagonal hk_0 lattice and are therefore, low angle peaks (100), (110), (200) and (210) are obsreved. The repeating distance d directly gives the unit cell (lattice) parameter a. One can clearly distinguish between a hexagonal, cubic or lamellar mesoporous phase using PXRD measurements. Furthermore, if the same X-ray diffraction pattern is displayed by the final functionalized material, it means that the mesoporous network remains unaltered after the grafting processes.

1.2.4.4. Thermogravimetric analysis

Thermogravimetric analysis (TGA) measures weight changes in a material as a function of temperature (or time) under a controlled atmosphere. The method

offers valuable information for quality control, development and research. TGA can be used to study thermal stability and composition of materials. A TGA is performed by gradually raising the temperature of a sample in a furnace as its weight is measured on a balance that remains outside of the furnace. Changes in the mass of a sample are studied while the sample is subjected to the program. The weight/mass of the sample is plotted against temperature or time to illustrate its transformations. TGA measurements are commonly used to assess the amount of organic matter grafted in hybrid materials.

1.2.4.5. Dynamic light scattering

DLS is a non-invasive technique for measuring the size and size distribution of molecules and particles typically in the submicron region. DLS is applied for the characterization of particles, emulsions or molecules, which have been dispersed or dissolved in a liquid. DLS measures the speed of particles undergoing Brownian motion. Smaller particles fluctuate more rapidly than large particles. When a sample is illuminated by a light source, such as a laser, it scatters light in all directions. DLS gives an intensity-weighted distribution, where the contribution of each particle in the distribution relates to the intensity of light scattered by the particle. Rayleigh approximation describes the intensity of scattering to be proportional to the sixth power of the particle diameter. For a sample consisting of particles of two sizes the bigger particles scatter more light resulting in larger peak area by intensity. When comparing particle size data for the same sample obtained by different techniques, it is important to realize that the types of distribution being measured and reported can produce very different particle size results. The diameter measured by DLS is called the hydrodynamic diameter and refers to the way a particle diffuses within a fluid. The diameter obtained by this technique will depend not only on the size of the particle 'core', but also on any surface structure, as well as the concentration and type of ions in the medium. Thus, the size obtained by DLS will be larger than that measured by TEM, where the particle is removed from its native environment.

1.2.5. Functional organic-inorganic mesoporous hybrid materials

In the last ten years, anchoring organic molecules or supermolecules onto mesoporous inorganic scaffoldings has led to the development of hybrid materials. These hybrid materials presented cooperative functional supramolecular behaviors that are not found in the unanchored molecules or in the unfunctionalized solids alone. One appealing concept in this novel field relates to the development of ***gated nanodevices*** for controlled delivery applications. These functional materials contain ***molecular gates***, which are switchable molecular or supramolecular entities that controlled either the on-command release of confined guests or the on-command entrance of molecular species to certain sites (see **Figure 1.10**).

Figure 1.10. Scheme of a nanoscopic "molecular gate"

These gated nanodevices usually contain two components: (i) a switchable molecular gate ensemble capable of being "opened" or "closed" upon the application of certain external stimuli; (ii) a suitable inorganic support acting as a nanocontainer (for loading the carrier), to which molecular gates can be easily grafted. Both components are important, and their selection determines the

controlled release performances of the hybrid support. Mesoporous silicas of different pore sizes and morphologies are selected and used as inorganic scaffolds in gated ensembles. The design of gated mesoporous materials proves to be a promising starting point for applying the versatility of supramolecular ideas to the design of nanoscopic gating solids, and a way of studying the factors that can influence the design of molecular gating functions based on molecular, biomolecular, or supramolecular concepts. A suitable and general protocol to verify the performance of these gated materials is to load the mesoporous framework with a dye and study its delivery through UV and/or fluorescence spectroscopy. Once demonstrated the possibility of load and deliver organic dyes in a controlled manner from a mesoporous matrix, it is also possible to load the biocompatible mesoporous hybrid materials with bioactive molecules (such as vitamins, cytotoxic specices, hormones, etc.). The external stimuli, able to induce the controlled release of the entrapped cargo, can be classified in: physical (temperature, magnetic fields, light) or chemical (pH, reducing agents, presence of certain molecules), or biochemical (enzymes, DNA, aptamers).

The first example of a molecular gate was reported by Fujiwara and coworkers in 2003. [57, 58] They used a photoresponsive coumarin derivative grafted on the pore outlet of Si-MCM-41 as molecular gate. Irradiation of UV light longer than 310-nm wavelength to this coumarin-modified MCM-41 induced the photodimerization of coumarin to close the pore outlet with cyclobutane dimer. Guest molecules such as phenanthrene neither can enter nor escape from the onedimensional, isolated, individual pores of MCM-41. On the other hand, the irradiation to the dimerized-coumarin-modified MCM-41 with shorter wavelength UV light around 250 nm regenerates the coumarin monomer derivative by the photocleavage of cyclobutane dimer, and guest molecules included inside are released from the pore void. For the first time, this intermolecular reversible photodimerization-cleavage cycle realized photo-switched storage and release of guest molecules from coumarin-modified MCM-41. Coumarin-modified MCM- 41 was able to store 21.6 wt % of phenanthrene as guest molecule after photodimerization. Since this firt work, inorganic nanoparticles, polymers, and

larger supramolecular assemblies have been used as blocking caps that control the opening /closing mechanism of the pore in mesoporous scaffolds.

In 2003, Lai and coworkers used surface-derivatized cadmium sulfide (CdS) nanocrystals as chemically removable caps to encapsulate several pharmaceutical drug molecules and neurotransmitters inside organically functionalized MSN.[59] The molecules of interest were encapsulated inside the porous framework of the MSN by capping the openings of the mesoporous channels with size-defined CdS nanoparticles to physically block the drugs/ neurotransmitters from leaching out. The authors capped MSN *in situ* by allowing the pore surface-bound 2-(propyldisulfanyl)ethylamine functional groups to covalently capture the water-soluble mercaptoacetic acid-derivatized cadmium sulfide (CdS) nanocrystals via an amidation reaction. The resulting disulfide linkages between the MSNs and the CdS nanoparticles were chemically labile in nature and were cleaved with various disulfide-reducing agents, such as dithiothreitol (DTT) and mercaptoethanol (ME)(see **Figure 1.11**).

Another early example was reported in 2005 by Lin and co-workers.[60] The authors covalently capped *in situ* the openings of the mesopores through amidation of the 3-(propyldisulfanyl)propionic acid functional groups bound at the pore surface with 3-aminopropyltriethoxysilyl-functionalized superparamagnetic iron oxide (APTS-Fe_3O_4) nanoparticles. The disulfide linkages between the MSNs and the Fe_3O_4 nanoparticles are chemically labile and were cleaved with various cell-produced antioxidants and disulfide reducing agents such as dihydrolipoic acid (DHLA) and dithiothreitol (DTT). The release of the magnetic nanoparticle caps from the dye-loaded MSNs was regulated by the concentration of triggering molecules.

Other early example was based on polymers or larger supramolecular assemblies. In 2007 Zink and coworkers [61] developed a system based on the use of interpenetrating supermolecules (pseudorotaxanes) or interlocked molecules (bistable rotaxanes) with movable and switchable properties. Redox-switchable

[2]pseudorotaxanes and bistable [2]rotaxanes, having a cyclobis(paraquat-p-phenylene) ($CBPQT^{4+}$) tetracationic ring, were tethered to MCM-41 to act as supramolecular nanovalves. In addition, the authors reported a supramolecular nanovalve system (switchable pseudorotaxane) based on a dibenzo[24]crown-8/dialkylammonium ion complexation that responded to a range of bases.

In 2008, Feng and coworkers [62] developed for the first time a cross-linked polymeric network as a "gatekeeper" on the surface of mesoporous silica-based materials. The gate operation was based on redox reactions in which the cross-linked polymeric network works as an off-on switch in response to redox signals. The system consisted of poly(N-acryloxysuccinimide)-grafted mesoporous silica in which the polymers were attached at the pore entrance of MCM-41 particles.

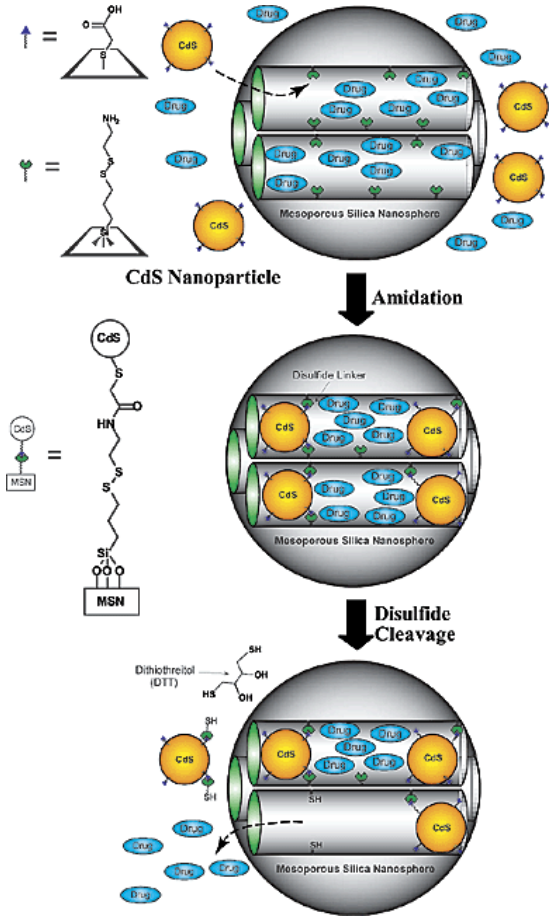

Figure 1.11. Schematic representation of the CdS nanoparticle-capped MSN based drug/neurotransmitter delivery system. The controlled-release mechanism of the system is based on chemical reduction of the disulfide linkage between the CdS caps and the MSN. *Reprinted with permission from J. Am. Chem. Soc.* ***2003****, 125, 4451-4459, Copyright © **2003**, American Chemical Society.*

1.2.6. Application of mesoporous hybrid materials

As can be observed in **Scheme 1.6** mesoporous silica-based hybrid materials found applications in several scientific and technological fields such as catalysis, drug delivery, sensing or gene transference. At this respect, mesoporous silicas were used to catalyze the formation of conductive polymers within their pores,[63]

or even as templates for some of the first synthetic procedures of conductive carbon nanowires.[64]

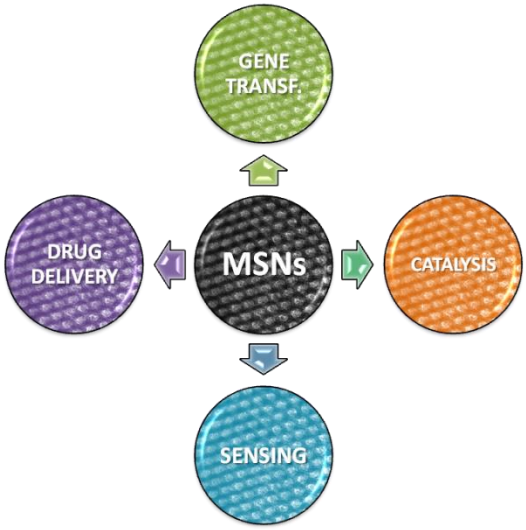

Scheme 1.6. Applications of Mesoporous silica nanoparticles.

Synthetic mesoporous silicas were also proposed for environmental remediation. Upon functionalization with amino, thiol, mercato, ethylendiamine tetraacetic acid, chloride, urea or sulfonic acid groups, the materials proved to be able to remove heavy metals from water forming stable coordination compounds.

Heidari et al. [65] investigated MCM-41 modified with amine as absorbent for Ni(II), Cd(II) and Pb (II) ions obtaining maximum adsorption capacities of 12.36, 18.25 an 57.75 mg/g respectively. In addition, Lee et al [66] studied different mesoporous silica materials functionliazed with amine groups obtaining the best activity for the adsorption of Cu(II). A thiol-functionalized magnetic mesoporosu silica material was studied as a convenient and effective adsorbent for heavy metal ions by Li et al. [67] An adsorption material (called MTTZ-MCM-41) was prepared using mesoporous silica nanoparticles and 5-mercapto-1-methyltetrazole by Pérez-Quintanilla et al.[68] obtaining a maxim absorption for

Zn(II) of 1.59 mmol/g. Another example was the work of Park [69] and coworkers that used thiol functionalized porous silica with pore size of 6nm to remove silver and cadmium heavy metals.

Feng and co-workers [70] synthesized mesoporous silica materials containing functionalized organic monolayers. The authors introduced to the pore surface of mesoporous silica functional groups (thiol groups in this case) as the terminal groups of organic monolayers. The hydrocarbon chains aggregated and formed close-packed arrays on the substrate. The siloxane groups then underwent hydrolysis and ultimately became covalently attached to the substrate and cross-linked to one another. As a result, was obtained a cross-linked monolayer of mercaptopropylsilane covalently bound to mesoporous silica and closely packed on the surface. The relative surface coverage of the monolayers was systematically varied up to 76 percent. These materials are extremely efficient in removing Hg(II) and other heavy metals from both aqueous and non-aqueous waste streams, with distribution coefficients up to 340,000. The stability of these materials and the potential to regenerate and reuse them was also demonstrated. Compared with conventional remediaton technologies for heavy metals at this moment, this kind of materials have (i) high initial loading capacity because of the densely populated thiol groups on the large surface area mesoporous oxides, and (ii) high selectivity to heavy metals against background electrolytes. These materials bind metallic, inorganic, organic, charged, and neutral mercury compounds and were used in a variety of media such as water, oil, and gas. In a similar fashion, Omorogie and co-workers reported the immobilization of *Nauclea diderrichii* seed waste biomass (an agro-waste) with eco-friendly mesoporous silica and graphene oxide-MS nanoparticles.[71] The abstractive potential of the new hybrid materials was explored for uptake of Cr(III) and Pb(II) ions. The authors concluded that agro-wastes modified with nanoparticles are potential adsorbents for efficient removal of toxic heavy metal ions from water and wastewater.

Another important application field of mesoporous materials is heterogeneous catalysis. At this respect hybrid mesoporous solids have been considered for a wide range of catalytic processes.[72] Besides, immobilization of active centers in the mesoporous surface can improve the overall efficiency of the catalytic processes because:

1. It is easier to retain the solid catalyst in the reactor or to separate it from the liquid stream by filtration.
2. Often the catalyst can be regenerated and recycled
3. Confinement of the catalyst within mesopores provides a means of introducing size and/or shape selectivity and thus greater specificity for a reaction.

MSN can also be useful in other industries, for example agrochemical, where it can be used for pesticide storage and delivery in a predictable manner.[73,74] MSN based encapsulation and delivery of pesticides could have some positive environmental implications as well as decreasing the extermination of non-target insects.

Even molecules as large as proteins could be immobilized in mesoporous materials, as demonstrated by Dıaz and Balkus.[75] Also, a great variety of enzymes have been immobilised onto various mesoporous silica materials in order to improve their stability and reusability. It is expected that immobilised enzymes have a high enzyme activity and minimum enzyme desorption (leaching).[76]

Furthermore, due to their features such as uniform pore systems, high load capacity and well-known functionalization chemistries, one of the most appealing applications of MSN is their use for controlled delivery of drugs, vaccines, RNA and DNA. As nanocarriers, mesoporous silica nanoparticles have been explored as effective drug delivery systems for a variety of therapeutic agents to fight against various kinds of diseases including bone/tendon tissue engineering, diabetes, inflammation, and cancer.[77,78]

1.3. Nanoparticles for biomedical applications

The development of new drugs or therapeutic species is an expensive and time consuming process. For this reason, researchers turned their attention to “old” drugs in an attempt to improve its safety and efficacy ratio using different methods such as individualizing drug therapy, dose titration, and therapeutic drug monitoring. Other strategies to enhance the applicability of these “old” drugs consisted in its targeted and rate controlled release using several technological materials (such as inorganic beads, liposomes, micelles, organic polymers or inorganic nanoparticles). Some examples of this controlled release technology (CRT) are transdermal and transmucosal delivery systems, nasal and buccal aerosol sprays, drug-impregnated lozenges, encapsulated cells, oral soft gels, iontophoretic devices to administer drugs through skin, and a variety of programmable implanted drug-delivery devices. The development of CRT has increased in the last years as an alternative to conventional drug administration methods because the problems related with these traditional protocols may be potentially avoided using these devices.

For example, one method to achieve long-acting drug levels is the use of ***beaded delivery formulations***. These materials consisted on multiple small beads that are composed of inert substances (such as polystyrene). The active drug is overlaid on the beads and encased in a delivery capsule. These systems are used for the controlled release of certain drugs in acidic environments.

Drug delivery systems can in principle provide enhanced efficacy and/or reduced toxicity for anticancer agents. Long circulating macromolecular carriers such as ***liposomes*** can exploit the ‘enhanced permeability and retention’ (EPR) effect for preferential extravasation from tumor vessels.[79] Liposomes are spherical vesicles most often composed of phospholipids. These vesicles can be loaded with water soluble drugs (inside the liposome core) or also with hydrophobic molecules (into the phospholipid bilayer). Liposomal delivery

systems are still largely experimental; the precise mechanisms of their action in the body are under study, as are ways in which to target them to specific diseased tissues.[80]Liposomal anthracyclines have achieved highly efficient drug encapsulation, resulting in significant anticancer activity with reduced cardiotoxicity, and prolonged circulation such as liposomal daunorubicin and pegylated liposomal doxorubicin. Pegylated liposomal doxorubucin has shown substantial efficacy in breast cancer treatment both as monotherapy and in combination with other chemotherapeutics. Additional liposome constructs are being developed for the delivery of other drugs. The next generation of delivery systems will include true molecular targeting (immuno-liposomes and other ligand-directed constructs) using an integration of biological components capable of tumor recognition with delivery technologies.[81] Currently approved liposomal drug delivery systems provide stable formulation, improved pharmacokinetics, and a degree of 'passive' or 'physiological' targeting to tumor tissue.[82] However, these carriers do not directly target tumor cells. The design modifications, that protect liposomes from undesirable interactions with plasma proteins and cell membranes, also prevent interactions with tumor cells. Instead, after extravasation into tumor tissue, liposomes remain within tumor stroma as a drug-loaded depot. Liposomes eventually become subject to enzymatic degradation and/or phagocytic attack, leading to release of drug for subsequent diffusion to tumor cells. The next generation of drug carriers under development featured direct molecular targeting of cancer cells via antibody-mediated or other ligand-mediated interactions. Immuno-liposomes, in which antibody fragments are conjugated to liposomes, represent a strategy for molecularly targeted drug delivery.

Colloidal drug carrier systems (such as micellar solutions, vesicle and liquid crystal dispersions, as well as nanoparticle dispersions consisting of small particles) also show great promise as drug delivery systems. The goal is to prepare systems with optimized drug loading and release properties, long shelf-life and low toxicity. The incorporated drug participates in the microstructure of the

system, and may even influence its properties due to molecular interactions (especially if the drug possesses amphiphilic and/or mesogenic properties). [83]

Micelles formed by the self-assembly of amphiphilic block copolymers (5-50 nm) in aqueous solutions are of great interest for drug delivery applications. The drugs can be physically entrapped in the core of block copolymer micelles and transported at concentrations that can exceed their intrinsic water solubility. Moreover, the hydrophilic blocks can form hydrogen bonds with the aqueous surroundings yielding a tight shell around the micellar core. As a result, the contents of the hydrophobic core are effectively protected against hydrolysis and enzymatic degradation. In addition, the corona may prevent recognition by the reticuloendothelial system and therefore preliminary elimination of the micelles from the bloodstream. The fact that their chemical composition, total molecular weight and block length ratios can be easily changed allowed control of the size and morphology of the micelles. Functionalization of block copolymers with cross linkable groups can increase the stability of the corresponding micelles and improve their temporal control.[84]

Other drug delivery systems are based on ***polymeric nanoparticles*** made of natural or artificial polymers ranging in size between about 10 and 1000 nm (1 mm). In these nanoparticles drugs may be adsorbed onto the surface or chemically attached. These nanoparticles and nanoformulations have already been applied as drug delivery systems with great success. Besides, also have still greater potential for many applications, including anti-tumors, AIDS and gene therapies, radiotherapy, in the delivery of proteins, antibiotics, virostatics, and vaccines and as vesicles to pass the blood-brain barrier.[85]

Very recently, as an alternative to the purely organic vehicles, multifunctional ***mesoporous silica nanoparticles*** (MSNs, size typically < 500 nm) have attracted substantial attention due to their advantageous structural properties. At this respect MSNs have a high external surface area, remarkable pore volume, tunable pore sizes, colloidal stability, and the possibility to specifically functionalize the

inner pore system and/or the external particle surface. These and others features make MSNs a promising and widely applicable platform for diverse biomedical applications including bioimaging for diagnostics,[86] biosensing,[87] biocatalysis,[88] bone repair and scaffold engineering,[89] and drug delivery.[90]

Inorganic-organic core-shell hybrid nanoparticles based on mesoporous silica have received great attention as drug delivery vehicles. In these hybrid materials decoration of the inner or outer surface of the nanoparticles with organic (bio)molecules can impart important features for successful controlled drug delivery.[91] At this respect, in 2001, MSNs were used as drug nanocarriers (without any control over cargo release). Inspired by this simple concept, many efforts were made in recent years to create multifunctional stimuli-responsive nanocarrier systems consisting of MSNs as host materials.[92] These multifunctional nanocarriers included (bio)molecules attached onto its external surface that allowed a spatiotemporal control cargo release. Delivery of anticancer therapeutics into cancer cells by using hybrid MSNs has made significant progress in recent years.[93] Besides, MSNs can be designed as multifunctional platforms.

1.3.1. Targeting and cellular uptake of nanoparticles

1.3.1.1. Targeting

Insufficient target selectivity of drugs can cause unfavorable side effects and reduce therapeutic efficacy. Especially in anticancer chemotherapy, limited selectivity of cytostatins and cytotoxins toward tumor cells is responsible for many undesired side effects. The efficacy of the treatment can be affected when nonspecific toxicity to normal cells prevents an effective dose that is necessary to eradicate malignant cells.[94,95] Extensive studies showed passive targeting of nanocarriers in tumor tissue.[96,97] Well-stabilized nanoparticles with optimal size and appropriate antifouling surface can remain in blood vessels long enough to accumulate at the tumor site.

Passive targeting relies on the EPR effect, which was discovered by Matsumura and Maeda in 1986.[98] The authors found that macromolecules, with molecular mass higher than 50 kDa, could preferentially distribute to the tumour interstitium and remain there for extended time periods. This fact increased ca. 70-fold macromolecules concentration in tumours. This preferential distribution to the tumours was ascribed to two main phenomena: (i) the presence of fenestrations in the imperfect tumour blood vessels (permeability) and (ii) the poor lymphatic drainage (retention) in the tissue. The origin of EPR effect is associated with the rapid growth of solid tumours. Thus, when a solid tumour reaches a given size, the normal vasculature present in its surroundings is not enough to provide the required nutrient and oxygen supply for its further proliferation. As cancer cells start to die, they secrete growth factors that promote the formation of new blood vessels from the surrounding capillaries, the process of which is termed as angiogenesis. This lead to a rapid development of new, irregular blood vessels exhibiting discontinuous epithelium and presenting fenestrations that can reach sizes in the 200-2000 nm range depending on the tumour type and location. Unlike normal tissues, where the extracellular fluid is constantly drained to the lymphatic vessels, in tumours the lymphatic drainage is defective. Consequently, whereas molecules with less than 4 nm size can diffuse back to the blood circulation, the diffusion of nanoparticles (NPs) is hindered by their hydrodynamic radii and accumulates in the tumour interstitium (See **Figure 1.12**).

Particle circulation time and the ability to overcome biological barriers are essential to attain successful passive targeting. Three main properties of nanoparticles affect these phenomena, namely: (i) particle size, (ii) particle shape, and (iii) surface features. Enhanced passive bioaccumulation via the EPR effect could be achieved by neutralizing the nanoparticles surface charge with positively charged groups.[98] However, the EPR effect is not universal for all types of tumor cells, and a lack of cell-specific interactions might decrease therapeutic efficacy and induce multiple drug resistance (MDR).[99,100]

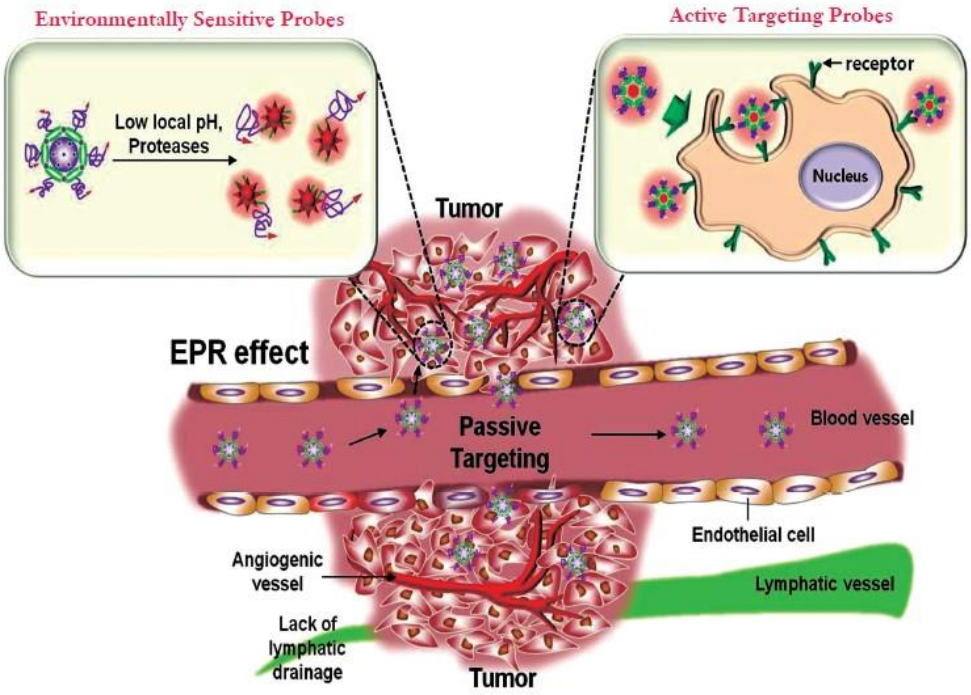

Figure 1.12. Passive and active targeting approaches of nanoprobes in cancer diagnosis. Passive tumor targeting is achieved by extravasation of nanoprobes through increased permeability of the tumor vasculature and ineffective lymphatic drainage (EPR effect). Environmentally sensitive nanoprobes (left inset) are another example of passive targeting that takes advantage of the characteristics of the tumor-associated microenvironments (i.e., acidic environment, and overexpressing enzymes). Active tumor targeting (right inset) can be achieved by functionalization of nanoprobes with targeting ligands that promote cell-specific recognition and binding. *Reproduced with permission of K.Park, Quant Imaging Med. Surg.,* ***2012****, 2(2), 106-113. Copyright © 2009-2017 Quantitative Imaging in Medicine and Surgery.*

Active targeting, also known as ligand-mediated targeting, involves the use of ligands attached to the surface of the nanoparticles for specific retention and uptake by the targeted disease cells.[101] To this aim, ligands are selected to bind surface molecules or receptors overexpressed in diseased organs, tissues, cells or organelles. Typical ligands include antibodies, proteins, aptamers, saccharides, peptides and small molecules such as vitamins (**Figure 1.13**). Nanoparticle surface functionalization reduces unspecific interactions with proteins and thus has a positive influence on circulation times. Besides, active cellular uptake at the tumor site and enhanced tumor retention times can be further facilitated by active targeting. The attachment of targeting ligands to the nanoparticles provides specific nanoparticle–cell interactions and enhance cellular uptake (**Figure 1.12**). The ligand-mediated binding of the nanoparticles to the cell is regulated by the availability, affinity and the density of the targeting moiety. Surface functionalization should be regulated for optimized ligand coupling and prevention of protein adsorption that might block active targeting and lead to rapid clearance of the particles from the body defense mechanisms (the reticuloendothelial system, RES). The efficiency of the active targeting is related to the ability of the nanoparticle-grafted ligand to bind with the cell-surface receptors.

The main challenge for targeted nanocarriers is to achieve proper balance of nanoparticle functionalization (that influence circulation times, passive accumulation and retention at the site of action) and active cellular uptake (that will offer the optimal therapeutic *in vivo* outcome). Understanding how nanoparticle functionalization and further ligand coupling influence biodistribution and tumour accumulation *in vivo* is a highly interesting and important endeavor.

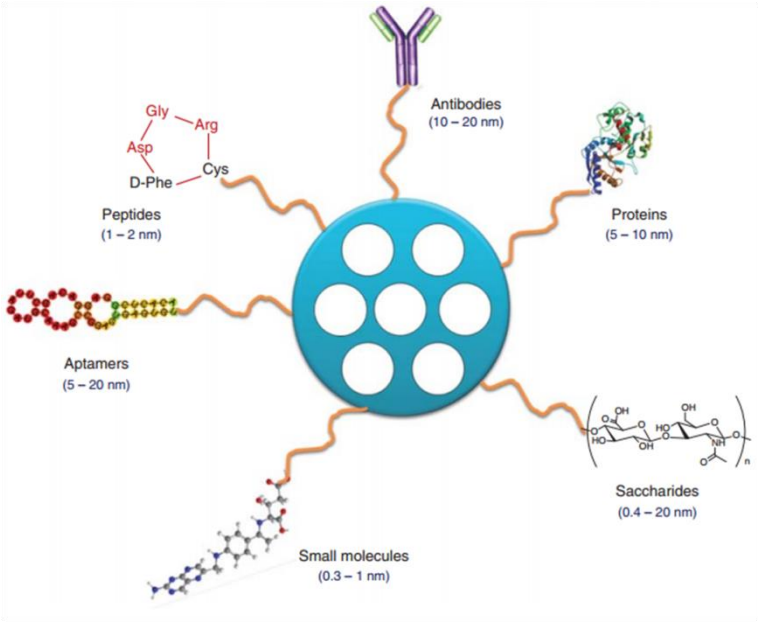

Figure 1.13. Schematic representation of active targeting possibilities on MSNs. *Reprinted with permission from A.Baeza, M.Colilla, M. Vallet-Regí, Expert Opin. Drug Del,* ***2015****, 12(2), 319-337, Copyright ©* ***2015*** *Taylor & Francis.*

Active targeting could be achieved using ***antibodies***. Antibodies are attached to the surface of nanoparticles to target specific antigens present on the membrane of different cancer cells. Sometimes biocompatible hydrophilic polymers have been used as cross-linkers between the antibody and the nanoparticles surface. At this respect, Chen and co-workers reported the first example of *in vivo* tumour targeting using MSNs functionalized with an antibody as targeting molecule.[102] Anti-TRC105 provided nanoparticles with specificity to CD105 receptors overexpressed in the vasculature of 4T1 murine breast tumor-bearing mice.

Certain ***proteins*** have also been used for active targeting. For example, transferrin (Tf) was conjugated with MSNs for tumour-targeting purposes. Tf is a membrane glycoprotein that operates together with its receptor, TfR, to assist the uptake of iron by the cell. The TfR may be overexpressed by up to 100-fold on tumour cells, making it an attractive alternative for targeted delivery of

chemotherapeutics via MSNs-based carriers. Using this approach, Ferris and co-workers demonstrated an up to 10-fold increase in MSNs functionalized with Tf uptake by PANC-1 and BT-549 cancer cells.[103] ***Small peptides*** have also been used as targeting ligands. The smaller sizes of peptides when compared to proteins offer several advantages such as improved stability, resistance to the environment and easier synthesis and conjugation.

Aptamers emerged as a powerful alternative to provide active targeting capabilities to nanoparticles. Aptamer are single-stranded RNA of DNA or unnatural oligonucleotides that presented a high ability to bind a target molecule. Aptamers folds, through intramolecular interactions, adopting tertiary conformations able to recognize several (bio)molecules with high affinities. Their advantages, when compared to antibodies and proteins, are their small size, their non-immunogenic character, their non-complicated synthesis and modification procedures, and their high specificity and affinity for their targets (comparable to that of antibodies).[104]

Saccharides and ***polysaccharides*** (such as mannose, galactose, lactobionic acid (LA) and hyaluronic acid (HA)) have been also used as targeting ligands. Carbohydrates are recognized by ubiquitous cellular membrane proteins called lectins and many types of tumours overexpress carbohydrate receptors. Among polysaccharides, HA is receiving growing attention as targeting ligand because many types of tumour cells overexpress HA receptors. Futhermore, HA also interacts with several cell surface receptors (including receptor for hyaluronan-mediated motility CD168 and HA receptor for endocytosis). Taking into account the above mentioned facts, HA is used as targeting ligand in the preparation of nanodevices for controlled release in certain cells. For instance, Yu and co-workers prepared MSNs functionalized with HA and demonstrated that these nanodevices were able to specifically deliver Dox in HCT-116 cells (CD44-overexpressed).[105] In another recent work, Chen and co-workers used HA grafted onto the external surface of MSNs as both capping and targeting agent.[106]

Small molecules have also been used for targeting purposes being folic acid (FA) one of the most widely studied because folate receptor is upregulated in several types of human cancer cells. One of the first examples of MSNs functionalized with FA was reported by Liong and co-workers in 2008.[107] The authors prepared iron oxide nanocrystals coated with a mesoporous silica shell. Then, the pores of the nanoparticles were loaded with camptothecin (CPT) or paclitaxel (PTX) and the external surface funcionalized with phosphonate moieties and FA. The cytotoxicity of the prepared nanoparticles was higher in cell lines overexpressing folate receptor (PANC-1) than in normal cells (HFF). Methotrexate (MTX), an anti-tumour drug structurally similar to FA, was also grafted onto MSNs, playing a dual role, as targeting ligand and as cytotoxic agent.

1.3.1.2. Cellular uptake

All types of cells in the body use ***endocytosis process*** to communicate with the biological environments. This is an energy-dependent process through which cells internalize ions and biomolecules.[108] In particular, the cells internalize nutrients and signaling molecules to obtain energy and interact with other cells, respectively. The endocytosis pathways are typically classified into phagocytosis, macropinocytosis, pinocytosis, clathrin- and caveolae-mediated endocytosis (see **Table 1.1**):

- ***Phagocytosis***, which was executed by specialized professional phagocytes. The phagocytosis pathway is used when phagocytic cells internalize foreign materials with sizes larger than 0.5 μm. The phagocytosis pathway is actin-dependent and restricted to professional phagocytes, such as macrophages, dendritic cells, and neutrophils.

- ***Macropinocytosis*** pathway is a non-specific process to internalize fluids and particles together into the cell, whereas the ***pinocytosis*** pathway absorbs biological fluids from the external environment of a cell. These pathways are very important to translocate single nanoparticles with sizes below 10 nm into the cell.

- ***Clathrin-dependent endocytosis*** is a process whereby guest matters are internalized via clathrin-coated vesicles and subsequently transformed to endosomes. A fraction of internalized guest matters would be recycled back to the cell exterior, while the remaining fractions are transferred into lysosomes.

- ***Caveolae-dependent endocytosis*** is characterized by the evolution of caveolae-derivatives of the subdomains of sphingolipid and cholesterol-rich cell membrane fractions. After internalization, the guest matters would be transported to caveosomes and then either translocated to the endoplasmic reticulum/Golgi body, or entered the endosomal pathway.

Clathrin- and caveolae-independent endocytosis includes those pathways not usually classified by the above criteria, such as macropinocytosis, actin-, flotillin-, or Arf6-dependent pathways. All these pathways are energy-dependent and involve active formation of membrane invaginations, membrane ruffles and transport vesicles. Many of their regulatory mechanisms are still unclear. Also, clathrin- and caveolae-mediated endocytosis indicates receptor-mediated endocytosis. Many types of cells use the clathrin- and caveolae-mediated endocytosis pathways to internalize nanoscale materials, including viruses and nanoparticles. These endocytosis pathways are the most important for the internalization of nanoparticles into cells (See **Figure 1.14**). The coating of the nanoparticles with plasma proteins, when exposed to physiological solutions facilitated endocytosis.

Table 1.1 Classification of endocytosis pathways

	Pathway	Definition
Specific pathway		
Endocytosis	Clathrin- and caveolin-mediated	Energy-dependent process by which cells internalize biomoléculas,
Phagocytosis	Mannose receptor-, complement receptor-, Fcγ receptor-, and scavenger receptor-mediated	Actin-dependent endocytic process by which professional phagocytes (macrophages, dendritic cells and neutrophils) engulf particles with sizes large than 0.5 um
Non-specific pathway		
Macro-pinocytosis	-	Endocytic process by which cells internalize fluids and particles together, and large vesibles (0.2-4 um) are formed
Pinocytosis	-	Endocytic process by which cells absorb extracellular fluids, small molecules and small vesicles(100nm) are formed

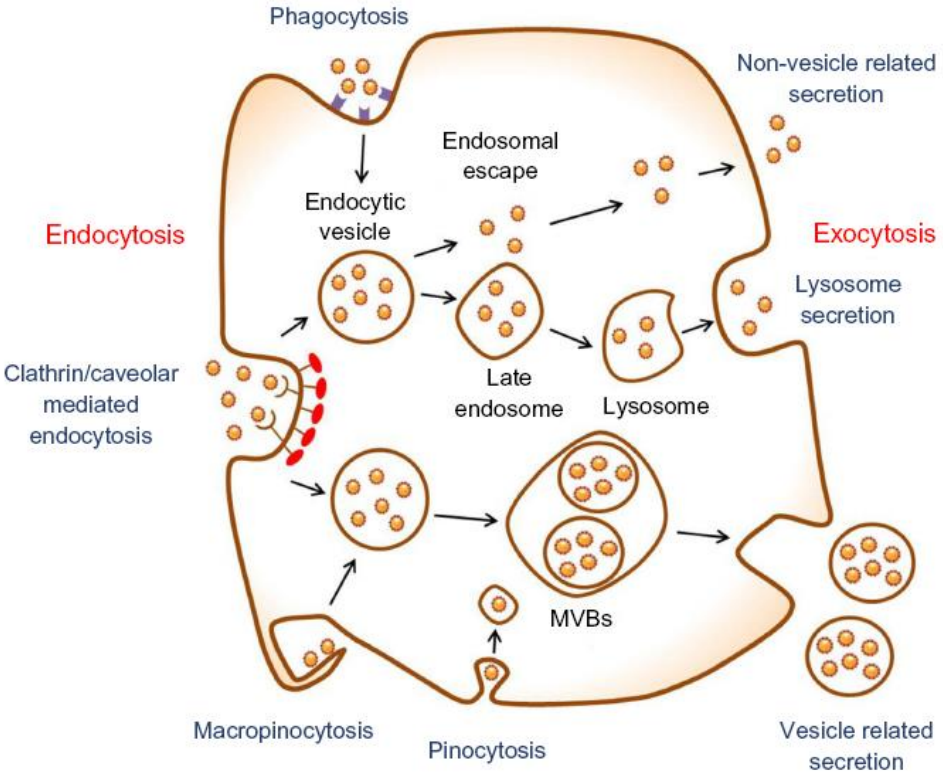

Figure 1.14. Schematic of endocytosis and exocytosis patterns of nanoparticles. Nanoparticles enter the cell via four types of pathway: clathrin/caveolar-mediated endocytosis, phagocytosis, macropinocytosis, and pinocytosis. Nanoparticles exit the cell via three types of pathway: lysosome secretion, vesicle-related secretion, and non-vesicle-related secretion. *Reproduced with permission of O. Nuri, J.H.Park ,Int. J. Nanomed.* ***2014****, 9, 51–63. Copyright ©* ***2017*** *Dove Press Ltd.*

When nanoparticles are systemically administered into the body, they are confronted with many types of cells. Since nanoparticles have emerged as effective drug carriers to treat complex diseases, it has become crucial to understand nanoparticle endocytosis mechanisms. It is believed that the endocytosis efficiency of nanoparticles is dependent on its physicochemical properties, such as size, shape and surface functionalization.

Nanoparticles circulating in the bloodstream can be internalized into many types of cells through the plasma membrane. The plasma membrane is a selectively permeable cellular component that transfers materials that are essential for sustaining the cell's life. Naturally, materials necessary for the cell's life (such as ions and nano-sized proteins) can pass through the lipid bilayer using specialized membrane-transport protein channels. On the other hand, the plasma membrane of cells select the endocytosis pathways of nanoparticles depending on their size, shape, and surface functionalization.

There are two common strategies than can be used to study the endocytosis mechanism of nanoparticles: (i) colocalization of nanomaterials with specific endocytosis markers and (ii) exclusion of specific endocytosis mechanisms using inhibitors. For endocytosis inhibitors, chlorpromazine, wortmannin, phenylarsine oxide, dynasore, and sucrose are known to affect the formation of clathrin-coated vesicles and would therefore limit any potential internalization by clathrin-dependent endocytosis. On the other hand, potassium depletion, genestein, filipin, mycostatin, and methyl-β-cyclodextrin can act as inhibitors of caveolae-dependent endosytosis. In addition, regarding clathrin- and caveolae-independent endocytosis, nocodazole and cytochalasin D are effective internalization inhibitors of actin-dependent endocytosis, and sodium azide, 2-deoxyglucose, and 6-deoxyglucose can serve as inhibitors of energy-dependent endocytosis.

In a recent study, Hao and co-workers investigated the effect of aspect-ratio (AR) in MSNs on cellular endocytosis pathway.[109] For this purpose PEGylated fluorescent mesoporous silica nanoparticles with different AR (1, 2 and 4, ca. 100 nm in diameter) were selected. The authors found that the cellular endocytosis mechanism of the prepared nanoparticles into Hela cells was regulated by particle shape. At this respect, observed that spherical particles preferred to be internalized via the clathrin-dependent pathway, whereas MSNs with larger AR favored to be internalized via caveolae-dependent pathway.

Slowing and co-workers demonstrated that the uptake of MCM-41-type MSNs by HeLa cells can be regulated by different surface functionalization.[110] This study also show that surface functionalities could also affect MSNs ability to escape from the endosomal entrapment. The authors synthesized four MSNs functionalized with fluorescein (FITC), 3-aminopropyl (AP), guanidinopropyl (GP) and *N*-folate-3-aminopropyl (FAP) groups. The uptake by cells of non-functionalized and negatively charged bare MSNs occurs through a nonspecific adsorptive endocytosis. The obtained results indicated that only FITC-MSN and FAP-MSN were endocytosed via a clathrin-mediated mechanism, as the uptakes were inhibited by sucrose. In addition, the uptake of FAP-MSN was partially inhibited in presence of folic acid, whereas the endocytosis of FITC-MSN was not perturbed. This observation along with the higher uptake observed for FAP-MSN suggests that the mechanism of endocytosis for this material is mediated by folic acid receptors on the cell surface. In contrast, the endocytosis of AP-MSN and GP-MSN was affected by a caveolar inhibitor, genistein, suggesting that these materials are endocytosed via a caveolae-mediated mechanism.

Furthermore, Gan and co-workers studied the effect of size nanoparticles in the cellular uptake.[111] The authors prepared MSNs in the 55-440 nm range using a modified base-catalyzed sol–gel method. The uptake of the nanoparticles by MC3T3-E1 cells was studied after 12 h of incubation and the results indicated that the best efficiency, in terms of internalization and endosomal escape, was obtained with 100 nm MSNs.

1.3.2. Key issues in intracellular drug delivery using nanoparticles

1.3.2.1. Particle size and shape

Very recently, studies in order to assess the effect that size, shape and surface functionalization of nanoparticles exerted into their controlled delivery performances have been carried out. The sizes and shapes of these drug carriers play an important role in therapeutic delivery processes, such as particle adhesion, distribution and cell internalization. Nanoparticles have to bypass the reticulo-endothelial system and avoid the clearance by the spleen and liver before they reach the targeted disease sites.

The ***size*** of the particles plays an important role in accumulation at diseased sites. Vallhov et al. showed that smaller particles and lower concentrations of nanoparticles affected human monocyte-derived dendritic cells to a minor degree in terms of viability, uptake, and immune regulatory markers compared to larger particles and higher concentrations.[112] The nanoparticles used in nanomedicine usually range from 20 to 200 nm, because sizes larger than 200 nm are mechanically filtered in the spleen, while those smaller than 100 nm leave the blood vessels through fenestrations in the endothelial lining. For particles larger than 200 nm, deformability is required in order to navigate through the liver and spleen. Particularly, for the treatment of tumors and cancer, 100–200 nm nanoparticles are attractive because of the unique feature known as the enhanced permeability and retention effect.[113] Decuzzi and Ferrari considering buoyancy, hemodynamic forces, van der Waals and electrostatic interactions and steric factors concluded that particles used for drug delivery should have a radius smaller than 100 nm in order to facilitate their margination toward and interaction with the endothelium wall.[114,115]

Similar to size, ***shape*** is a fundamental property of nanoparticles that may be critically important for their intended biological functions. Up to now, there are few reports on the effect of nonspecific cellular uptake of different shaped mesoporous nanocarriers on cellular functions, even though this is of great

interest for the design of high performance delivery systems for therapeutic drugs. This may be due to the limited availability of techniques to produce nonspherical nanoparticles.[116] At this respect, Huang and co-workers found that different shaped nanoparticles can be internalized in cells through nonspecific cellular uptake and can influence some cell functions, including proliferation, apoptosis, adhesion, migration and cytoskeleton organization.[117] The effect of different shaped MSNs (spheres, and short and long rods) functionalized with fluorescein isothiocyanate (FITC) and rhodamine B isothiocyanate (RITC) for imaging and quantification of cellular uptake was studied. The ability of different shaped MSNs to be transported into model A375 cells was compared, and the effects of the shape on cell proliferation, apoptosis, adhesion, migration and cytoskeleton formation were investigated. Their results shown that internalization of the MSNs by A375 cells appears to depend on the aspect ratio of the particles. Results suggest that larger AR particles are taken up in greater amounts and at faster internalization rates as previous studies suggested.[118] A possible explanation for this behavior could be differences in the curvature of the different shaped nanoparticles. Furthermore, sphere-shaped and short rod-shaped particles do not disrupt the cell cytoskeleton, while long rod-shaped particles cause disorder in the organization of the cytoskeleton. These results suggested a link between cytoskeleton organization and endocytosis.[119]

Cell adhesion experiments showed that the number of cells adhering to slides was not affected by sphere-shaped MSNs, while cell adhesion ability became significantly weaker as a result of nonspecific cellular uptake of short rod-shaped and long rod-shaped particles. Also the long rod-shaped MSNs reduced cell viability/apoptosis severely compared to short rod-shaped and sphere-shaped MSNs. Taking into account these facts, sphere-shaped inorganic nanoparticles may circulate in the blood for a longer period and are thus more suitable for targeted drug delivery than short rod-shaped and long rod-shaped solids.

Although the experimental results introduced here showed size-dependent cellular uptake of nanoparticles in of cells, the physical size would not be fully

reflected when they meet the plasma membrane of the cell. Most nanoparticles tend to aggregate in biological solutions, increasing their overall size. The results regarding the size effect would be influenced by nanoparticle aggregation before entering the cell. Thus, it should be tested whether nanoparticles prepared to study their size-dependent endocytosis retain their singularity in the biological media before they enter the cell.[120]

1.3.2.2. Surface functionalization and zeta potential

Nanoparticles surface functionalization is another important factor that could influence cellular uptake and an efficient intracellular drug delivery. At this respect, cellular transfection is controlled by electrostatic interactions and hydrophobic-hydrophilic forces between the cell membrane and nanoparticles surface.

Electrostatic attraction/repulsion could play a major role in adhesive interaction between the drug delivery carrier and the cell membrane and this property acts as an impulsive force to drive the nanoparticles to approach the cell membrane.[121-123] On the other hand, hydrophilic and hydrophobic interactions between drug delivery carrier and cellular compartment are responsible for the recognition of specific domains of cell surface.

Potential electrostatic interactions between the nanocarriers and the cell membrane can be assessed easily by measuring the Zeta potential at the nanoparticles surface. Zeta potential value indicated the net charge at the particle surface which affects the distribution of ions in the surrounding medium, resulting in an increased concentration of counter ions close to the surface. Zeta potential is represented by a numerical value which can range between -50 to +50. A higher zeta potential represents a higher driving force, where there will be a fast approach and quick adhering of drug delivery carrier onto the surface of the cells. The force or speed at which particles adhere to the cell surface can be slow at lower zeta potential. This sometimes may be disadvantageous since the drug delivery carrier flow away from the targeted cells during circulation. The Zeta

potential can vary based on the ambient condition and applications. There may be an optimum zeta potential for the intracellular drug delivery of nanoparticles to specific cells.

Surface functionalization plays also a vital role in targeting cells or even nucleus. By appropriate surface functionalization, many objectives can be accomplished such as increasing drug delivery carrier biocompatibility, increasing the uptake by specific cells, targeting the cellular localization in cells and organs and increase the therapeutic efficiency.[124,125]

1.3.2.3. Biocompatibility and biodistribution

Biocompatibility is an important issue in the design of nanocarriers for drug delivery applications. Since the drug delivery carrier will be in direct contact with the biological environment it should not cause any adverse effects in the individual who undertakes the treatment. The biocompatibility of any drug delivery carrier can be determined only by understanding how it interacts with the biological system.

Biocompatibility is the study of the interaction of biomaterials with the body of experimental animals to evaluate possible toxicity effects. MSN biodegradation and clearance are strongly interdependent processes. MSN dissolve fairly rapidly under physiological conditions when the concentration levels are kept below the saturation level of silica, as demonstrated in several studies.[126] The rate of silica dissolution is dependent on parameters such as the particle size, functionalization and the degree of silica condensation, which in turn is highly dependent on the heat-treatment history of the silica particles. For circulating particles, the liquid (aqueous) volume is larger with respect to the silica concentration and, therefore, it can be expected that the particles dissolve under *in vivo* conditions. Dissolved silica is known to be adsorbed by the body or excreted in urine in the form of silicic acid or oligomeric silica species.[127] Here, forces exerted by blood pressure would be expected to assist in disintegration of partially dissolved particles, which

can be expected to have a lower mechanical stability as compared with the original particles.

Interestingly, it has been observed that, depending on the particle size, the particles can dissolve from inside out leaving the initial particle size virtually intact under static conditions.[128] Recent *in vivo* data showed that partially degraded MSN have particle dimensions close to that of the injected suggesting the same degradation mechanisms may also be operative *in vivo*.[129] However, the renal cut-off limit is approximately 5 nm, which is why the exact excretion process remains unclear in this case. Landry and co-workers investigated rat urine after intraperitoneal injection of tetraethylene glycol functionalized Gd-containing mesoporous microparticles and found particle-shaped objects most likely originating from the microparticles, and concluded that particulates could also be partially excreted renally.[130] This observation was also corroborated by Magnetic Resonance Imaging (MRI) of the lower abdominal cavity of the Wistar rats used, demonstrating enhanced contrast in the bladder at time points 2–25 h post-injection. Huang and co-workers found the same phenomenon for MSN rods. At this respect, the authors were able to image MSN rods in both urine and fecal samples at 24 h post administration.

Lu and co-workers used MSN of ca. 100–130 nm diameter to investigate their biocompatibility and biodistribution in mice with established human cancer xenograft by using *in vivo* imaging fluorescence microscopy and mass spectrometry.[131] The authors also test the ability of MSN to deliver anticancer drugs into xenografted mice and to suppress tumor growth. The two month studies showed that no apparent histopathological abnormalities or lesions in the mice treated with MSN were observed. The obtained data also suggested that the dosage used (50 mg kg^{-1}) was adequate for pharmacological application for cancer therapy. On the other hand, Hudson and co-workers reported that 30 mg of intraperitoneally injected MSN resulted in death or distress necessitating euthanasia.[132] The authors correlated the obtained results with the extremely high dosage used (1.5 g kg^{-1}) and the different size and composition of the MSN

employed. The above mentioned examples demonstrated that biocompatibility of MSN may depend on the materials size, morphology, composition, and surface functionalization in addition to the dosage used.

Souris and co-workers showed that positively charged nanoparticles are excreted from the liver into the gastrointestinal tract and excreted from the animal in the feces while negatively charged MSN are sequestered within the liver.[133] Besides, Lo and co-workers studied the effect of the surface charge on the two proposed MSN elimination routes. The authors found that positively charged MSN exhibited rapid hepatobiliary excretion. For the two differently charged particles studied concluded that while both were sequestered by the liver the one with the higher charge could have been more opsonized by serum proteins and thus more amenable to hepatobiliary excretion into the gastrointestinal tract. Thus, surface charge tuning could not only constitute a complement for targeting but also a means for regulation of the rate of excretion.

The importance of surface functionalization was demonstrated by Blumen and co-workers.[134] At this respect, the authors prepared PEGylated MSN that were nontoxic in peripheral tissue, suggesting that coating strategies may systemically reduce toxicity. Also, experiments using MSN as bio-imaging vehicles *in vivo* at several dosages (100 and 200 mg kg^{-1}) did not reveal any toxic effect.

Dealing with ***bio-distribution***, Lu and co-workers using fluorescent MSN, observed a quick and dense accumulation of nanoparticles in tumors.[135] Furthermore, targeting of the MSN to cancer cells by attaching folate onto their surface resulted in an increase in tumor accumulation. These results were ascribed to the EPR effect, that is, leaky vasculature of blood vessels in the tumor. On the other hand, He and co-workers studied the bio-distribution and degradation of PEGylated MSN.[136] The authors found less degradation products in the urine at shorter times (30 min) for PEGylated MSN than for non-PEGylated counterparts. Also the degradation products increased with the enhancement of particle size because larger MSN were more easily captured by the liver and

spleen in short time, which led to their faster biodegradation and thus larger excreted quantities of their degradation products. As a contrast, PEGylation of MSN would hinder its capture by organs of the reticuloendothelial system (RES) and consequently slow down the biodegradation.

Other factor that affects the bio-distribution of nanodevices is the shape of the nanoparticles. At this respect, Huang and co-workers showed that short rod-shaped MSN accumulate in the liver whereas long rod-shaped nanoparticles accumulate in the spleen.[137] The excretion of MSN through the urine and feces has been reported by various groups. In the Lu and co-workers study using folate-MSN up to 94% of the silica was excreted from the mice 4 days after injection with 73% being detected in the urine and 21% in the feces.[135]

Chen and coworkers report an in vivo tumor targeted positron emission tomography (PET)/near-infrared fluorescence (NIRF) dualmodality imaging and drug delivery of hollow mesoporous silica nanoparaticles (HMSN). Using CD105 ,known as endoglin, which is a validated marker for tumor angiogenesis and almost exclusively expressed on proliferating tumor endothelial cells, they developed a targeting strategy. The results found a higher uptake of TRC105 (which binds to CD105 on tumor neovasculature) conjugated HMSN in the 4T1 murine breast cancer model than in a non-targeted group. These results make surface engineered HMSN a highly attractive drug delivery nano-platform for future cancer theranostics. Systematic *in vitro* and *in vivo* studies were performed to investigate the stability, targeting efficacy and specificity, biodistribution and drug delivery capability of functionalized HMSN nanoconjugates. Furthermore, optical imaging of organs after injection of nanoparticles shown accumulation in tumor and in liver. Although they found liver is the dominant organ for HMSN nano-conjugates accumulation, as evidenced in a PET/NIRF imaging and biodistribution studies, only weak optical signal could be observed based on *ex vivo* optical imaging because and strong absorbance of visible DOX fluorescence (**Figure 1.15**).[138]

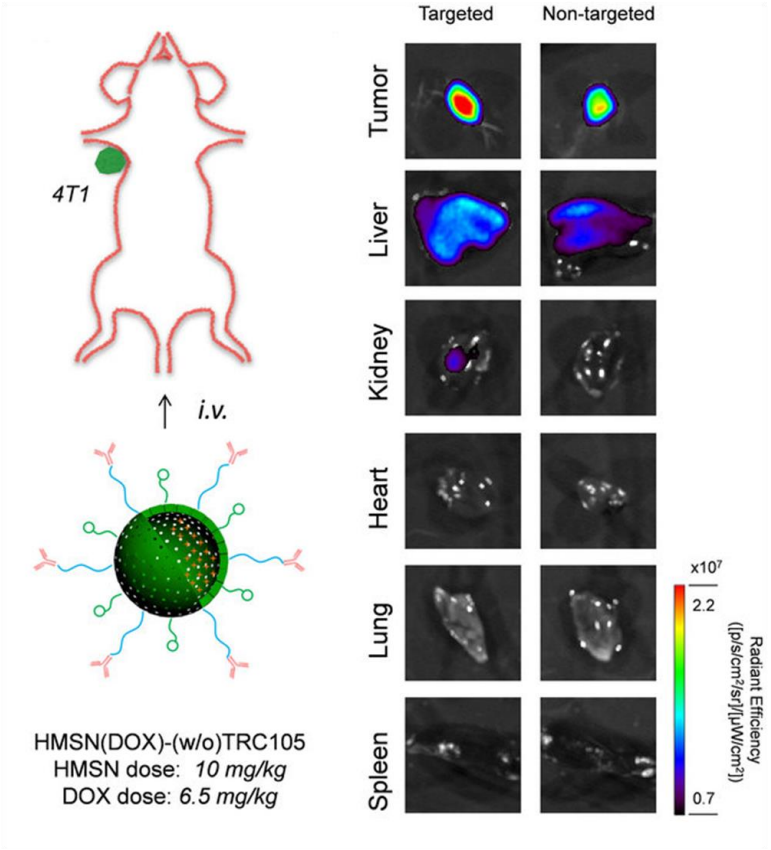

Figure 1.15. A schematic illustration showing the in vivo drug delivery after i.v. injection of hollow mesoporous silica nanoparticles loaded with doxorubicin and funciontalized with TRC105 (which binds to CD105 on tumor neovasculature) in 4T1 tumor-bearing mouse and *ex vivo* optical imaging of major organs after *i.v.* injection of nanoparticles in mice. Reproduced with permission of F. Chen, H. Hong S. Chi, S. Goel, H.F. Valdovinosm R. Hernandez, C.P. Theuer, T.E. Barnhart, W.Ca, *Scientific reports* **2014**, *4*, 1. Copyright © **2014**, Rights Managed by Nature Publishing Group.

In another work, Fu and co-workers studied the biodistribution of MSNs containing paclitaxel for intraperitoneal (i.p.) delivery. An *in vivo* study using xenograft mice bearing peritoneal human pancreatic carcinoma MIA PaCa-2 demonstrated that the MSN-paclitaxel formulation, compared to free paclitaxel, exhibited a 3.2-fold increase in peritoneal cavity residence time, slower absorption into the systemic circulation with one third systemic exposure, but a

6.5-fold increase in peritoneal tumor accumulation. Tissue distribution imaging showed significantly greater accumulation of fluorescent MSNs in tumor tissues compared to other peritoneal tissues (**Figure 1.16**). In conclusion, intraperitoneal administration of drug-containing MSNs was effective at reducing systemic exposure and increasing the peritoneal tumor accumulation of the drug.[139]

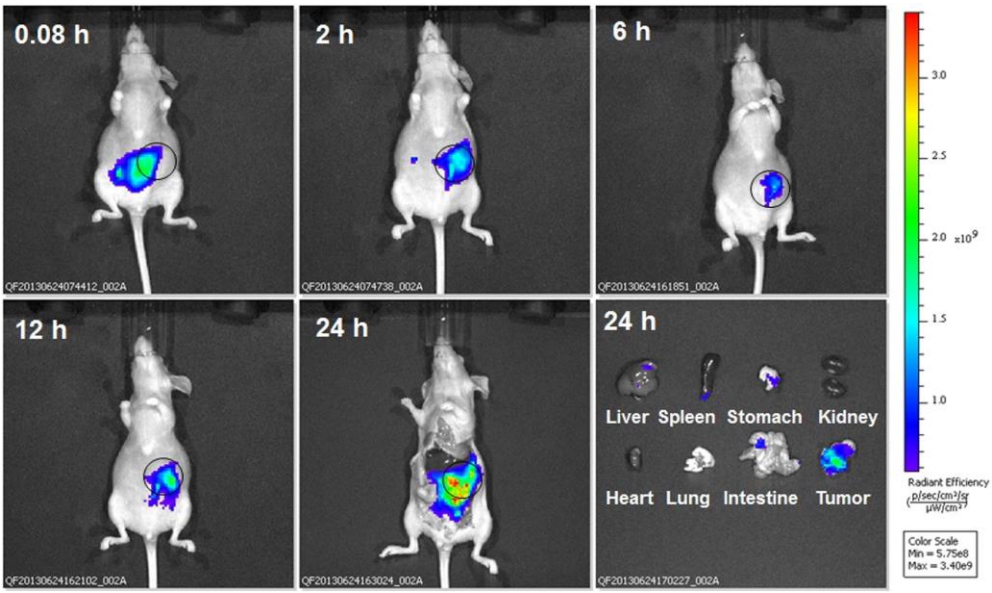

Figure 1.16. Peritoneal distribution of MSNs containing paclitaxel with imaging at 0.08, 2, 6, 12, 24 hours post intraperitoneal administration. Tumors are circled. Reprinted with permission from Q. Fu, D. Hargrove, X. Lu, *Nanomedicine: Nanotechnology, Biology, and Medicine*, **2016**, 12 (7), 1951-1959. © **2016** Elsevier Inc.

1.3.3. Endosomal escape

Recent studies have demonstrated that MSN are able to undergo smooth cell internalization, but endosomal escape has been identified as a bottleneck for the efficient delivery of macromolecular substances or nanoparticles.

Many anticancer therapeutics such as DOX feature cell membrane permeability, and consequently, a trigger for endosomal escape is not required. These permeable drugs only require a means of preventing premature release from the nanocarrier to avoid global distribution in the organism and targeted transport into cancer tissue to achieve a sufficiently high local drug concentration.

Nevertheless, a large number of molecular and macromolecular therapeutics are either hydrophobic or membrane impermeable. Therefore, the multifunctional nanocarrier vehicles should provide an efficient endosomal escape mechanism for the local delivery of the drug molecules into the cytoplasm, thus gaining access to the targeted cell compartments or to the nucleus. There is little consensus in the literature around the mechanism of trafficking across the endosomal membrane, and there are a number of diverse mechanisms that can be employed to induce endosomal escape (**Figure 1.17**). We have focused on three proposed strategies for inducing endosomal escape; however, it is highly likely that more than one of the mechanisms are required for efficient cytoplasmic delivery of therapeutics.

Excellent strategies for achieving endosomal escape are provided by nature. Evolution created bacteria and viruses, which are able to penetrate membranes via different mechanisms to escape the endosomal pathway and to reach their target sites. Different mechanisms such as pore formation in the endosomal membrane, pH-buffering effects of protonable groups (“proton sponge”), or fusion into the lipid bilayer of endosomes have been proposed to facilitate the endosomal escape.[140] In addition, photochemicaly active moieties able to induce the rupture the endosomal membrane have been implemented onto MSN.[141,142]

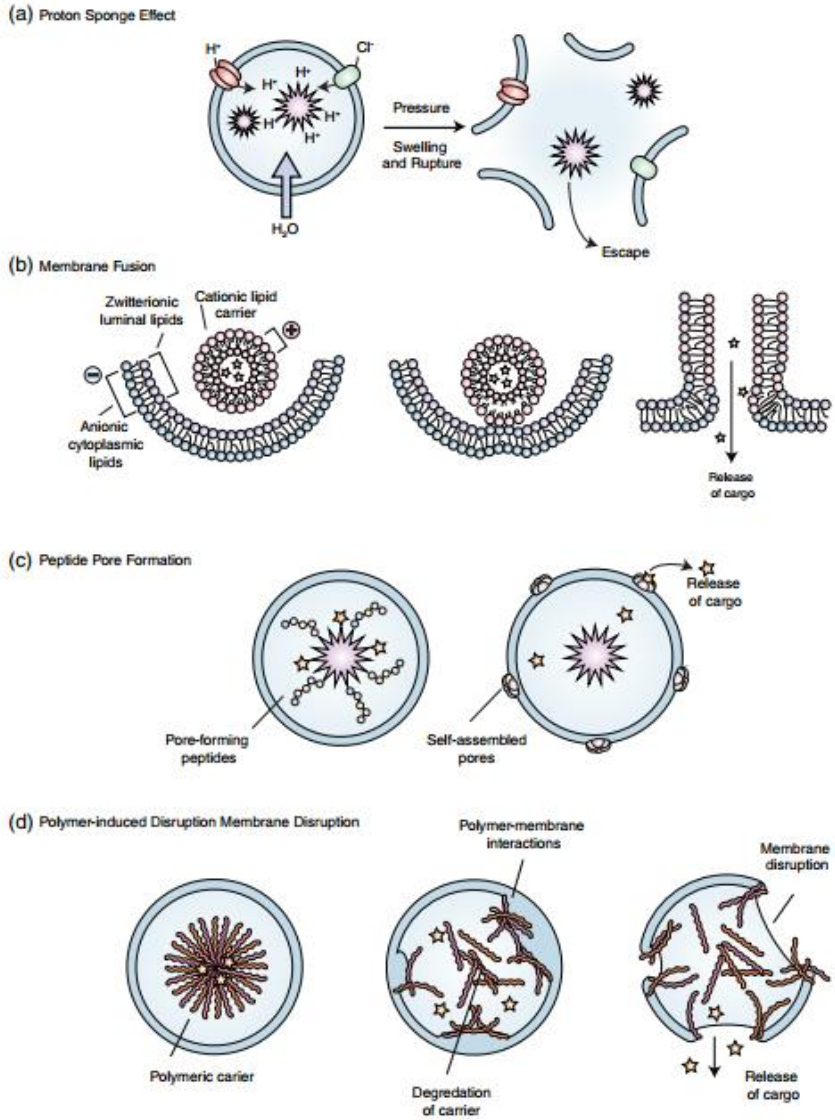

Figure 1.17. Mechanisms of endosomal escape. (a) Proton sponge effect, (b) Membrane fusion (c) Pore formation, (d) Membrane disruption. Reprinted with permission from L.I. Selby, C.M. Cortez-Jugo, G.K. Such, A.P.R. Johnston, *WIREs Nanomed Nanobiotechnol* **2017**, e1452. Copyright © 2017 Wiley Periodicals, Inc.

Photochemical internalization (PCI) using photosensitizers (PS) that generate reactive oxygen species upon photoactivation is a powerful tool to overcome the trapping by the endosomal membrane. In the initial approaches the PS was

adsorbed onto the MSN with the possible subsequent uncontrolled spreading of the compound and toxic effects on the cells.[143] To achieve a more spatially controlled activity of nanodevices operating with PS, it is desirable to bind the PS directly to the surface of the particles. Thus, a mesoporous core-shell system with covalently surface linked PS was designed that provided an on-board trigger for light-activated endosomal membrane rupture.[144] In order to create a general photoactivatable drug delivery platform being applicable in biological environments, such as cancer tissue, further improvements have to be accomplished. The activation of the photosensitizer with low energy light reduces the phototoxicity and significantly increases the depth of tissue penetration, which will be crucial when activation *in vivo* is required. Sauer and co-workers showed that MSN were taken up into cells and transported within endosomes, but no release of the cargo into the cytoplasm could be detected during incubation.[145] In order to overcome the barrier of endosomal entrapment, photoinduced endosomal release via excitation of a PS was employed by the authors.

Another promising endosomal release strategy is based on the ***proton sponge effect***, in which osmotic swelling and membrane rupture of endosomes is initiated by macromolecules with high buffering capacities. This mechanism does not require an external stimulus, and custom-made nanocarriers can activate an "automatic" pathway for endosomal escape. Several cationic lipids and polymers possess substantial buffering capacity below the physiological pH which is a potential trigger to escape the endosomal entrapment.[146] The cationic polymers or particles enter the cell via endocytosis, subsequently being entrapped in the endosome. Upon intracellular trafficking to late endosomes or lysosomes, the compartment is acidified from an initial physiological pH value of 7.4 to around 5. The accumulation of positive charge inside the endosome is coupled with a passive influx of chloride anions through ion channels to maintain electro-neutrality. The large increase of ion concentration within the endosome in turn results in an inflow of water molecules, which causes osmotic swelling and subsequent membrane rupture.

Another related mechanism proposed by Battaglia and co-workers describes the role of osmotic pressure upon the disassembly of nanoparticles in the endosome.[147] In this mechanism, rather than the buffering capacity of the polymer inducing the osmotic pressure and subsequent lysis, it is proposed that the disassembly of a particle into many polymer subunits causes an osmotic shock that ruptures the endosome.

The use of the proton sponge effect provides an elegant solution for the problem of endosomal entrapment of MSN. However, the exact mechanism is not fully understood. At this respect, Lin and co-workers studied the impact of surface functionality in endosome escape. The authors stained the endosomes with a red fluorescent endosome marker and monitored the confocal fluorescence micrograph of MSNs marked with fluorescein and derivatized with different functional groups in HeLa cells. They found that the more negatively charged nanoparticles appeared to be able to escape from endosomes within 6 h, while those with more positive Z-potentials, remained trapped within endosomes. This behavior could be attributed to the Proton Sponge effect, where the more negatively charged materials would have a better buffering capacity, which is important for the endosome escape.[148] The zeta potential of the silica nanoparticles seems to have a great impact on the ability of particles to escape the endolysosomal pathway. However, such highly negatively charged nanoparticles exhibit unfavorable cellular uptake behavior due to electrostatic repulsion with the negatively charged cell membrane. Nanocarriers providing protonable groups at mildly acidic conditions should result in much more efficient cellular uptake and subsequent drug release to the cytosol. In general, the proton sponge effect is a promising intrinsic endosomal escape pathway that should be further investigated.

As an alternative mechanism, endosomolytic peptides can be utilized to achieve endosomal release. Lipid bilayer-enclosed MSNs reported by Brinker and coworkers were decorated with such an endosomolytic peptide (H5WYG). This peptide sequence is a subunit of the glycoprotein hemagglutinin of the influenza

virus A, and undergoes a conformational change upon protonation. H5WYG peptides were often employed in combination with nanocarriers, but experimental evidence for the exact molecular mechanism was not provided so far. Different endosomal escape pathways were believed to take place, such as the proton sponge effect (protonation of the histidin residues of the peptide) or fusion of the endosomal membrane.[149]

Membrane fusion is another mechanism for endosomal escape. Viruses can induce endosomal escape by fusion of the viral envelop with the endosomal membrane allowing the viral capsid to enter the cytoplasm. In a similar process particles assembled from lipids or amphiphilic materials generate a phospholipid bilayer that can fuse with the endosomal membrane, inverting the structure of the particle and delivering the therapeutic core to the cytoplasm. For instance, haemagglutinin (which is a peptide of the influenza virus coat) acts as a fusogenic agent that is converted from an anionic, hydrophilic coil at pH 7.4 to a hydrophobic helical conformation at the acidic endosomal pH. This new α-helical structure leads to fusion of the viral membrane into the cellular membrane.[150]

Destabilizing the endosomal membrane can allow therapeutic cargo to diffuse out of the endosomal compartment through holes or pores. ***Endosomal disruption*** can occur through the direct interaction of polymers or peptides with the endosomal membrane or via peptides that self-assemble across the membrane to create defined pores.[151] Typically, the dimensions of transmembrane pores are ca. 1-2 nm, which generally limits their usefulness to induce efficient release of therapeutic cargo.[152] Coarse-grain molecular simulations with asymmetric lipid membranes demonstrated that insertion of dendrimers induced an asymmetry with subsequent defect formation. Supported lipid bilayer studies with atomic force microscopy visually demonstrate that dendrimers and PEI induce thinning or hole formation.[153] Is well known that simulations and artificial membranes are not able to fully represent the complexities of cell membranes but in vitro experiments have shown similar results. Whole-cell patch-clamp conductance measurements show that

polycations cause membrane defects and that these can heal over time.[154] In addition, electron microscopy shows direct interaction and disruption of lysosomal membranes by PEI.[155] The escape mechanism for polyanionic polymers is attributed to an increase in hydrophobicity due to protonated carboxylate groups, which results in membrane insertion and subsequent membrane disruption.[156]

It is important to understand the mechanism by which endosomal escape can occur when designing a delivery system. Endosomal lysis and membrane fusion have the potential to deliver cargo to the cytoplasm regardless of its size, while membrane disruption and pore formation will inherently have limits to the molecular weight than can diffuse across the destabilized membrane. Additionally, how the cargo is encapsulated or attached to the delivery vehicle can affect the therapeutic outcome. It is also important to consider the potentially toxic side effects of endosomal escape. Lysosomes play an important role in regulating apoptosis, and the uncontrolled release of cathepsin as well as calcium ions can significantly affect the viability of cells.[157]

Further investigations are needed to evaluate the exact mechanism, which could lead to the full exploitation of this endosomal escape pathway. In general, endosomal entrapment was found to be a bottleneck in efficient cytosolic delivery. A complete understanding of the diverse escape mechanisms is highly desirable.

1.3.4. Controlled release of cargo

Thanks to the fact that MCM-41 MSN exhibits a unique porous network composed of parallel pores without connections between them, it is possible to prepare drug delivery systems (DDS) using these nanoparticles as inorganic scaffold. These DDS present zero premature release of the loaded drugs after placing on the pore outlets different organic or inorganic moieties than acts as

pore blockers or gatekeepers. These organic or inorganic moieties are designed in such a way that application of external stimuli induce pore opening and cargo release. Cargo delivery in a controlled fashion can drastically reduced side effects by inducing release to single cells or target tissue. Delivery of antitumor drugs and other pharmaceutical cargos (such as enzymes or oligonucleotides) requires effective protection from undesired degradation in harsh environments (such as the stomach and intestines). The most common pore sealing strategies can be classified into three main different types i.e. (i) coating of the external particle surface, [158] (ii) molecular/particle pore closing, [159] and (iii) cargo coupling to the internal wall of the pores [160] (See **figure 1.18**). These smart nanocarriers can transport the drug to the target tissue and once there, the presence of a certain stimulus, which may be internal or external, triggers the release of the entrapped drugs achieving a better control on the administered dose.

Over the past years, many research groups have made great efforts in the development of MSN based drug delivery systems with stimuli-responsive triggered release features. The stimuli used for the control of cargo delivery can be internal or external. Internal stimuli are present in living organisms and do not require an external input to trigger the release of the selected cargo. Besides, internal stimuli (such as pH changes, enzymatic reactions, and reducing agents) can provide intrinsic and autonomous release of the loaded cargo molecules from the mesoporous host system. However, the control on the administered dosage is lower than in the case of devices that employ an external stimulus. Triggers such as light, external magnetic fields and temperature require activation of the release mechanism from the outside. These systems provide perfect control over temporal and spatial release of the drugs into the targeted tissue or cells, but tissue penetration in *in vivo* studies can limit their performances.

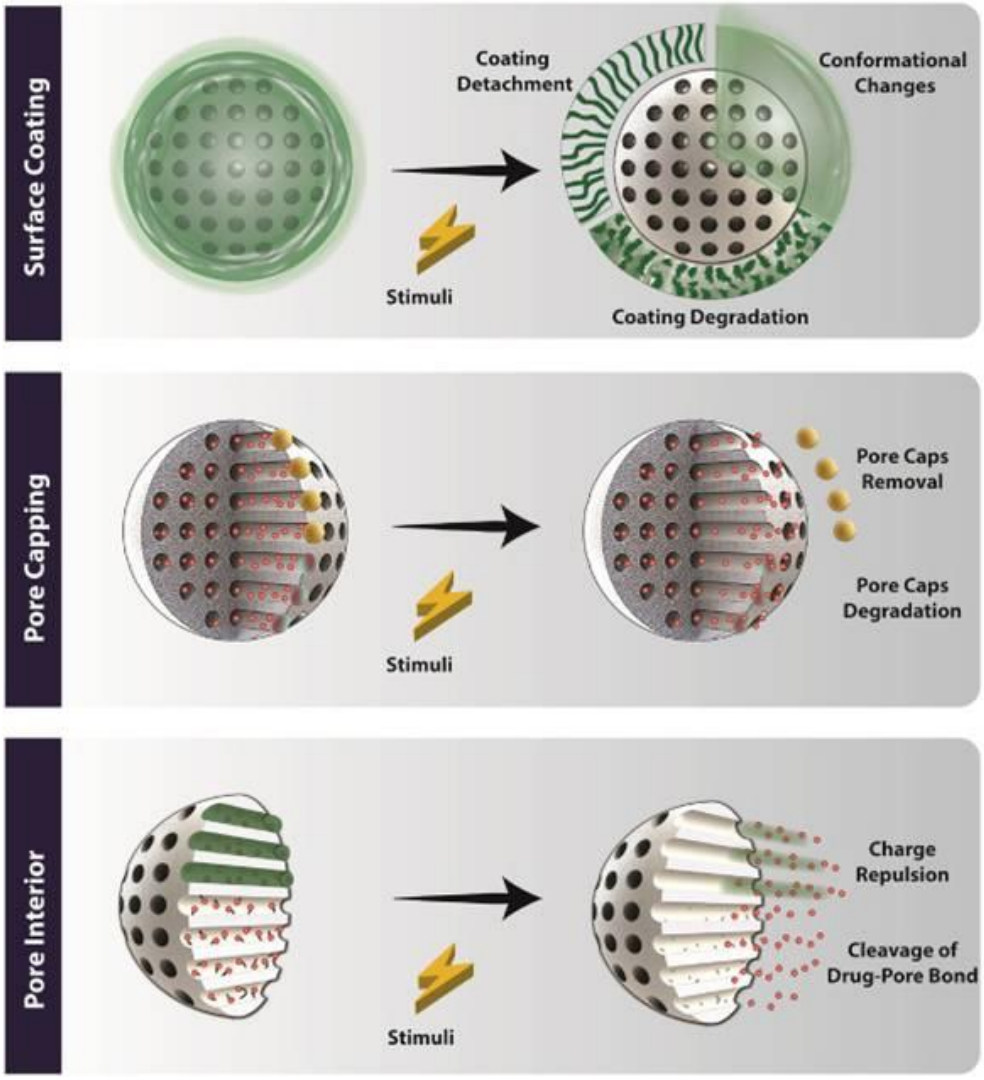

Figure 1.18. Representation of the strategies utilized to create stimuli-responsive MSNs and the most common responses to the stimuli exposition. The stimuli responsiveness of MSNs can be achieved at three different levels, surface coating, pore capping or through drug interactions with internal pore wall. In turn, the changes that the stimuli exposition promote on MSNs will allow the drug diffusion to out of the pores Reprinted with permission from A.F. Moreira, D.R. Dias, I.J. Correia, *Microporous and mesoporosu materials* **2016**, 236, 141-157. Copyrigh © 2016 Elsevier Inc. All rights reserved.

1.3.4.1 Endogenous stimuli-responsive drug delivery materials

Endogenous/internal stimuli (pH changes, overexpression of certain enzymes, temperature, high concentrations of reducing agents) are present in living organisms and can provide an intrinsic and autonomous delivery of payload from the mesoporous gated materials. These materials makes use of (bio)chemical conditions presented in certain cells or tissues as triggers for the release of different cargoes.

pH-Triggered release

One of the most commonly employed endogenous stimuli used in the preparation of nanodevices with applicability in cancer therapies is pH. The tumor microenvironment is characterized by pH values lower than that displayed by normal tissues. These lower pH values can be attributed to the high cellular proliferative rate (e.g. augmented lactic acid production), the increased efflux of intracellular protons and low blood perfusion of tumor tissues.[161,162] All these factors lead to a decrease in oxygen content and a limited capacity to remove the acidic waste products resultant from metabolism.[161] Furthermore, at a subcellular level, in late endosomes and lysosomes, the nano-sized transporters can find even more acidic environments, with pH values ranging from 4.5 to 5.5.[163] Therefore, this acidic pH found in tumor and inflammatory tissues as well as in the endosomal and lysosomal compartments of cells provides a potential internal trigger for the release of drugs from a pH-responsive drug carrier.

Polyelectrolytes, which are polymers with ionisable repeating units, are either absorbed or covalently bonded onto the surface of MSN to serve as pH-responsive capping agents. Under neutral or weakly basic conditions the polyelectrolytes tightly wrap around the particle surface blocking the loaded pores. However, at acidic pH, the polyelectrolytes are protonated acquiring an open rigid conformation that allowed cargo release from the unblocked pores.

Bein and co-workers prepared MSN coated with a bifunctional polymer consisting on poly(2-vinylpyridine) (PVP) covalently linked with poly-ethilenglycol (PEG) to deliver DOX in T24 cancer cells (see **Figure 1.19**).[164] Furthermore, the authors functionalized the end of PEG fragment with FA (as targeting ligand) and with a PS (in order to allow endosomal escape). Aqueous suspensions of the prepared nanoparticles at pH 7.4 showed negligible cargo release (ca. only 4%) while at acidic pH (5.0) a marked DOX delivery was observed. The observed release at pH 5.0 was ascribed to PVP protonation that induced a change in the conformation of the polymer from a hydrophobic state to an extended hydrophilic one. The prepared nanoparticles were efficiently uptake by T24 cancer cells (overexpressing FA receptors) and were able to release the entrapped Dox inducing a marked reduction in cell viability.

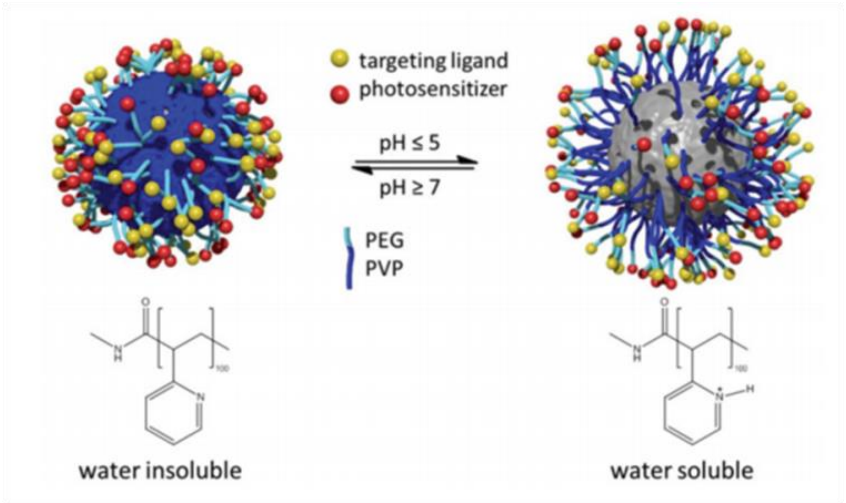

Figure 1.19. Representation of the pH-responsive delivery system which pores can be reversibly opened and closed through changes in the solubility of the polymer. At pH values around 5.5 or higher, the polymer is deprotonated producing a hydrophobic state, which causes a collapse of the polymer onto the silica surface, thus preventing release of the cargo. At lower pH the polymer is soluble and lead to a switch of the particle into its open state. Reprinted with perimission from S. Niedermayer, V. Weiss, A. Herrmann, A. Schmidt, S. Datz, K. Müller, E. Wagner, T. Bein, C. Bräuchle, *Nanoscale* **2015**, 7, 7953. Copyright ©2015 Nanoscale.

Using a similar approach, Feng and co-workers used, as gate, a biocompatible polyelectrolyte multilayers (PEM) composed of poly (allylamine hydrochloride) (PAH) and sodium poly(styrene sulfonata (PSS) using a layer-by-layer technique (See **Figure 1.20**).[165] In another work, the same authors used multilayers of alginate/chitosan assembled on MSN surface.[166] The prepared MSN exhibited a pH-dependent DOX release. Nanoparticles *in vitro* evaluation on HeLa cells showed a sustained intracellular DOX release and a prolonged accumulation in the nucleus, thus resulting in an enlarged therapeutic efficacy. In addition, the pharmacokinetic and biodistribution studies in healthy rats showed that DOX-loaded nanocarriers had longer systemic circulation time and slower plasma elimination rate than free drug. The histological results also revealed that the nanocarriers had good tissue compatibility. Thus, MSN functionalized with biocompatible multilayers holds the substantial potential to be further developed as effective and safe drug-delivery carriers.

Yang and co-workers also used polyelectrolytes as pH-responsive gatekeepers.[167] The authors grafted poly(glutamic acid) (PLGA) onto the external surface of MSN loaded with DOX. The used drug is located in the inner of the pores and also adsorbed onto the polymer layer. DOX release from the PLGA-MSN at pH 8.0 was negligible whereas at acidic pH a marked drug delivery was observed. This finding can be attributed to the fact that the protonation of PLGA results in the dissociation of the electrostatic interaction between the polymer and Dox and consequently facilitates drug release. As the release rate of DOX from PLGA-MSN was pH-dependent a rapid drug release specifically in cancerous tissues was achieved. The study also demonstrated that PLGA-MSN had high drug-loading efficiency, superior stability, and significantly high drug release rates compared to the unmodified MSN carrier. The *in vitro* cellular cytotoxicity test indicated that PLGA-MSN was biocompatible and had the potential to be utilized as drug carriers. Furthermore, nanoparticles loaded with DOX showed potent cytotoxicity, comparable to DOX alone.

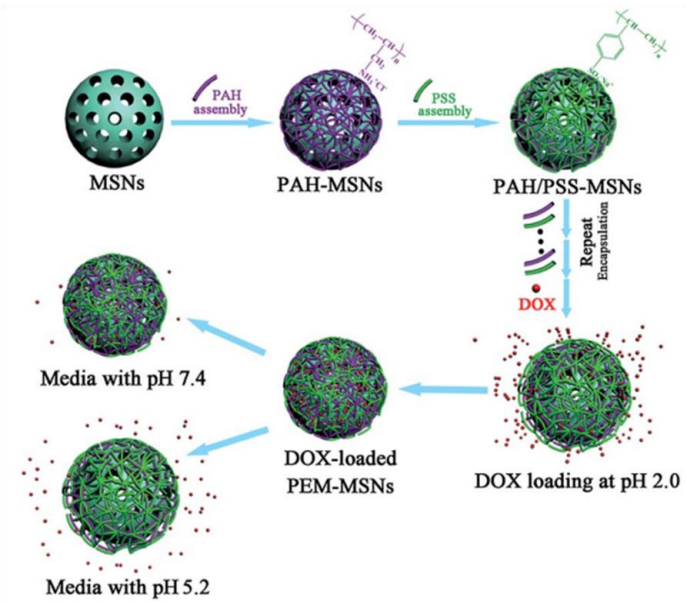

Figure 1.20. Schematic illustration for the fabrication of pH-responsive carrier systems based on PEM-MSNs. The polyelectrolyte pairs of PAH/PSS were alternately deposited onto the MSN surface via the LbL technique, DOX was then loaded into the mesoporous channels and inside the polymer shell of PEM-MSNs at pH 2.0, thus constructing a pH-responsive drug delivery system from which the release of DOX is accelerated under acidic conditions. Reprinted with permission from Feng W, Zhou X, He C, Qiu K, Nie W, Chen L, et al., *J. Mater. Chem. B* **2013**, 1, 5886. Copyright © **2013** The Royal Society of Chemistry.

Another approach used for the preparation of pH-triggered materials is the use of nanovalves based on supramolecular inclusion complexes. One example of this approach is the work of Stoddart and co-workers that reported a MSN based material capped with β-cyclodextrin (β-CD) nanovalves that were responsive to the acidic conditions of endosomes in cancer cells.[168] For this purpose the authors used MSN, as inorganic scaffold, and loaded the pores of the support with DOX. Then, the external surface was functionalized with *N*-methylbenzimidazole (pK_a 5.67) and the pores capped upon addition of β-CD (that formed inclusion complexes with the grafted aromatic heterocycles). At neutral pH negligible DOX release was observed. However, at acidic pH a marked delivery was found due to benzimidazole protonation and subsequent dethreading of the supramolecular

complexes. These nanoparticles were internalized by KB-31 cells and DOX release induced apoptotic cell death.

Another approach, for the development of pH-triggered controlled release materials, consisted in the use of linkers that contained pH-sensitive bonds (acetal, ester, hydrazine) connected with bulky moieties. These bulky units are able to block the pores controlling cargo release. Besides, the use of acidic-decomposable inorganic materials as gatekeepers to control drug release has also been reported.

At this respect, Chen and co-workers prepared MSN loaded with DOX and then capped the pores with ultra-small lanthanide doped upconverting nanoparticles using a pH-sensitive linker containing acetal bonds.[169] Aqueous suspensions of the capped MSN at pH 7.0 showed negligible Dox release. However, at acidic pH, a marked DOX delivery was observed due to hydrolysis of acetal bonds allowing the removal of the capping upconverting nanoparticles. The effectiveness of the nanomaterial was also tested in HeLa cells. Besides, this nanodevice allowed for passive tumor targeting and increased tumor accumulation via the EPR effect, which was visualized by MRI *in vivo*.

On the other hand, Moreira and co-workers developed calcium carbonate coated MSN for ibuprofen and DOX delivery to prostate cancer cells.[170] The incubation of the coated MSN at pH 7.4 showed a slow drug release, while at acidic pH a faster cargo delivery was obtained. Such results can be explained by the rapid calcium carbonate dissociation into Ca^{2+} and CO_3^{2-}, when exposed to acidic media, whereas at physiological pH this material was relatively stable and present a much slower degradation rate.

In a similar approach, Guo, Zhu and co-workers employed acid-decomposable luminescent ZnO quantum dots (QD) to seal the nanopores of MSN in order to inhibit premature drug (DOX) release.[171] After internalization into HeLa cells, the

ZnO QD caps are dissolved rapidly in the acidic intracellular compartments, followed by loaded drug release from MSN into cytosol.

Redox-triggered release

Redox reactions have been also frequently used as triggers in the development of gated materials based on MSN. In the human body, the glutathione (GSH)/glutathione disulfide is one of the major redox couples that plays a relevant role in avoiding the damage caused by ROS species.[172] In fact, the GSH concentration in tumor cells is 100-1000 times superior to that found in the extracellular fluids.[173,174] Therefore, redox responsible gated nanoparticles are aimed to disassemble and release their cargo in the cell, using as a trigger the redox potential. Usually, redox responsive nanodevices incorporate disulfide bonds (general structure R–S–S–R) which are degraded in the presence of reducing agents (such as GSH). One common strategy employed for the production of redox responsive MSN is based on the grafting of polymers onto the particle surface through disulfide bonds.

Zhang and co-workers reported on a novel redox-responsive MSN based nanocarrier capped with the therapeutic peptide $(RGDWWW)_2KC$ containing an RGD target motif, for tumor targeting synergistic therapy.[175] For this purpose, the pores of MSN were loaded with DOX and then the external surface was functionalized with $(RGDWWW)_2KC$ through a disulfide bond. The two branches of the peptide containing tryptophan that allowed the pores to be blocked via π-π and hydrophobic interactions. Once the loaded nanoparticles were internalized by cancer cells, the therapeutic peptide (on the surface of MSN) and the DOX (entrapped in the inner of the pores) were release. Both releases were ascribed to the rupture of the disulfide bonds, which linked the peptide onto the external surface of the MSN, due to the high concentration of GSH in cancer cells. At the same time, tryptophan in the peptide chains interacted with DNA, through strong π interactions, causing cell apoptosis.

Yang and co-workers used MSN as inorganic support and MnO_2 as capping agent in order to prepare a redox-triggered hybrid material that allows a sustained DOX delivery to HepG2 cancer cells.[176] In the presence of GSH a marked DOX delivery was observed due to the dissolution of the cap (reduction of MnO_2 to Mn^{2+}). Cellular studies revealed that MnO_2 coated MSN have a higher cytotoxic effect to HepG2 cancer cells when compared to L02 cells. Such result is justified by the higher GSH content displayed by HepG2 cancer cells.

Chen and co-workers designed a hybrid capped material where transferrin (Tf), a naturally existing protein, was grafted onto the external surface of DOX-loaded MSN via redox-cleavable disulfide bonds.[177] In this hybrid material Tf plays a dual role as capping agent and as targeting ligand (See **Figure 1.21**). A burst DOX release was observed when the caped MSN were exposed to GSH, indicating good capping efficiency of Tf and redox-responsive features. Owing to the Tf shell, the hybrid nanocarriers exhibited excellent biocompatibility in a wide concentration range and enhanced intracellular accumulation and targeting capability to tumor cells *in vitro*.

In another work, Zhang and coworkers used cytochrome C (CytC) as pore-sealing agents in order to control DOX release.[178] The nanodevice was prepared by immobilizing CytC onto the external surface of DOX-loaded MSN using disulfide bonds-containing linkers for redox-responsive intracellular drug delivery. AS1411 aptamer was further grafted onto MSN for cell/tumor targeting. This MSN-based therapeutic drug delivery system demonstrated great potential for synergetic triplex cancer therapy in vitro and in vivo, with combination of the advantages of the payload DOX, the gatekeeper of CytC and the target component of AS1411 aptamer.

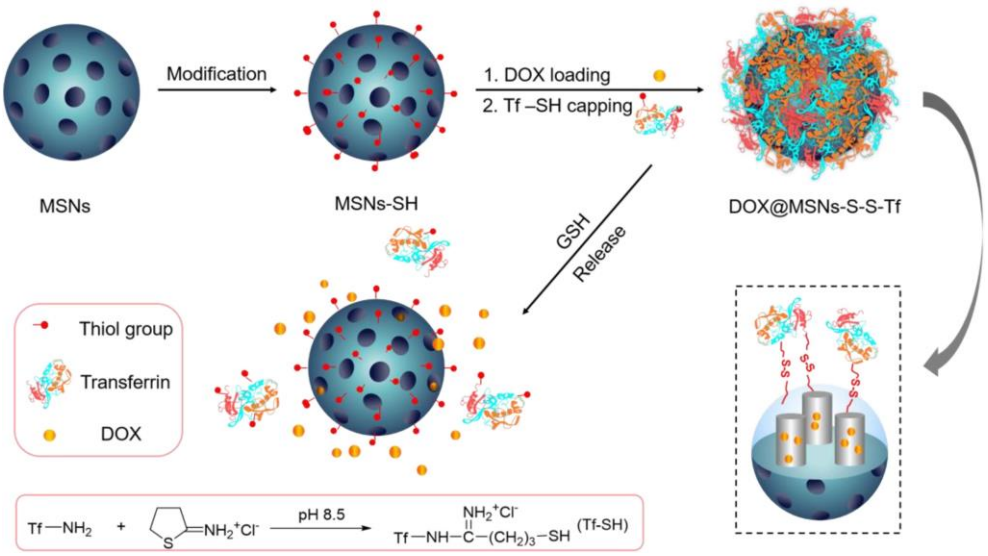

Figure 1.21. Schematic representation of drug loaded and transferrin capped MSNs, and the redox-responsive drug release behavior. Reprinted with permission of X. Chen, H. Sun, J. Hu, X.Han, H. Liu, Y. Hu, *Colloids and Surfaces B: Biointerfaces* **2017**, 152, 77–84.Copyright © **2017** Elsevier Inc. All rights reserved.

Chen and co-workers prepared MSN loaded with DOX and capped by gadolinium-based bovine serum albumin complex (BSA-Gd) and hyaluronic acid (HA) through a GSH-sensible disulfide bond.[179] In this multifunctional nanoparticle, BSA-Gd component was prepared by biomineralization and acted as both smart gatekeeper and contrast agent for MRI, while HA served as targeting molecule to improve the specific affinity of the final nanoparticles toward cancer cells. The functional BSA-Gd complex then acted as capping agent to block MSN via a reductive-cleavable disulfide bond linkage. Hyaluronic acid (HA) was subsequently grafted onto the BSA-Gd through amide bond formation to improve the cancer cell uptake of the nanocarrier, denoted as MSN-ss-GHA. The redox-sensitive drug release behavior of DOX loaded in the nanoparticles MSN-ss-GHA (DOX@MSN-ss-GHA) was verified. Comparatively, the MSN-ss-GHA exhibited excellent biocompatibility and distinctly enhanced cell uptake by 4T1 cells. More importantly, the improved in vitro MR imaging ability of MSN-ss-GHA than that the commercial T1 contrast agent of MR imaging Gd-

diethylenetriaminepentaacetic acid (Gd-DTPA) used as a control, was confirmed. The results also suggested that the DOX@MSN-ss-GHA could efficiently deliver DOX into 4T1 cells and showed enhanced cytotoxicity than that of non-targeted nanocarrier. The in vivo experiment also demonstrated the negligible toxicity of MSN-ss-GHA and improved anti-tumor suppression of DOX@MSN-ss-GHA. (See **Figure 1.22**)

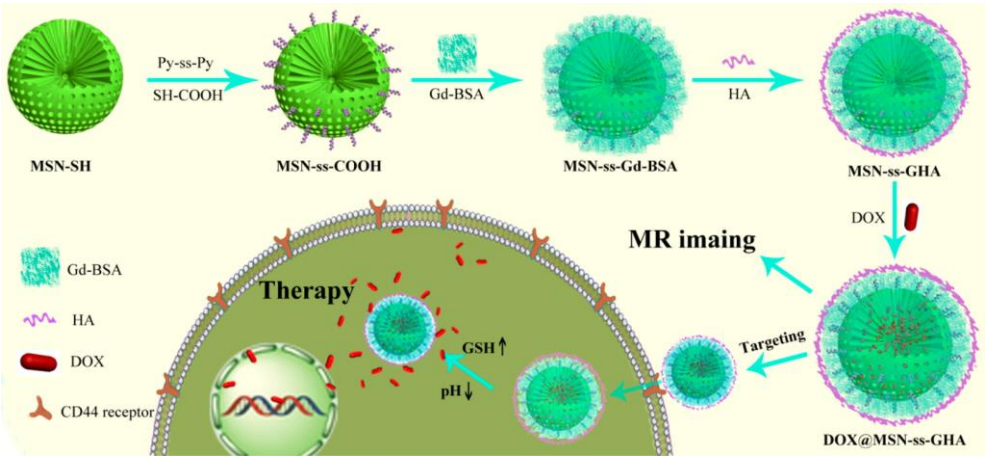

Figure 1.22. The schematic diagram of synthetic process of multifunctional mesoporous silica nanoparticles for redox-responsive targeting drug delivery and MR imaging. Reprinted with permission of L.Chen, X. Zhou, W. Nie, Q. Zhang, W. Wang, Y. Zhang, C. He, *ACS Appl. Mater. Interfaces*, **2016**, *8* (49), pp 33829–33841. Copyright©**2016** American Chemical Society.

Enzyme-triggered release

Other strategy used to achieve a site-specific drug release involves enzymes which are overexpressed in certain tumor cells and tissues. The upregulated expression profile of specific enzymes in pathological conditions (such as cancer or inflammation) makes it an interesting stimulus to achieve enzyme-mediated drug release. The crucial aspect in the design of enzyme-triggered gated MSN is the correct selection of the gatekeepers. These capping agents must contain certain functional groups or biomolecules that can be hydrolyzed by the selected

enzyme. Enzyme-responsive controlled release can be highly efficient once the nanocarriers have entered the cancer tissue or the cytosol of targeted cells. Many intracellular and extracellular enzymes are overexpressed in cancer tissue and exhibit increased activity, resulting in preferential cargo release at those locations.

In 2012, Martínez-Mañez's research group prepared a new nanodevice based on MCM-41 silica nanoparticles able to display selective and controlled cargo delivery in senescent cells. Their strategy involves the use of MSNs capped with a galacto-oligosaccharide (GOS) and the presence of senescence associated β-galactosidase (SA-β-gal) specifically in senescent cells. The presence of SA-β-gal in this kind of cells were explained by the overexpression of the endogenous lysosomal β -galactosidase that specifically occurs in senescent cells. The source of SAβ-gal activity in senescent cells is encoded by the GLB1 gene and its presence is a surrogate marker for increased lysosome number or activity, which has long been associated with replicative senescence and organismal aging. These nanoparticles were able to selectively deliver ther cargo in senescent cells because of β-galactosidase-mediated hydrolysis of the cap. These nanoparticles were tested in aged human fibroblasts DC1787, and in X-DC1774 and XDC4646 cells from human Dyskeratosis Congenita patients, whereas no cargo release was observed in control experiments with H460 non-small-cell lung-cancer cells and wild-type yeast cells.[180]

As one of the important physiological changes in the tumor microenvironment, matrix metalloproteinases (MMP), especially MMP2 and MMP9, are overexpressed in almost all types of cancers and associated with tumor invasiveness, metastasis, and angiogenesis, whereas they are minimally expressed in healthy tissues.[181] Recently, specific protease-sensitive peptide sequences have been designed as linkers that allow the controlled release of chemotherapeutics from MSN. At this respect, van Rijt and co-workers prepared MSN loaded with cisplatin and capped with avidin (that was grafted onto the external surface of the nanoparticles using a peptidic sequence that could be

specifically cleaved by MMP9).[182] These nanoparticles are able to release cisplatin in high MMP9-expressing lung tumor cells inducing apoptosis.

Liu and co-workers grafted, as capping agent, phenylboronic acid conjugated human serum albumin (PBA-HSA) onto the surfaces of MSN loaded with DOX .[183] PBA-HSA was grafted onto the external MSN surface using a linker that consisted in a polypeptide composed of two functional units: a cell penetrating peptide (CPP) polyarginine and a matrixmetalloproteinase 2 (MMP-2) substrate (PLGLIG sequence) (See **figure 1.23**). *In vitro* tests showed that MMP2 enzyme can degrade PVGLIG sequence, resulting in serum albumin removal and drug diffusion from the inner of the pores. Results showed that anticancer drug released efficiently induced cell apoptosis *in vitro*. Furthermore, PBA was employed as targeting motif in this study. A previous study indicated that sialic acid (SA) was an important marker for tumor metastasis [184] due to sugar chains on the cell membranes of tumor cells enhanced sialylation abnormality and promoted metastasis of tumor cells.[185] The authors used HepG2 cells that were reported to overexpress SA.[186] PBA was confirmed to have high affinity to SA with good biocompatibility.[187] Thus, the PBA had great potential to be as targeting motif for specifically delivering anticancer drug to HepG2 cells within liver tumor. To investigate the cell apoptosis induced by different MSNs nanoparticles, the morphologies of cells nuclei were observed by confocal laser scanning microscopy (CLSM) in HepG2 cells. After incubation for 12 h, HepG2 cells cultured with MSNs and MSNs with PBA-HSA, displayed similar oval morphology of cells nuclei with intact features. However, HepG2 cells co-cultured with free DOX and MSNs-HSA-PBA loaded with DOX showed irregular cells nuclei in shape with slight shrinkage features, nuclei became extremely irregular and severe condensation phenomenon was observed. More importantly, the *in vivo* tumor experiments confirmed that the release of the drug efficiently inhibited the growth of tumor with minimal side effects. Their study demonstrated several features as PBA actively targeted tumor cells; HSA sealed the mesopores of MSNs for controlled drug release with reduced inflammatory responses; polycation CPP actively increased the enhanced permeability; and MMP-2 enzyme existing in tumor

environment specifically cleaved the substrate peptide and the CPP readily penetrated the cells membranes and release DOX for tumor inhibition.

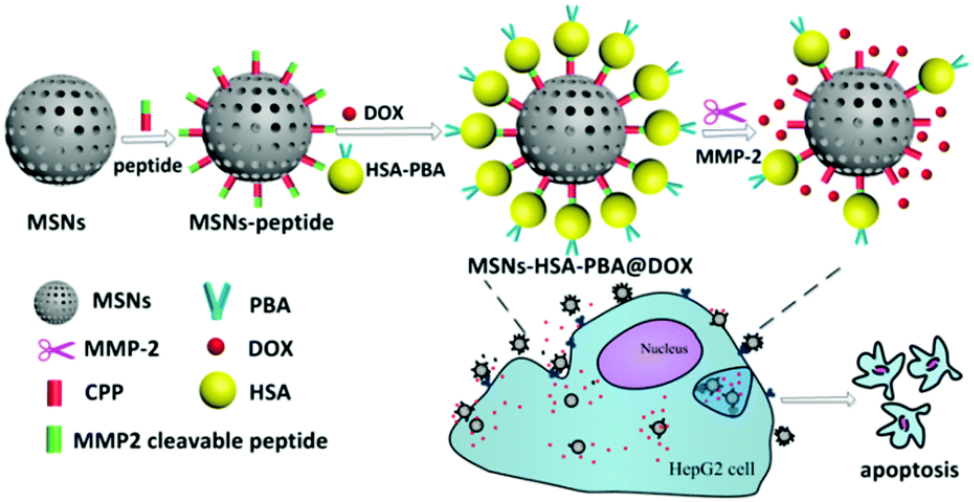

Figure 1.23. Schematic illustration of the enzyme mediated biological response of the MSN-based drug delivery system. MSNs were employed as drug container and were functionalized with a polypeptide. The polypeptide consists of two components: a cell penetrating peptide (polyarginine) and MMP-2 cleavable substrate peptide (PVGLIG). Phenylboronic acid (PBA) was conjugated with human serum albumin (HSA), which was used as the end-capping agent for sealing the mesopores of MSNs and immobilized onto MSNs via the intermediate linker of polypeptides. When the system reaches the tumor site, guided by the targeting motif of PBA, the over-expressed MMP-2 in the tumor microenvironment break down the intermediate linker. Reprinted from J. Liu, B. Zhang B, Z. Luo, X. Ding,J. Li,L. Dai,J. Zhou,X. Zhao,J. Ye,K. Cai, *Nanoscale* **2015**, 7(8), 3614–3626. Copyright © **2015**, Royal Society of Chemistry.

Small molecule-triggered release

The overproduction of reactive oxygen species (ROS) is one of the main inducers of ischemia/reperfusion injury. Hydrogen peroxide is the most abundant form of ROS produced during ischemia/reperfusion, which usually induces the

release of pro-inflammatory cytokines and triggers apoptosis, leading to the oxidative damage of tissues.

Geng and co-workers prepared MSN, loaded with rhodamine B and capped with human immunoglobulin G (IgG) that can release the entrapped cargo in the presence of H_2O_2.[188] For this purpose, the external surface of the rhodamine B-loaded MSN was functionalized with an aryl boronic acid derivative. Finally, pores were capped upon addition of IgG due to the formation of stable boronate cyclic esters with the saccharides of the antibody. Aqueous suspensions of the nanoparticles showed negligible dye release whereas in the presence of H_2O_2 a marked rhodamine B delivery, due to the hydrolysis of boronate esters and detachment of the IgG, was observed. A similar material was prepared but using metal chelator as cargo instead of rhodamine B. Metal ions play important roles in amyloid aggregation and neurotoxicity. Metal-ion chelation therapy has been used in clinical triasl for Alzheimer's disease (AD) treatment. Clinical trial studies have shown that metal chelator, clioquinol (CQ), can decrease Aβ aggregate deposits and improve cognition in early. However, clinical trial studies have shown that long-term use of metal chelator can cause adverse side effect such as subacute myelo-optic neuropathy. To verify the feasibility of the IgG-MSN system for AD therapeutic applications, the authors chose clioquinol (CQ) as guest molecule to study its effect on amyloid-beta (Aβ) aggregation and H_2O_2 formation. A hallmark of AD is the accumulation of plaques in the brain of AD patients. The plaques predominantly consist of aggregates of amyloid-beta (Aβ), a peptide of 39-42 amino acids generated *in vivo* by specific proteolytic cleavage of the amyloid precursor protein. The metal-induced aggregation of Aβ was monitored by quantification of soluble protein, which ascertains the fraction of protein that did not precipitate from solution. The results show that MSN-CQ-IgG itself neither induces nor prevents metal-induced Aβ aggregation. However, in the presence of H_2O_2, the band of the Aβ monitored became strong due to the release of CQ. The authors also studied the effects of the delivery system on Aβ-induced cytotoxicity using rat pheochromocytoma PC12 cells. IgG-MSN containing CQ prevented cell

death in a dose-dependent manner, indicating that the decrease of cytotoxicity was due to the release of CQ.

As one important biogenic molecule, adenosine triphosphate (ATP) is a multifunctional nucleotide that provides ubiquitous energy for all biological processes, including muscle contraction, cells function, synthesis and degradation of essential cellular compounds, and membrane transport, by breaking the phosphoanhydride bond. There is growing evidence that upregulated ATP levels are correlated with many pathological processes which make it a significant marker in distinguishing cancerous cells from normal cells. Many researchers tried to design ATP-responsive drug-release systems.

Lai and co-workers[189] described the development of a polypeptide-wrapped mesoporous-silica (MSN) coated multicolor upconversion nanoparticle (UCNP) as an adenosine triphosphate (ATP)-responsive drug delivery system for long-term tracking and real-time monitoring of drug release. As illustrated in **Figure 1.24**, the system consists of two key components: i) a multicolor upconversion nanoparticle (UCNP) core with distinct emission peaks present in UV to NIR region, when excited at 980 nm and ii) a mesoporous silica shell-based "bio-gate" system for ATP-responsive drug release. The bio-gate for ATP-responsive drug release comprises of a zinc-dipicolylamine analog (TDPA-Zn^{2+}) immobilized on the external surface of the nanoparticles to serve as binding sites for the capping ligands, i.e. branched polypeptides [poly(Asp-Lys)-b-Asp] with multiple pendant carboxylate side chains. The high binding affinity of the oligo-aspartate moieties in polypeptide side chains to TDPA-Zn^{2+} moieties on the surface of the UCNP@MSN allows the loaded drugs to remain entrapped inside the mesopores. It is expected that, owing to the overlap of broad absorption peaks of loaded model drugs [e.g., DOX and CPT] with the multiple sharp emission peaks of UCNP, as well as their close proximity, luminescence resonance energy transfer (LRET) would occur from UCNP (donor) to drug moieties (acceptor), which will result in quenching of the UV-Vis emission of UCNPs. On the other hand, the NIR emission from our UCNPs will remain constant and can be utilized as a tracking signal. When the stimulus is

present, it can lead to a competitive displacement of the surface bound polypeptide by ATP molecule, due to its higher binding affinity to TDPA-Zn^{2+} as compared to the oligo-aspartate in the polypeptide. As a result, drugs encapsulated within the mesopores can be released and the LRET process between the drugs and UCNPs is diminished, which in turn enhances the UV-Vis emission of UCNPs. The drug released from the mesopores of the UCNPs is accompanied by a simultaneous change in the LRET signal that can be measeured. The system can be used to monitor the real-time release of the entrapped drugs over an extended period of time via a ratiometric signal using the NIR emission of the UCNPs as an internal reference. Given the importance of ATP in tumor and neural microenvironment, developing such ATP-responsive multifunctional DDS can open new opportunities for cancer therapy and neuroscience.

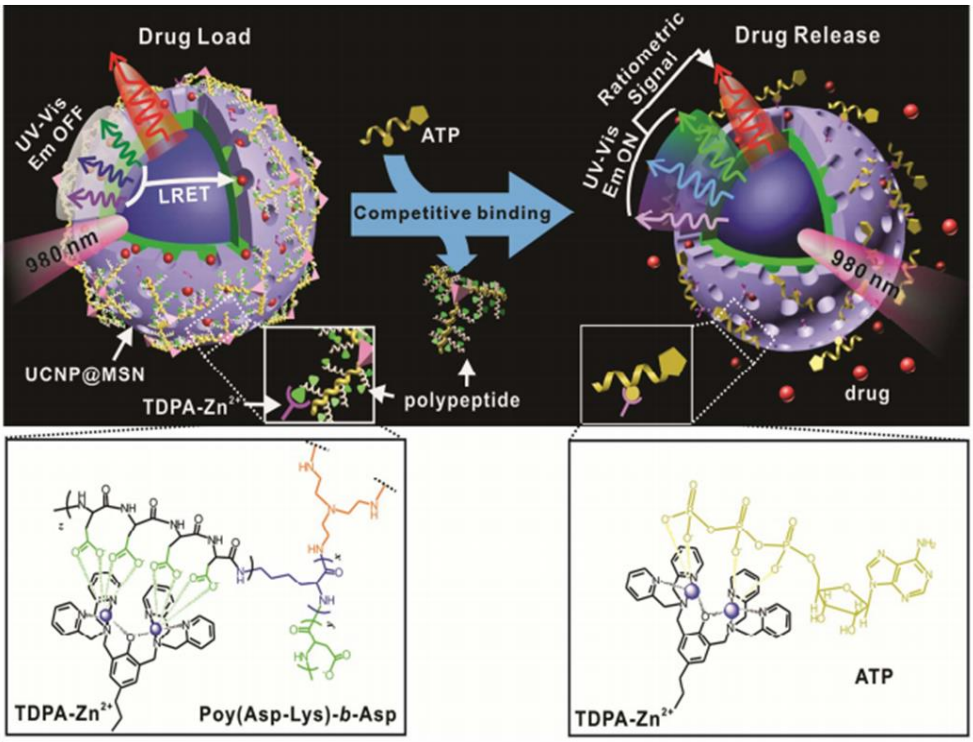

Figure 1.24. Schematic representation of the real-time monitoring of ATP-responsive drug release from polypeptide wrapped TDPA-Zn^{2+}-UCNP@MSNs. The UV-vis emission from the multicolor UCNP was quenched due to the LRET between the loaded drugs and the UCNP. Addition of ATP led to a competitive binding of ATP to the complex which

displaced the surface bound compact polypeptide due to the higher binding affinity. The drug release was accompanied with an enhancement in the UV-vis emission of UCNP, which allows for realtime monitoring of the drug release using the NIR emission of UCNP as an internal reference. Reprinted with permission from J.Lai, B.P.Shah, Y.Zhang, L.Yang, K.B.Lee, *ACS Nano* **2015**, *9 (5)*, 5234-5245. Copyrigh © **2015** American Chemical Society.

Another example of ATP-responsive control release system was developed by He and coworkers.[190] The system consisted on MSN functionalized with an ATP aptamer as cap. In this system, the ATP aptamer was first hybridized with arm single-stranded DNA1 (arm ssDNA1) and arm single-stranded DNA2 (arm ssDNA2) to form a sandwich-type DNA structure. Then, sandwith-type DNA structure was grafted onto the MSN surface through click chemistry resulting in blockage of pores and inhibition of guest molecules release. In the presence of ATP, the aptamer coordinated ATP getting away from the pores, leaving the arm ssDNA1 and ssDNA2 on the surface of MSN and resulting in drug delivery.

Glucose-sensitive drug delivery systems, which can continuously and automatically regulate drug release based on the concentration of glucose, have attracted much interest in recent years. Self-regulated drug delivery platforms have potential application in diabetes treatment to reduce the intervention and improve the quality of life of patients. Chen et al [191] reported a glucose-responsive controlled-release system based on the competitive combination between glucose oxidase, glucosamine and glucose. MSN was first functionalized with D-(+)-glucosamine, an effective inhibitor of glucose oxidase (GOD). As a capping agent GOD was selected because it can combine with the D-(+)-glucosamine to form an enzyme–inhibitor (EI) complex, which act as a ‘‘bio-gate’’, resulting in the closing of the mesopores. The opening event occurs by a highly effective competitive combination of glucose (substrate) and GOD.

Temperature-triggered controlled release

The unique architecture of the tumor tissue originates an increment of the local temperature, giving the opportunity to explore the temperature difference

between the tumor site and the surrounding healthy tissues to trigger a controlled release of cargo from nanocarriers. This temperature difference results from the high cellular proliferation rate, abnormal vasculature and the presence of defective vascular nerve receptors found in the tumor tissues.[192] The abnormal tumor vasculature impairs the blood circulation through the tissue, which difficult the heat diffusion/removal from that area. On the other side, the malfunctioning of the vascular nerve receptors hinders the effective temperature control by the nervous system. To take advantage of this temperature increase it is desirable to design temperature-responsive drug carriers that only release drugs above 37°C, but confer protection when these systems are in blood circulation.

Chen et al [193] reported a thermo-responsive DDS synthesized by covalent functionalization of mesoporous silica nanoparticles with poly(N-isopropylacrylamide) (PNIPAM) by a combination of reversible addition-fragmentation chain transfer and click chemistry (see **Figure 1.24**). The thermal-induced conformational changes of the NIPAM polymer layer on the exterior surface of the MSN was used as a switch to control the cargo release. When the temperature increases above 30°C, PNIPAM acquires hydrophobic character, the chains of polymers aggregated on the SiO_2 surface and the drug molecules are blocked in the nanopores of MSN. At a temperature between 25°C and 30°C, the outer zone of PNIPAM brushes are hydrophilic and the chains of polymers are extended and swollen in an aqueous solution. Thus, the entrapped drug could be quickly released.

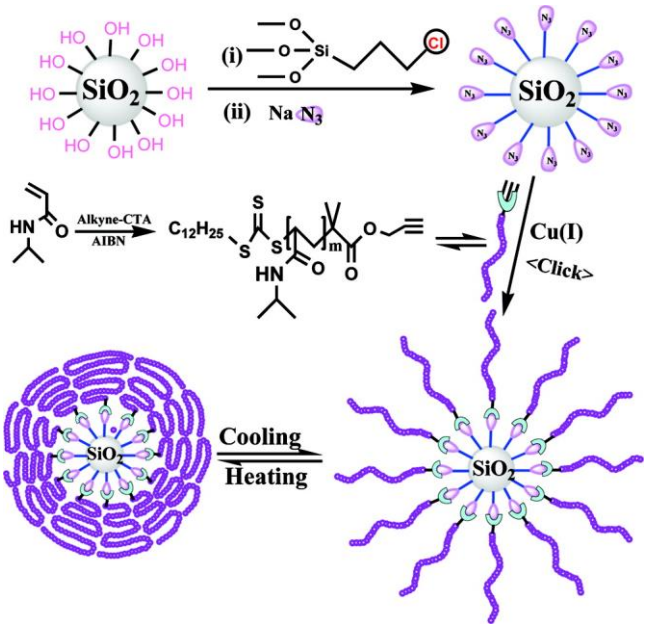

Figure 1.24. Schematic Illustration of the synthesis of hybrid silica nanoparticles coated with thermoresponsive PNIPAM brushes via reversible addition-fragmentation transfer (RAFT) polymerization and click chemistry. Reprinted with permission from J. Chen, M. Liu, C. Chen, H. Gong, C. Gao, *ACS Appl Mater Interfaces* **2011**, 3, 3215. Copyright © **2011** American Chemical Society.

Another example was reported by Tang et al [194] based on mesoporous silica and reversible single-stranded DNA valves. The DNA-gated nanocarrier can release the guests controllably at different temperatures and the critical release temperature of the nanocarrier can be turned by changing the length of single-stranded DNA oligonucleotides. Carboxyl modified single-stranded DNA were anchored to the amino group on the surface of MSNs. As the DNA was negatively charged while MS-NH_2 was positively charged, the DNA valves adsorbed on the surface of the silica shell via electrostatic interaction, resulting in the ‘‘off’’ state. When the temperature increased, the weak electrostatic interaction between mesoporous silica and DNA was destroyed, leading to the ‘‘on’’ state of the valves and the release of the cargo molecules from the nanocarrier. When the temperature decreased, the DNA valves returned to the original state to cap the pores and prevent the cargo from leaking. (See **Figure 1.25**) Intracellular release

experiments were carried out in a human breast cancer cell line (MCF-7). The results demonstrated that the nanocarriers could be triggered by temperature in living cells.

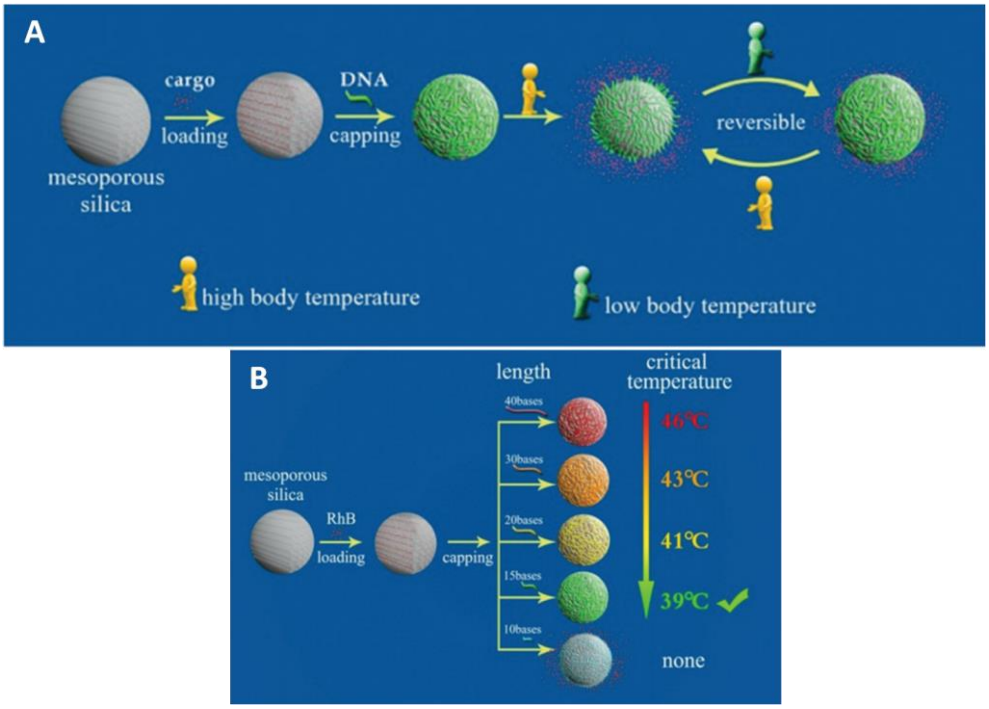

Figure 1.25. **A)** Schematic illustration of the temperature-responsive nanocarrier for controlled release. The amino functionalized mesoporous silica support was loaded with rhodamine B (RhB), then carboxyl modified single-stranded DNA with different lengths (10–40 bases) were anchored to the amino group on the surface of the MSNs acting as the valve. **B)** Different critical temperatures for different DNA valves, the critical temperature of the nanocarriers decreased with the decrease of the DNA valve length A valve that opens at 39 °C was chosen for intracellular (or *in vivo*) applications. Reprinted with permission of Z. Yu, N. Li, P. Zheng, W. Pan, B. Tang, *Chem. Commun.* **2014**, 50, 3494-3497. Copyright © **2014**, Royal Society of Chemistry.

Another temperature-responsive hybrid system was reported by R.Martínez-Mañez et al.[195] In this case, authors functionalized mesoporous silica nanoparticles with octadecyltrimethoxysilane. The alkyl chains interact with

paraffins, which build a hydrophobic layer around the particle. Upon melting of the paraffin, the guest molecule is released, as demonstrated in cells for the guest DOX. The release temperature can be tuned by choosing the appropriate paraffin. For the preparation of gated materials the paraffins docosane (melting point 42 ^{o}C), heneicosane (melting point 39 ^{o}C) and tetracosane (melting point 49 ^{0}C) were selected. To demonstrate the possible application of these nanoparticles as temperature-dependent drug carriers for on command delivery inside cells, a derivative of heneicosane nanoparticles was prepared that contained the chemotherapeutic agent DOX. A temperature dependent release of DOX in cells was observed.

1.3.4.2 Exogenous stimuli responsive drug delivery materials

Unlike endogenous stimuli, exogenous stimuli are generated using an external physical treatment. Although this approach seems unappealing, exogenous stimuli-responsive drug delivery systems might be more encouraging and favorable due to the heterogeneous physiological conditions of human population. In this section, drug delivery triggered by externally applied stimuli including magnetic fields, ultrasounds, light and electric fields, are discussed.

Light-triggered controlled release

Due to their non-invasiveness and the possibility of remote spatiotemporal control, a variety of light-responsive systems have been developed in recent years to achieve on-demand drug release in response to irradiation at a specific wavelength (in the ultraviolet, visible, or near-infrared regions). The release mechanism relies on photo-sensitiveness-induced conformational changes of the nanocarriers. The major drawback of light-triggered drug delivery is its low penetration depth (~10 mm) in the UV-visible region (wavelength < 700 nm). However, it is possible to replace UV-visible with near infrared light (range 700–1000 nm), which showes deeper tissue penetration, lower scattering properties and minimal harm to tissues. It is possible to distinguish between two kinds of ligh-trigrered systems: ones in which the response is activated by direct light and

others in which an indirect or transduced actuation of the nanomachine through light occurs.

Direct actuation

Azobenzene (AB) derivatives are light-sensitive molecules. When irradiated with UV light AB is able to isomerize from the more stable *trans* to a less stable *cis* configuration. Previous studies, in aqueous solutions, have demonstrated that there was a high binding affinity between β-CD and *trans*-AB derivatives whereas the formation of the inclusion complex with the *cis* form is disabled. According to this principle, several light-responsive drug delivery materials have been designed. An example, reported by Ferris and co-workers, consisted on MSN loaded with rhodamine B and with the external surface functionalized with several AB derivatives.[196] The pores were finally capped upon formation of inclusion complexes between β-CD and the grafted AB. The inclusion complexes sealed cargo molecules tightly inside the pores of MSN. Upon irradiation with UV light, the AB derivatives isomerized to their *cis* forms, resulting in a strong decrease of the binding affinity to β-CD and concomitantly in a dethreading of the β-CD from AB, pore opening and cargo release.

Tarn et al. developed a fully reversible nanovalve based on the same principle, [197] by attaching adamantane "stoppers" to the end of the stalks. In the *trans* form the binding affinity of cyclodextrin to the azobenzene unit was larger than its affinity to adamantane, and the cyclodextrin rings stayed bound to the azobenzene units close to the pore openings, tightly sealing cargo inside. However, after a light induced isomerization to the *cis* form the binding affinity of cyclodextrin to the adamantane unit exceeded that to the *cis* azobenzene, causing the cyclodextrin to slide to the end of the stalk, opening the valves and releasing the cargo. When the azobenzene reverted back to its *trans* form in the dark, the cyclodextrin slided back to its previous location in close proximity to the pore openings and closed the pores again, thus resulting in a reversible opening and closing of the nanovalve.

Transduced actuation

There are also examples in which an indirect or transduced actuation of nanomachines through light is used. At this respect, Zink and co-workers used propidium iodide loaded MSN and functionalized its external surface with two subunits (i) a photoacid that is a molecule that has a significantly lower pK_a value in its excited state than in its ground state and (ii) a pH-responsive nanovalve.[198] 8-hydroxypyrene-1,3,6-trisulfonate was used as photoacid and the inclusion complexes formed between an aniline derivative and α-CD was used as a capping unit. When irradiated with blue light (408 nm), the photoacid released protons that protonated the aniline derivatives, resulting in dethreading of the α-CD and cargo release. The pH change was localized onto the vicinity of the nanoparticle surface, and no change in the bulk solution could be detected after irradiation. Later, the same authors showed that these nanoparticles could be used for the light-triggered cargo release in buffered solutions and *in vitro* in MCF-7 breast cancer cells.[199]

There are redox-responsive systems in which the initial stimulus is produced by light irradiation. Guardado-Alvarez et al. covalently attached photosensitizers to MSNs that were also functionalized with redox-responsive disulfide snaptop nanovalves.[200] These disulfide snaptop nanovalves consisted of an adamantane unit bound to the surface of MSNs through a disulfide bridge. Supramolecular interactions between β-cyclodextrin and adamantane were used to tightly cap the pores with the bulky cyclodextrin ring acting as a gatekeeper. When the disulfide bonds were reduced, the covalent S-S bond was broken and two thiols were formed, which allowed cargo release. When additionally a photosensitizer was attached to the MSN surface, the reduction could also be triggered through a light-induced electron transfer, demonstrating the possibility of actuation through an external stimulus (**Figure 1.26**). The photosensitizer used in this study absorbed light in the UV region, and the resulting excited state then acted as an electron donor with a redox potential strong enough to reduce disulfide bonds. The photosensitizer chosen in this study also has a high two-photon absorption cross-section, which means that the cap could also be cleaved off successfully by

irradiating the MSNs with high-intensity near-infrared (NIR) light (800 nm) instead of UV light.

Other temperature-triggered nanomaterials are constructed in such a way that carbon, copper or gold nanoparticles, which are capable of producing heat in response to specific wavelengths such as near infrared (NIR) radiation, are included in their structure. For biological applications, NIR is a very interesting alternative, since biological components such as proteins, melanin, hemoglobin, collagen and water present low or insignificant absorption of this radiation.[201]

Gold nanoparticles or nanorods presented plasmonic properties and showed high efficiency to transform NIR radiation into thermal energy. Taking into account these facts, Cheng and co-workers prepared gold nanorods coated with a mesoporous silica shell and loaded the pores with DOX. Then, a double stranded DNA, than acted as gatekeeper, was grafted onto the external surface of the nanoparticles using 4-maleimidobutyric acid *N*-succinimidyl ester linker.[202] When this nanodevice was irradiated with a NIR laser (808 nm, 1.5 W/cm^2), the generated heat enables denaturing of the duplex oligonucleotides of the DNA strands opening the pores and allowing DOX to diffuse out of the carrier.

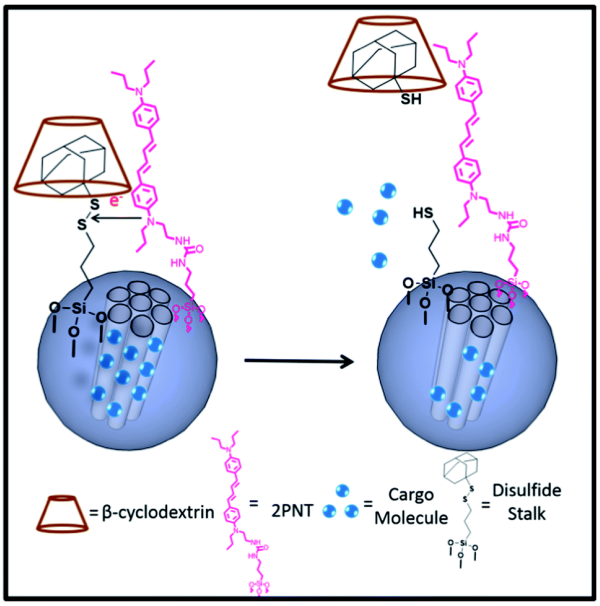

Figure 1.26. Disulfide snaptop opening mechanism. Photo-excitation of the photosensitizer causes an electron transfer to the snaptop cleaving the disulfide bond and opening the nanopores. Reproduced with permission from T. M. Guardado-Alvarez, L. S. Devi, J.-M. Vabre, T. A. Pecorelli, B. J. Schwartz, J.-O. Durand, O. Mongin, M. Blanchard-Desce, J. I. Zink, *Nanoscale* **2014**, 6, 4652– 4658. Copyright © **2014**, Royal Society of Chemistry

Zhang and co-workers developed MSN coated with DNA tagged with copper sulfide nanospheres in order to develop a thermo-responsive DOX delivery system for HeLa and MCF-7 cancer cells.[203] For that purpose, a selected oligonucleotide was grafted onto the external surface of DOX-loaded MSN using succinimidyl 4-*N*-malemidomethyl cyclohexane-1-carboxylate (SMCC) as crosslinker. On the other hand, copper sulfide nanospheres coated with a DNA strand (complementary to that grafted onto the MSN) were prepared. The final capped nanodevice was obtained when the single stranded DNA of the copper sulfide nanospheres hybridized with the complementary grafted onto the external surface of the MSN (**Figure 1.27**). Controlled delivery assays showed that NIR laser irradiation of suspensions of the capped MSN triggered DOX release. Moreover, longer

irradiation periods resulted in higher release rates. The release profile displayed by MSN is justified by the generation of heat by the copper sulfide nanospheres when they are exposed to the NIR radiation, leading to DNA melting and consequent DOX diffusion out of the pores.

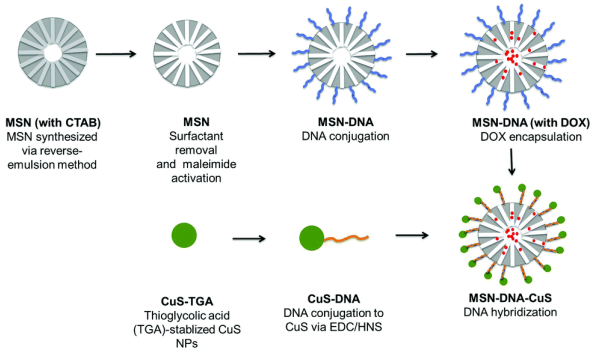

Figure 1.27. Schematic representation of the synthesis of MSN–DNA–CuS. Reprinted with permission from L. Zhang, Y. Li , Z. Jin , J.C. Yu, K. M. Chan, Nanoscale 2015,7 ,112614-12624.Copyright © 2015, Royal Society of Chemistry

Ultrasounds-triggered controlled release

Among non-invasive external stimuli, the use of ultrasound has drawn a lot of attention recently. High tissue penetration, non-invasiveness and spatiotemporal control of drug delivery are responsible for the increased use of low energy ultrasound (LEUS), also known as therapeutic ultrasound. Ultrasound can be used to induce heating, create cavitation bubbles, or break chemical bonds.

At this respect, Vallet-Regí and co-workers prepared MSN and loaded its porous network with fluorescein or $[Ru(bipy)_3]^{2+}$ complex. Then, the external surface was functionalized with the copolymer poly(2-(2-methoxyethoxy) ethyl methacrylate-*co*-2-tetrahydropyranyl methacrylate which is sensitive to both temperatura and high intensity focused ultrasound (HIFU).[204] Upon ultrasound irradiation the hydrophobic tetrahydropyranyl methacrylate groups were hydrolyzed into hydrophilic methacrylic acid groups. This polarity change induced

the polymer to adopt an open coil-like conformation with subsequent pore opening and dye release.

Magnetic-responsive controlled release systems

Magnetic-responsive drug delivery systems (containing a magnetic core) are able to release an entrapped cargo upon the application of an external magnetic field. The external magnetic field can not only drive the nanoparticles to the desired location precisely, but also can act as an exogenous stimulus to induce controlled drug release. Superparamagnetic iron oxide nanoparticles are one of the most widely employed for the development of hybrid gated materials for controlled cargo release. This is a novel strategy that could play an important role in the development of thermo- and magnetic-responsive drug delivery systems against cancer.

One interesting example is the work of Vallet-Regí and co-workers.[205] The authors grafted a single stranded DNA sequence onto the external surface of MSN containing an iron oxide paramagnetic core and loaded with fluorescein. Then, the pores of the loaded magnetic support were capped with iron oxide nanoparticles functionalized with the DNA complementary strand (See **Figure 1.28**). When exposed to an alternating magnetic field, the fluorescein-loaded particles quickly heated the environment to reach hyperthermia in a few minutes. This enhancement in temperature induced a progressive double-stranded DNA melting, giving rise to uncapping and subsequent dye release.

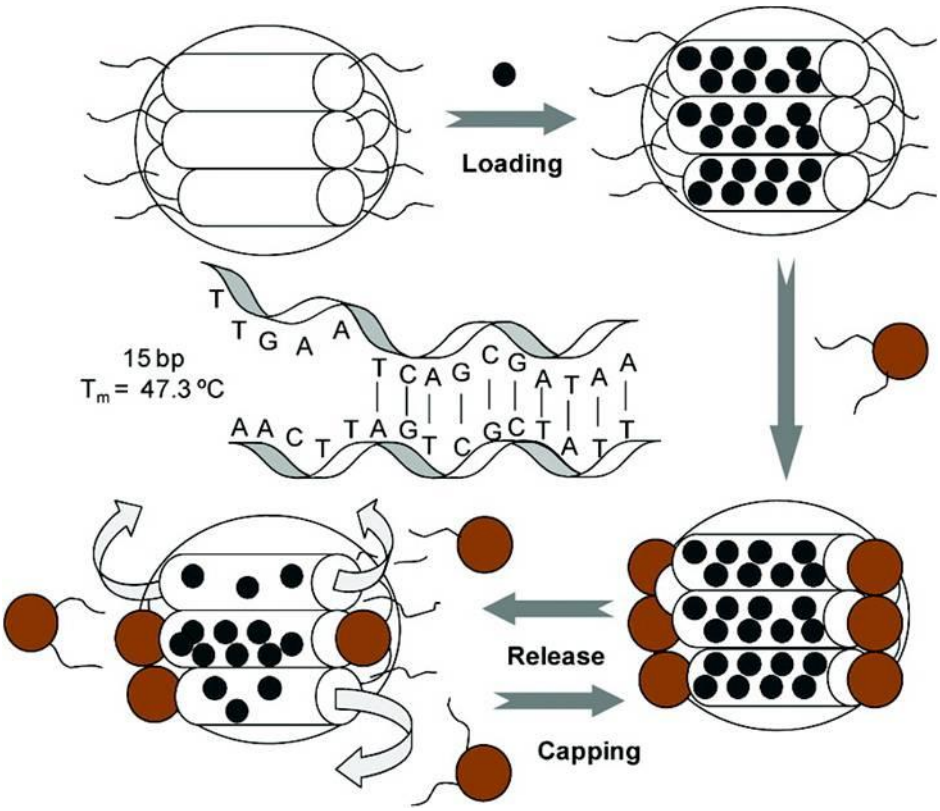

Figure 1.28. Reversible magnetic nanogates drive drug release from magnetic mesoporous silica particles through DNA hybridization/dehybridization. Reprinted with permission from E. Ruiz-Hernández, A.Baeza A, M. Vallet-Regí, *ACS Nano*. **2011**, 5(2), 1259–1266. Copyright © **2011** American Chemical Society.

The same group, developed a MSN-based drug delivery system with superparamagnetic maghemite nanocrystals entrapped within its structure and coated with poly(ethyleneimine)-b-poly(N-isopropylacrylamide), a thermosensitive copolymer. The system is able to perform remotely controlled release of small molecules and proteins in response to an alternating magnetic field.[206] The controlled delivery assays performed with the capped materials revealed that the exposition to an alternated magnetic field promotes fluorescein release reaching a final value of almost 50%, whereas in the absence of the magnetic field only a small leaching of the dye from MSN was observed. Such behavior indicates that the local increase in temperature leads to a phase

transition change on the polymeric coating, allowing fluorescein diffusion from the inner of the pores.

Electro-responsive controlled release systems

Weak electric fields can be used to achieve pulsed or sustained drug release through a variety of actuation mechanisms with the advantages of simplicity, accurate dosage control, and easy coupling to bioelectronics.

For instance, Zhao and co-workers designed a complex pH and electro responsive system made of chitosan hydrogel with embedded MSN as drug release system using ibuprofen (IB) as model drug.[207] Loaded nanoparticles were dispersed in a chitosan solution and then a chitosan-MSN film of 2 mm thickness was deposited as a hydrogel on the titanium electrode. The co-deposition of components was performed under a negative biasing of the titanium. The ibuprofen release from the film was studied as dependent on pH of the media and electrical conditions applied to the titanium plate. When incubating the complex hydrogel film in buffers with different pH the IB release followed a near zero-order profile. Compared to the spontaneous IB release from the hydrogel at 0 V, the application of negative biases to the coated titanium plate had profound effluences on the release behaviour. The results imply that a rapid, mild and facile electrical process for covering titanium implants by complex IB-MSN/ chitosan hydrogel films can be used for controlled drug delivery applications.

Intrinsically conducting polymers (ICP) films can be used as nano-switches to gate the release of therapeutics from other materials, which do not necessarily need to be electro-responsive. For instance, the cavities in nano-porous films can act as depots for payloads that can be sealed with a thin ICP film. Application of an electric potential actuates the contraction/expansion of the ICP, which changes the permeability of the capping film. Luo and Cui have created a nano-porous polypyrrole (PPy) film by colloidal lithography and loaded two different payloads.[208] The first payload, fluorescein, was doped within the PPy matrix

during electro-polymerization, and the anti-inflammatory agent DEX was loaded into the nanopores. Both payloads were released upon exposure to negative potentials. This strategy can be used to physically encapsulate additional drugs that do not comply with the requirements of being dopants within PPy. A related example was reported by Jiang et al., [209] who created a porous PPy network of nanowires, which they capped with a PPy film by chemical vapor deposition. The porous network could be loaded with both hydrophilic and lipophilic drugs, owing to the amphiphilicity of the PPy nanowire network. The authors stimulated drug release by cycling between 0.9 and +0.6 V (vs. SCE) in a repetitive manner and observed a greater release at higher scanning rates (i.e., 200 mV s^{-1} versus 50 mV s^{-1}).

Another example was described by Sttodard et al.[210] The authors developed ferrocene-based mesoporous nanoparticles (FMNPs), in which the storage and release of the payload were controlled by the host–guest interaction between the ferrocene moiety (guest) and both cucurbit[7]uril (CB7) and β-cyclodextrin (β-CD). The oxidation of the ferrocence unit in H_2O (0.1 M NaCl used as supporting electrolyte) was performed electrochemically by applying a voltage (1 V). The experiment was carried out in a custom-built optically transparent electrochemical cell by using platinum (Pt) grid as the working electrode, a Pt wire as the counter electrode and an Ag wire as pseudo-reference electrode. To ensure the maximum contact of the nanoparticles with the Pt grid, the solution was stirred slowly. Oxidation of the ferrocene unit initiates the dissociation of the host-guest inclusion complex and leads to the release of the dye particles from the pores. The fluorescence emission of the rhodamine B was measured before (V = 0 V) and after oxidation (V = 1 V) of the ferrocene unit (**Figure 1.29**).

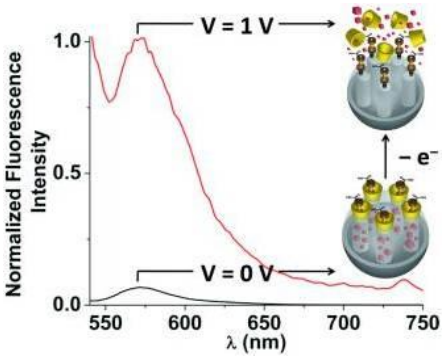

Figure 1.29. Emission spectrum showing the controlled release of rhodamine B under redox conditions. The black spectrum (t = 0 min) was recorded at V = 0 V, and the red spectrum was recorded after applying 1 V for 400 min. Reprinted with permission from N.M. Khashab, A. Trabolsi, Y.A. Lau, M.W. Ambrogio, D.C. Friedman, H.A. Khatib, J. Zink, J. Fraser Stoddart, *Eur. J. Org. Chem.* **2009**, 1669–1673. Copyright © 2009 WILEY-VCH Verlag GmbH & Co. KGaA, Weinheim

1.3.5. Biological and pharmaceutical relevance

Clinically has been demonstrated that nanomedicines improve the therapeutic index of anticancer drugs by modifying their pharmacokinetics and tissue distribution to improve delivery to the site of action.

Designed to exploit the EPR effect, liposomal doxorubicin (Doxil™/Caelyx™) was the first anticancer nanomedicine approved by the FDA in 1995.[211]Doxil™/Caelyx™ achieve a differential distribution of DOX versus the free drug. The volume of distribution is close to the blood volume, and the area under the concentration-time curve (AUC) is increased at least 60-fold compared with free doxorubicin. Studies of tissue distribution indicated preferential accumulation into various implanted tumours and human tumour xenografts, with an enhancement of drug concentrations in the tumour when compared with free drug. In clinical studies Doxil™ has achieved a nearly 300-fold increase in AUC

relative to free DOX. Furthermore, clearance and volume of distribution are drastically reduced.

Other nanomedicines approved for clinical use for cancer treatment include: Myocet™, DaunoXome™, Epocyt™, Abraxane™, Genexol-PM™, and, most recently, Onivyde™. Alongside the more well-known organic systems, such as liposomes and polymeric particles, inorganic particulates are now also being developed. Recently, silica nanoparticles in the form of Cornell dots were US FDA approved for stage I human clinical trial.[212] Amorphous silica was proposed as a drug delivery carrier as early as 1983.[213] Since then, many different amorphous silica materials have been proposed as drug delivery matrixes.[214] Amongst these, ordered mesoporous silica materials have been recognized as one promising class due to the controllable structural and morphological features on the nanometer and micrometer scale. An increasing number of *in vivo* studies are reported, mainly in small-animal models. For example, mesoporous silica has been applied orally with the aim to enhance the oral bioavailablity of the poorly soluble drug itraconazole,[215] implanted into rabbit femurs to act as bone therapeutic implants releasing gentaimicin,[216] administered directly onto an open wound in powder form doped with calcium and silver in order to achieve hemorrhage control,[217] and implanted into the basolateral amygdale of the brain to function as reservoirs for valproic acid and sodic phenytoin to treat temporal lobe epilepsy.[218]

The approval of new nanomedicines has been based primarily on improving therapeutic benefit by enhancing safety, with patient survival being equivalent to that resulting from the use of standard treatments.[219] The significant anti-cancer activity demonstrated pre-clinically by many novel nanomedicines has yet to be recapitulated clinically,[220] and the development of the marketed nanomedicines has often been slow. At AstraZeneca, improved success in translating new drug projects to the clinic has been achieved by evaluating a drug's 5Rs: ‘right target/efficacy’, ‘right tissue/exposure’, ‘right patients’, ‘right safety’, and ‘right commercial potential’.[221] This means that the pre-clinical data, at a minimum, must be consistent with the agent being able to achieve target engagement or

inhibition in man through the appropriate level of drug exposure at the target tissue, as determined from *in vitro* and *in vivo* screening. The 5Rs are the pivotal technical determinants of project success. Applying a 5Rs framework to nanomedicine development requires the influence of tumour pathophysiology on nanomedicine accumulation, distribution, retention, and efficacy, and the correlation between delivery system properties and in vivo behaviour. Until now, drug delivery system engineering has been the priority in nanomedicine research.[222]

An important benefit of some nanomedicines is the ability to formulate a drug without using dose-limiting toxic excipients present in current marketed formulations, often improving tolerability and enabling more drugs to be administered to patients. For instance, higher doses of PTX can be administered to patients using Abraxane™ (Celgene) or the polymeric micelle formulation Genexol-PM™ (Samyang Biopharmaceuticals) because these formulations avoid the use of Cremophor™ needed to formulate Taxol™. While not considered to be the major focus for many nanomedicine research projects, such solubilisation benefits can be considerably cost-effective. Moreover, by achieving the 'right safety' profile, this approach can make a significant difference to the patients and the clinical outcome, as the maximum tolerated dose of the active agent can be increased by avoiding the tolerability problems caused by the solubilizing surfactants. However, without improved efficacy, the increased cost of nanomedicine systems can prevent them from being a mainstream treatment choice.

As was the case for early antibody therapeutics, the probability of success with nanomedicines is perceived to be low. Progressing nanomedicines therapeutics to market is often slow. This may be because their clinical efficacy is not sufficient to warrant accelerated development, or that technical or cost challenges in scale-up and manufacturing can delay investment. However, the greatest drivers of failure may be our poor understanding of the disease heterogeneity in the patient population, inability to fine tune the system based on the disease biology or stage

of the target patients, and failure to build a platform of evidence supporting a specific end clinical application. To exploit the significant advancements in nanomedicine engineering, focusing how nanomedicine therapeutics is tested clinically is important.

To date we have been focused largely on cancer therapy and diagnosis using nanoparticles but another important field is its use in regenerative medicine, which is still an emerging field. Available nanoparticle platforms include polymers, metal nanoparticles, calcium phosphate nanoparticles, liposomes, carbon nanotubes and MSN that can be incorporated as drug delivery vehicles in stem cell scaffolds offering a possibility for targeted and controlled delivery of biological cues. Scaffolds with defined morphology and mechanical properties can function as templates to guide and improve neotissue formation.[223] Biomaterial-based scaffolds can also be used as delivery vehicles for cells in stem cell therapy.[224] The continued advancement of such 'smart' biomaterial systems holds the promise of improved therapies.

1.4 Chemistry of molecular recognition: molecular chemical sensors.

Molecular recognition becomes a matter of concern around the middle of the last century, when it was noticed that certain molecules may recognize selectively its partner through diverse molecular forces or interactions. In molecular recognition these forces include hydrogen bonding, metal coordination, hydrophobic forces, van der Waals forces, etc. Important concepts, which have been emerged from supramolecular chemistry studies, include molecular self-assembly, molecular recognition, host-guest chemistry, mechanically-interlocked molecular architectures and so on.

In particular a molecular recognition event can take place only if a host molecule or (***receptor***) selectively interacts with a guest molecule (***substrate***) usually through ***non-covalent bonds***. Often, the definition of which species is the "host" and which is the "guest" is arbitrary. However, in this area, the receptor or host is usually a large molecule or aggregate, such an enzyme or synthetic compound, possessing a sizeable hole or cavity. The guest molecule may be a monoatomic cation, an inorganic anion or a more sophisticated molecule, with a geometric size or shape complementary to the receptor.

The first and simplest model of molecular recognition is the lock-key principle suggested by Dr. Hermann Emil Fischer in 1894.[225] In this model, an enzyme (host) can discriminate among different substrates (guests) through the specific geometric complementarity between host and guest. Thus, only one guest fit exactly into one host like only a key enter in a specific lock. Knowledge of this simple principle allowed explaining the enzymatic catalysis (**Figure 1.30**), the compression of many complex biological processes and setting up the foundation for the preparation and optimization of new synthetic hosts (receptors).

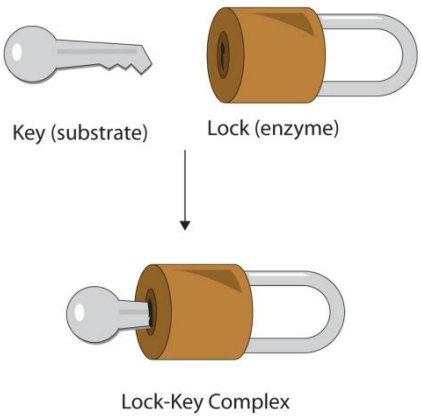

Figure 1.30. The lock-and-key model of enzyme action. The substrate and the active site of the enzyme have complementary structures and bonding groups, they fit together as a key fits a lock.

To produce this recognition event, specific conditions of spatial and electronic compatibility between the host and guest binding sites must be satisfied. In particular we have to consider that the recognizing event is an equilibrium between the unbound state, in which the host (H) and the guest (G) are separate from each other, and the bound state, in which there is a structurally defined host-guest complex (HG):

$$H + G \rightleftharpoons HG$$

This chemical equilibrium is displaced to the right, because there are several thermodynamic benefits deriving from the host guest cooperative non-covalent interaction that determine a reduction of the overall Gibbs free energy.

The chemistry of specific non-covalent interaction between host and guest molecules has allowed the development of new molecular devices with applications in nanomedicine, catalysis and sensing protocols. For example the use of dendrimers in medicine has shown to improve drug delivery by increasing the solubility and bioavailability of the drug. Besides, dendrimers can increase both cellular uptake and targeting ability, and decrease drug resistance.

In the supramolecular chemistry field, receptors specifically designed for sensing purposes are generally called ***chemosensors***. In general terms, a chemosensor is a molecule that produces a detectable and easy to measure signal, revealing the presence of the guest, as a result of molecular recognition. Signals widely used to detect the presence of certain guest molecules are changes in color, fluorescence or modulations in electrochemical properties. In this sensing process, information at the molecular level, such as the presence or not of a certain guest in solution, is amplified to a macroscopic level; hence, sensing might open the door to the determination of certain guests. In this sense, one interesting goal in the development of sensor deals with the synthesis of highly selective systems. Reversibility and fast response will be also appealing features for an applicable sensor to be taken into account in this design.

Usually, a molecular chemosensor is composed of two main units: a ***receptor subunit*** and a ***signaling subunit***. In particular the receptor subunit, which is the responsible of the recognition event and grants the host ability to discriminate a guest between many, must present a high grade of selectivity and complementarity with the guest in terms of size, shape, charge, etc. The second fundamental moiety of a chemosensor is the signaling subunit, which acts as a signal transducer, and informs that the recognition event takes place at molecular level, through a macroscopic measurable signal. Depending on the type of the signal transduced, chromo-fluorogenic changes and/or redox potential variations, different kind of chemosensors can be distinguished. The important advantages, with respect to other analytical methods, offered by chromo-fluorogenic chemosensors, are related to the possibility of use cheap and simple instrumentation, the need of very small quantity of sample and, in some cases, the possibility of *in situ* and on-time measurements. Moreover colorimetric sensors induce noticeable color changes, observable to the naked eye, and can be used for rapid qualitative determinations. On the other hand, fluorogenic sensors have a high degree of sensitivity and specificity due to the possibility of specifying excitation and emission wavelengths, and normally allow the achievement of lower detection limits when compared with colorimetric techniques. These chromo-fluorogenic chemosensors are constructed using one of the following tree main approaches (see **Figure 1.31**): (**i**) the ***binding site-signaling subunit*** protocol, (**ii**) the ***displacement*** aproach and (**iii**) the ***chemodosimeter*** paradigm.

In the ***binding site-signaling subunit*** approach *binding sites* and optical *signaling units* are covalently bonded in such a way that the interaction of the analyte with the binding site induces electronic modulations in the signaling subunit which result in color or emission changes (see **Figure 1.31**).[226] In this approach an active site for recognition is coupled to a chromophore or to a fluorophore. Then a non-covalent interaction between the analyte and the binding site induces measurable chromo-fluorogenic changes. The most common drawback of this approach is that the interaction of the analyte with the binding

sites usually relies on relatively weak hydrogen bonding interactions and, in most cases, optical modulations are only observed in organic solvents.

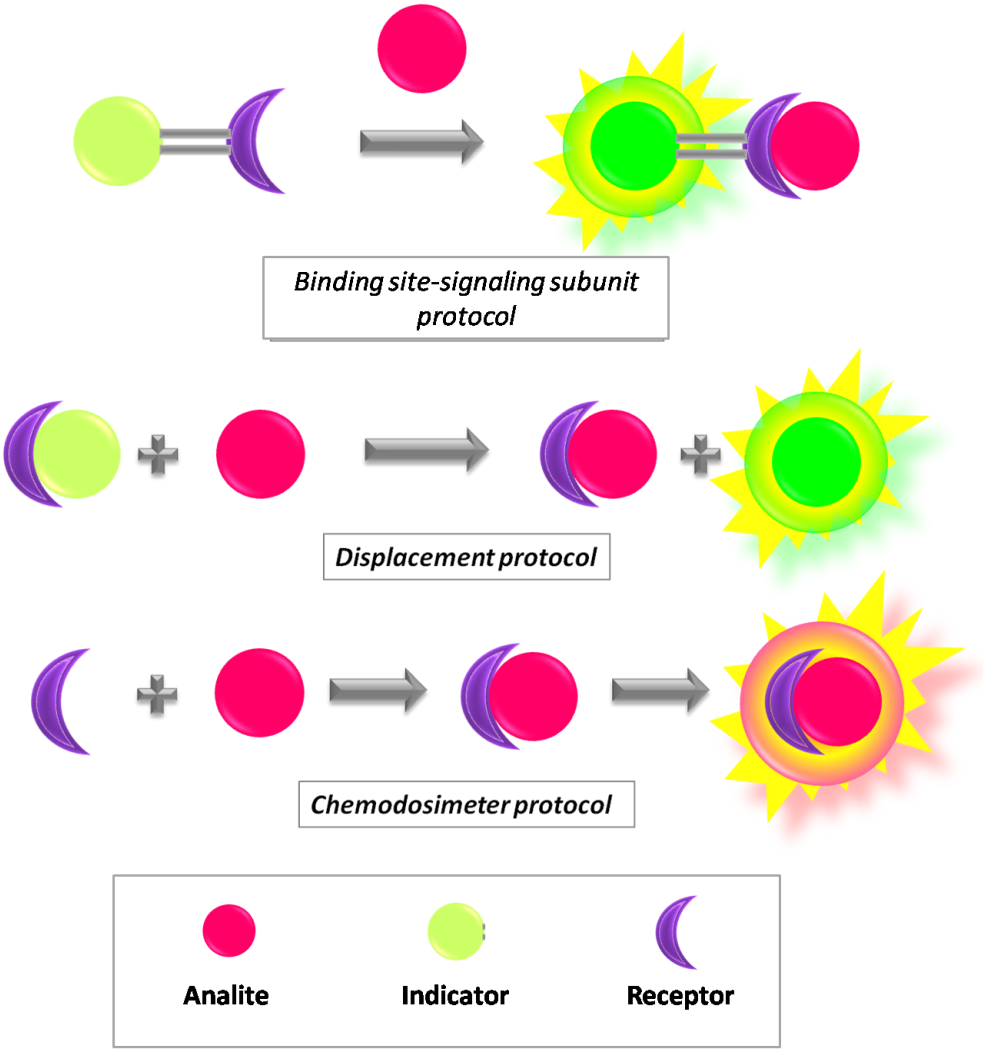

Figure 1.31. Schematic representation of the three different possible paradigms for the construction/operation of an optical chemosensor.

A second important chemosensing protocol is the ***displacement*** approach. In this modus operandi *binding sites* and *signaling units* are not covalently bonded but forms a supramolecular ensemble (see **Figure 1.31**).[227] In this case, the coordination of a certain analyte to the binding site results in the displacement of the signaling unit which is usually reflected in optical changes (taking into account that optical properties of the signaling unit are different when is free than when coordinated with the binding site).

Finally the ***chemodosimeter*** approach takes advantage of analyte-induced chemical reactions, usually irreversible, that results in changes in fluorescence or in color.[228] Although this approach was minimal some years ago, today is a well established procedure for the design of molecular probes. In this paradigm specific analyte-induced reactions commonly involving the rupture or formation of several covalent bonds occurs. This generally results in large chemical changes in the probe and remarkable spectroscopic modulations. The key issue in this paradigm consists in finding rather quick selective analyte-induced reactions that work preferably in water or mixed organic-aqueous solutions.

1.5 References

1 G.Kaur, T. Singh, A. Kumar, *IJEAR* **2012**, *2*, 50.

2 A. Alagarasi, *Introduction to Nanomaterials*, in B. Viswanathan, Nanomaterials, **2009**, Ed. Narosa Publishing House.

3. G.L. Wilkes, B. Orler, H. Huang, *Polym. Prepr.* **1985**, *26*, 300.

4. Y.Wei, R. Bakthavatchalam, C.K. Whitecar, *Chem. Mater.* **1990**, *2*, 337.

5. C.T. Kresge, M.E. Leonowicz, W.J. Roth, J.C. Vartuli, J.S. Beck, *Nature* **1992**,*359*, 710.

6. R. Roy, *Mater. Res. Soc. Symp. Proc*. **1993**, *286*, 241.

7. J. Wen, G.L. Wilkes, *J. Inorg. Organomet. Polym.* **1995**, *5*, 343.

8. D.Blanc, P. Peyrot, C. Sanchez, C. Gonnet, *Opt. Eng.* **1998**, *37*, 1203.

9. H. Schmidt, *Mater. Res. Soc. Symp. Proc.* **1990**, *171*, 3.

10. P.L. Shao, K.A. Mauritz, R.B. Moore, *Chem. Mater.* **1995**, *7*, 192.

11. D.E. De Vos, M. Dams, B.F.Sels, P.A. Jacobs, *Chem. Rev.* **2002**, *102*, 3615.

12. T.J. Saegusa, *Macromol. Sci. Chem.* **1991**, *A28*, 817.

13. D. Avnir, *Acc. Chem. Res.* **1995**, *28*, 328.

14. R.Pardo, M.Zayat, D.Levy, *Chem Soc Rev.* **2011**, *40*, 672.

15. K. M. Thomas, *Catal. Today* **2007**, *120*, 389.

16. G. Sneddon, A. Greenaway, H. H. P. Yiu, *Adv. Energy Mater*. **2014**, *4,* 130187.

17. C. Perego, R. Millini, *Chem. Soc. Rev.* **2013**, *42*, 3956.

18. R. E. Morris, P. S. Wheatley, *Angew. Chem. Int. Ed.* **2008**, *47*, 4966.

19. D. J. Wales, J. Grand, V. P. Ting, R. D. Burke, K. J. Edler, C. R. Bowen, S. Mintova, A. D. Burrows, *Chem. Soc. Rev.* **2015**, *44,* 4290.

20. C. T. Kresge, M. E. Leonowicz, W. J. Roth, J. C. Vartuli, J. S. Beck, *Nature* **1992**, *359*, 710.

21. C. T. Kresge, M. E. Leonowicz, W. J. Roth and J. C. Vartuli, Synthetic Porous Crystalline Material, Its Synthesis, US Patent 5,102,643, April 7, **1992.**

22. J. S. Beck, J. C. Vartuli, W. J. Roth, M. E. Leonowicz, K. D. Schmidt, C. T. W. Chu, D. H. Olson, E. W. Sheppard, S. B. McCullen, J. B. Higgins and J. L. Schlenker*, J. Am. Chem. Soc*. **1992**, *114*, 10834.

23. Z.A. AlOthman, A.W. Apblett, *Appl. Surf. Sci.* **2010**, *256*, 3573.

24. J.C. Vartuli, K.D. Schmitt, C.T.Kresge, W.J. Roth, M.E. Leonowich, S.B. McCullen, S.D. Hellring, J.S.Beck, J.L. Schlenker, D.H.Olson, E.W.Sheppard, *Chem. Mater*. **1994**, *6*, 2317.

25. N. Rahmat, A.Z. Abdullah, A.R. Mohamed, *Am. J. Appl.Sci.* **2010**, *7*, 1579.

26. a) J. Puputti,H. Jin, J. Rosenholm, H. Jiang, M. Lindén, *Micropor. Mesopor. Mat.* **2009**, *126*, 272. b) Colilla, M.; Balas, F.; Manzano, M.; Vallet-Regí, *Chem. Mater.* **2007**, *19*, 3099.

27. Z.A. ALOthman, *Materials* **2012**, *5*, 2874.

28. J.C.P. Broekhoff, *Stud. Surf. Sci. Catal.* **1979**, *3*, 663.

29. A. Steel, S.W. Carr, M. W. Anderson, *J. Chem. Soc., Chem. Commun.* **1994**, *13*, 1571.

30. Y. Wei, D. Jin, C. Yang, G. Wei, *J. Sol-Gel Sci. Technol.* **1996**, *7*, 191.

31. C.J. Brinker, R. Sehgal, S.L. Hietala, R. Deshpande, D.M. Smith, D. Loy, C.S. Ashley, *J. Membr. Sci.* **1994**, *94*, 85.

32. R.Zusman, D.A. Beckman, I. Zusman, R.L. Brent, *Anal. Biochem.* **1992**, *201*, 103.

33. S.T. Hobson, K. J. Shea **,** *Chem. Mater.* **1997**, *9*, 616.

34. B. E. Yoldas, *J. Non-Cryst. Solids* **1986**, *83*, 375.

35. J. Wen, G.L. Wilkes, *Poly. Mater. Sci. Eng.* **1995**, *73*, 429.

36. C.Brinker, G. Scherer, *Sol-Gel Science: The Physics and Chemistry of Sol-Gel Processing*; Academic Press, Inc.: New York, NY, USA, **1990**.

37. J.Wen, G.L Wilkes, *Chem. Mater.* **1996**, *8*, 1667.

38. L.L. Hench, J.K. West, *The sol-gel process. Chem. Rev*. **1990**, *90*, 33.

39. C.Brinker, G. Scherer, Sol-Gel Science: The Physics and Chemistry of Sol-Gel Processing; Academic Press, Inc.: New York, NY, USA, **1990**.

40. W. Stöber, A. Fink, E.J. Bohn, *Colloid Interface Sci.* **1968**, *26*, 62.

41. K. Nozawa, H. Gailhanou, L. Raison, P. Panizza, H. Ushiki, E. Sellier, J.P. Delville, M.H. Delville*, Langmuir* **2004**, *21*, 1516.

42. X.D. Wang, Z.X. Shen, T. Sang, X.B. Cheng, M.F. Li, L.Y. Chen, Z.S. Wang, *J. Colloid Interface Sci*. **2010**, *341*, 23.

43. N. Shimura, M. Ogawa, *J. Mater. Sci.* **2007**, *42*, 5299.

44. M.H. Kim, H.K. Na, Y.K. Kim, S.R. Ryoo, H.S. Cho, K.E. Lee, H. Jeon, R.Ryoo, D.H. Min, *ACS Nano* **2011**, *5*, 3568.

45. J. Zhang, X. Li, J.M. Rosenholm, H.C. Gu , *Colloid Interface Sci.* **2011**, *361*, 16.

46. L. Baiyan, Y. Zhang, D. Ma, Z. Shi, S. Ma*, Nature communications* **2014**, *5*, 1.

47. B.J. Melde, B.J. Johnson, P.T. Charles, *Sensors (Basel, Switzerland)* **2008,** *8*, 5202.

48. T. Sangvanich, J. Morry, C. Fox, W. Ngamcherdtrakul, S. Goodyear, D. Castro, D, W. Yantasee, *ACS Appl. Mat. Interfaces* **2014,** *6*, 5483.

49. T.G. Carter, W. Yantasee, T. Sangvanich, G.E. Fryxell, D.W. Johnson, R.S. Addleman, *Chem. Commun.* **2008,** *43*, 5583.

50. X.Wang, J. Gu, L. Tian, X. Zhang, X., *Sci. Rep.* **2017,** *7*, 44178.

51. C.G. Piscopo, *Open Chem.* **2015**, *4*, 383.

52. R. Anwander, C. Palm, J. Stelzer, O. Groeger, G. Engelhardt, *Stud. Surf. Sci. Catal.* **1998**, *117*, 135.

53. K. S. W. Sing, D. H. Everett, R. A. W. Haul, L. Moscou, R. A. Pieroti, J. Rouquerol, T. Siemieniewska., *Pure Appl. Chem.* **1985**, *57*, 603.

54. J. Rouquerol, F. Rouquerol, K. S. W. Sing, P. Llewellyn, G. Maurin. Adsorption by Powders and Porous Solids: Principles, Methodology and Applications, Academic Press **2014**.

55. S. Lowell, J. Shields, M. A. Thomas, M. Thommes, Characterization of Porous Solids and Powders: Surface Area. Porosity and Density, Springer, **2004**.

56. E. P. Barrett, L. G. Joyner, P. P. Halenda, *J. Am. Chem. Soc*. **1951**, *73*, 373.

57. N.K. MaI, M. Fujiwara, Y. Tanaka, *Nature* **2003**, *421*,350.

58. N.K. MaI, M. Fujiwara, Y. Tanaka, T. Taguchi, M. Matsukata, *Chem. Mater*.**2003**, *15*, 3385.

59. C.-Y. Lai, B. G. Trewyn, D. M. Jeftinija, K. Jeftinija, S. Xu, S. Jeftinija, V. S.-Y. Lin, *J. Am.Chem. Soc.* **2003**, *125*, 4451.

60. S. Giri, B.G. Trewyn, M.P. Stellmaker, V.S.-Y. Lin, *Angew. Chem. Int. Ed*. **2005**, *44*, 5038.

62. R. Liu, X. Zhao, T. Wu., P. Y. Feng*, J. Am. Chem. Soc*. **2008**, *130*, 14418.

63. V. S. Y. Lin, D. R. Radu, M.-K. Han, W. Deng, S. Kuroki, B. H. Shanks and M. Pruski, *J. Am. Chem. Soc.* **2002**, *124*, 9040.

64. C.-G. Wu, T. Bein, *Science* **1994**, *266*, 1013.

65. A.Heidari, H. Younesiadn, Z. Mehraban, *Chem. Engineering J.* **2009**, *153*, 70.

66. H.W. Lee, H.J. Cho, J.H. Yim, J.M. Kim, J.K.Jeon, J.M.Sohn, K.S.Yoo, S.S.Kimand, Y.K.Park, J. Ind Eng Chem. **2011**, *27*, 504.

67. G.Li, Z. Zhao, J. Liuand, G. Jiang, *J Hazard Mat*. **2011**, *192*, 277.

68. D.Pérez-Quintanilla, A. Sánchez, I.del Hierro, M. Fajardo, I. Sierra, *J. Colloid Interf. Sci.* **2007**, *313*, 551.

69. J. Park, H. Kim, J. Park, *IJEST* **2012**, *3*, 81.

70. X. Feng, G. E. Fryxell, L. Q. Wang, A. Y. Kim, J. Liu, K. M. Kemner, *Science* **1997**, *276*, 923.

71. M.O.Omorogie, J.O.Babalola, E.I. Unuabonah, J. R.Gong, *Environ Technol.* **2014**, *35*, 611.

72. S.E. Park, E.-Y. Jeong, *Heterogeneous Catalysis with Organic–Inorganic Hybrid Materials in Bridging Heterogeneous and Homogeneous Catalysis: Concepts, Strategies, And Applications **2014**,* Wiley-VCH Verlag GmbH & Co. KGaA, Weinheim, Germany. doi: 10.1002/9783527675906.ch3.

73. Z. Yi, H.I. Hussain, C.Feng, D. Sun, F.She, J.E. Rookes, D. M. Cahill, L. Kong, *ACS Appl. Mater. Interfaces* **2015**, *7*, 9937.

74. H.Wanyika, E.Gatebe, P. Kioni , Z. Tang , Y. Gao, *J. Nanosci. Nanotechnol*. **2012**, *12*, 2221.

75. J. F. Díaz, J.B. Kenneth, J. Mol. *Catal B- Enzym.* **1996**, *2*, 115.

76. A.Popat, S.B. Hartono, F. Stahr, J. Liu, S. Z. Qiao, G.Q. Lu, *Nanoscale* **2011**, *3*, 2801.

77. M. Vallet-Regi, A. Ramila, R. P. del Real, J. Perez-Pariente, *Chem. Mater*. **2001**, *13*, 308.

78. T. Hirano, T. Yui, K.-I. Okazaki, T. Kajino, Y. Fukushima, H. Inoue, T. Torimoto, K. Takagi, *J. Nanosci. Nanotechnol*. **2009**, *9*, 495.

79. H.Yin, L. Liao, J. Fang, *JSM Clin Oncol Res* **2014**, *2*, 1010.

80. V. Cauda, C. Argyo, A. Schlossbauer, T. Bein, *J. Mater. Chem.* **2010**, *20*, 4305.

81. R.Krishna, J.K. Pandit., *J. Pharm. Pharmacol.* **1996**, *48*, 367.

82. M. Bhat, D.S. Shenoy, N. Udupa, C.R. Srinivas, *Indian Drugs.* **1995**, *32*, 211.

83. P.Deol, G.K. Khuller, *Biochimica Biophysi Acta*. **1997,** *1334*, 161.

84. A.Schlossbauer, J. Kecht, T. Bein, *Angew. Chem. Int. Ed.* **2009**, *48*, 3092.

85. D.Peer, J.M. Karp, S. Hong, O.C. Farokhzad, R. Margalit, R. Langer, *Nat. Nanotechnol.* **2007**, *2*, 751.

86. J. Cui, Y. Yan, Y. Wang, F. Caruso, *Adv. Funct. Mater*. **2012**, *22*, 4718.

87. M. Vallet-Regi, A. Ramila, P.R. del Real, J. Perez-Pariente, *Chem. Mater*. **2001**, *13*, 308.

88. S.H. Wu, Y. Hung, C.Y. Mou, *Chem. Commun*. **2011**, *47*, 9972.

89. V. Cauda, C. Argyo, T. Bein, *J. Mater. Chem*. **2010**, *20*, 8693.

90. S.A. Mackowiak, A. Schmidt, V. Weiss, C. Argyo, C. von Schirnding, T. Bein, C. Brauchle, *Nano Lett*. **2013,** *13*, 2576.

91. C. Argyo, V. Weiss, C. Bräuchle, T. Bein, *Chem. Mater.* **2014**, *26*, 435.

92. F. Hoffmann, M. Cornelius, J. Morell, M. Fröba, *Angew. Chem. Int. Ed.* **2006**, *45*, 3216.

93. J. I. Hare, T. Lammers, M. B. Ashford, S. Puri, G. Storm, S. T. Barry, *Adv. Drug Deliv. Rev.***2017**, *108*, 25.

94. A. E. Nel, L. Madler, D. Velegol, T. Xia, E. M. V. Hoek, P. Somasundaran, F. Klaessig, V. Castranova, M. Thompson, *Nat. Mater*. **2009**, *8*, 543.

95. M. Ferrari. *Nat. Rev. Cancer* **2005**, *5*, 161.

96. H. Meng, M. Xue, T. Xia, Z. Ji, D.Y. Tarn, J.I. Zink, A. E. Nel. *ACS Nano,* **2011**, *5*, 4131.

97. J.E. Lee, N. Lee, H. Kim, J. Kim, S. H. Choi, J. H. Kim, T. Kim, I. C. Song, S. P. Park, W. K. Moon, T. Hyeon. *J. Am. Chem. Soc.* **2010**, *132*, 552.

98. H. Maeda, J. Wu, T. Sawa, Y. Matsumura, K. Hori. *J Control Release* **2000**, *65*, 271.

99. D. Tarn, C. E. Ashley, M. Xue, E. C. Carnes, J. I. Zink, C. Jeffrey Brinker. *Acc. Chem. Res*. **2013**, *46*,792.

100. C. E. Ashley, E. C. Carnes, G. K. Phillips, D. Padilla, P. N. Durfee, P. A. Brown, T. N. Hanna, J. Liu, B.Phillips, M. B. Carter, N. J. Carroll, X. Jiang, D. R. Dunphy, C. L. Willman, D. N. Petsev, D. G. Evans, A. N. Parikh, B. Chackerian, W. Wharton, D. S. Peabody, C. J. Brinker, *Nat. Mater.* **2011**, *10*, 389.

101. J. M. Rosenholm, C. Sahlgren, M. Linde, *Nanoscale*, **2010**, *2*, 1870.

102. F. Chen, H. Hong, Y. Zhang, H.F. Valdovinos, S. Shi, G.S. Kwon, C.P. Theuer, T.E. Barnhart, W. Cai, *ACS Nano* **2013**, *7*, 9027.

103. D.P.Ferris, J. Lu, C. Gothard ,R. Yanes , C.R. Thomas, J.C. Olsen, J.F.Stoddart, F.Tamanoi , J.L. Zink , *Small* **2011**, *7*, 1816.

104. LL.Li, Q. Yin, J. Cheng, Y. Lu, *Adv. Health Mater.* **2012**, 1, 567.

105. M. Yu, S. Jamhrunkar, P. Thorn, J. Chen, W. Gu, C. Yu, *Nanoscale* **2013**, *5*, 178.

106. Z. Chen, Z. Li, Y. Lin, M. Yin, J. Ren, X. Qu, *Chem. Eur. J*. **2013**, *19*, 1778.

107. M. Liong, J. Lu, M. Kovochich, T. Xia, S.G. Ruehm, A.E. Nel, F. Tamanoi, J.I. Zink, *ACS Nano* **2008**, 2, 889.

108. O. Nuri, J.H. Park, *Int J. Nanomedicine* **2014**, 9, 51.

109. N. Hao, L. Li, Q. Zhang, X. Huang, X. Meng, Y. Zhang, D. Chen, F. Tang, L. Li, *Micropor. Mesopor. Mater*. **2012**, *162*, 14.

110. I.Slowing , B.G. Trewyn , V.S.Lin, *J. Am. Chem. Soc*., **2006**, *128*, 14792.

111. Q. Gan, D. Dai , Y. Yuan, J. Qian, S. Sha, J. Shi, C.Liu, *Biomed. Microdevices* **2012**, *14*, 259.

112. K. Kang , J.S. Lim , *Immune Netw* **2012** , *12*, 104.

113. C.Bharti, U. Nagaich, A.K.Pal, N. Gulati, *Int J Pharm Investig.* **2015**, *5*, 124.

114. P.Decuzzi , S. Lee, B.Bhushan , M.Ferrari, *Ann Biomed Eng.* **2005**, *33*, 179.

115. P. Decuzzi, S. Lee, M. Decuzzi, M. Ferrari, *Ann Biomed Eng.* **2004**, *32*, 793.

116. J.A. Champion, Y.K. Katare, S. Mitragotri, *J Control Release* **2007,***121*,3.

117. X.Huang , X. Teng, D. Chen, F.Tang, J. He, *Biomaterials* **2010**, *31*, 438.

118. S.E. Gratton, P.A. Ropp, P.D. Pohlhaus, J.C. Luft, V.J. Madden, M.E Napier, J.M.DeSimone, Proc. Natl Acad Sci U.S.A **2008**, *105*, 11613.

119. A.K. Gupta, M. Gupta, S.J. Yarwood, A.S. Curtis, *J Control Release* **2004**, *95*, 197.

120. Y.Liu , J. Tan, A.Thomas , D.Ou-Yang , V.R. Muzykantov ,*Ther Deliv*. **2012**, *3*, 181.

121. T. Chung, M. Yao, C.W. Lu, Y.S. Lin, Y. Hung, C.Y. Mou, Y. Chen, D.M. Huang, *Biomaterials* **2007**, *28*, 2959.

122. S.W. Song, S. Kawi, *Langmuir* **2005**, *21*, 9568.

123. F. Torney, V.S.Y. Lin, K. Wang, Nat*. Nanotech*. **2007**, *2***,** 295.

124. J.C. Doadrio, I. Izquierdo-Barba, A.L. Doadrio, J. Perez-Pariente, M. Vallet-Regi*, J. Mater. Chem.* **2006**, *16*, 462.

125. C. Kneuer, M. Sameti, U. Bakowsky, T. Schiestel, H. Schirra, H. Schmidt, C.S. Lehr, *Bioconjug. Chem.* **2000**, *11*, 926.

126. V.Cauda, A. Schlossbauer, T. Bein, *Microporous Mesoporous Mater.* **2010**, *132*, 60.

127. *K.R. Martin, J. Nutr. Health Aging* **2007***, 11*, 94.

128. R.Mortera, S. Fiorilli, E. Garrone, E. Verné, B. Onida, *Chem. Eng. J.* **2010***, 156*, 184.

129. X. Huang, L. Li, T. Liu, N. Hao, H. Liu, D.Chen, F.Tang, *ACS Nano **2011**, 5*, 5390.

130. J.L.Steinbacher, S.A. Lathrop, K. Cheng, J.M. Hillegass, K.J. Butnor, R.A. Kauppinen, B.T. Mossman , C.C. Landry, *Small* **2010**, *6*, 2678.

131. J.Lu, Z.Li, J.I. Zink, F. Tamanoi, *Nanomed.* **2012**, *8*, 212.

132. S. P. Hudson, R. F. Padera, R. Langer, D. S. Kohane, *Biomaterials* **2008**, *29*, 4045.

133. J.S. Souris, C.H. Lee , S.H.Cheng , C.T. Chen, C.S Yang , J.A. Ho, *Biomaterials* **2010**, *31*, 5564.

134. S. R. Blumen, K. Cheng, M. E. Ramos-Nino, D. J. Taatjes, D. J. Weiss, C. C. Landry, B. T. Mossman, *Am. J. Respir. Cell Mol. Biol*. **2007**, *36*, 333.

135. J.Lu, M. Liong, Z. Li, J.I. Zink, F. Tamanoi, *Small* **2010**, *6*, 1794.

136. *Q.*He, Z. Zhang , F. Gao, Y. Li, J. Shi , *Small* **2011***, 7*, 271.

137. X. Huang, L. Li, T. Liu, N. Hao, H. Liu, D. Chen, F. Tang, *ACS Nano* **2011**, *5*, 5390.

138. F. Chen, H. Hong, S, Shi, S.Goel, H.F. Valdovinos, R. Hernandez, C.P. Theuer, T.E. Barnhart, W.Ca, *Scientific reports* **2014**, *4*, 1.

139. Q.Fu, D. Hargrove, X. Lu, *Nanomedicine* **2016**, *12*, 1951.

140. A. K. Varkouhi, M. Scholte, G. Storm, H.J. Haisma, *J. Controlled Release* **2011**, *151*, 220.

141. L. Prasmickaite, A. Hogset, K. Berg, *Photochem. Photobiol.* **2001**, *73* , 388.

142. N. Nishiyama, W.D. Jang Arnida, K. Date, K. Miyata, K. Kataoka, *J. Drug Target*. **2006** , *14*, 413.

143. K.G. de Bruin, C. Fella, M. Ogris, E. Wagner, N. Ruthardt, C. Bräuchle, *J. Controll. Rel*. **2008**, *130*, 175.

144. S.Angelos, E.Choi, F.Voegtle, L. De Cola, J.I. Zink, *J.Phys. Chem. C.* **2007**,*111*, 6589.

145. A.M. Sauer, A.Schlossbauer, N. Ruthardt, V.Cauda, T. Bein, C. Bräuchle, *Nano Lett.* **2010**, *10*, 3684.

146. I. Nakase, S. Kobayashi , S. Futaki, *Biopolymers* **2010**, *94*, 763.

147. I. Slowing, B.G. Trewyn, S. Victor, Y. Lin., *J. Am. Chem. Soc.* **2006**, *128*, 14792.

148. M. Massignani, C. LoPresti, A. Blanazs, J. Madsen, S. P. Armes, A. L. Lewis, G. Battaglia, *Small* **2009**, *5*, 2424.

149. S. Oliveira, I. van Rooy, O. Kranenburg, G. Storm, R. M. Schiffelers, *Int. J. Pharm.* **2007**, *331*, 211.

150. J.D. Mintern, C. Percival, M.M. Kamphuis, W.J. Chin, F. Caruso, A.P. Johnston, *Adv. Health Mater.* **2013**, *2*, 940.

151. M. Danial, S. Perrier, K.A. Jolliffe, *Org. Biomol. Chem.* **2015**, *13*, 2464.

152. S. Qian, W.Wang, L. Yang, H.W. Huang, *Biophysical Journal* **2008**, *94*, 3512.

153. P.R. Leroueil, S.A. Berry, K. Duthie,G. Han, V.M. Rotello, D.Q. McNerny, J.R. Baker, B.G. Orr, M.M. Holl, Nano Lett. **2008**, *8*, 420.

154. J. Chen, J.A. Hessler, K. Putchakayala, B.K.Panama, D.P. Khan, S.Hong, D.G.Mullen, S.C.Dimaggio, A. Som, G.N. Tew, A.N. Lopatin, J.R. Baker, M.M. Holl, B.G. Orr, *J. Phys. Chem. B* **2009**, *113*, 11179.

155. T. Bieber, W.Meissner, S.Kostin, A.Niemann, H.P.Elsasser, *J Control Release* **2002**, *82*, 441.

156. R.A. Jones, C.Y. Cheung, F.E.Black, J.K. Zia, P.S. Stayton, A.S. Hoffman, M.R. Wilson, *Biochem. J.* **2003**, *372*, 65.

157. B. Turk, V.Turk, *J. Biol. Chem.* **2009**, *284*, 21783.

158. Y. Zhang, C.Y. Ang, M. Li, S.Y. Tan, Q. Qu, Z. Luo, Y. Zhao, *ACS Appl. Mater.Interfaces* **2015**, *7*, 18179.

159. N. Song, Y.W. Yang, *Chem. Soc. Rev.* **2015**, *44*, 3474.

160. C.H. Lee, S.H. Cheng, I.P. Huang, J.S. Souris, C.S. Yang, C.Y. Mou, L.W. Lo, *Angew. Chem.* **2010**, *49*, 8214.

161. E.S. Lee, Z. Gao, Y.H. Bae, *J. Controlled Release,* **2008**, *132*, 164.

162. D.Hanahan, R.A. Weinberg, *Cell* **2011**, *144*, 646.

163. L.E. Gerweck, K. Seetharaman, *Cancer Res.* **1996**, *56*, 1994.

164. S. Niedermayer, V. Weiss, A. Herrmann, A. Schmidt, S. Datz, K. Müller, E. Wagner, T. Bein, C. Bräuchle, *Nanoscale* **2015**, *7*, 7953.

165. W. Feng, X. Zhou, C. He, K. Qiu, W. Nie, L. Chen, *J. Mater. Chem. B* **2013**, *1*, 5886.

166. W. Feng,W. Nie, C.He, X. Zhou, L. Chen, K. Qiu, W. Wang, Z. Yin, *ACS Appl. Mater. Interfaces* **2014**, *6*, 8447.

167. J. Zheng, X. Tian, Y. Sun, D. Lu , W. Yang, *Int. J. Pharm.* **2013**, *450*, 296.

168. Y.L. Zhao, Z. Li, S. Kabehie, Y.Y. Botros, J.F. Stoddart, J.I. Zink, *J Am Chem Soc* **2010**, *132*, 13016.

169. Y. Chen, K.Ai ,J. Liu, G. Sun, Q. Yin, L. Lu , *Biomaterials* **2015,** *60*, 111.

170. A. F. Moreira, V. M. Gaspar, E.C. Costa, D. de Melo-Diogo, P. Machado, C. M. Paquete, I. J. Correia, *Eur. J. Pharm. Biopharm.* **2014**, *88*, 1012.

171. F.Muhammad, M. Guo, W. Qi, F. Sun, A. Wang, Y. Guo, G. Zhu, *J. Am. Chem. Soc.* **2011**, *133*, 8778.

172. J.M. Estrela, A. Ortega, E. Obrador, *Crit. Rev. Clin. Lab. Sci.* **2006**, *43*, 143.

173. R. Cheng, F. Feng, F. Meng, C. Deng, J. Feijen, Z. Zhong, *J. Controlled Release* **2011**, *152*, 2.

174. F.Q. Schafer, G.R. Buettner, *Free Radicals Biol. Med.* **2001**, *30*, 1191.

175. D. Xiao, J. J Hu, J.Y. Zhu, S.B Wang, R,X Zhuo, X.Z Zhang, *Nanoscale* **2016**, *8*, 16702.

176. X. Yang, D. He, X. He, K. Wang, Z. Zou, X. Li, H. Shi, J. Luo, X. Yang, *Part. Part. Syst. Charact.* **2015**, *32*, 205.

177. X. Chen, H. Sun, J. Hu, X. Han , H. Liu, Y.Hu, *Colloids Surf B Biointerfaces* **2017**, *152*, 77.

178. B. Zhang, Z. Luo, J. Liu, X. Ding, J. Li, K. Cai, *J. Control. Release* **2014**, *192*, 192.

179. L. Chen, X. Zhou, W. Nie, Q. Zhang, W.Wang, Y. Zhang, C. He, *ACS Appl. Mater. Interfaces* **2016**, *8* , 33829.

180. A. Agostini, L. Mondragón, A. Bernardos, R. Martínez-Mañez, M. D. Marcos, F. Sancenón, J. Soto, A. Costero, C. Manguan-Garca, R. Perona, M. Moreno-Torres, R. Aparicio-Sanchis, J.R Murguía, *Angew. Chem. Int. Ed.* **2012**, *51*, 1.

181. K. Kessenbrock, V. Plaks, Z. Werb, *Cell*. **2010**, *141*, 52.

182. S. H. van Rijt, D. A. Bo¨lu¨kbas, C. Argyo, S. Datz, M. Lindner, O. Eickelberg, M. Königshoff, T. Bein and S. Meiners, *ACS Nano* **2015**, *9*, 2377.

183. J. Liu, B. Zhang, Z. Luo, X. Ding, J. Li, L. Dai, J. Zhou, X. Zhao, J. Ye, K. Cai, *Nanoscale* **2015**, *7*, 3614.

184. S. Deshayes, H. Cabral, T. Ishii, Y. Miura, S. Kobayashi, T. Yamashita, A. Matsumoto, Y. Miyahara, N. Nishiyama and K. Kataoka, *J. Am. Chem. Soc.* **2013**, *135*, 15501.

185. C. S. Geninatti, D. Alberti, I. Szabo, S. Aime and K. Djanashvili, *Angew. Chem. Int. Ed*., **2013**, *125*, 1199.

186. X. Zhang, Z. Zhang, X. Su, M. Cai, R. Zhuo, Z. Zhong, *Biomaterials* **2013**, *34*, 10296.

187. H. Liu, Y. Li, K. Sun, J. Fan, P. Zhang, J. Meng, S. Wang and L. Jiang, *J. Am. Chem. Soc*. **2013**, *135*, 7603.

188. J. Geng, M. Li, L. Wu, C. Chen, X. Qu, *Adv. Healthcare Mater.* **2012**, *1*, 332.

189. J. Lai, B.P. Shah, Y. Zhang, L.Yang, K.B.Lee, *ACS Nano*. **2015**, *9*, 5234.

190. X.He, Y. Zhao, D. He, K. Wang, F. Xu, J. Tang, *Langmuir*. **2012**, *28*, 12909.

191. M. Chen, C. Huang, C. He, W. Zhu, Y. Xu, Y. Lu, *Chem. Commun.* **2012**, *48*, 9522.

192. G. Lorusso, C.Rüegg, *Cell Biol.* **2008,** *130*, 1091.

193. J. Chen, M. Liu, C. Chen, H. Gong, C. Gao, *ACS Appl. Mater. Interfaces.* **2011**, *3*, 3215.

194. Z. Yu, N. Li, P. Zheng, W. Pan, B. Tang, *Chem. Commun.* **2014**, *50*, 3494.

195. E. Aznar, L. Mondragón, J.V. Ros-Lis, F. Sancenón, M.D. Marcos, R. Martínez-Máñez, J. Soto, E. Pérez-Payá, P. Amorós, *Angew. Chem. Int. Ed.* **2011**, *50*, 11172.

196. D. P. Ferris, Y.L. Zhao, N. M. Khashab, H. A. Khatib, J. F. Stoddart, J.I. Zink , *J. Am. Chem. Soc.* **2009**, *131*, 1686.

197. D. Tarn, D. P. Ferris, J. C. Barnes, M. W. Ambrogio, J. F. Stoddart, J. I. Zink, *Nanoscale* **2014**, *6,* 3335.

198. T. M. Guardado-Alvarez, M. M. Russell, J. I. Zink, Chem. Commun. ***2014,*** *50*,8388.

199. A.Noureddine, L. Lichon, M. Maynadier, M. Garcia, M. Gary-Bobo, J.I. Zink, X. Cattoën, M.W. Chi Man, *Nanoscale* ***2015***, *7*, 11444.

200. T. M. Guardado-Alvarez, L. S. Devi, J.-M. Vabre, T. A. Pecorelli, B. J. Schwartz, J.-O. Durand, O. Mongin, M. Blanchard-Desce, J. I. Zink*, Nanoscale* **2014**, *6*, 4652.

201. J. Cho, M. Chung, M.S. Shim*, J. Ind. Eng. Chem.***2015**, *31*, 15.

202. Y.T. Chang, P.-Y.Liao, H.-S. Sheu, Y.-J. Tseng, F.-Y. Cheng, C.-S.Yeh, *Adv. Mater.* **2012**, *24*, 3309.

203. L. Zhang, Y. Li , Z. Jin , J.C. Yu, K. M. Chan, *Nanoscale* **2015**, *7*, 112614.

204. J.L. Paris, M. V. Cabañas, M. Manzano, M. Vallet-Regí, *ACS Nano*. **2015**, *9*, 11023.

205. *E.* Ruiz-Hernández, A.Baeza A, M. Vallet-Regí, *ACS Nano*. **2011**, *5*, 1259.

206. A. Baeza, E. Guisasola, E. Ruiz-Hernández, M. Vallet-Regí**,** *Chem Mater* **2012**, *24*, 517.

207. P. Zhao, H. Liu, H. Deng, L. Xiao , C. Qin, Y. Du, X. Shi, *Colloids Surf B Biointerfaces*. **2014**, *123*, 657.

208. X. Luo and X. T. Cui, *Electrochem. Commun.* **2009**, *11*, 1956.

209. S. Jiang, Y. Sun, X. Cui, X. Huang, Y. He, S. Ji, W. Shi, D. Ge, *Synth. Met.* **2013**, *163*, 19.

210. N.M. Khashab, A. Trabolsi, Y.A. Lau, M.W. Ambrogio, D.C. Friedman, H.A. Khatib, J. Zink, J. Fraser Stoddart, *Eur. J. Org. Chem.* **2009**, *11*, 1669.

211. Y.C. Barenholz*, J. Control. Release* **2012**, *160*, 117.

212. M. Benezra,O. Penate-Medina, P.B. Zanzonico, D. Schaer, H. Ow, A. Burns, E. DeStanchina, V.Longo, E. Herz, S-Iyer, J. Wolchok,S.M. Larson, U. Wiesner, M.S. Bradbury, *J. Clin. Invest*. **2011**, *121*, 2768.

213. J.W. Nichols, Y.H. Bae, Nano Today **2012**, *7* , 606.

214. E. Blanco, H. Shen, M.Ferrari, Nat. Biotechnol. **2015**, *33*, 941.

215. E. Geretti, S.C. Leonard, N. Dumont, H. Lee, J. Zheng, R. De Souza, D.F. Gaddy, C.W. Espelin, D.A. Jaffray, V. Moyo,U.B. Nielsen,T.J. Wickham , B.S. Hendriks, *Mol. Cancer Ther*. **2015**, *14*, 2060.

216. R. van der Meel, L.J. Vehmeijer, R.J. Kok, G. Storm, E.V. van Gaal, *Adv. Drug Deliv. Rev*. **2013**, *65*, 1284.

217. G.J. Weiss, J. Chao , J.D. Neidhart, R.K. Ramanathan, D. Bassett , J.A. Neidhart, C.H. Choi, W. Chow, V. Chung, S.J. Forman, E. Garmey, J. Hwang, D.L. Kalinoski M. Koczywas,J. Longmate, R.J. Melton, R. Morgan, J. Oliver, J.J. Peterkin, J.L. Ryan , T. Schluep, T.W. Synold, P. Twardowski, M.E. Davis, Y.Yen, *Investig. New Drugs* **2013**, *31*,986.

218. M. Maiarù,K.K. Tochiki, M.B. Cox, L.V.Annan, C.G.Bell, X.Feng, F.Hausch, S.M. Géranton, *Sci. Transl. Med.* **2016**, *8*, 325.

219. M. E. R. O'Brien,N. Wigler, M. Inbar, R. Rosso, E. Grischke, A. Santoro,R. Catane,D. G. Kieback, P. Tomczak, S. P. Ackland, F. Orlandi, L. Mellars,L. Alland, C. Tendler, *Ann. Oncol*. **2004**, *15*, 440.

220. V.J. Venditto, F.C. Jr. Szoka, *Adv. Drug Deliv. Rev.* **2013**, *65*, 80.

221. D. Cook, D. Brown, R. Alexander, R. March, P. Morgan, G. Satterthwaite, M.N. Pangalos, *Nat. Rev. Drug Discov.* **2014**, *13*, 419.

222. T. Sun, Y.S. Zhang, B. Pang, D.C. Hyun, M. Yang, Y. Xia, *Angew. Chem. Int. Ed. Engl.* **2014**, *53*, 12320.

223. H.S. Yang, N. Ieronimakis, J.H. Tsui, H.N.Kim, K.Y. Suh, M. Reyes, D.H. Kim, *Biomaterials* **2014,** *35*, 1478.

224. C.L. Hastings, E.T. Roche, E. Ruiz-Hernandez, K. Schenke-Layland, C.J. Walsh, G.P Duffy, *Adv. Drug Deliv. Rev.* **2015,** 84, 85.

225. A. Aldrey, C- Núñez, V. García, R. Bastida, C. Lodeiro, A. Macías, *Tetrahedron Letters*, **2010**, *66*, 9223.

226. a) T. W. Bell, N.M. Hext, Chem. Soc. Rev. **2004**, *33*, 589. b) T. Gunnlaugsson, M. Glynn, G. M. Tocci, P. E. Kruger, F. M. Pfeffer, *Coord. Chem. Rev.* **2006**, *250*, 3094. c) V. Amendola, D. Esteban-Gómez, L. Fabbrizzi, M. Lichelli, *Acc. Chem. Res.* **2006**, *39*, 343. d) T. Gunnlaugsson, H. D. P. Ali, M. Glynn, P. E. Kruger, G. M. Hussey, F. M. Pfeffer, C. M. G. Dos Santos, J. Tierney, *J. Fluoresc*. **2005**, *15*, 287.

227. a) S. L. Wiskur, H. Aït-Haddou, J. J. Lavigne, E. V. Anslyn, *Acc. Chem. Res.* **2001**, *34*, 963. b) B. T. Nguyen, E. V. Anslyn, *Coord. Chem. Rev.*, **2006**, *250*, 3118.

228. Z. Yu, X.Chen, H.N. Kim, J. Yoon, *Chem. Soc. Rev.* **2010**, *39*, 127.

2. Peptides in Nanomedicine: targeting ligands, protease substrates and molecular gates.

2.1. Introduction

2.1.1. Peptides as targeting ligands

Most traditional delivery methods (except for time-release formulations) release drugs instantaneously, and this can result in peak concentrations that are toxic to tissues. Also, the nontargeted distribution of the drugs can cause undesired effects at sites other than those intended. Moreover, many drugs partially degrade before they reach the desired site, leading to a reduction in therapeutic effects. Proteins and peptides, carbohydrates, vitamins, antibodies, and aptamers are common ligands used to increase the specificity of targeting systems.

Several monoclonal antibodies that target cell surface receptors have gained approval by the U.S. Food and Drug Administration and are widely used in the treatment of some cancers. The efficacy of this cancer immunotherapy modality is, however, limited by the large size of the antibodies and its relatively nonspecific binding to the reticuloendothelial system. This latter property is particularly problematic if the antibody is used as a vehicle to deliver radionuclides, cytotoxic drugs, or toxins to the tumor site.

Peptides, peptidomimetic, or small molecules are an attractive alternative. One of the main reasons for the increasing interest for peptides and peptide receptors in cancer is the possibility of targeting, as peptide receptors are often expressed in many primary human cancers. In comparison to their expression in normal tissue adjacent to the neoplasm and/or in its normal tissue of origin. Some of the advantatges that makes peptides attractive compounds to act as a bullet targeted are sumarised in **table 2.1.**

On the one hand, as small and usually hydrophilic molecules, peptides are characterized by an excellent permeability that permits an easy and rapid access to the tumor site after systemic injection. There is one exception: peptides will usually not cross a normal blood-brain barrier and will not enter the brain in

significant amounts (0.1% of total peptide injected) after systemic injection. This is a clear advantage when peripheral organs or tumors are the intended targets; because the brain expresses a high density of most of the peptide receptors and brain targeting could be at the origin of numerous central nervous system side effects. However, peptides may be able to penetrate through the blood-brain barrier when the latter is disturbed, as seen in undifferentiated glial tumors such as glioblastomas. The peptide will then be able to reach the tumor site and remain there.[1] Peptides are usually rapidly excreted from the body.

Furthermore, peptides are physiological compounds, intrinsically nontoxic, as compared with current chemotherapeutic drugs. If side effects occurs, may be due to the physiological actions of the peptides and may be expected after administration of pharmacological doses of the nontoxic compounds, for instance during long-term treatment of tumors. Because peptides usually play a modulatory role in various biological systems, their actions will often be counterbalanced and possibly annihilated by other hormones, growth factors, or neurotransmitters acting in these same systems. Another important characteristic of peptides is their usual lack of antigenicity, because their small sizes.

Another important point is that peptides are quite easily synthesized and modified. They withstand the rather harsh conditions for modification or labeling. However, their natural structural conformation makes them extremely sensitive to peptidases; they are rapidly broken down due to cleavage of peptide bonds by several types of peptidases present in most tissues. Thus, metabolically stable analogs must be developed for successful clinical applications. For example, through a long effort of development, somatostatin analogs octreotide, lanreotide, and vapreotide, compared with natural somatostatin have a prolonged half-life in plasma and tissue and a longer action. For many of the other peptides, only limited efforts have been made to develop analogs having an improved stability in the order of hours.

One of the most attractive feature of peptides is the possibility of their radiolabeling. Using chelators such as diethylenetriaminopentaacetic acid (DTPA) or 1,4,7,10-tetraazacyclododecane-1,4,7,10-tetraacetic acid (DOTA) which are molecules able to coordinate with certain types of metallic radioisotopes. However, those relatively large molecules may affect the binding properties of the compound to which they are attached. Small (8–20 amino acids) peptides are usually large enough to provide an adequate attachment site for a chelator molecule that is sufficiently distant from the binding area to prevent a complete loss of the binding affinity of the peptide to the receptor.[2]

Table 2.1. Advantages and disadvantages of peptides as targeting agents

ADVANTAGES	DISADVANTAGES
• Small molecules	• Rapidly degraded by peptidases
• Excellent permeability	
• No antigenicity	
• Minimal side effects	
• Easy to synthesize and modify chemically	
• Easy to link to chelators	
• Easy to radiolabel	
• High-affinity receptor binding	
• Rapid clearance from the body	
• No brain targeting due to inability to cross the blood-brain barrier	

Cancer cell surface targeting peptides can be derived from known native peptide hormones such as somatostatin and bombesin, or they can be identified through screening combinatorial peptide libraries against unknown cell surface receptor targets. Phage-display peptide library and one-bead one-compound

(OBOC) combinatorial library methods have been successfully used to discover peptides that target cancer cells or tumor blood vessel endothelial cells. The phage-display peptide library method,[3,4] because of its biological nature, can only display L-amino acids and peptides. In contrast, the OBOC combinatorial library method allows for bead-surface display of peptides that contain L-amino acids, D-amino acids, unnatural amino acids, or other organic moieties. To date, numerous peptide ligands have been discovered for various types of receptors or cells, such as integrin receptors,[5,6] thrombin receptors,[7] tumor cells,[8] cardiomyocytes,[9] and pancreatic β cells.[10]

The most widely used peptides in targeted delivery applications are still integrin-targeted RGD peptides. In the mid-1980s, Ruoslahti and Pierschbacher reported on the importance of the Arginine-Glycine-Aspartic acid (RGD) tri-sequence in fibronectin as an essential cell recognition site for integrin α5β1. This observation has rapidly led to other evidences for the central role of RGD as a general ligand for additional proteins.[11] In parallel, a family of glycoprotein cell surface receptors was discovered that were recognized by the RGD sequence.[12] This class of cell surface were termed “Integrins” in 1986 for their role as “an integral membrane complex involved in the transmembrane association between the extracellular matrix and the cytoskeleton”. Since integrins are involved in processes which are usually associated with tumor progression such as angiogenesis, invasion and metastasis, and since the RGD peptidic ligand selectively targets them, integrins have attracted special focus. Currently, 24 distinct integrins are known and they have been shown to play key roles in many processes including cell adhesion, migration, and proliferation.[13] Enhanced expression of specific integrins in cancer cells is crucial for promoting metastasis,[14] angiogenesis,[15] proliferation, migration and invasion,[16] as well as for the proteolytic destruction of extra cellular matrix (ECM), all essential components in the process of tumor progression.[17]

The overexpression of integrins and their important role in different cancers, make them an obvious target for therapeutic intervention,[18] as well as for the

selective delivery of chemotherapeutics,[19] nanoparticles,[20] and imaging agents.[21] For example, Ruoslahti and co-workers published a paper in which RGD peptides were used to selectively deliver cytotoxic compounds to cancer cells. The researchers showed that DOX covalently conjugated to the nonapeptide CDCRGDCFC considerably improved survival rates of mice bearing human MDA-MB-435 breast carcinomas. Sherz and co-workers reported on selective accumulation of the cyclic RGD analog conjugated to the fluorescent bacteriochlorophyll analog in the tumor necrotic domain in MDA-MB-231-RFP bearing mice, allowing early detection of tumor proliferation. Conjugation of highly potent microtubulin poison paclitaxel to the bicyclic RGD peptide $Ec(RGDyK)_2$ resulted in increased drug efficacy towards tumor cells and decrease in off-target toxicity. Other highly effective RGD analogs include 9-RGD,[22] iRGD,[23] and the cyclic penta-peptide Cilengitide, the latter being developed by Kessler and co-workers.[24] Cilengitide has reached phase III clinical trials for the treatment of glioblastoma and phase II clinical trials for some other tumors.[25]

Other attractive target for a selective delivery of chemotherapeutics is the overexpression of luteinizing hormone releasing hormone (LHRH) receptors in hormone-associated cancers. In the mid-1980s, analogs of LHRH peptide were introduced to target LHRH receptor in prostate and breast cancers. Since then, this class of peptides has been extensively tested as carriers of chemotherapeutic agents to cancer cells. For example, LHRH analogs were conjugated to DOX (conjugate AN-152) or its counterpart 2-pyrollino-DOX (conjugate AN-207), resulting in targeted therapeutic conjugates in various cancer models. Conjugation of LHRH analogs with other toxic agents, such as membrane disrupting peptide,[26] toxins,[27] and PEGylated delivery systems containing the apoptotic agent camptothecin,[28] for targeted therapy of cancer cells, were prepared and tested as well.

Somatostatins are a five-membered family of transmembrane G-protein coupled cell-surface receptors widely distributed in a variety of tumors,[29] which also makes them an attractive target for selective delivery of chemotherapeutics.

While the native somatostatin peptide has high affinity to all five receptor subtypes, it's very short *in vivo* half-life limits its utility as a targeting agent.[30] However, several effective analogs of this peptide have been developed, including two FDA approved and clinically applied radiolabeled conjugates, Octreoscan and Depreotide.[31] Apart from radiolabeled conjugates of somatostatin analogs, several drug conjugates for targeted delivery were reported as well.[32]

Mammalian Bombesins (BN) are a family of growth receptors that included gastrin-releasing peptide receptors (GRPR), neuromedin B receptor (NMBR) and Bombesin receptor subtype 3 (BRS3) which are frequently overexpressed by a number of common cancers such as prostate, breast, lung, gastric, malignant gliomas and colon.[33] It has been observed that various types of cancers can also synthesize bombesin and GRP. The autocrine mode of action of these peptides brings about stimulation of the growth of the tumor that produces them via BN receptors expressed on their surfaces.[34] Consequently, BN receptors are interesting targets for targeted drug delivery to cancer cells. Development of various camptothecin-BN conjugates has led to the discovery of a potent BN agonist drug conjugate (CTP-L2-BA3) that is cytotoxic for cells overexpressing all mammalian BN receptor subtypes.[35] With the aim of improving the targeting efficacy of the BN–drug conjugate, a multi-ligand approach, whereby PTX is conjugated to a divalent BN analog BBN carrier was prepared, resulting in a product with enhanced cytotoxicity.

Angiopeptin-2 receptor-mediated transcytosis expedites blood-brain-barrier crossing of various macromolecules after initial binding of a targeting molecule to a receptor expressed on brain endothelial cells.[36] Low-density lipoprotein receptor (LDLr) is targeted by angiopeptin-2, defining it as a specific "gate" for delivery of payloads to brain malignancies. The most promising peptide based drug conjugated (PDC) based on this peptide ligand is 19-amino-acid linear angiopeptin-2-paclitaxel PDC (ANG1005) that targets LDLr-1 over expressed on solid tumor and is associated with enhanced transcytosis across the blood-brain-barrier.[37] ANG1005 is composed of three molecules of paclitaxel connected to

the two Lys at positions 5 and 9, and to the *N*-terminal Thr. ANG1005 exerts remarkable efficiency in preclinical studies and was well tolerated in phase I clinical studies in glioblastoma. However, phase II clinical trials utilizing ANG1005 were finished because of lack of efficacy.[38] Other angiopeptide drug conjugates include ANG1007 (angiopep-2–doxorubicin), ANG1009 (angiopep-2–dimethylglycine etoposide), and ANG4043 (angipep 2–trastuzumab). ANG4043 is a novel brain-penetrating peptide–mAb (monoclonal antibody) conjugate that is efficient against HER2-positive intracranial tumors in mice.[39]

Despite only a few recent examples are discussed here, peptides as targeting ligands of nanoparticles are steadily gaining momentum in cancer research.[40] Peptide ligands, mostly created by phage display or other reiterative random library approaches, have been successfully used as targeting agents even though their target epitopes are still in the process of discovery. Peptides derived from different larger proteins or ligands are rapidly being developed for targeting as well. Their small size, compared to protein ligands, yet high targeting ability, makes them easy to produce and modify, and could yield favorable pharmacokinetics in vivo. The targeting peptides are often fused with other functional peptides, such as Cell penetrating peptides (CPPs), or attached to nanoparticles to facilitate drug delivery (See section 2.1.3).

As the number of targeting peptide–nanoconjugate examples increases, new ideas on how to use these polyvalent assemblies keep emerging. New ways to combine targeting peptides with other functional peptides and with various diagnostic or therapeutic molecules have been made available by the rapid progress of nanobiotechnology, and these novel agents often afford very different properties than the starting materials used in its preparation. Moreover, peptide targeting itself is becoming combinatorial — with the use of more than one peptide in a single entity, the use of peptides that also serve as proteolytic substrates to provide more function etc. These discoveries and the experience gained could yield completely novel approaches to cancer treatment by nanomedicine.

2.1.2. Biocompatibility-cytotoxicity

In nanomedicine the most important advantage of peptides would be its biocompatibility. Biocompatibility refers to the ability of a biomaterial to perform its desired function with respect to a medical therapy, without eliciting any undesirable local or systemic effects in the recipient or beneficiary of that therapy, but generating the most appropriate beneficial cellular or tissue response in that specific situation, and optimizing the clinically relevant performance of that therapy. For therapeutic purposes, a biomaterial has to be bioactive and interact with the cells. However, the reactivity of the biomaterial and its interaction with the cells often cause an undesired response from the cells. For example, one of the challenges in drug delivery is the immune response of the host body. One way to address this immune response is to use biocompatible biomaterials. PEG brushes grafted on the surface of nanoparticles have been tested to create a 'stealth' effect by mimicking a bacterial cell glycocalyx and resulting in delayed immune clearance by macrophages. However, PEG brushes may also hinder uptake by targeted diseased cells and while the resistance of PEG to serum degradation is useful from a stability standpoint, the coating should be degraded within a defined time. Furthermore its efficacy diminishes due to its undesired degradation by light, heat, or sheer stress.

Multiple studies on biocompatibility of a few peptide nanostructures have been published over the past years. However, because of the wide variety of peptide nanostructures, there are still many other possible sequences which need more in-depth investigation. In this regard, Ghanaati and co-workers reported excellent in vivo biocompatibility of two angiogenic peptide amphiphile (PA) nanofibers.[40] Their static analysis revealed that the nanofiber gels persisted in the tissue for 30 days, and as they biodegraded, a new vascularized tissue was developed. They also performed dynamic experiments using a dorsal skinfold chamber which demonstrated minimal dilation of the vessel and very few leukocytes adhesion to the endothelium near the nanofiber gel. This study

supported the great potential of these nanofibers in regenerative medicine for revascularization of damaged tissues and healing chronic wounds.

In another example of peptide nanostructure's biocompatibility studies, Jayawarna and co-workers used nanostructured hydrogels of fluorenylmethoxycarbonyl (FMOC)-dipeptides for 3D cell culture.[41] They tested nine dipeptide systems with different amino acids and showed that three of them were stable at physiological pH. Then these self-assembled FMOC-dipeptides were used for proliferation and retention of phenotype bovine chondrocytes, and they showed good ability to support proliferation of these cells. Wagh and co-workers compared biocompatibility of previously designed peptide nanofibers to other common nanomaterials of different shapes, compositions, sizes, and charges, and also investigated their biodistribution and hemocompatibility.[42] They reported that optimized peptide nanofibers were nontoxic, hemocompatible with a minimum uptake by macrophages, and therefore, they were more efficient than other nanomaterials as tumoral delivery platforms for cancer treatment.

Targeting diseased cells with ligand-modified particles has been investigated to enhance adsorption and uptake of nanoparticles on the target cells. However, some ligands also promote rapid clearance by phagocytes.[43,44] One of the plausible reductionist approaches is the use of peptides that specifically bind to the target cells while being stealthy to phagocytes so as to inhibit their clearance. In addition to the advantages of biocompatibility and affinity, peptides generally have better mechanical stability against light, heat, and shear stress. The rate of serum degradation of peptides can be readily controlled by substituting their enantiomers.[45] In addition, the side effects of peptides appear to be minimal according to the pharmacokinetic study by Khafagy and Morishita.[46]

2.1.3. Cell penetrating peptides (CPPs)

The hydrophobic nature of cellular membranes protects cells from an influx of exogenous compounds, including bioactive molecules such as peptides, proteins,

and oligonucleotides. Several strategies have been developed to deliver therapeutic agents across cellular membranes. These include electroporation, microinjection, liposomes and viral based vectors. However, these methods presented several drawbacks such as low efficiency, high toxicity, poor bioavailability or small specificity.

In the eighteens, it has been demonstrated that the trans-activator of transcription (TAT) protein of the Human Immunodeficiency Virus was able to efficiently enter tissue-cultured cells and promote the viral gene expression. Moreover, Antennapedia homeodomain, a transcription factor of *Drosophilia melanogaster*, was also shown to enter nerve cells and regulate neural morphogenesis. The interesting spontaneous entry of both proteins led to extensive structure/function studies to find the shortest amino acid sequence necessary for the uptake. This resulted in the identification of the first cell-penetrating peptides (CPPs): (i) ***TAT*** peptide, corresponding to the basic domain of HIV-1 TAT protein and (ii) ***penetratin***, corresponding to the third helix of the Antennapedia homeodomain.[47,48] TAT and penetratin served as the foundation for the development of a new type of molecular vectors able to promote the delivery of a variety of cargos.

CPPs are short peptides (generally not exceeding 30 residues) that have the capacity to cross cellular membranes with very limited toxicity, via energy-dependent and/or independent mechanisms, without the necessity of a chiral recognition by specific receptors. Most common CPPs are positively charged peptides even if the presence of few anionic or hydrophobic peptides was also demonstrated. A primary or secondary amphipathic character is also implicated but not strictly required for the internalization. According to their origin, we can distinguish three main classes of CPPs: (i) peptides derived from proteins, (ii) chimeric peptides that are formed by the fusion of two natural sequences, and (iii) synthetic CPPs which are rationally designed sequences usually based on structure–activity studies.

As more CPPs emerged, different research groups developed purely synthetic sequences that are also able to penetrate cells; in some cases, these are even more effective penetrators that protein-derived CPP sequences. These synthetic peptides have been developed using prediction programs, rational design strategies, or even trial and error. The membranolytic properties of a given CPP can also be governed by its secondary structure, specifically helicity. It has been shown that peptides with an R-helical region can more efficiently enter cells. Initially, CPPs were composed of only natural amino acids but recently, it is necessary to include nonprimarty and unnatural aminoacids to improve existing CPPs or to create new ones. For example, when lysine residues are replaced with ornithines, the peptide becomes more resistant to cellular degradation. [49]

Each modification must be carefully designed to avoid problems that could lead to low synthesis yields, poor solubility, aggregation, or toxicity. The need for further modifications arises when CPPs are used to deliver larger biomolecules (nucleic acids, proteins) inside cells. For example, *in vivo* delivery requires a longer drug circulation time, which in turn requires a more stable complex to form between the CPP and its cargo.

The common virtue of all CPPs is that they are able to efficiently pass through cell membranes while carrying a wide variety of cargos inside cells. Interestingly, CPP sequences are known to vary considerably with several similarities between the structural nature of these short peptides as can be seen in **Table 2.2**.

Table 2.2. Sequences of Common CPPs . Adapted from permission from Copolovici et al., ACS Nano, 2014, 8, 1972, Copyrigh © **2014**, American Chemical Society.

NAME	SEQUENCE	ORIGIN
TAT (48-60)	GRKKRRQRRRPPQ	Human immunodeficiency virus type 1 (HIV-1) TAT
Penetratin	RQIKIWFQNRRMKWKK	Drosophila Antannapedia homeodomain
MAP	KLALKLALKALKAALKLA[a]	Amphipathic model peptide
Transportan/ TP10	GWTLNS/AGYLLGKINLKALAALAKKIL[a]	Galanin-Lys-mastoparan
VP22	NAKTRHERRRKLAIER	Herpes simplex virus
Polyarginine	R_n[a], n=8.9	Positively charged sequence
Pep-1	KETWWETWWTEWSQPKKKRKV[b]	NLS from Simian Virus 40 large T antigen and reverse transciptas
MPG	GALFLGFLGAAGSTMGA[b]	A hydrophobic domain from the fusion sequecnce fo HIV gp41 and NLS of SV4
pVEC	LLILRRRIRKQAHAHSK[a]	VE-cadherin
YTA2	YTAIAWVKAFIRKLRK[a]	MMP cleavage site as seeding sequence
YTA4	IAWVKAFIRKLRKGPLG[a]	MMP cleavage site as seeding sequence
M918	MVTVLFRRLRIRRACGPPRVRV[a]	The tumor suppressor protein p14ARF
CADY	GLWRALWRLLRSLWRLLWRA[b]	Derived from PPTG1 peptide, W and charged aminoacids.

In recent years, a vast number of interdisciplinary studies report numerous applications for CPPs in the delivery of various cargos. The main characteristics of the CPPs are low cytotoxicity, their ability to be taken up by a variety of cell types, their dose-dependent efficiency, and no restriction with respect to the size or type of cargo. However, one of the major concerns about using CPPs as a delivery system deals with the fact that drug delivery must often be highly specific. This has also become a major issue in the design of CPPs because they tend to enter in

cells in a nonselective manner. The use of a specific drug alleviates this problem, but there are also ways to improve the delivery vector.

Studies in the cellular context mainly aim to follow the CPP and/or the cargo uptake, or to reveal the molecular mechanisms of the internalization. The methods used are generally indirect, based on fluorescence (and to a lesser extent on radiolabelling) or on the detection of the biological activity of the cargo.[50] Another method that enables direct quantification of the intact CPPs inside the cells or bound to the cellular membranes had been developed, based on matrix-assisted laser desorption-time of flight mass spectrometry (MALDI-TOF MS).[51] Changes in the membrane structure induced by CPPs and the peptides distribution in living cells were studied by electron microscopy. Also cell Raman spectroscopy was used to reveal the peptide secondary structure in the cellular compartments.[52]

Although numerous studies report on the uptake mechanisms that transport CPPs across the plasma membrane, the exact pathways through which CPPs enter cells have not been absolutely resolved.[53] Despite many similarities among CPPs, the mechanism of their uptake has been seen to vary considerably. Several mechanisms studies for CPP cellular entry could exist, and may even coexist, depending on several factors such as the physicochemical properties, concentration, charge, and length of the CPP and the type, size, and charge of the cargo molecule. However, as can be seen in **Figure 2.1** there are different proposed mechanisms for cellular internalization of CPPs: (i) the endocytosis-mediated pathway, (ii) the inverted micelle, (iii) the carpet-like mechanism, and (iv) the pore formation model.[54]

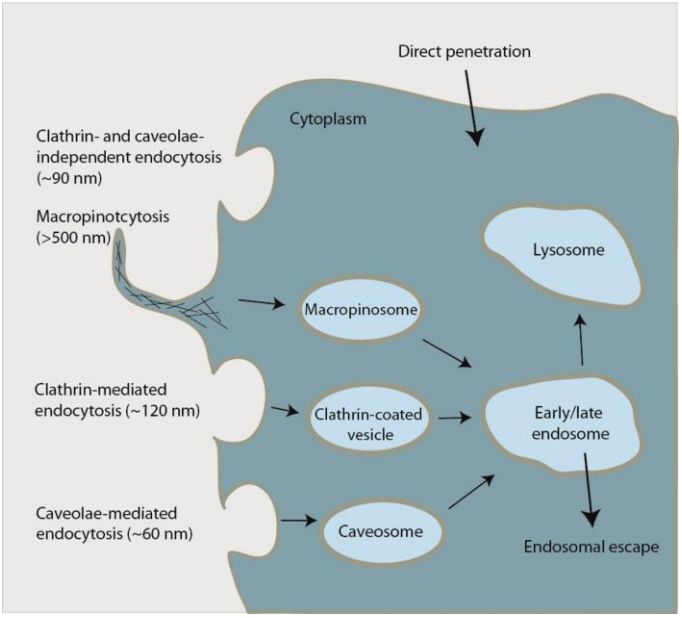

Figure 2.1. Uptake and release mechanisms of cell-penetrating peptides. Reprinted with permission from Copolovici et al., *ACS Nano*, **2014**, 8, 1972, Copyrigh © **2014**, American Chemical Society.

The ***endocytosis*** mechanism provides the major cellular uptake pathway for most CPPs. Although comprising two steps (endocytotic entry and endosomal escape), endocytosis may in fact involve several pathways. Among them are clathrin-mediated endocytosis, clathrin-independent endocytosis (such as endocytosis via lipid rafts or caveolae) and micropinocytosis. Although various endocytotic mechanisms result in the penetration of CPPs into cells, problems concerning the escape of CPPs from the endosomes persist. As an example, TAT fused to a large molecule will remain primarily in the endosomes, while TAT attached to a small cargo will be distributed in the cytoplasm. These differing outcomes indicate that the type and size of CPP cargo exerts an influence on its uptake pathway and distribution.[55]

The ***inverted micelle*** model of internalization was proposed by Professor Alain Prochiantz based on NMR studies of the interaction between penetratin and

phospholipid membranes. Although this model can explain the translocation for some CPPs (for example penetratin) it is not sufficient to explain the uptake of other TAT or polyarginine peptides, which do not contain the hydrophobic amino acids necessary for the translocation process.

In the ***carpet-like*** model, the internalization starts with the peptide binding with negatively charged phospholipids, and following this, the rotation of the peptide leads to interactions between the hydrophobic residues of the peptide and the hydrophobic core of the membrane. Lastly, a small disruption occurs in the lipid packing, which allows the internalization of the peptide.

The final proposed model for cellular translocation is the ***pore formation*** (barrel-stave) model, which results from the formation of bundles by amphipathic R-helical peptides. In this model, the outwardly facing hydrophobic residues of CPP interact with the lipid membrane and the inwardly facing hydrophilic surfaces forms a pore when the concentration of the peptide is higher than a certain concentration threshold, which is different for different peptides.

It is also possible that peptides may enter the cell by an unknown biological mechanism that works through interactions with other cell surface components, especially when the peptides exist in excessive concentrations. However, it is still a matter of debate which cell surface molecules act as potential electrostatic binding partners for CPPs and how they trigger or mediate their biological uptake.

CPPs are able to facilitate the intracellular delivery of covalently or noncovalently conjugated bioactive cargos. It has been reviewed the ability of CPPs for transport inside cells a variety of cargos such as nanoparticles,[56] peptides,[57] proteins,[58] antisense oligonucleotides,[59] small interfering RNA,[60] double stranded DNA,[61] and liposomes[62]. The transport of the smallest cargo to large proteins had been successfully carried out both *in vitro* and *in vivo*. For instance, activable CPPs (ACPPs) were recently employed *in vivo* to target cancer cells over-expressing metalloproteinase-2,[63] while treatment of various

inflammatory diseases was also effective *in vivo* by coupling the inhibitors to different CPPs. Taking this into account, Orange and May[64] developed a panel of CPP-linked inhibitors (CPP-Is) to directly inhibit nuclear factor kappa B (NF-κB). These transcription factors are activated by a range of stimuli including pro-inflammatory cytokines. Active NF-κB regulates the expression of genes involved in inflammation and cell survival and aberrant NF-κB activity plays pathological roles in certain types of cancer and diseases characterized by chronic inflammation. Remarkably, several of these NF-κB-targeting CPP-Is are effective *in vivo* and therefore offer exciting potential in the clinical setting. Tumor-targeting was also achieved *in vivo* for the (D)R8–doxorubicin conjugate.[65] Another *in vitro* study on mouse neuronal hypothalamic cells revealed that the *N*-terminal sequence derived from the prion protein could penetrate cells and disabled the formation of prions.[66]

To summarize, the ability of CPPs to cross the plasma membrane and deliver cargo to specific intracellular components provides a promising solution to problems commonly encountered in the delivery of conventional cancer chemotherapeutics. Although many preclinical studies now show promising results through the CPP-mediated delivery of small molecules, peptides, and oligonucleotides in treating cancer, no CPP-based therapeutic has yet gained FDA approval. Thus, further experimental studies are needed to decisively address several hurdles between current research efforts, FDA approval, and the achievement of CPP potential in the clinic. One drawback for CPP use lies in their short blood plasma half-life, owing to proteolysis and rapid renal and/or liver clearance. Pharmacokinetics and short blood plasma half-life can be improved by using unnatural amino acids and by coupling CPPs and drugs to macromolecular carriers, such as liposomes or biopolymers. Nonspecific CPP-mediated delivery to normal tissue, with subsequent adverse effects and toxicity, represents a further crucial barrier that would diminish CPP-mediated therapeutic efficacy. At this respect, different controlled delivery strategies using endogenous or extrinsic stimuli to selectively increase uptake of CPPs at the disease site has been extensively studied.

The promising results obtained in preclinical studies indicate that CPPs may have a significant role in the development of novel anticancer therapeutics. CPPs *effectiveness* in penetrating tissues and the cell membrane could offer a framework to enable the development of CPP-based therapeutics. Further investigations into the structure and mechanisms of uptake of CPPs cargo complexes will be required to evaluate its use as potential delivery tools for biomolecules in *in vitro* and *in vivo* models.[67]

2.1.4. Peptides as protease substrates

The genetic instructions for proteases account for about 2% of the human genome, and the pivotal roles that proteases play in regulatory pathways makes them useful as prognostic indicators and as important targets for a large number of existing drugs as well as drugs that are still under development.[68] Proteolysis is a simple hydrolytic cleavage of the amide bond between two adjacent amino acid residues catalyzed by proteases. Without the catalytic assistance of protease, protein hydrolysis would be a very slow process. Proteases play a key role in regulating many physiological conditions, and protease activity is dysregulated in many diseases, including cancer, diabetes and neurological disorders.[69]

To date, five major families of proteases have been described: serine, cysteine, metallo, aspartyl and threonine proteases (**Figure 2.2**). The most abundant are the serine and cysteine proteases, named bearing in mind the reactive nucleophilic groups in their active sites – the hydroxyl group in serine and thiol group in cysteine. Mechanistically, proteases could hydrolyze peptide bonds in the substrate (endopeptidases) or at the N or C termini (exopeptidases).[70]

An exopeptidase is any ***peptidase*** that ***catalyzes*** the cleavage of the terminal (or the penultimate) ***peptide bond***. This process releases a single ***amino acid*** or ***dipeptide*** from the peptidic chain. Depending on whether the amino acid is released from the N or the C terminal, an exopeptidase is further classified as an aminopeptidase or a carboxypeptidase, respectively.

Cancer associated proteases (CAPs) have gained attraction recently as a new method of tumour targeting. CAPS are a set of proteases that are usually absent from or at very low concentrations in healthy tissues but are often highly up-regulated in cancerous tissues. Some of extensively studied CAPs include urokinase plasminogen activator (uPA), certain MMPs, and some of the capthepsins. [71]

Deeveloping a prodrug, a drug delivery system, or an imaging agent that could be cleaved and activated by CAPs could be a workable method for targeting drugs/imaging agents to tumor sites. Development of "smart" biomaterials by exploiting increased endoprotease activity at disease sites is an area of drug development showing great promise. Indeed, discoveries of a wide variety of cellular signaling pathways related with disease-associated proteases have already led to the development of numerous prodrugs, functional biomaterials (including nanoparticles), and imaging probes. Generally, such pharmacophores and/or imaging probes are restrained or masked by various carefully-designed mechanisms. Then, proteolysis by target proteases releases or unmasks the active ingredients producing the desired therapeutic activity or imaging sensitivity *in situ*. Furthermore, as proteolysis is a catalytic reaction, one protease could potentially release a large number of active ingredients. Therefore, it could amplify signal outputs and improves detection limits significantly for diseases detection and diagnosis. In addition to improving tumor-selective delivery of cancer therapeutics or imaging probes, these protease-sensitive nanodevices could reduce their undesired activity/signal in normal tissues, including liver, heart and bone marrow. Despite the advantages and promises shown by protease-responsive nanodevices, some issues remains unresolved for future development and clinical use. Since disease-associated protease activities vary by individual and by stage of disease, greater understanding is required of targeting protease structures, mechanisms, distribution, and regulation *in vivo*.

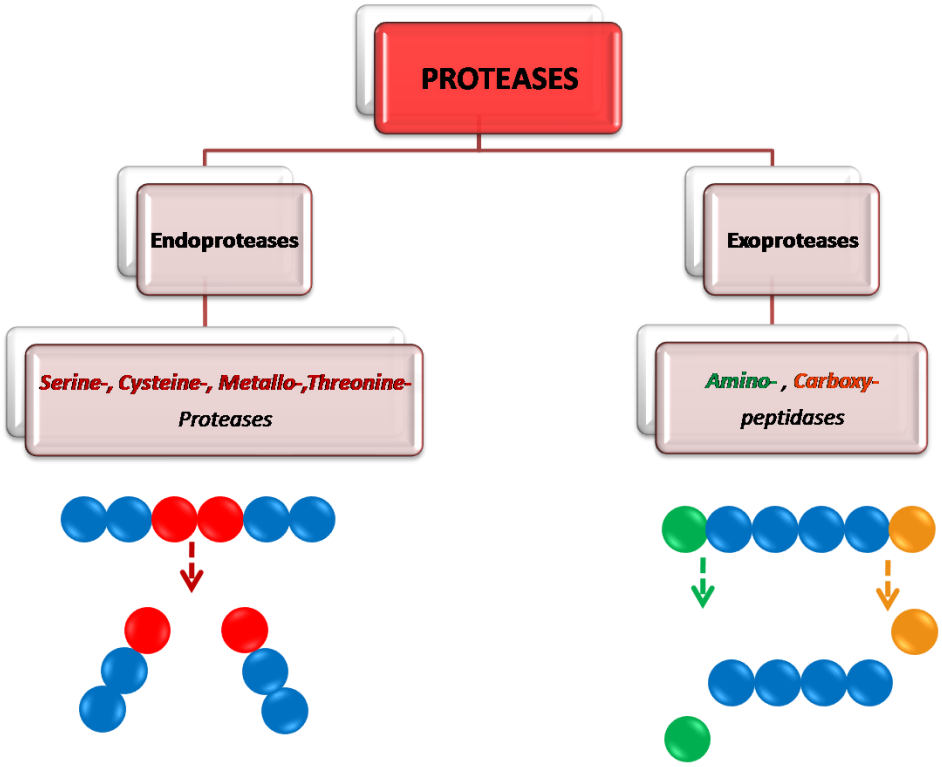

Figure 2.2. Schematic representation of proteases and their catalytic properties.

2.1.4.1. Serine proteases

Serine proteases, a type of endoproteases, are involved in an enormous number of biological processes. In every type of organism that scientists examine, they continue to discover new enzymes belonging to this group. These enzymes are powerful as they digest our food, help our blood clot, fight infections, and help sperm enter eggs. Besides, proteases also regulate the development of organisms and degrade flesh after a snake bite.[72] In humans, they are prevalent in many physiological functions, both normal and disease-related.[73]

Neutrophil serine proteases (NSPs) of primary granules are some of the most abundant serine proteases present in almost all organism. The NSPs family includes neutrophil elastas (NE), Cathepsin G, proteinase 3 (PR3) and neutrophil

serie proteinase 4 (NSP4). NSPs are involved in many diseases, particularly associated with the lungs; thus, they are considered valuable drug targets.

Human granzyme (Gr) are closely related protease with a nucleophilic serine residue stabilized by histidine and aspartic acid at the enzyme's active site and are expressed in cytotoxic T lymphocytes and natural killer (NK) cells. Those protesases are packet into cytoplasmic granules and are secreted during stimulation.

The human tisusue kallikrein family comprises at least 15 serine proteases which are enconded by the largest protease gene cluster and are expressed in almost every tissue, including brain, breast and skin, among others.

2.1.4.2. Cysteine proteases

Cysteine proteases, also known as thiol proteases, share a common ***catalytic mechanism*** that involves a ***nucleophilic cysteine thiol*** in ***a catalytic triad*** or dyad. Cysteine proteases are commonly encountered in fruits including the papaya, pineapple, fig and kiwi. In fact, dozens of latices of different plant families are known to contain cysteine proteases. Cysteine proteases are used as an ingredient in ***meat tenderizers***.

Caspases are cysteine proteases that display very narrow preferences at the P1 (amino acid residues in a substrate undergoing cleavage are designated P1, P2, P3, P4 etc. in the N-terminal direction from the cleaved bond. Likewise, the residues in C-terminal direction are designated P1', P2', P3', P4') position primarily recognizing aspartic acid (with some exceptions). Such primary specificity is quite rare among proteases. However, Wells and co-workers have recently shown that these enzymes can also cleave substrates after glutamic acid and phosphoserine residues, shedding new light on their physiological functions.[74] Since the discovery and characterization of caspases 20 years ago, hundreds of papers have been published on their substrates and inhibitors. Unfortunately, their exclusive

specificity for aspartic acid at the P1 position greatly difficults its identification.[75]. Based on these profiles, caspases were divided into three groups: caspase-1, -4 and -5, which prefer the (W/L)EHD sequence, caspase-3, -7 and -2, which recognize DE(V/H)D peptides, and caspase-6, -8 and -9, which favor (V/L)EHD motifs. Nevertheless, the specificity matrix clearly shows that these proteases display overlapping substrate specificity, and the 'optimal sequences' proposed by the authors may not be specific for only one enzyme. Because potent and selective caspase inhibitors appear as potential drug candidates, this area of research has been explored more rigorously than the identification of caspase substrates. To date, thousands of caspase inhibitors have been synthesized and evaluated. Some caspase inhibitors have been synthesized and used to study apoptosis *in vitro* and *in vivo*, whereas others are primarily used in pharmaceutical research.[76]

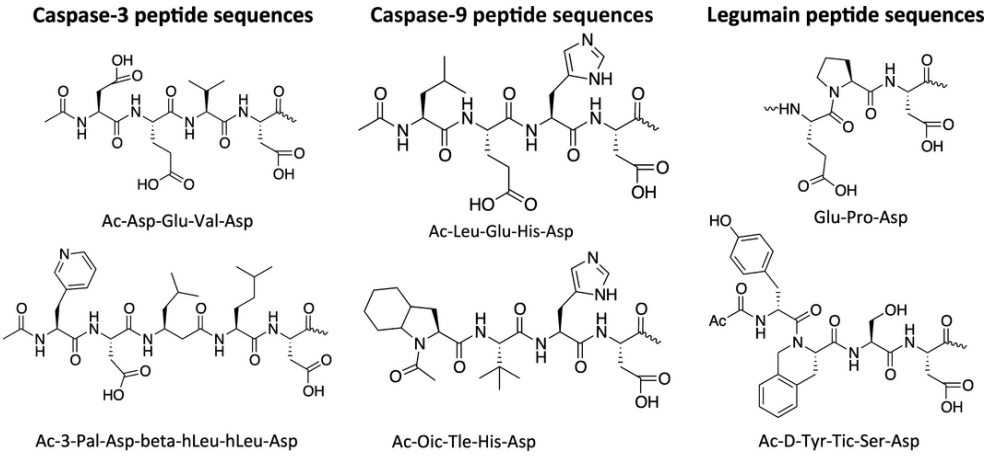

Figure 2.3. Examples of specific peptide sequences used in substrates and inhibitors for cysteine proteases. Reprinted with permission from P. Kasperkiewicz et al., Copyright © *The FEBS Journal* **2017** Federation of European Biochemical Societies.

Mammalian cysteine proteases form a diverse group of proteolytic enzymes characterized by an active site cysteine residue. They can be localized in the lysosome (*cathepsins* B, L, H and S) or the cytosol (*calpains*), and are secreted in some cell types under pathological conditions. Mammalian cysteine proteases mediate general functions such as intracellular protein catabolism and specialized

functions such as selective activation of signalling molecules (interleukin, enkephalin, protein kinase C) or extracellular protein degradation (bone resorption, macrophage function). A great number of reports have shown a correlation between the activity of lysosomal cysteine proteases and tumor progression. The family of cathepsin cysteine proteases can degrade both intracellular and extracellular matrix (ECM) proteins. The action of cathepsins is regulated by the equilibrium between their endogenous inhibitors and activation of their inactive forms.[77] Cathepsins have been shown to function intracellularly as well as extracellularly, which puts them in a unique position that contrasts with most other proteases such as metalloproteases or serine proteases.[78]

Cathepsin B was the first lysosomal protease to be associated with breast carcinoma.[79] Early reports indicating a link between cathepsin B and cancer. These reports showed that the protease is released from malignant human breast tumor explants and is found in the serum of patients with neoplastic vaginal lesions. Cathepsin B has been actually shown to participate in the dissolution and remodeling of connective tissue and basement membrane in the processes of tumor growth, invasion, and metastasis[80] by podosomemediated extracellular matrix degradation and invasion via secreted lysosomes.[81] Increased levels of cathepsins B and L in tumors or in some extracellular fluids are associated with the disease-free and overall survival periods and may therefore serve as prognostic factors for cancer patients.[82] In addition, cathepsins are useful markers for identifying patients who are suffering from breast cancer, colorectal cancer, tongue carcinoma and pancreatic cancer. Elevated levels of other lysosomal proteases, such as cathepsins H, L, or S have also been reported in many cancer types.[83]

Calpains are cytosolic calcium-dependent cysteine proteases composed of one or two subunits. Calpain cleavage sites are not sequence-specific, and tertiary structure elements rather than primary amino acid sequences seem to be responsible for directing cleavage to a specific site. A broad range by proteins can be cleaved by calpain, including cytoskeletal proteins such as α-fodrin, ion

channels, growth factor receptors and adhesion molecules. Calpain activation has been implicated in neuronal apoptosis in ischemic brain injury and neurodegenerative diseases such as Alzheimer's.

Legumain is a cysteine protease that is up-regulated in inflammatory diseases and multiple human cancers. Legumain is also very active in the tumor microenvironment; thus, it is thought to promote tumorigenesis.

2.1.4.3. Aspartyl proteases

Aspartyl proteases form a group of enzymes that consist of two lobes separated by a cleft containing the catalytic site made up of two aspartate residues. Some examples of the aspartyl proteases are pepsins, cathepsins (D and E) and renins. The aspartic protease cathepsin D, a marker of poor prognosis in breast cancer,[84] is overexpressed and secreted at high levels by human epithelial breast cancer cells.[85] Cathepsin D stimulates cancer cell proliferation, fibroblast outgrowth, angiogenesis and metastasis.[86]

2.1.4.4. Threonine proteases

Threonine proteases (proteasomes) have the task of eliminating cellular proteins, tagged for degradation through a complex modification termed polyubiquitinization. This process consist in the addition of a series of ubiquitin molecules to a protein targeted for degradation.[87] Although the mechanisms are not fully elucidated, it is clear that proteasome inhibition can promote degradation of anti-apoptotic proteins and prevent degradation of proapoptotic proteins, resulting in programmed cell death in malignant cells.

2.1.4.5. Metalloproteinases

MMPs include the 23 members of the zinc-dependent endopeptidase family in the metzincin class of metalloendopeptidases that share a common domain structure.[88] The most common classification of MMPs is based on the historical assessment of their catalytic preferences and their cellular localization. Therefore, one can distinguish four groups of MMPs: collagenases, gelatinases, stromelysins and membrane-type MMPs. Nevertheless, there are several MMPs that are not classified into these traditional groups.[89]

Over the last years, the relevance of MMPs family in cancer research has grown considerably. These enzymes were initially associated with the invasive properties of tumour cells, owing to their ability to degrade all major protein components of the extracellular matrix and basement membranes. Moreover, further studies have demonstrated the implication of MMPs in early steps of tumour evolution, including stimulation of cell proliferation and modulation of angiogenesis.[90] MMPs allows local expansion of the tumor mass through the disruption of normal tissue structure and facilitates invasion of blood vessels and lymphatics by metastatic cells, thus promoting tumor spread. MMPs secretion and activation seems to result from a specific interaction between tumour and stromal cells.[91] The breakdown of tissue architecture, mediated by these activated enzymes, allows the primary tumour to expand, invade the neighbouring blood vessels and spread to distant sites in the body. Invasive growth in these secondary sites also appears to be facilitated by the action of MMPs.[92] MMPs induction mechanisms appear to be different depending on the characteristics of the diverse cells, with ability to produce these enzymes. A wide variety of agents, including cytokines, growth factors and oncogene products, cause spatial and temporal variations of MMPs expression.

2.1.5. Therapeutic role of peptides

More than 7000 naturally occurring peptides have been identified, and these often have crucial roles in human physiology, including actions as hormones, neurotransmitters, growth factors, ion channel ligands, or anti-infectives.[93,94] In general, peptides are selective and efficacious signaling molecules that bind to specific cell surface receptors, such as G protein-coupled receptors (GPCRs) or ion channels, where they trigger intracellular effects. Given their attractive pharmacological profile and intrinsic properties, peptides represent an excellent starting point for the design of novel therapeutics and their specificity has been seen to translate into excellent safety, tolerability, and efficacy profiles in humans. This aspect might also be the primary differentiating factor of peptides compared with traditional small molecules. Furthermore, peptide therapeutics are typically associated with lower production complexity compared with protein-based biopharmaceuticals and, therefore, the costs are also lower, generally approaching those of small molecules. Thus, in several ways, peptides are in the sweet spot between small molecules and biopharmaceuticals. Naturally occurring peptides are often not directly suitable for use as convenient therapeutics because they have intrinsic weaknesses, including poor chemical and physical stability, and a short circulating plasma half-life. These aspects must be addressed for their use as drugs. Some of these weaknesses have been successfully resolved through what we term the 'traditional design' of therapeutic peptides. Besides traditional peptide design, a range of peptide technologies has been emerging that represent the opportunities and future directions within the peptide field. These include multifunctional and CPPs, as well as peptide drug conjugates and technologies focusing on alternative routes of administration. All the above mentioned facts lead to the conclusion that peptides offer enormous growth potential as future therapeutics. During the past decade, peptides have gained a wide range of applications in medicine and biotechnology, and therapeutic peptide research is also currently experiencing a renaissance for commercial reasons. For example, the peptide-based medicine LupronTM from Abbott Laboratories (for the treatment of prostate cancer) achieved global sales of more

than US$ 2.3 billion in 2011[95]. In addition, LantusTM from Sanofi (which is really at the border between a peptide drug and a small biopharmaceutical) reached sales of US$ 7.9 billion in 2013. Currently, there are more than 60 US Food and Drug Administration-approved peptide medicines on the market and this is expected to grow significantly, with approximately 140 peptide drugs currently in clinical trials and more than 500 therapeutic peptides in preclinical development. An overview was presented in a recent review by Kaspar and Reichert.[95]

The main disease areas currently driving the therapeutic use of peptide drugs are metabolic diseases and oncology. The former can be characterized by the epidemic growth in both obesity and type 2 diabetes mellitus (T2DM) , the latter by a rising mortality and need for chemotherapy replacement, as well as cancer supportive care. The use of peptide therapeutics in the treatment of diabetes and obesity is probably why North America currently represents the largest share of the peptide drug market, with the Asian market expected to have the largest growth. The movement of the pharmaceutical industry into rare diseases and orphan drugs has also been extended to peptides, and marketed examples in this area include teduglutide, a GLP-2 receptor agonist for short bowel syndrome, and pasireotide, a somatostatin receptor agonist for the treatment of Cushing's syndrome. Moreover, there seems to be a current trend towards the areas of infectious diseases and inflammation, where several peptides are undergoing clinical testing. Currently, most peptide drugs are administered by the parental route and approximately 75% are given as injectables. However, alternative administration forms are gaining increasing a traction, including oral, intranasal, and transdermal delivery routes, according to the respective technology developments.[96] One example of an alternative administration route evaluated for application to peptides is the transbuccal delivery via the combination of gold nanoparticles (Midatech) and the PharmFilmTM (Monosol Rx) technology. Accordingly, Midasol Therapeutics is currently carrying out clinical development of a transbuccal delivery system that utilizes insulin-passivated gold glyconanoparticles.[97] Another example is the TopActTM technology platform from ActoGeniX, which might enable oral delivery of peptides directly expressed

in the gastrointestinal tract.[98] The use of alternative administration forms could also enable greater usage of peptide therapeutics in other disease areas, such as inflammation, where topical administration of peptides could be the basis for highly efficacious novel treatments. Also, peptides are often excellent biomarkers and, therefore, can also be used for diagnostic purposes.[99] Finally, peptides have also found an application as vaccines.

The development of multifunctional peptides could present a challenge in the sense that the prediction of the *in vivo* outcome for the drug candidates is more complex with dual versus single target pharmacology. One challenging aspect of the translation from *in vitro* to *in vivo* effects is the potential biased signaling that might arise from novel ligands aimed at two or more receptors.[100] Most peptide therapeutics are injectables and there are only a few oral peptide drugs in existence, cyclosporine (NeoralTM) and desmopressin (MinirinTM) being prominent examples. However, it is expected that the market will see an increase in orally bioavailable peptides in development because they offer greater convenience for patients. The challenges relating to development of oral peptides include acidic and enzymatic degradation of the molecules in both the gastrointestinal tract, and when crossing the intestinal mucosa via either active transport or passive diffusion.

Native peptides in general do not cross cell membranes, which has previously limited their therapeutic use to extracellular targets. However, over recent years, technologies have been invented for the insertion of membrane permeability elements, including CPPs, such as penetratin or the TAT sequences, making it possible to reach intracellular targets with peptides to some degree. One challenge of CPPs, which is likely to be also shared by orally bioavailable peptides, is a probable loss of efficacy because usually only a fraction of the peptide drug reaches the target. Another important aspect to consider when developing CPPs is whether their molecular properties resemble those of small molecules more, including lower specificity and, therefore, greater safety risk because of an increased volume of distribution.

2.2. References

1. A) E.Ruoslahti, N.B.Sangeeta, M.J. Sailor, *J. Cell Bio.* **2010**,*188*, 759. B) T.Teesalu, K.N. Sugahara, E.Ruoslahti, T.Teesalu, Kazuki N. Sugahara, Erkki Ruoslahti, *Front. Oncol.* **2013**, *216*, 1. c) S. Farkona, E.P. Diamandis, I. M. Blasutig, *BMC Medicine* **2016**, *14*, 73.

2. J.C. Reubi, *Endocrine Reviews* **2003**, *24*, 389.

3. G.P. Smith, V.A. Petrenko, *Phage Display. Chem Rev.* **1997,** *97*, 391.

4. E. Koivunen, W. Arap, D. Rajotte, J. Lahdenranta, R. Pasqualini, *J Nucl Med*. **1999**, *40*, 883.

5. E. Koivunen, B. Wang, E. Ruoslahti, *Nat Biotechnol*. **1995**, *13*, 265.

6. R. Pasqualini, E. Koivunen, E. Ruoslahti, *Nat Biotechnol*. **1997**, *15*, 542.

7. J. Doorbar, G. Winter, *J Mol Biol*. **1994**, *244*, 361.

8. T. Oyama, K.F. Sykes, K.N. Samli, J.D. Minna, S.A. Johnston, K.C. Brown, *Cancer Lett.* **2003**, *202*, 219.

9. M. J. McGuire, K.N. Samli, S.A. Johnston, K.C. Brown, *J Mol Biol.* **2004**, *342*, 171.

10. K. N. Samli, M.J. McGuire, C.B. Newgard, S.A. Johnston, K.C. Brown, *Diabetes.* **2005**, *54*, 2103.

11. T. K. Gartner, J.S. Bennett, *J. Biol. Chem.* **1985,** *260*, 11891.

12. P.J. Brown, R.L. Juliano, *Science* **1985**, *228*, 1448.

13. M.A. Schwartz, M.D. Schaller, M.H. Ginsberg, *Annu. Rev. Cell Dev. Biol*. **1995**, *11*, 549.

14. D. Taverna, D. Crowley, M. Connolly, R.T. Bronson, R.O. Hynes, *Cancer Res.* **2005**, *65*, 10324.

15. C. J. Avraamides, B. Garmy-Susini, J.A. Varner, *Nat. Rev. Cancer* **2008**, *8*, 604.

16. A) Q. Chen, C. Manning, H. Millar, F. McCabe, C. Ferrante, C. Sharp, L. Shahied-Arruda, P. Doshi, M. Nakada,G.M. Anderson, *Clin. Exp. Metastasis* **2008**, *25*, 139. B) W. Guo, F.G. Giancotti, *Nat. Rev. Mol. Cell Biol*. **2004**, *5*, 816.

17. D. Cox, M. Brennan, N. Moran, *Nat. Rev. Drug Discov.* **2010**, *9*, 804.

18. K. Chen, X. Chen, *Theranostics* **2011**, *1*, 189.

19. F. Danhier, B. Vroman, N. Lecouturier, N. Crokart, V. Pourcelle, H. Freichels, C. Jérôme, J. Marchand, J. Brynaert, O. Feron, V. Préat, *J. Control. Release* **2009**, *140*, 166.

20. Y. Wu, X. Zhang, Z. Xiong, Z. Cheng, D.R. Fisher, S. Liu, S.S. Gambhir, X. Chen, *J. Nucl. Med.* **2005**, *46*, 1707.

21. P. Hölig, M. Bach, T. Völkel, T. Nahde, S. Hoffmann, R. Müller, R.E. Kontermann, *Protein Eng. Des. Sel.* **2004**, *17*, 433.

22. K.N. Sugahara, T. Teesalu, P.P. Karmali, V.R. Kotamraju, L. Agemy, D.R. Greenwald, E. Ruoslahti, *Science* **2010**, *328*, 1031.

23. M.A. Dechantsreiter, E. Planker, B. Mathä, E. Lohof, G. Hölzemann, A. Jonczyk, S.L. Goodman, H. Kessler, *J. Med. Chem.* **1999**, *42*, 3033.

24. G. Tabatabai, M. Weller, B. Nabors, M. Picard, D. Reardon, T. Mikkelsen, C. Ruegg, R. Stupp, *Oncol.* **2010**, *5*, 175.

25. C. Leuschner, F.M. Enright, B. Gawronska–Kozak, W. Hansel, *Prostate* **2003**, *56*, 239.

26. J.-L. Schlick, P. Dulieu, B. Desvoyes, P. Adami, J. Radom, M. Jouvenot, *FEBS Lett.* **2000**, *472*, 241.

27. S.S. Dharap, B. Qiu, G.C. Williams, P. Sinko, S. Stein, T. Minko, *J. Control. Release* **2003**, *91*, 61.

28. X.Q. Ji, X.J. Ruan, H. Chen, G. Chen, S.Y. Li, B. Yu, *Med. Sci. Monit*. **2011,** *17*, RA169.

29. R. Mazzucchelli, D. Morichetti, A. Santinelli, M. Scarpelli, *Cell Oncol***. 2011**, *34*, 235.

30. M. De Jong, W.A. Breeman, D.J. Kwekkeboom, R. Valkema, E.P. Krenning, *Acc. Chem. Res*. **2009**, *42*, 873.

31. Y. Menda, D.Kahn, Semin. *Nucl. Med.* **2002**, *32*, 92.

32. L.C. Sun, D.H. Coy, *Curr. Drug Deliv*. **2011**, *8*, 2.

33. A) J.C. Reubi, S. Wenger, J. Schmuckli-Maurer, J.-C. Schaer, M.Gugger, *Clin.Cancer Res.* **2002**, *8*, 1139. B) R.T. Jensen, J.F. Battey, E.R. Spindel, R.V.Benya, *Pharmacol. Rev.* **2008***, 8*, 1139.

34. T.W. Moody, D.N.Carney, F.Cuttitta, K.Quattrocchi, J.D.I. Minna, *Life Sci.***1985,** *37*, 105.

35. T.W. Moody, L.C. Sun, S.A. Mantey, T. Pradhan, L.V. Mackey, N. Gonzales, J.A. Fuselier, D.H. Coy, R.T. Jensen, *J Pharmacol Exp Ther.* **2006**, *318*, 1265.

36. J. Drappatz, A. Brenner, E.T. Wong, A. Eichler, D. Schiff, M.D. Groves, T. Mikkelsen, S. Rosenfeld, J. Sarantopoulos, C.A. Meyers, R.M. Fielding, K. Elian, X. Wang, B. Lawrence, M. Shing, S. Kelsey, *Clin. Cancer Res.* **2013,** *19*, 1567.

37. F. Elamrawy, A.A. Othman, C. Adkins, A. Helmy, M.I. Nounou, *J. Cancer Metastasis Treat*. **2016**, *2*, 112.

38. Y. Gilad, M. Firer, G.Gellerman, *Biomedicines* **2016**, *4*, 11.

39. A. Regina, M. Demeule, S. Tripathy, S. Lord-Dufour, J.C. Currie, M. Iddir, B. Annabi , J.P. Castaigne, J.E. Lachowicz, *Mol Cancer Ther.* **2015**, *14*, 129.

40. S. Ghanaati, M.J. Webber, R.E. Unger, C. Orth, J.F. Hulvat, S.E. Kiehna, M. Barbeck, A. Rasic, S.I. Stupp, C.J. Kirkpatrick, *Biomaterials* **2009**, *30*, 6202.

41. V. Jayawarna, M. Ali, T.A. Jowitt, A.E. Miller, A. Saiani, J.E. Gough, R.V. Ulijn, *Adv. Mater*. **2006**, *18*, 611.

42. A. Wagh, J. Singh, S. Qian, B. Law, *Nanomedicine* **2013**, *9*, 449.

43. J.V. Jokerst, T. Lobovkina, R.N. Zare, S.S. Gambhir, *Nanomedicine* **2011**, *6,* 715.

44. W.T. Lim, E.H. Tan, C.K. Toh, S.W. Hee, S.S. Leong, PC.S. Ang, N.S. Wong, B. Chowbay ,*Ann Oncol* **2010**, *21*, 382.

45. I. Nakase, Y. Konishi, M. Ueda, H. Saji, S. Futaki, *J Control Release* **2012**, *159*. 181.

46. E.S. Khafagy, M. Morishita, *Adv Drug Deliv Rev* **2012**, *64*, 531.

47. F. Heitz, M.C. Morris, G. Divita, *Br. J. Pharmacol.* **2009**, *157*, 195.

48. Ü. Langel, Handbook of Cell-Penetrating Peptides, 2nd ed.; CRC Press: Boca Raton, FL, **2007**.

49. K. Ezzat, S. El Andaloussi, E.M. Zaghloul, T. Lehto, S. Lindberg, P.M.D. Moreno, J.R. Viola, T. Magdy, R. Abdo, P. Guterstam, R. Sillard, S.M. Hammond, M.J. Wood, A.A. Arzumanov, M.J. Gait, C.I. SmithI, M. Hällbrink, Ü. Langel. *Nucleic Acids Res.* **2011**, *39,* 528.

50. T. Holm, S.E. Andaloussi, U. Langel, *Methods Mol. Biol.* **2011**, *683*, 207.

51. F. Burlina, S. Sagan, G. Bolbach, G. Chassaing, *Nat. Protoc.* **2006**, *1*, 200.

52. H. Hirose, T. Takeuchi , H. Osakada, S.Pujals, S. Katayama, I. Nakase, S. Kobayashi, T. Haraguchi , S.Futaki, *Mol. Ther*. **2012,** *20*, 984.

53. S.B. Fonseca, M.P. Pereira, S.O. Kelley, *Adv. Drug Delivery Rev.* **2009**, *61*, 953.

54. D.M. Copolovici, K. Langel, E. Eriste, Ü.Langel, *ACS Nano*, **2014**, *8*, 1972.

55. A) I.A. Khalil, K. Kogure, S. Futaki, H. Harashima, J Biol Chem. **2006**, *281*,3544. B) I.M. Kaplan, J.S. Wadia, S.F. Dowdy, *J Control Release.* **2005,** *102*, 247. C) J.S. Wadia, R.V. Stan, S.F. Dowdy, *Nat Med.* **2004**, *10*, 310. D) M. Fretz, J. Jin, R. Conibere, N.A. Penning,S. Al-Taei, G. Storm, S. Futaki, T. Takeuchi, I. Nakase, A.T. Jones, *J Control Release*. **2006**, *116*, 247.

56. B. Gupta, T.S. Levchenko, V.P. Torchilin, *Adv. Drug Deliv. Rev.* **2005**, *57*, 637.

57. G.P. Dietz, M. Bahr, *Mol. Cell Neurosci.* **2004**, *27*, 85.

58. A) M. Mae, U. Langel, *Curr. Opin. Pharmacol.* **2006**, *6*, 509. B) T. Lehto, K. Kurrikoff, U. Langel, *Drug Deliv.* **2012**, *9*, 823.

59. P. Jarver, K. Langel, S. El-Andaloussi, U. Langel, *Biochem. Soc. Trans*. **2007**, *35*, 770.

60. B.R. Meade, S.F. Dowdy, *Adv. Drug Deliv. Rev.* **2008**, *60*, 530.

61. Y. Wu, X. Yao, Y. Chen, Y. Li, W. Tian , *Biomed Mater Eng*. **2017**, *28*, 255.

62. H. Gao, Q. Zhang, Z. Yu, Q. He, *Curr Pharm Biotechnol.* **2014**, *15*, 210.

63. E.S. Olson, T.A. Aguilera, T. Jiang, L.G. Ellies, Q.T. Nguyen, E.H. Wong, L.A. Gross, R.Y. Tsien, *Integr. Biol.* **2009**, *1*, 382.

64. J.S. Orange, M. May, *J. Cell. Mol. Life Sci.* **2008**, *65*, 3564.

65. I. Nakase, Y. Konishi, M. Ueda, H. Saji, S. Futaki, *J. Control Release* **2012**, *159*, 181.

66. K. Löfgren, A. Wahlström, P. Lundberg, Ü. Langel, A. Gräslund, K. Bedecs, *FASEB J*. **2008**, *22*, 2177.

67. V. Sebbage, *Biosci. Horizons* **2009**, 2, 64, B) J. Regberg, A. Srimanee, Ü. Langel, *Pharmaceuticals* **2012**, *5*, 991.

68. C. Seife, *Science* **1997,** 277, 1602.

69. M. Drag, G.S. Salvesen, *Nat Rev Drug Discov* **2010**, *9*, 690.

70. N.D. Rawlings, D.P.Tolle, A.J.Narrett, *Nucleic Acids Res* **2004**, *32*, 160.

71. X.-X. Zhang, H.S. Eden, X. Chen, *J Control Release* **2012**, *159*, 2.

72. M.M. Krem, T. Rose, E. Di Cera, *Trends Cardiovasc Med.* **2000**, *10*, 171.

73. S. Rakashanda, F. Rana, S. Rafiq, A. Masood, S. Amin, *Biotechnology and Molecular Biology Review* **2012**, *7*, 90.

74. J.E. Seaman, O. Julien, P.S. Lee, T.J. Rettenmaier, N.D. Thomsen, J.A. Wells, *Cell Death Differ* **2016**, *23*, 1717.

75. M.Poreba, A. Strozyk, G.S. Salvesen, M. Drag, *Cold Spring Harb Perspect Biol* **2013**, *5*, a008680.

76. J. Kudelova, J. Fleischmannova, E. Adamova, E. Matalova, *J Physiol Pharmacol*. **2015**, *66*, 473.

77. M. Abrahamson, M. Alvarez-Fernandez, C.M. Nathanson, *Biochem Soc Symp* **2003**, *70*, 179.

78. M.L. Biniossek, D.K. Nagler, C. Becker-Pauly, O. Schilling, *J Proteome Res* **2011**, *10*, 5363.

79. A.R. Poole, K.J. Tiltman, A.D. Recklies, T.A.M. Stoker, *Nature* **1978**, *273*, 545.

80. J.A.Joyce, D. Hanahan, *Cell Cycle* **2004**, *3*, 1516.

81. C. Tu, C.F. Ortega-Cava, G. Chen, N.D. Fernandes, D. Cavallo-Medved, B.F. Sloane, V. Band, H. Band, *Cancer Res*. **2008**, *68*, 9147.

82. N. Koshikawa, S. Hasegawa, Y. Nagashima, K. Mitsuhashi, Y. Tsubota, S. Miyata , *Am. J. Pathol.* **1998**, *153*, 937.

83. N. Fujise, A. Nanashima, Y. Taniguchi, S. Matsuo, Y. Hatano Matsumoto, Y. Tagawas, H. Ayabe, *Lung Cancer* **2000**, *27*,19.

84. A) B.R. Westley, F.E. May, *Br. J. Cancer* **1999**, *79,* 189. B) J. Rodriguez, J. Vazquez, M.D. Corte, M. Lamelas, M. Bongera, *Int. J. Biol. Markers* **2005**, *20*, 103.

85. A) A. Vashishta, S.S. Ohri, V. Vetvicka, *Endocr. Metab. Immune. Disord. Drug Targets* **2009**, *9*, 385. , B) G. Nicotra, R. Castino, C. Follo, C. Peracchio, G. Valente, Cancer. Biomark. **2010**, *7*, 47, C) O. Masson, P. Christine, D.Danielle, M.Aline, C.Dray, Q.Didier, V.Philippe, M.Catherine, E.Liaued-Coopman, *PLos ONE* **2011**, *6*, 16452.

86. A) A. Vashishta, S.S. Ohri, M. Proctor, M. Fusek, V. Vetvicka, *Int. J. Oncol.* **2007**, *30*, 1223. B) S.S. Ohri, A. Vashishta, M. Proctor, M. Fusek, V. Vetvicka , *Int. J. Oncol.* **2008**, *32*, 491.

87. B.S. Mitchell, NEJM Perspective **2003**, *348*, 2597.

88. U. Eckhard, P.F. Huesgen, O. Schilling, C.L. Bellac, G.S. Butler, J.H. Cox, A. Dufour, V. Goebeler, R. Kappelhoff, U.A.D. Keller, T.Klein, P.F.Lange, G. Marino, C.J. Morrison, A. Prudova, D. Rodriguez, A.E. Starr, Y. Wang, C.M. Overall, *Matrix Biol* **2016**, *49*, 37.

89. A.R. Folgueras, A.M. Pendas, L.M. Sanchez, C. Lopez-otin, *Int. J. Dev. Biol.* **2004**, *48*, 411.

90. A) B.S. Nielsen, F. Rank, J.M. Lopez, M. Balbin, F. Vizoso, L.R. Lund, K. Dano, C. Lopez-otin *, Cancer. Res.* **2001**, *61*, 7091. B) O. De Wever, M. Mareel, *J. Pathol.* **2003**, *200*, 429.

91. D.R. Bonfil, M.L. Cher, IBMS BoneKEy **2011**, *8*, 16.

92. X.-X. Zhang, H.S. Eden, X. Chen, *J Control Release*. **2012**, *159*, 2.

93. A. Padhi, M. Sengupta, S. Sengupta, K.H. Roehm, A. Sonawane, Tubercolosis **2014**, *94*, 363.

94. C.Giordano, M. Marchiò, E. Timofeeva, G. Biagini, *Front.Neurol.* **2014**, *5*, 1.

95. A.A. Kaspar, J.M. Reichert, *Drug Discov. Today* **2013**, *18*, 807.

96. Transparency Market Research, **2012.** Peptide Therapeutics Market: Global Industry Analysis, Size, Share, Growth, Trends and Forecast 2012–2018. Transparency Market Research.

97. C. Sheridan*, Nat. Biotechnol*. **2012**, *30*, 471.

98. L. Steidler, P.Rottiers, B.Couline*., Ann. N. Y. Acad. Sci.* **2009**, *1182*, 135.

99. I. Schulte, H. Tammen, H.Selle, P.Schultz, Expert Rev. Mol. Diagn. **2005**, *5*, 145.

100. L. Zhou, L.M. Bohn, *Curr. Opin. Cell Biol.* **2014**, *27*, 102.

2.3 Objectives

As reported above, our aim, in this part of the PhD thesis, was the design and synthesis of new systems for the controlled release of molecules with possible future application in nanomedicine.

The objectives of this chapter of the pHD theis is to use peptides as molecular gates for the development of capped MSNs. Specifically our aims were:

- Design, synthesis, characterization and application of a MSN using peptides as molecular gate in which the cargo delivery can be triggered by temperature changes.

- Design, synthesis, characterization and application of a peptide capped material for controlled cargo release induced by Cathepsin B enzyme.

- Design, synthesis, characterization and application of a new MSN to target apoptotic cells and able to release their cargo in these particular cells for the treatment of cell-death related disorders.

- Design, synthesis and characterization of a targeted delivery system based on MSN to B-NHL cells making use of the great affinity of T22 peptide to CXCR4 receptor which is overexpressed in lymphoma cells.

- Design, synthesis and characterization a controlled delivery systems based on MSNs loaded with a peptide, for its delivery inside the cells by the action of intracelular proteases and the subsequent apoptosis induction.

2.4. Temperature-controlled release by changes to the secondary structure of peptides anchored on mesoporous silica supports

Cristina de la Torre,[a,b,c] Alessandro Agostini,[a,b,c] Laura Mondragón,[a,b,c] Mar Orzaez,[d] Félix Sancenón,[a,b,c] Ramón Martinez-Máñez,[a,b,c]* María D. Marcos,[a,b,c] Pedro Amorós[e] and Enrique Pérez-Payá[d]*

[a] *Centro de Reconocimiento Molecular y Desarrollo Tecnológico (IDM), Unidad Mixta Universidad Politécnica de Valencia-Universidad de Valencia.*

[b] *Departamento de Química, Universidad Politécnica de Valencia, Camino de Vera s/n, 46022, Valencia, Spain.*

[c] *CIBER de Bioingeniería, Biomateriales y Nanomedicina (CIBER-BBN)*

[d] *Centro de Investigación Príncipe Felipe, Laboratorio de Péptidos y Proteínas. Avda. Autopista del Saler 16, 46012 Valencia, Spain.*

[e] *Institut de Ciència del Materials (ICMUV), Universitat de València. P.O. Box 22085, E-46071 València, Spain.*

Received: ***Dec 2013***
Published online: ***Jan 2014***

Chem. Commun. **2014*, 50, 3184***

Changes in the conformation of a peptide anchored onto the external surface of silica mesoporous nanoparticles have been used to design novel temperature-controlled delivery systems.

In the last few years, anchoring organic or biological molecules on certain inorganic supports has resulted in the design of hybrid materials showing advanced cooperative functional behaviors.[1] One appealing concept in this area is related with the design of gated solids for advanced delivery applications.[2] These new materials contain switchable molecular-based entities which control the on-command release of previously entrapped guests. In this context, silica mesoporous supports have been widely used as scaffolds given their distinctive characteristics, such as inertness, robustness, thermal stability, high homogeneous porosity, tunable pore sizes and high loading capacity.[3] Moreover, by decorating the mesoporous material with a wide collection of organic moieties, linkers and capping agents, researchers have prepared systems that can be triggered with target stimuli, such as light,[4] changes in pH [5] or redox potential,[6] temperature,[7] and the presence of certain ions, molecules or biomolecules.[8] In particular, the development of gated mesoporous silica nanoparticles using bio-molecules is highly appealing and, for instance, aptamers,[9] antibodies,[10] DNA fragments [11] and peptides,[12] have been used as caps in the preparation of advanced gated nanodevices.

When dealing with the stimuli available for uncapping protocols, changes in temperature are an attractive trigger that can be used by simply selecting global or local temperature changes. In previously reported examples, delivery at a certain temperature has been achieved using the thermosensitive poly(*N*-isopropylacrylamide) (PNIPAAm) polymer,[13] paraffins [14] or supramolecules such as rotaxanes [15] as caps. Yet despite these interesting abiotic examples, the use of bio-molecules for the preparation of nanoscopic gated materials that are able to release an entrapped cargo upon changes in temperature is rare. In this context, unique reported examples deal with the use of temperature-induced ds-DNA melting processes.[16] Moreover, the use of small peptide sequences to prepare

temperature-driven-controlled delivery nanodevices has been described very recently.[17]

In this context, we envisioned a new approach to design gated materials in which peptides could act as caps and in which uncapping process would be triggered by changes in temperature. The underlying idea was to use the well-known temperature-controlled α-helix-to-disordered transformation that occurs in certain peptides in order to design new gated supports. With this aim in mind, a self-aggregating 17-mer peptide, designed to adopt a high level of alpha-helical conformation, was used as a bio-molecular gate. Folding in α-helical bundles was expected to inhibit cargo delivery, whereas transformation to a disordered conformation would reduce the steric crowding around the pore outlets with the subsequent cargo release.

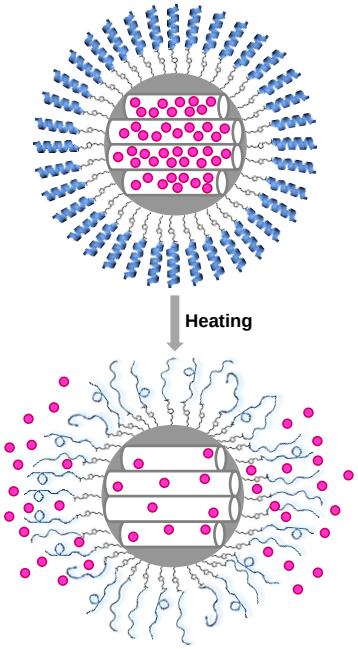

Scheme 1. Schematic representation of gated material **S1-P**. The release of the loaded safranine dye was achieved by a progressive α-helix-to-disordered transformation when temperature increased.

The designed capped support is depicted in Scheme 1. It is based on the use of mesoporous silica nanoparticles loaded with a suitable dye (i.e., safranine O) and containing the 17-mer peptide anchored on the external surface. The capping peptide sequence was based on the previously well-characterized peptide scaffold Ac-SAAEAXAKXXAEAXAKG-NH_2.[18] Fixed and variable positions on the scaffold were designed to preserve the tendency of the peptide to fold into a α-helix conformation, and to minimize alternative secondary structures while allowing sequence diversity. Residues Ser-1 and Gly-17 have N-and C- terminal α-helical, end-capping properties.[19] Two charged residues Glu (E; positions 4 and 12) and Lys (K; positions 8 and 16), were incorporated to favor both aqueous solubility and the formation of salt bridges, which stabilize the helical-bundle conformation.[20] Alanine residues were chosen for their intrinsic alpha-helix-stabilizing properties.[21] The final sequence selected was H-SAAEAYAKRIAEALAKG-OH (**P**).

The starting MCM-41 mesoporous support was prepared by using tetraethyl orthosilicate (TEOS) as a hydrolytic inorganic precursor and the surfactant hexadecyltrimethylammonium bromide (CTABr) as a porogen species.[22] After removing the surfactant by calcination, the MCM-41 solid was obtained. The MCM-41 structure of the starting material was confirmed by X-ray diffraction and transmission electron microscopy (TEM, see Figure 1). The N_2 adsorption-desorption isotherms of the prepared phase show a typical type IV-curve with a specific surface area of 1096.5 m^2g^{-1}, a narrow pore size distribution and an average pore diameter of 3.09 nm. The inorganic support was then loaded with safranine O as a suitable reporter and the outer surface was functionalized with the 3-(azidopropyl)triethoxisylane groups (solid **S1**). In another step, the final capped nanoparticles **S1-P** were prepared by grafting the corresponding 4-pentynoic**-P** derivatives onto the surface of **S1** by using the copper(I)-catalyed Huisgen azide/alkne 1,3-dipolar cycloaddition “click” reaction.[23]

Solid **S1** was characterized by using standard procedures (see Supporting Information). The X-ray diffraction pattern of **S1** (see Figure 1) indicates that the loading process with the dye and the further functionalization with azido groups

did not modify the structure of the mesoporous scaffold. This can be concluded from the presence of the (100) diffraction peak characteristic of the MCM-41-type mesoporous materials. Furthermore, the presence of the mesoporous structure in the final functionalized solid **S1-P** was also confirmed by TEM analysis (see Figure 1). The final **S1-P** material was obtained as spherical particles with diameters of approximately 80-100 nm. The N_2 adsorption-desorption isotherm of **S1** (see Supporting Information) was typical of mesoporous systems with filled mesopores, and a significant decrease in the N_2 volume adsorbed was observed (a specific surface area of 90.7 m^2g^{-1} for **S1** was determined) when compared with the starting MCM-41 material. The organic content in **S1** and **S1-P** was determined by thermogravimetric and elemental analyses. In particular, solid **S1** contained 0.544 mmol of safranine O/g SiO_2 and 0.246 mmol of azide/g SiO_2, whereas the amount of organic matter in **S1-P** was 0.250 mmol of safranine O/g SiO_2 and 0.041 mmol of **P**/g SiO_2. Taking into account an external surface area of **S1** (ca. 80 m^2g^{-1}) and the amount of azide and peptide in **S1** and **S1-P** solids the surface coverage was estimated to be 1.56 azide/nm^2 and 0.26 peptide/ nm^2 with average distances of 8 and 19.6 Å for azide and peptide respectively.

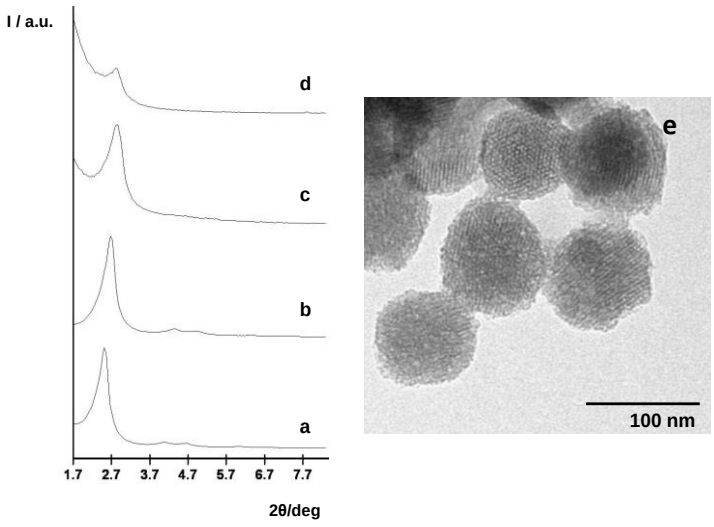

Figure 1. Powder X-ray patterns of a) as-synthesized MCM-41, b) calcined MCM-41, c) solid **S1** containing safranine dye and 3-azidopropyltriethoxysilane and d) final solid **S1-P**.

TEM images of e) solid **S1-P** showing the typical hexagonal porosity of the MCM-41 mesoporous matrix.

To evaluate the structural changes of peptide **P** in solution, circular dichroism (CD) spectroscopy studies were performed in 10 mM phosphate buffer at pH 7 with 25 mM NaCl, and the thermal denaturation curves were recorded at different temperatures to study the thermal stability of the peptide. The CD spectra of **P** at low temperatures exhibited two strong negative bands at 222 nm (assigned to the amide n→ π * transition) and 208 nm (amide π → π *) and a strong positive band at 190 nm (amide π→ π *), which are characteristic of the peptides adopting a helicoidal conformation that changes to a random coil disposition upon heating (see Figure 2). Moreover, the CD spectrum evidences that the partial helicity loss (or denaturation) is reversible upon cooling to the original temperature.

In another step, the gating properties of the solid were studied. In a typical experiment, **S1-P** was suspended in phosphate buffer (pH 7) and the suspension was stirred at the same temperatures as those used for the CD measurements. At a certain time (3 h), the suspension was centrifuged to remove the solid. Dye delivery into the solution was then measured by safranine O fluorescence at 585 nm (λ_{exc} 520 nm). The delivery profile of the dye at different temperatures is displayed in Figure 2. Solid **S1-P** was tightly capped up to a temperature of ca. 40 °C and then the amount delivered increased with temperature. Whereas a simple temperature-dependent diffusion-controlled process would result in a continuous cargo delivery, Figure 2 shows that no payload release was observed from **S1-P** over a wide temperature range (from 4 °C to ca. 40 °C), which corresponds to the temperature range within which the peptide was in a α-helix conformation. Cargo delivery correlated well with the change in the peptide conformation to the random coil.

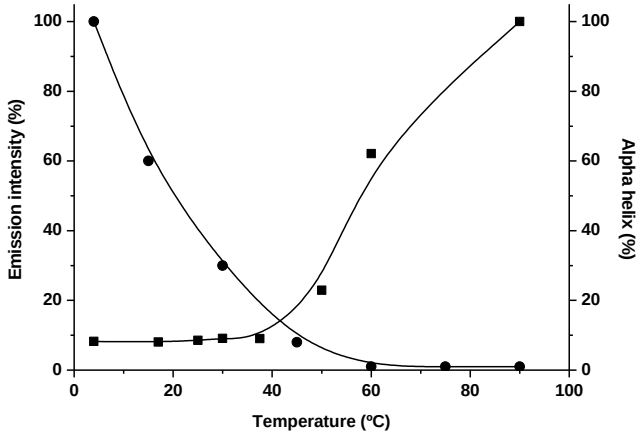

Figure 2. Release profile of safranine O from solid S1-P (■) in PBS and % of α-helix conformation (●) of peptide P at different temperatures.

This result suggests that mesoporous nanoparticles functionalized with certain peptides can be used to design capped materials in which the cargo delivery can be triggered by temperature changes. After bearing in mind that the transformation from α-helix to a random coil is reversible (*vide ante*), it also occurred to us that **S1-P** could be reloaded and reused. In order to test this appealing possibility, solid **S1-P** was suspended in PBS at 90 °C until safranine O was completely released. Then the solid was filtered and dried under vacuum. Afterward, the empty solid was suspended in a PBS solution of safranine O at 90 °C. Then the solid was suddenly introduced into an ice bath (in order to assure the rapid transformation of peptides into their α-helix conformation), filtered and dried. By means of UV-vis studies, the safranine O content in the reloaded material was determined as 0.147 g dye/g SiO_2, a value which comes close to that found in the starting **S1-P**. Furthermore, the re-loaded solid was suspended in PBS at 4 °C for 12 h and no delivery was observed (< 4% of loaded dye). Moreover, the studies of the cargo release at different temperatures displayed a similar profile to that shown in **Figure 2**.

In summary, herein we report for the first time a mesoporous hybrid material capped with a peptide sequence capable of releasing an entrapped dye (safranine

O) by changes in temperature. Cargo delivery correlated well with the change of the peptide conformation from α-helix to a random coil. Moreover, the peptide-functionalized support can be reloaded and reused by taking advantage of the fact that the α-helix to the random coil conformation transformation is a reversible process. The possibility of using different mesoporous supports and a large variety of peptide sequences makes this approach appealing for the design of new temperature-responsive reusable gated materials for different applications.

Aknowledgments

Financial support from the Spanish Government (Project MAT2012-38429-C04) and the Generalitat Valencia (Project PROMETEO/2009/016) is gratefully acknowledged. C.T. is grateful to the Spanish Ministry of Science and Innovation for her grant.

Notes and references

1. A. B. Descalzo, R. Martínez-Máñez, F. Sancenón, K. Hoffmann, K. Rurack, Angew. *Chem. Int. Ed.* **2006**, *45*, 5924.

2. (a) C. Coll, A. Bernardos, R. Martínez-Máñez, F. Sancenón, *Acc. Chem. Res.* **2013**, *46*, 339; (b) A. Popat, S. B. Hartono, F. Stahr, J. Liu, S. Z. Qiao, G. Q. Lu, *Nanoscale* **2001**, *3*, 2801.

3. (a) A. P. Wright, M. E. Davis, *Chem. Rev.* **2002**, *102*, 3589; (b) G. Kickelbick, Angew. *Chem. Int. Ed.* **2004**, *43*, 3102.

4. N. K. Mal, M. Fujiwara, Y. Tanaka, *Nature* **2003**, *421*, 350.

5. S. Angelos, N. M. Khashab, Y. –W. Yang, A. Trabolsi, H. A. Khatib, J. F. Stoddart, J. I. Zink, *J. Am. Chem. Soc*. **2009**, *131*, 12912.

6. S. Saha, K. C. –F. Leung, T. D. Nguyen, J. F. Stoddart, J. I. Zink, *Adv. Func. Mater*. **2007**, *17*, 685.

7. Y. Zhou, W. Guo, J. Cheng, Y. Liu, J. Li, L. Jiang, *Adv. Mater.* **2012**, *24*, 962.

8. (a) M. Chen, C. Huang, C. He, W. Zhu, Y. Xu, Y. Lu, *Chem. Commun.* **2012**, *48*, 9522; (b) Y. L. Choi, J. Jaworski, M. L. Seo, S. J. Lee, J. H. Jung, *J. Mater. Chem.* **2011**, *21*, 7882; (c) A. Popat, B. P. Ross, J. Liu, S. Jambhrunkar, F. Kleitz, S. Z. Qiao, *Angew. Chem. Int. Ed.* **2012**, *51*, 12486.

9. M. Oroval, E. Climent, C. Coll, R. Eritja, A. Aviñó, M. D. Marcos, F. Sancenón, R. Martínez-Máñez, P. Amorós, *Chem. Commun.* **2013**, *49*, 5480.

10. E. Climent, A. Bernardos, R. Martínez-Máñez, A. Maquieira, M. D. Marcos, N. Pastor-Navarro, R. Puchades, F. Sancenón, J. Soto, P. Amorós, *J. Am. Chem. Soc.* **2009**, *131*, 14075.

11. E. Climent, R. Martínez-Máñez, F. Sancenón, M. D. Marcos, J. Soto, A. Maquieira, P. Amorós, *Angew. Chem. Int. Ed.* **2010**, *49*, 7281.

12. C. Coll, L. Mondragón, R. Martínez-Máñez, F. Sancenón, M. D. Marcos, J. Soto, P. Amorós, E. Pérez-Payá, *Angew. Chem. Int. Ed*. **2011**, *50*, 2138.

13. (a) Q. Fu, G. V. R. Rao, L. K. Ista, Y. Wu, B. P. Andrzejewski, L. A. Sklar, T. L. Ward, G. P. López, *Adv. Mater.* **2003**, *15*, 1262; (b) Y. –Z. You, K. K. Kalebaila, S. L. Brock, D. Oupický, *Chem. Mater.* **2008**, *20*, 3354.

14. E. Aznar, L. Mondragón, J. V. Ros-Lis, F. Sancenón, M. D. Marcos, R. Martínez-Máñez, J. Soto, E. Pérez-Payá, P. Amorós, *Angew. Chem. Int. Ed.* **2011**, *50*, 11172.

15. H. Yan, C. Teh, S. SreejithL. Zhu, A. Kwok, W. Fang, X. Ma, K. T. Nguyen, V. Korzh, Y. Zhao, *Angew. Chem. Int. Ed.* **2012**, *51*, 8373.

16. (a) N. Li, Z. Yu, W. Pan, Y. Han, T. Zhang, B. Tang, *Adv. Func. Mater*. **2013**, *23*, 2255; (b) X. Yang, X. Liu, Z. Liu, F. Pu, J. Ren, X. Qu, *Adv. Mater.* **2012**, *24,* 2890; (c) X. Ma, O. S. Ong, Y. Zhao, *Biomater. Sci*. **2013**, *1*, 912; (d) A. Schlossbauer, S. Warncke, P. M. E. Gramlich, J. Kecht, A. Manetto, T. Carell, T. Bein, *Angew. Chem. Int. Ed.* **2010**, *49*, 4734.

17. G. Martinelli, H. R. Zope, M. B. Capell, A. Kros, *Chem. Commun.* **2013**, *49*, 9932.

18. (a) V. Mas, L. Pérez, J. A. Encinar, M. T. Pastor, A. Rocha, E. Pérez-Payá, A. Ferrer-Montiel, J. M. Gonzalez, A. Estepa, *J*. M. Coll*, J. Gen. Virol.* **2002**, *83*, 2671; (b) C. Blanes-Mira, M. T. Pastor, E. Valera, G. Fernanze, J. M. Merino, L. M. Gutierrez, E. Pérez-Payá, A. Ferrer-Montiel, *Biochem. J.* **2003**, *375*, 159.

19. (a) C. A. Rohl, A. Chakrabartly, R. L. Baldwin, Protein Sci., 1996, 5, 2623; (b) J. M. Cavanes, M. Montal, *J. Biol. Chem.* **1998**, *273*, 3414.

20. (a) V. Esteve, S. Blondelle, B. Celda, E. Perez-Payá, *Biopolymers* **2001**, *59*,467; (b) S. Marquese, R. L. Baldwin, *Proc. Natl. Acad. Sci. USA*, **1987**, *85*, 8898.

21. (a) K. T. O'Neil, W. F. De Grado, *Science* **1990** , *250*, 646; (b) P. J. Gans, P. C. Lyu, M. C. Manning, R. W. Woody, N. R. Kallenbach, *Biopolymers*, **1991**, *31*, 1605.

22. S. Cabrera, J. El Haskouri, C. Guillem, J. Latorre, A. Beltrán, D. Beltrán, M. D. Marcos, P. Amorós, *Solid State Sci.* **2000**, *2*, 405.

23. (a) H. C. Kolb, M. G. Finn, K. B. Sharpless, *Angew. Chem. Int. Ed.*, **2001**, *4*0, 2004;
(b) J. Gao, X. Zhang, S. Xu, F. Tang, X. Li, Y. Zhang, Z. Qu, X. Quan, J. Liu, *Chemistry* **2014**, *20*, 1957.

Chem. Commun. **2014**, *50*, *3184*

Temperature-controlled release by changes to the secondary structure of peptides anchored on mesoporous silica supports

Cristina de la Torre, Alessandro Agostini, Laura Mondragón, Mar Orzaez, Félix Sancenón, Ramón Martinez-Máñez, María D. Marcos, Pedro Amorós and Enrique Pérez-Payá

Supporting Information

Chemicals

The chemicals tetraethylorthosilicate (TEOS), *n*-cetyltrmethylammonium bromide (CTABr), sodium hydroxide (NaOH), safranine O, diisopropylethylamine (DIEA), 4-pentynoic acid, anhydrous dimethylformamide (DMF), trifluoroacetic acid (TFA), 2,2,2-trifluoroethanol (TFE), triisobutylsilane (TIS) and sodium ascorbate were purchased from Sigma-Aldrich Química (Madrid, Spain) and used without further purification. Copper (II) sulfate pentahydrate ($CuSO_4 \cdot 5H_2O$) was purchased from Scharlab (Barcelona, Spain). HPLC grade amino acids and resin TG SRAM were purchased from Iris Biotech. Oxyma pure, azidopropyltriethoxysilane, tripyrrolidinophosphonium hexafluorophosphate (PyBOP) and HPLC grade solvents were obtained from Merck (Barcelona, Spain).

General techniques

PXRD, TG Analysis, elemental analysis, EDX microscopy, N_2 adsorption-desorption were employed to characterize the prepared materials. Power X-ray measurements were performed on a Philips D8 Advance diffractometers using Cu K_α radiation. Thermogravimetric analysis were carried out on a TGA/SDTA 851e Mettler Toledo balance, using an oxidant atmosphere (air, 80 ml/min) with a heating program consisting on a heating ramp of 10 ^{o}C per minute from 393 to 1273 K and an isothermal heating step at this temperature during 30 minutes. Fluorescence spectroscopy was carried out on a Felix 32 Analysis Version 1.2 PTI (Photon Techonology International). TEM images were obtained with a 100 kV Philips CM10 microscope. Peptides were synthesized employing an automatic peptide synthesizer 422A from Applied Biosystems. Purification and analysis of the complete peptide sequence by HPLC were carried out by means of a Merck Hitachi L-2130 HPLC pump and a sample carrier L-2200 with a Lichospher 100 C18 (250x10 mm) column. The eluent was monitored at 220 nm employing a Merck Hitachi UV Detector L-2200 autosampler and employing a Licrhsopher 100 C18 (150x3.9 mm) column, and as mobile phase different acetonitrile-aqueous TFA (0.1%) mixtures. Mass spectrometry analysis was performed employing a MALDI TOF/TOF 4700 Proteomics Analyzer from Applied Biosystems. Circular dichroism measurements were carried out in a JASCO 810.

Synthesis of peptide sequence (P)

Peptide sequence H-SAAEAYAKRIAEALAKG-OH was synthesized by Fmoc-based solid phase chemistry using a 433A Applied Biosystem Peptide Synthesizer. Once, the complete sequence of the peptide was obtained, 4-pentynoic acid was added to the sequence at the *N*-terminal side through an amide bond using PyBOP, DIEA and oxyma pure. The peptide was cleaved from the resin by treatment with trifluoroacetinc acid (TFA 94%, TIS 1% and H_2O 5%) during 4 hours and purified by preparative RP-HPLC (Lycrospher 100 C18, 10 mm) using acetonitrile-aqueous TFA (0.1%) mixtures. The identity and purity was confirmed by HPLC and MALDI-TOF mass spectrometry.

Synthesis of Mesoporous silica nanoparticles

The MCM-41 mesoporous nanoparticles were synthesized by the following procedure: *n*-cetylmethylammonium bromide (CTABr, 1.00 g, 2.74 mmol) was first dissolved in 480 ml of deionized water. Then 3.5 ml of NaOH 2.00 M in deionized water was added to the CTABr solution, followed by adjusting the solution temperature to 80 ^{o}C. TEOS (5.00 ml, 2.57 x 10^{-2} mol) was then added dropwise to the surfactant solution. The mixture was allowed to stir for 2h to give a white precipitate. Finally the solid product was centrifuged, washed with deionized water and ethanol, and was dried at 60 ^{o}C (MCM-41 as-synthesized). To prepare the final porous material (MCM-41), the as-synthesized solid was calcined at 550 ^{o}C using oxidant atmosphere for 5 h in order to remove the template phase.

Synthesis of solid S1

Calcined MCM-41 (500 mg) and safranine O (140 mg, 0.4 mmol) were suspended in acetonitrile (15 mL). Then the suspension was stirred for 24 hours at room temperature with the aim of achieving the maximum loading in the pores of the MCM-41 scaffolding. Afterward an excess of 3-(azidopropyl)triethoxysilane (0.62 g, 2.5 mmoles) was added, and the suspension was stirred for 5.5 h. Finally, the solid was filtered off and dried at vacuum.

Synthesis of solid S1-P

For the preparation of the solid **S1-P**, azide-functionalized nanoparticles **S1** (30 mg) and the peptide **P** (30 mg) were suspended in a 50:50 v/v DMF-H_2O mixture (30 ml) in the presence of an excess of safranine O (200 mg, 0.8 mmol) in order to avoid the delivery of the dye from the pores to the bulk solution during the synthesis of the final solid. Then, 100 µL of a solution of $CuSO_4 \cdot 5H_2O$ (10^{-3} mol dm^{-3}) and 100 µL of sodium ascorbate (10^{-2} mol dm^{-3}) were added. The reaction mixture was stirred at 90 ^oC for 3 days. The nanoparticles were centrifuged and washed thoroughly with water to remove unreacted and absorbed molecules. The resulting red nanoparticles were finally dried under vacuum.

Materials characterization

Solid **S1** was characterized using standard procedures. Figure SI-1 shows powder X-ray patterns of the nanoparticulated MCM-41 support and the **S1** functionalised material. The PXRD of siliceous nanoparticulated MCM-41 as-synthesized shows four low-angle reflections typical of a hexagonal array that can be indexed as (100), (110), (200) and (210) Bragg peaks. A significant displacement of the (100) peak in the PXRD powder of the nanoparticulated MCM-41 calcined sample is clearly appreciated in curve b, corresponding to an approximate cell contraction of 4 Å. This displacement and the broadening of the (110) and (200) peaks are related to further condensation of the silanol groups during the calcinations step. Curve c corresponds to the **S1** PXRD pattern. In this case, a slight intensity decrease and the disappearance of the (110) and (200) reflections were observed, most likely related to a loss of contrast due to the filling of the pore voids with the safranine O. Nevertheless, the value and intensity of the (100) peak in this pattern strongly evidences that the loading process with the dye and the further functionalization with 3-(azidopropyl)triethoxysilane have not damaged the mesoporous 3D MCM-41 scaffolding. The curve d corresponds to the **S1-P** PXRD pattern.

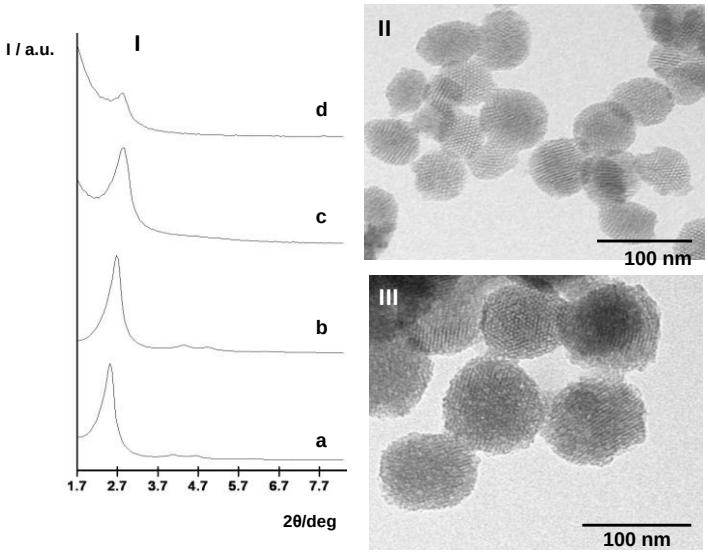

Figure SI-1. (I) Power X-ray diffraction patterns of the solids (a) MCM-41 as-synthesized, (b) calcined MCM-41, (c) solid **S1** containing safranine O dye and 3-(azidopropyl)triethoxysilane and (d) solid **S1-P** containing safranine O dye and the peptide **P**. TEM images of MCM-41 calcined (II) and final solid **S1-P** (III).

Preservation of the mesoporous structure in the final functionalized solids was also confirmed by means of TEM. Figure SI-1 shows the morphology of the MSN materials. As it can be seen, the MCM-41 material was obtained as spherical particles with diameters of ca. 80 nm, and the loaded and functionalized derivative **S1-P** keep the initial morphology of the MCM-41 matrix. The figure also shows the typical channels of the MCM-41 matrix either as alternate black and white stripes or as a pseudohexagonal array of pore voids. These channels are visualized not only in the calcined material but also in **S1-P**.

Further DLS (Dynamic Light Scattering) studies showed particles with a mean diameter of 75.92 nm for MCM-41 and of 89.01 nm for **S1-P** materials (see Table SI-1). The differences in the nanoparticle diameter could be ascribed to the surface functionalization with the bulky 17-mer peptide **P**. Also, Figure SI-2 showed that calcined MCM-41 nanoparticles and the final material **S1-P** formed aggregates of 271.35 and 545.07 nm of diameter, respectively. However, only

about 4% of the total nanoparticles are in the aggregated state (see also Table SI-1).

Table SI-1. Diameter of MCM-41 calcined and **S1-P** nanoparticles.

	Diameter (nm)	% of nanoparticles
MCM-41	75.92	96.75
	271.35	3.25
S1-P	89.01	96.13
	545.07	3.87

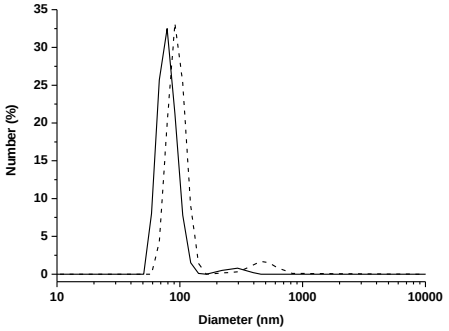

Figure SI-2. Size distribution by number of particles obtained by DLS studies. The average size of nanoparticles of calcined MCM-41 (straight), **S1-P** (dash) was found to be ca. 90-100 nm.

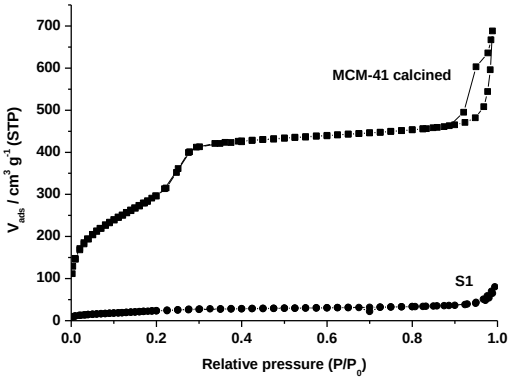

Figure SI-3. Nitrogen adsorption-desorption isotherms for MCM-41 mesoporous material and **S1**.

The N_2 adsorption-desorption isotherms of the nanoparticulated MCM-41 calcined material shows an adsorption step at intermediate P/P_0 value (0.1-0.3)

typical of this solids (see Figure SI-3). This step can be related to the nitrogen condensation inside the mesopores by capillarity. The absence of a hysteresis loop in this interval and the narrow BJH pore distribution suggest the existence of uniform cylindrical mesopores. The application of the BET model resulted in a value for the total specific surface of 1096.5 m^2/g and a pore volume of 0.78 cm^3/g. From the PXRD, porosimetry and TEM studies, the a_0 cell parameter (4.43 nm), the pore diameter (2.45 nm) and the value for the wall thickness (1.98 nm) were calculated. In addition to this adsorption step associated to the micelle generated mesopores, a second feature appears in the isotherm at a high relative pressure. This adsorption corresponds to the filling of the large void among the particles, present a volume of 0.24 g/cm (calculating by using the BJH model) and must be considered as a textural-like porosity. In this case, the curves show a characteristic H1 hysteresis loop and a wide pore size distribution.

The N_2 adsorption-desorption isotherm of **S1** is typical of mesoporous systems with filled mesopores, and a significant decrease in the N_2 volume adsorbed and in the specific surface area (90.7 m^2/g) is observed (see Figure SI-3). In fact, this solid shows flat curves when compared (at the same scale) to those of the MCM-41 parent material, this indicates a significant pore blocking and the subsequent absence of appreciate mesoporosity. Additionally, a certain textural porosity is preserved. BET specific surface values, pore volumes and pore sizes calculated from the N_2 adsorption-desorption isotherms for MCM-41 and **S1** are listed in Table SI-2.

Table SI-2. BET specific surface values, pore volumes and pore sizes calculated from the N_2 adsorption-desorption isotherms for selected materials.

	S_{BET} ($m^2\ g^{-1}$)	Total pore volume ($cm^3\ g^{-1}$)	BHJ pore (nm)
MCM-41	1096.5	0.78	2.45
S1	90.7	0.06	-

The content of 3-(azidopropyl)triethoxysilane, safranine O and peptide in **S1** and **S1-P** solids were determined by elemental and thermogravimetric analysis. Values of contents are detailed in table SI-3.

Table SI-3. Content in mmol of anchored molecules and dye in mmol g^{-1} SiO_2 for solids **S1** and **S1-P**.

	Azide (mmol g^{-1} SiO_2)	Safranine O (mmol g^{-1} SiO_2)	Peptide (mmol g^{-1} SiO_2)
S1	0.246	0.544	-
S1-P	0.246	0.250	0.041

Dye delivery studies

To investigate the temperature-responsive gating properties of **S1-P**, 4 mg of solid were suspended in 5.5 ml of water and then fractioned into seven parts of 500 µL. The seven fractions were stirred at different temperatures (4, 17, 25, 30, 37.5, 60 and 90 ºC). After 3 hours of stirring the delivery of safranine O from the seven samples was determined through the measurement of their emission band centered at 580 nm (upon excitation at 520 nm). The release kinetic curve is shown in Figure SI-4.

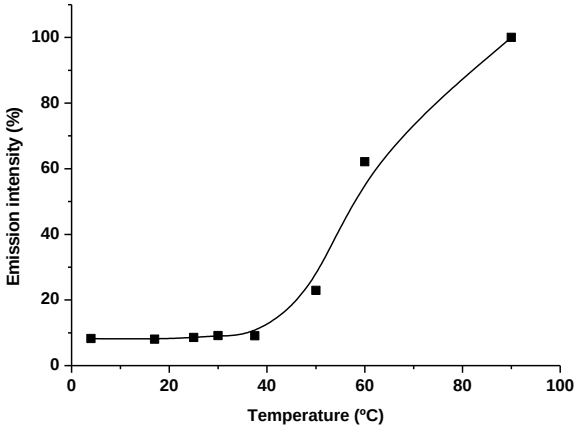

Figure SI-4. Dye release profiles of **S1-P** solid at different temperatures.

Reloading procedure.

Bearing in mind that the transformation from α-helix to random coil is reversible, it occurred to us that **S1-P** could be reloaded and reused. In order to test this appealing possibility solid **S1-P** (2 mg) was suspended in PBS (2 mL) at 90 °C in order to achieve a nearly complete safranine O release. After 24 hours of stirring (the PBS solution was replaced each 2 hours) the vast majority of the entrapped dye was released. Then the solid was dried under vacuum and suspended again in a 2 ml of concentrated safranine O solution at stirred at 90 °C during 12 hours. After that, solid was suddenly introduced in an ice bath (in order to assure that **P** is in their α-helix conformation), filtered and again dried. From a safranine O calibration curve and by measuring the absorbance of the solution before and after their contact with solid **S1-P** the quantity of dye reloaded is determined (0.147 g dye / g SiO_2). The reloaded solid was suspended in buffer solution (2 mL) and stirred at 4 ^{o}C during 12 hours (the solid is in their closed state because **P** is in their α-helix conformation). After that, the solid was centrifuged and the safranine O release was determined through UV-visible measurements. Only 4% of the loaded safranine O was released at this temperature. Moreover studies of cargo release at different temperatures displayed a similar profile to that shown in Figure 2.

Circular dichroism (CD) studies

In order to investigate the conformation of peptide **P** in solution, circular dichroisms measurements were carried out. The dichroism spectra in the UV region were obtained in a JASCO 710 circular dichroism spectrometer. The spectra were recorded between 193 and 240 nm using 1 mm optical path cuvettes. The scan speed was fixed at 0.2 nm s^{-1} with an integration time constant of 1 s. The final spectrums were obtained as an average of 20 scans for each sample. The blank spectra were performed in the same conditions as the samples spectra. Solutions of peptide **P** (50 μM) were prepared in 10 mM phosphate buffer at pH 7 with 25 mM NaCl. The concentration of the peptide was determined by UV spectroscopy, using ε_{276} =1460 $M^{-1}cm^{-1}$ for the tyrosine residue.[1] Also 30% TFE were used as a secondary structure stabilizer.[2,3] The spectra were measured at

different temperatures starting from the lower until the higher. Then, the spectra were measured in the inverse gradient to check that the changes in the secondary structure of the peptide were reversible. The temperatures chosen were 4, 15, 30, 45, 60, 75 and 90 ^{o}C waiting at least five minutes between each change in order to equilibrate all the system. The CD spectra in the far UV region of **P** at lower temperatures showed one maxima (at ca. 190 nm) and two minima (centered at ca. 207 and 222 nm) characteristic of peptides adopting an helicoidal conformation (see Figure SI-5).[4] The CD measurements also showed that peptide **P** adopts an α-helix conformation at lower temperatures that changed to a random coil disposition upon heating (see Figure SI-6 for the distribution of α -helix conformation at several temperatures).

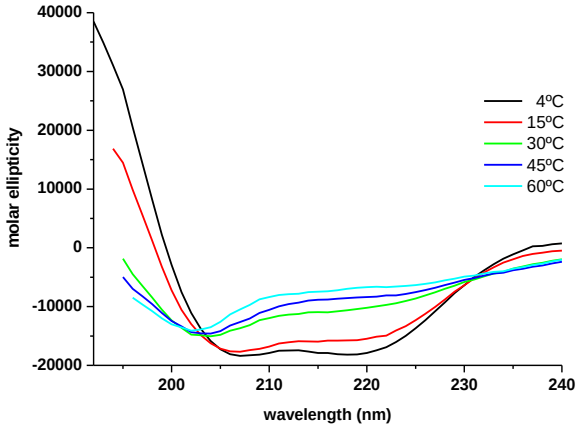

Figure SI-5. CD spectra of 17-mer peptide **P** at different temperatures.

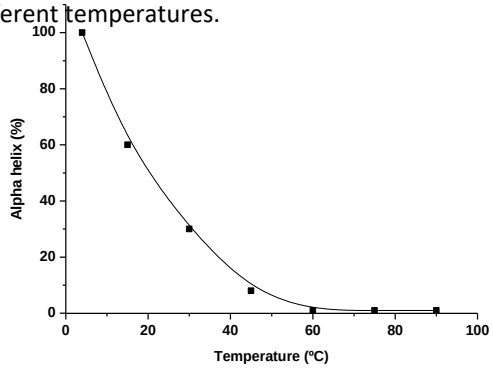

Figure SI-6. CD spectra of 17-mer peptide **P** at different temperatures. The % of α-helix in the peptide was predicted using the AGADIR algorithm.[5]

References

1. S. C. Gill, P. H. von Hippel, *Chem. Biol*. **1989**, *182*, 319.

2. S. Y. Lau, A. K. Taneja, R. S. Hodges, *J. Biol. Chem.* **1984**, *259*, 13253.

3. T. M. Cooper, R. W. Woody, *Biopolymers* **1990**, *30*, 657.

4. G. Holzwarth, P. Doty, *J. Am. Chem. Soc.* **1965**, *87*, 218.

5. (a) V. Muñóz, L. Serrano, *Nat. Struct. Mol. Biol*. **1994**, *1*, 399; (b) V. Muñóz, L. Serrano, *J. Mol. Biol.* **1994**, 245, 275; (c) V. Muñóz, L. Serrano, *J. Mol. Biol*. **1994**, *245*,297.

2.5. Cathepsin-B induced controlled release from peptide-capped mesoporous silica nanoparticles

Cristina de la Torre, [a,b,c] Laura Mondragón,[d] Carmen Coll, [a,b,c] Félix Sancenón, [a,b,c] María D. Marcos,[a,b,c] Ramón Martínez-Máñez, [a,b,c*] Pedro Amorós,[e] Enrique Pérez-Payá[f†] and Mar Orzáez [f*]

[a] Centro de Reconocimiento Molecular y Desarrollo Tecnológico (IDM), Unidad Mixta Universidad Politécnica de Valencia-Universidad de Valencia.

[b] Departamento de Química, Universidad Politécnica de Valencia. Camino de Vera s/n, 46022, Valenicia, Spain.

[C] CIBER de Bioingenieria, Biomateriales y Nanomedicina (CIBER-BBN)

[d] Centre Méditerranéen de Médecine Moléculaire (C3M), équipe "contrôle métabolique des morts cellulaires," Institut national de la santé et de la recherche médicale (Inserm) U1065, BP 2 3194, 06204, Nice, France.

[e] Institut de Ciència dels Materials (ICMUV), Universitat de València, P.O. Box 2085, 46071 Valencia, Spain.

[f] Centro de Investigación Príncipe Felipe, Laboratorio de Péptidos y Proteínas. Avda. Autopista del Saler 16, 46012 Valencia, Spain.

[†] Deceased.

Received: ***July 2014***
Published online: ***Oct 2014***

Chem. Eur. J., 2014, 20, 1530

Abstract

New capped silica mesoporous nanoparticles for intracellular controlled cargo release within cathepsin B expressing cells are described. Nanometric mesoporous MCM-41 supports loaded with safranin O (**S1-P**) or doxorubicin (**S2-P**) containing a molecular gate based on a cathepsin B target peptidic sequence were synthesized. Solids were designed to show "zero delivery" and to display cargo release in the presence of cathepsin B enzyme which selectively hydrolysed *in vitro* the capping peptide sequence. Controlled delivery in HeLa, MEFs WT and MEFs lacking cathepsin B cell lines were also tested. Release of safranin O and doxorubicin in these cells took place when cathepsin B was active or present. Cells treated with **S2-P** showed a fall in cell viability due to nanoparticles internalisation, cathepsin B hydrolysis of the capping peptide and cytotoxic agent delivery proving the possible use of these nanodevices as new therapeutic tools for cancer treatment.

In the treatment of cancer, chemotherapy constitutes the main therapeutic approach. Traditional chemotherapeutic agents target cells that divide rapidly, one of the main characteristics of cancer cells. However, this also means that cells belonging to healthy tissues that divide quickly are also targeted and destroyed constituting one of the main drawbacks of chemotherapy. To diminish these side-effects, several strategies have been developed, among them; i) the development of chemotherapeutic derivatives and analogs with less toxic effects and better pharmacological properties or ii) the design of new drug delivery systems for better targeting cancer cells. The arrival of nanotechnology has fuelled the latter approach and has brought about new innovative concepts to drug-delivery therapies.[1] Specifically attention has been put on drug-delivery systems capable of releasing active molecules to certain cells in a controlled fashion.[2] Among the different drug-delivery materials developed till present, silica mesoporous supports (SMPS) have undergone an exponential growth as carriers for drug storage and delivery in recent years, thanks to their unique properties, such as large loading capacity, low toxicity and easy functionalization.[3] Notwithstanding, the most appealing feature of SMPS as carriers is, perhaps, the possibility of functionalizing them with molecular/supramolecular ensembles in their external

surface to develop gated-SMPS, which show "zero delivery" and can release their cargo on-command in response to specifically designed external stimuli.[4]

Since the first example of gated SMPS developed by Fujiwara's laboratory[5] a certain number of capped supports have been created responding to a wide variety of stimuli such as light,[6] redox reactions,[7] pH,[8] changes in polarity,[9] temperature[10] etc. However, it was the use of biomolecules[11] as triggers the ultimate prove of the possible use of SMPS in more biological and realistic settings. In this context, the possibility of using enzymes as "biological-keys" has opened a wide range of new perspectives for the development of biocompatible gated SMPS carriers and this approach is envisioned to have large potential to provide exquisite selectivity in the design of advanced gate-opening devices. [12] This development is reinforced by the cellular internalization mechanism of nanoparticles, dependant on endocytosis and the subsequent arrival to lysosomes, where the existent lysosomal enzymes can degrade the capping molecules in SMPS allowing the release of the cargo that will reach its target and provide the therapeutic benefit expected.

Seminal examples of capped SMPS containing peptides were able to be opened by enzymes present in the lysosomes with broad spectra of action such as esterases,[13] amylases,[14,15] amidases[16] or proteases.[17] However a more advanced approach could be envisioned via the use of gated ensembles that could be opened by lysosome enzymes which are overexpressed in certain target diseases. In this context some of us have recently described the first example of cell specific cargo release based on a nanoparticle able to display a selective and controlled cargo delivery in senescent cells.[15] Despite these interesting results, there are not, as far as we know, other examples that, via the use of gated SMPS, are able to deliver the cargo selectively in particular cells overexpressing a target enzyme which is related with a certain disease.

In this context it is well-known that cathepsins are highly associated to cancer development and metastasis.[18] Cathepsins are a family of fifteen enzymes distinguished by their structure, catalytic mechanism, and proteins they cleave.

Inside this family there are 11 cystein proteases (B, C, F, H, L, K, O, S, V, W, X), 2 aspartic proteases (D and E) and 2 serine carboxiproteases (A and G). Most of them are only active thanks to the low pH of the lysosomes and they are able to cleave specific substrates. Cysteine cathepsins exhibit broad specificity, cleaving their substrates preferentially after basic or hydrophobic residues.[18c] Cathepsin B is probably one of the most well-known cathepsin enzymes and many studies have shown that cathepsin B overexpression is correlated with invasive and metastatic phenotypes in cancers.[18c] In this context some strategies developed till present are based on the development of cathepsin B inhibitors[19] or in the use of cathepsin B target sequences for the release of therapeutic agents.[20] These examples have been based on polymer-therapeutics or small peptides bound to cytotoxic agents. However, capped SMPS able to be preferentially opened by cathepsin B have not been described so far.

Among sequences targeted by cathepsin B. Silva et al.[21] demonstrated recently that the peptide Abz-GIVRAK(Dnp)-OH, was able to be hydrolyzed highly specifically by cathepsin B and proved that this peptide is highly selective for this enzyme among lysosomal cysteine proteases. Taking into account the above cited facts, the aim of this study was to design capped mesoporous materials capable of selectively delivering their cargo in the presence cathepsin B enzyme that is overexpressed in certain types of cancers. In order to achieve this goal MCM-41 silica mesoporous nanoparticles were selected as inorganic scaffold [22] and were loaded with safranin O dye (**S1**). Then, based in the study of B. Silva et al.[21] the outer surface was functionalized, through a "click chemistry" reaction,[23] with the peptide alkynyl-GIVRAKEAEGIVRAK-OH (**P**) that contains the cathepsin B target sequence. This procedure yielded the final material, **S1-P** (see Figure 1A). The specific cargo release of the solid synthesized was studied employing several cell lines expressing or not cathepsin B enzyme and using specific cathepsin B inhibitors.

Once synthesized, solids were characterized by using standard procedures. The mesoporous structure of **S1-P** was confirmed by XRD and TEM studies (see Figures

1B and 1C). The nanoparticles obtained presented a spherical structure with an average diameter of 106 nm (confirmed by dynamic light scattering measurements, see Supporting Information) and an average pore diameter of 3.23 nm. N_2 adsorption-desorption isotherm of **S1** were typical of mesoporous systems with capped mesopores, and a markedly reduction in the N_2 volume adsorbed and surface area (90.7 m^2/g) were observed when compared with the initial MCM-41-based MSN (1028.5 m^2/g). Finally, the content of grafted peptide and cargo in solid **S1-P** was determined by thermogravimetric and elemental analysis and amounted to 0.084 and 0.185 g/g SiO_2, respectively (see Supporting Information for further details).

As a final step in the characterization of the nanoparticles, *in vitro* studies of the delivery of the safranin O from **S1-P** solid were performed (see Figure 1D). For that purpose, lysosomal extracts from HeLa cells were prepared and the presence of cathepsine B in the extract was confirmed using the Z-RR-AMC fluorogenic substrate of this enzyme (see Supporting Information).[24] In a typical experiment **S1-P** was suspended at 37 ^oC and pH 5.4 in the presence of lysosomal extract and dye release was tracked by following the emission of the safranin O in the solution as a function of time (λ_{ex} = 520 nm, λ_{em} = 585 nm). Moreover, as a control, the same amount of solid **S1-P** was suspended in aqueous media at the same pH and a mixture of proteins with the same concentration than that measured for the lysosomal extract, was added (see Supporting Information). In the absence of the lysosomal extract a poor release was found indicating that the safranin O cargo remained in the nanoparticles without delivery. In contrast, in the presence of the lysosomal extracts delivery of the safranin O was found as an increase of the dye fluorescence as a function of time. In additional studies we also found that the presence of recombinant cathepsin B enzyme was able to induce cargo delivery whereas enzymes such as amylases or ureases were unable to open the gate in **S1-P** (see Supporting Information). Cargo release in these experiments was attributed to the specific cathepsin B cleavage of the capping peptide, **P**. This cleavage was expected to occur in the amide bond from positively charged arginine (R) and alanine (A) amino acids in the target GIVRAK sequence which

resulted in a reduction of the size of the attached peptides finally allowing delivery of the entrapped cargo.[21] Moreover note that although it is known that many proteins could be adsorbed onto the nanoparticle surface and formed a 'corona', a selective delivery in a complex medium such as a lysosomal extract was observed.[25]

After demonstrating the effective safranin O release from **S1-P** in the presence of cathepsin B *in vitro*, our next goal was to prove the possible use of the peptide capped materials as specific delivery system in cell models. HeLa cells and primary culture cells from wild-type mouse embryonic fibroblasts (WT MEFs) were employed for the experiments. In a first step, the internalization of **S1-P** nanoparticles was confirmed by flow cytometry analysis. MEFS and HeLa cells were treated for 24h with **S1-P** and safranin O associated fluorescence was monitored (Figure 2A). Almost all the cell population incorporated the nanoparticle. In a further analysis cell lines were treated with **S1-P** for 12 h and safranin O associated fluorescence was monitored by confocal microscopy (see Figure 2B). Cytoplasmic safranin O associated fluorescence was observed in both treated cells indicating the proper internalization and release of the content of **S1-P**. Once confirmed cellular uptake, evidence of the cathepsin B-dependant aperture of the nanodevice was studied. For that purpose, HeLa and WT MEFs were treated with the inhibitor of cathepsin B enzyme Ac-LVK-CHO[26] 4 h prior the addition of **S1-P**. A remarkable reduction in the presence of cytoplasmic safranin O was perceived when compared to cells treated only in the presence of **S1-P**, thus indicating the reduction in the degradation of **P** when cathepsin B is not active. To further confirm this fact, MEFs primary cells deficient for cathepsin B were also employed (MEFs CatB -/-).[27] These cells lack of the enzyme cathepsin B and therefore there were not able to induce the degradation of **P**. When MEFs CatB -/- were treated with **S1-P** no cytoplasmic safranin O was detected (see Figure 2B). Furthermore, pretreatment of MEFs CatB -/- with Ac-LVK-CHO before the addition of **S1-P** did not induce changes in the cytoplasmic safranin O associated fluorescence, proving the specific role of cathepsin B in the peptide degradation. Subsequent quantification of the cytoplasmic fluorescence (see

Figure 2C) associated to nanoparticles among the different treatments indicated very significant differences in HeLa and WT MEFs when cathepsin B is inhibited whereas no significant delivery was observed in case of MEFs CatB -/- cells. Moreover WST-1 cell viability assays with HeLa cells demonstrated that **S1-P** nanoparticles were not toxic at concentrations up to 200 μg/ml.

In order to extend the potential applicability of the peptide-capped nanoparticles, new SMPS containing peptide **P** and loaded with doxorubicin were prepared (**S2-P**). When characterised, **S2-P** presented similar cargo delivery profile to **S1-P** in the presence of lysosomal extract at 37 ^{o}C. Moreover, the content of grafted peptide and cargo in solid **S2-P** amounted to 0.068 and 0.085 g /g SiO_2, respectively (see Supporting Information for further details). Doxorubicin is commonly employed in the treatment of various types of cancer. However, the non-specific cellular internalization of this drug is associated to major secondary effects such as cardio- and nephrotoxicity.[28] Confining doxorubicin in nanoparticles for more specific cellular release has been reported to be an interesting strategy to decrease the unwanted secondary effects, thereby increasing the efficiency of this drug. In order to prove the possible therapeutic application of this new nanodevice, confocal microscopy studies were developed to test the internalization of **S2-P** nanoparticles by HeLa cells. Cells treated with **S2-P** presented a cell death associated phenotype with cell detaching from the plate and a reduction in cellular density compared to control samples (see Figure 3A). Subsequent quantification of cell viability employing WST-1 assays shown a decrease of 35% in cell viability of HeLa cells treated with **S2-P** when compared to control cells (see Figure 3B). Moreover HeLa cells treated with **S2-P** in the presence of cathepsin B inhibitor showed non altered cell viability due to the lack of capping-peptide degradation by cathepsin B. Similar results were obtained for MEFs WT; in this case a 50% reduction in cell viability was obtained when cathepsin B was present. Finally, no significant cell death was detected in MEFs CatB -/- cells (lacking cathepsin B) treated with **S2-P** (see Figure 3B). In summary these results supported the cathepsin B hydrolysis of the anchored peptide in **S2-**

P as responsible mechanism for doxorubicin release and the subsequent reduction in cell viability.

In summary, we have reported here the synthesis and characterization of two hybrid organic-inorganic capped nanoparticles **S1-P** and **S2-P**. Both solids consisted of a MCM-41 nanoparticulated mesoporous scaffold loaded with the dye safranin O (**S1-P**) or with the cytotoxic drug doxorubicin (**S2-P**) and capped with a peptidic sequence designed to be selectively hydrolysed by cathepsin B enzyme overexpressed in several cancer cells. We demonstrated how this cathepsin B target peptidic sequence was only opened in the presence of cathepsin B in *in vitro* and in cellular assays. These results validate the potential use of silica mesoporous supports as therapeutic tools for the treatment of cathepsin B overexpressing cancer cells thanks to the specific enzyme-dependent cargo release. Besides, the data obtained in this study opens a wide range of possibilities in the design of advanced nanodevices for enzyme controlled delivery applications, and a number of new advances in this area are anticipated.

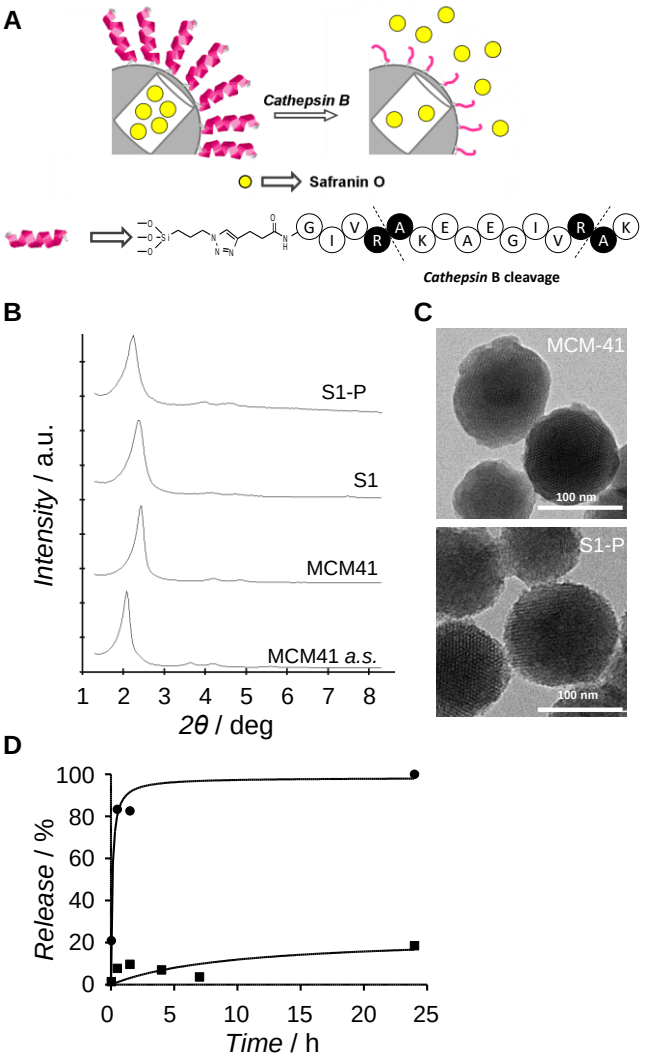

Figure 1. Synthesis and characterization of **S1**- nanoparticles. A) Representation of the gated material **S1-P** functionalized with 3-(azidopropyl)triethoxysilane and capped with the peptide **P** and the selective delivery mechanism in the presence of cathepsin B. B) Power X-ray patterns of MCM-41 as synthesized, calcined MCM-41, **S1** and final **S1-P**. C) TEM images of calcined MCM-41 and solid **S1-P** showing the typical porosity of the MCM-41 mesoporous matrix. D) Release profiles of safranin O in the absence (■) and in the presence of lysosomal extracts from HeLa cells (♦) at 37 ºC and pH 5.4.

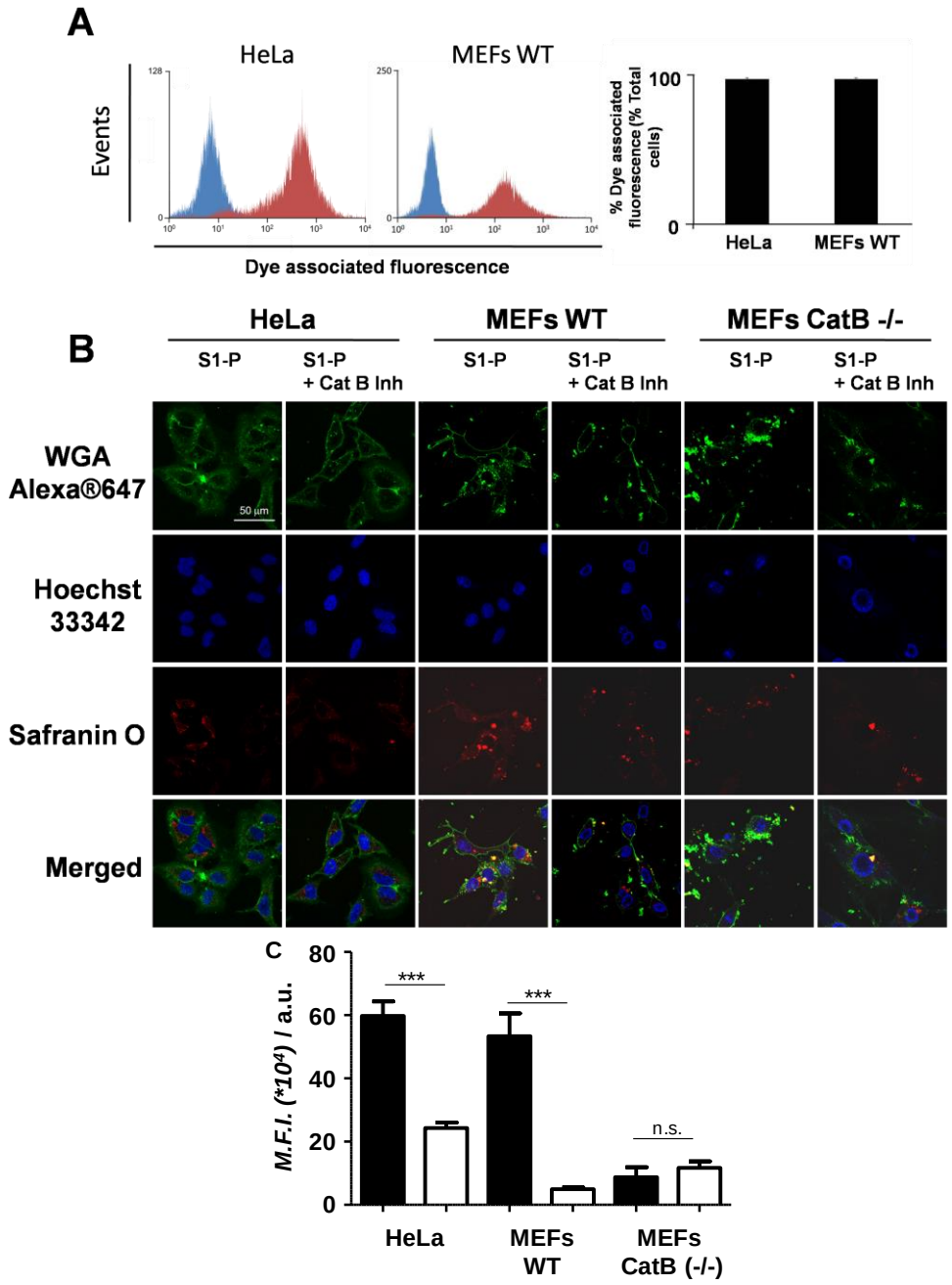

Figure 2. Cellular uptake and lysosomal cathepsin B cargo release of **S1-P** studies. A) HeLa and MEFs WT were incubated 24 h with 100 μg/mL of **S1-P**. Then, nanoparticle internalization was monitored by measuring safranin O-associated fluorescence by flow cytometry. Histograms corresponding to HeLa and MEFs WT treated (red) or not with the nanoparticle are depicted. Quantification of safranin O positive cells is shown in the

graphic. B) Once confirmed the internalization, HeLa, MEFs WT and MEFs Cat B -/- were incubated 12 h in the presence of **S1-P** 100 μg/mL. The cellular uptake of **S1-P** was followed by safranin O-associated fluorescence (red) in the presence of DNA marker Hoechst 33342 (blue) and plasma membrane marker WGA-Alexa-Fluor 647 (green). Cytoplasmic safranin O-associated fluorescence was observed except in cells lacking cathepsin B enzyme (MEFs Cat B -/-). In order to determine the specific role of cathepsin B in cargo release, cells were also pre-treated for 4 h with the cathepsin B inhibitor 4 μM Ac-LVK-CHO (CatB Inh) previous to the addition of **S1-P** 100 μg/mL for 12 h. A reduction or disappearance of safranin O cytoplasmic signal was clearly observed in all cell lines. C) Quantification of the safranin O-associated fluorescence intensity of the different cell samples was carried out. Comparison among the non (black bars) and cathepsin B inhibitor treated (white bars) cells was done. Three independent experiments were developed obtaining similar results. Data are expressed as mean ± s. Asterisc indicates significant differences *** ($p < 0.001$) when paired t Student tests were applied, while n.s. indicates non significant differences statistically.

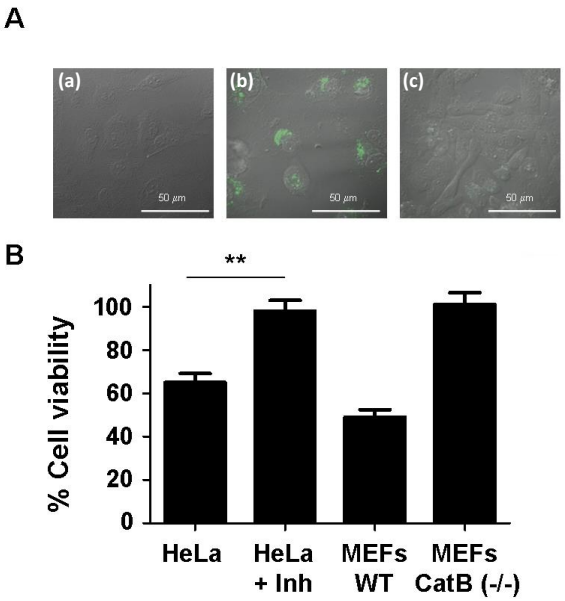

Figure 3. Cellular uptake of **S2-P** and cell viability studies. A) HeLa cells were treated with **S2-P** for 48 h in the absence or in the presence of cathepsin B inhibitor Ac-LVK-CHO. Cellular uptake was determined by confocal microscopy. Transmitted light images and doxorubicin-associated fluorescence (green) images were taken. Control cells showed no fluorescence (a). Doxorubicin-associated fluorescence was located in the cytoplasm of the cells when they were treated with **S2-P** (b). Cells previously treated with cathepsin B inhibitor did not show doxorubicin cytoplasmic associated fluorescence (c). B) WST-1 viability assays in HeLa, MEFs WT and MEFs CatB -/- cells treated with 100 μg/mL of **S2-P**. In case of HeLa cells studies were performed in the absence or the presence of the cathepsin B inhibitor Ac-LVK-CHO. Three independent experiments containing triplicates were carried out. Data are expressed as mean ± s.e. Asterisc indicates significant differences ** ($p < 0.01$) when paired t Student tests were applied.

Acknowledgements

We thank the Spanish Government (Project MAT2012-38429-C04 and SAF2010-15512) and the Generalitat Valenciana (Project PROMETEO/2009/016) for support. C.T. is grateful to the Spanish Ministry of Science and Innovation for her PhD fellowship. L.M. thanks the Generalitat Valenciana and Nice city council

for their post-doctoral contracts VALI+D and "Aides Individuelles aux Jeunes Chercheurs - 2011". C.C. thanks the Generalitat Valenciana for their post-doctoral contract VALI+D. M.O. thanks the CIPF for her post-doctoral fellowship. We thank the confocal microscopy service, Alberto Hernández and Eva María La Fuente from CIPF for their technical support.

References

1. a) Z. Ge, S. Liu, *Chem. Soc. Rev*. **2013**, *42*, 7289; b) O. C. Farokhzad, R. Langer, *ACS Nano* **2009**, *3*, 16; c) S. Wang, *Microporous Mesoporous Mater*. **2009**, *117*, 1; d) X. -X. Zhang, H. S. Eden, X. Chen, *J. Controlled Release* **2012**, *159*, 2; e) Q. He, J. Shi, *Adv. Mater*. **2014**, *26*, 391**.**

2. a) K. M. L. Taylor-Pashow, J. Della Rocca, R. C. Huxford, W. Lin, *Chem. Commun*. **2010**, *46*, 5832; b) P. Yang, S. Gai, J. Lin*, Chem. Soc. Rev*. **2012**, *41*, 3679; c) Z. Li, J. Barnes, A. Bosoy, J. F. Stoddart, J. I. Zink, *Chem. Soc. Rev.* **2012**, *41*, 2590; d) M. Colilla, B. Gonzlez, M. Vallet-Regí, *Biomat. Sci*. **2013**, *1*, 114; e) Q. He, J. Shi, *J. Mater. Chem.* **2011**, *21*, 5845**.**

3. a) J. S. Beck, J. C. Vartuli, W. J. Roth, M. E. Leonowicz, C. T. Kresge, K. D. Schmitt, C. T. W. Chu, D. H. Olson, E. W. Sheppard, S. B. McCullen, J. B. Hoggins, J. L. Schlenker, *J. Am. Chem. Soc*. **1992**, *114*, 10834; b) A. P. Wight, M. E. Davis, *Chem. Rev.* **2002**, *102*, 3589; c) G. Kickelbick, *Angew. Chem. Int. Ed.* **2004**, *43*, 3102.

4. K. Cotí, M. E. Belowich, M. Liong, M. W. Ambrogio, Y. A. Lau, H. A. Khatib, J. I. Zink, N. M. Khashab, J. F. Stoddart, *Nanoscale* **2009**, *1*, 16**.**

5. N.K. Mal, M. Fujiwara, Y. Tanaka, *Nature* **2003,** *421*, 350**.**

6. a) J. Lai, X. Mu, Y. Xu, X. Wu, C. Wu, C. Li, J. Chen, Y. Zhao, *Chem. Commun.* **2010**, *46*, 7370; b) A. Agostini, F. Sancenón, R. Martínez-Máñez, M. D. Marcos, J. Soto, P. Amorós, *Chem. Eur. J.* **2012**, *18*, 12218; c) J. Lee, J. Park, K. Singha, W. J. Kim, *Chem. Commun.* **2013**, *49*, 1545; d) T. M. Guardado-Alvárez, L. S. Devi, M. M. Russell, B. J. Schwartz, J. I. Zink, *J. Am. Chem. Soc.* **2013**, *135*, 14000.

7. a) R. Hernandez, H. R. Tseng, J. W. Wong, J. F. Stoddart, J. I. Zink, *J. Am. Chem. Soc*. **2004**, *126*, 3370; b) R. Mortera, J. Vivero-Escoto, I. I. Slowing, E. Garrone, B. Onida, V. S.-Y. Lin, *Chem. Commun*. **2009**, 3219; c) L. Wang, M. Kim, Q. Fang, J. Min, W. I. Jeon, S. Y. Lee, S. J. Son, S. –W. Joo, S. B. Lee, *Chem. Commun.* **2013,** *49*, 3194; d) C. Wang, Z. Li, D. Cao, Y. –L. Zhao, J. W. Gaines, O. A. Bozdemir, M. W. Ambrogio, M. Frasconi, Y. Y. Botros, J. I. Zink, J. F. Stoddart, *Angew. Chem. Int. Ed.* **2012**, *51*, 5460.

8. a) H. Meng, M. Xue, T. Xia, Y. L. Zhao, F. Tamanoi, J. F. Stoddart, J. I. Zink, E. A. Nel, *J. Am. Chem. Soc.* **2010**, *132*, 12690; b) R. Guillet-Nicolas, A. Popat, J. –L. Bridot, G. Monteith, S. Z. Qiao, F. Kleitz, *Angew. Chem. Int. Ed*. **2013**, *52*, 2318; c) M. Xue, J. I. Zink, *J. Am. Chem. Soc*. **2013**, *135*, 17659**.**

9. C. Coll, R. Casasús, E. Aznar, M. D. Marcos, R. Martínez-Máñez, F. Sancenón, J. Soto, P. Amorós, *Chem. Commun.* **2007**, 1957.

10. a) E. Aznar, L. Mondragón, J. V. Ros-Lis, F. Sancenón, M. D. Marcos, R. Martínez-Máñez, J. Soto, E. Pérez-Payá, P. Amorós, *Angew. Chem. Int. Ed.* **2011**, *50*, 11172; b) C. de la Torre C, A. Agostini, L. Mondragón, M. Orzáez, F. Sancenón, R. Martínez-Máñez, M.D. Marcos, P. Amorós, E. Pérez-Payá, *Chem. Com.* **2014**, *50*, 3184; c) A. Schlossbauer, S. Warncke, P. M. E. Gramlich, J. Kecht, A. Manetto, T. Carell, T. Bein, *Angew. Chem. Int. Ed.* **2010**, *49*, 4734.

11. a) P. Zhang, F. Cheng, R. Zhou, J. Cao, J. Li, C. Burda, Q. Min, J. J. Zhu, *Angew. Chem. Int. Ed.* **2014**, *53*, 2371; b) E. Climent, R. Martínez-Máñez, F. Sancenón, M. D. Marcos, J. Soto, A. Maquieira, P. Amorós*, Angew. Chem. Int. Ed.* **2010**, *49*, 7281; c) M. Oroval, E. Climent, C. Coll, R. Eritja, A. Aviñó, M. D. Marcos, F. Sancenón, R. Martínez-Máñez, P. Amorós, *Chem. Commun.* **2013**, *49*, 5480; d) E. Climent, L. Mondragón, R. Martínez-Máñez, F. Sancenón, M.-D. Marcos, J. R. Murguía, P. Amorós, K. Rurack, *Angew. Chem. Int. Ed.* **2013**, *52*, 8938; e) F. J. Hernandez, L. I. Hernandez, A. Pinto, T. Schäfer, V. C. Özalp, *Chem. Commun.* **2013**, *49*, 1285; f) E. Climent, R. Martínez-Máñez, A. Maquieira, F. Sancenón, M.D. Marcos, E.M. Brun, J. Soto, P. Amorós, *ChemistryOpen* **2012**, *1*, 251.

12. C. Coll, A. Bernardos, R. Martínez-Máñez, F. Sancenón, *Acc. Chem. Res.* **2013**, *46*, 339.

13. a) Y. –L. Sun, Y. Zhou, Q. –L. Li, Y. –W. Yang, *Chem. Commun.* **2013**, *49*, 9033; b) A. Agostini, L. Mondragón, L. Pascual, E. Aznar, C. Coll, R. Martínez-Máñez, F. Sancenón, J. Soto, M.D. Marcos, P. Amorós, A.M. Costero, M. Parra M, S. Gil, *Langmuir.* **2012**, *28*, 14766.

14. a) Z. Chen, Z. Li, Y. Lin, M. Yin, J. Ren, X. Qu, *Chem. Eur. J.* **2013**, *19*, 1778; b) A. Bernardos, L. Mondragón, E. Aznar, M. D. Marcos, R. Martínez-Máñez, F. Sancenón, J. Soto, J. M. Barat, E. Pérez-Payá, C. Guillem, P. Amorós, *ACS Nano* **2010**, *4*, 6353; c) A. Bernardos, E. Aznar, M.D. Marcos, R. Martínez-Máñez, F. Sancenón, J. Soto, J.M. Barat, P. Amorós, *Angew Chem Int Ed Engl.* **2009**, *48*, 5884; d) C. Park, H. Kim, S. Kim, C. Kim, *J. Am. Chem. Soc.* **2009**, *131*, 16614.

15. A. Agostini, L. Mondragón, A. Bernardos, R. Martínez-Máñez, M.D. Marcos, F. Sancenón, J. Soto, A. Costero, C. Manguan-García, R. Perona, M. Moreno-Torres, R. Aparicio-Sanchis, J.R. Murguía, *Angew Chem Int. Ed. Engl*. **2012**, *51*, 10556.

16. a) A. Agostini, L. Mondragón, C. Coll, E. Aznar, M.D. Marcos, R. Martínez-Máñez, F. Sancenón, J. Soto, E. Pérez-Payá, P Amorós, *ChemistryOpen.* **2012**, *1*, 17; b) I. Candel, E. Aznar, L. Mondragón, C. de la Torre, R. Martínez-Máñez, F. Sancenón, M.D. Marcos, P. Amorós, C. Guillem, E. Pérez-Payá, A.M. Costero, S. Gil, M. Parra, *Nanoscale.* **2012**, *4*, 7237**.**

17. a) L. Mondragón, N. Mas, V. Ferragud, C. De la Torre, A. Agostini, R. Martínez-Máñez, F. Sancenón, P. Amorós, E. Pérez-Payá, M. Orzáez, *Chem. Eur. J.* **2014**, *20*, 5271; b) C. Coll, L. Mondragón, R. Martínez-Máñez, F. Sancenón, M.D. Marcos, J. Soto, P. Amorós, E. Pérez-Payá, *Angew Chem Int Ed Engl.* **2011**, *50*, 2138.

18. a) G. J. Tan, Z. K. Peng, J. P. Lu, F. Q. Tang. *World J Biol Chem.* **2013**, *4*, 91; b) C. S. Gondi, J. S. Rao, *Expert Opin. Ther. Targets* **2013**, *17*, 281; c) V. Turk, V. Stoka. O. Vasiljeva, M. Renko, T. Sun, B. Turk, D. Turk, *Biochim. Biophys. Acta***. 2012**, *1824*, 68.

19. S. Gobec, R. Frlan, *Curr. Med. Chem.* **2006**, *19*, 2309.

20. M. Calderon, R. Graeser, F. Kratz, R. Haag, Bioorg. Med. Chem. Lett. 2009, 19, 3725–3728; b) R. Haag, F. Kratz, *Angew. Chem. Int. Ed*. **2006**, *45*, 1198; c) R. Duncan, *Nat. Rev. Cancer.* **2006**, *6*, 688; d) K. L. Kiick, *Science* **2007**, *317*, 1182; e) Y. J. Zhong, L.H. Shao Y. Li, *Int. J. Oncol.* **2013**, *42*, 373.

21. S. Silva Cotrin, L. Puzer, W. A. de Souza Judice, L. Juliano, A. K. Carmona, M. A. Juliano*, Anal. Biochem*. **2004**, *335*, 244**.**

22. a) C. Argyo, V. Weiss, C. Bräuchle, T. Bein, *Chem. Mater.* **2014**, *26*, 435; b) J. El Haskouri, D. Ortiz de Zarate, C. Guillem, J. Latorre, M. Cald s, A. Beltrán, D. Beltrán, A. B. Descalzo, G. Rodríguez-López, R. Martínez-Máñez, M. D. Marcos, P. Amorós, *Chem. Commun***. 2002**, 330**.**

23. a) V. V. Rostovtsev, L. G. Green, V. V. Fokin, K. B. Sharpless, *Angew. Chem. Int. Ed.* **2002**, *41*, 2596; b) C. W. Tornoe, C. Christensen, M. Meldal, *J. Org. Chem*. **2002**, *67*, 3057; c) H. C. Kolb, M. G. Finn, K. B. Sharpless, *Angew. Chem. Int. Ed.* **2001**, *40*, 2004.

24. L. Foghsgaard, D. Wissing, D. Mauch, U. Lademann, L. Bastholm, M. Boes, F. Elling, M. Leist, M. Jäättelä, *J. Cell. Biol*. **2001**, *153*, 999.

25. a) I. Lynch, K. A. Dawson *Nano Today*, **2008**, *3*, 40; b) M. Lundqvist, J. Stigler, G. Elia, I. Lynch, T. Cedervall, K. A. Dawson, *Proc. Natl. Acad. Sci. USA* **2008***, 105***,** 14265.

26. R. M. McConnell, J. L. York, D. Frizzell, C. Ezell, *J. Med. Chem*. **1993**, *36*, 1084**.**

27. J. Deussing, W. Roth, P. Saftig, C. Peters, H. L. Ploegh, J. A. Villadangos, *Proc. Natl. Acad. Sci. U. S. A.,* **1998**, *95*, 4516.

28. F. A. Formari, J. K. Randolph, J. C. Yalowich, M. K. Ritke, D. A. Gewirtz, *Mol. Pharmacol.* **1994**, *45*, 649.

Chem. Eur. J., 2014, 20, 15309.

Cathepsin-B induced controlled release from peptide-capped mesoporous silica nanoparticles

Cristina de la Torre, Laura Mondragón, Carmen Coll, Félix Sancenón, María D. Marcos, Ramón Martínez-Máñez, Pedro Amorós, Enrique Pérez-Payá and Mar Orzáez.

Supporting Information

1.- Chemicals.

The chemicals tetraethylorthosilicate (TEOS), n-cetyltrimethylammonium bromide (CTABr), sodium hydroxide (NaOH), 3-aminopropyltriethoxysilane, tissue culture grade dimethylsulfoxide (DMSO), PBS, 4-pentynoic acid, anhydrous methylformamide (DMF), trifluoroacetic acid (TFA), and HPLC grade amino acids were purchased from Sigma-Aldrich Química S. A. (Madrid, Spain) and used without further purification. 3-(Azidopropyl)triethoxysilane was provided by SelectLab Chemicals. Sodium ascorbate and copper(II) sulphate pentahydrate ($CuSO_4 \bullet 5H_2O$) were from Scharlab (Barcelona, Spain). HPLC grade solvents and (benzotriazol-1-yloxy)tripyrrolidinophosphonium hexafluorophosphate (PyBOP) were obtained from Merck (Barcelona, Spain). TentaGel S RAM (90 μM, 0.2-0.25 mmol g^{-1}) resin was purchased from Iris Biotech (Marktredwitz, Germany). All other reagents were of general laboratory grade and were purchased from Merck unless otherwise stated. Cathepsin B enzyme, fluorogenic substrate and Ac-LVK-CHO cathepsin B inhibitor were purchased from Merk. D-MEM with L-glutamine, fetal bovine serum (FCS), trypan blue solution (0.4%) cell culture grade, trypsin, wheat germ agglutinin Alexa Fluor 647, and Hoechst 33342 were provided by Gibco-Invitrogen (Barcelona, Spain). The cell proliferation reagent WST-1 was obtained from Roche Applied Science (Madrid, Spain). Doxorubicin hydrochloride was provided by Sequoia Research Products, Ltd. (UK). All the products were used as received.

2.- **General methods.**

XRD, TGA, elemental analysis, TEM, N_2 adsorption-desorption, NMR, and fluorescence spectroscopy techniques were employed to characterize the synthesized materials. Powder X-ray measurements were performed on a Philips D8 Advance Diffractometer using CuKα radiation. Thermogravimetric analyses were carried out on a TGA/SDTA 851e Mettler Toledo balance, using an oxidant atmosphere (air, 80 mL/min) with a heating program consisting of a heating ramp of 10°C per minute from 393 to 1273 K and an isothermal heating step at the final temperature for 30 min. TEM images were obtained with a 100 JEOL JEM-1010 microscope. N_2 adsorption-desorption isotherms were recorded with a

Micromeritics ASAP2010 automated sorption analyzer. The samples were degassed at 120°C in vacuum overnight. The specific surface areas were calculated from the adsorption data in the low pressure range using the BET model. Pore size was determined following the BJH method. The size distribution of particle dispersions was measured with a Malvern Masterisizer 2000 (Malvern, UK) using acetonitrile as dispersant. For data evaluation, an optical model based on the Mie theory was created using the instrumental software assuming 1.45 as the real and 0.001 as the imaginary part of the refractive index of the particles. Results given are the mean of 5 successive measurements. Purifications and analysis of the complete peptide sequence by preparative HPLC were carried out by means of a Merck Hitachi L-2130 HPLC pump and a sample carrier L-2200 with a Lichrospher® 100 C18 (250 x 10 mm) column. The eluent was monitored at 220 nm employing a Merck Hitachi UV Detector L-2400 spectrophotometer. HPLC analysis was performed using a Merck Hitachi L-2130 HPLC pump and L-2200 autosampler and employing a Lichrospher® 100 C18 (150 x 3.9 mm) column, and as mobile phase different acetonitrile gradients in aqueous 0.1 % TFA. Mass spectrometry analysis was performed employing a MALDI TOF/TOF 4700 Proteomics Analyzer from Applied Biosystems. Live cellular internalization studies were performed in a confocal Leica microscope handled with a TCS SP2 system, equipped with an acoustic optical beam splitter (AOBS) and Leica microscope TCS SL. Cell viability measurements were carried out with a Wallac 1420 workstation.

3.- Synthesis of peptide P.

Peptide sequence alkynyl-GIVRAKEAEGIVRAK-OH (**P**) was synthesized employing Fmoc-based solid phase Chemistry in a 433A Applied Biosystems Peptide synthesizer. In order to prepare the attachment of the peptide to the solid, a molecule of 4-pentinoic acid was attached to the N-terminal side of the peptide by formation of an amide bond. The peptide was cleaved from the resin by treatment with trifluoroacetic acid (TFA 94%, TIS 1% and H_2O 5%) and purified by preparative RP-HPLC (Lichrospher 1 100 C18, 10 mm) using different acetonitrile gradients in aqueous 0.1 % TFA. The identity and purity was confirmed by HPLC and MALDI-TOF mass spectrometry.

4.- Synthesis of mesoporous MCM-41 nanoparticles.

The MCM-41 mesoporous nanoparticles were synthesised by the following procedure: n-cetyltrimethylammonium bromide (CTABr, 1.00 g, 2.74 mmol) was first dissolved in 480 mL of deionised water before adding 3.5mL of a solution of NaOH 2M till getting a basic pH 8. Then, the solution was heated to 80 °C and TEOS (5.00 mL, $2.57 \cdot 10^{-2}$ mol) was then added dropwise to the surfactant solution at maximum stirring. The mixture was stirred for 2 h at 80 °C. A white precipitate was obtained and isolated by centrifugation. Once isolated, the solid was washed with deionised water and ethanol till obtaining neutral pH in the solution, and was dried at 60 °C (MCM-41 as-synthesised). To prepare the final porous material (MCM-41), the as-synthesised solid was calcined at 550 °C using an oxidant atmosphere for 5 h in order to remove the template phase.

Synthesis of solid S1.

500 mg of calcined MCM-41 and 140 mg (0.4 mmol) of safranin O dye were suspended in 15 ml of acetonitrile. Then the mixture was stirred for 24 h at room temperature with the aim of achieving the maximum loading in the pores of the MCM-41 scaffolding. Afterward an excess of 3-(azidopropyl)triethoxysilane (0.62 g, 2.5 mmoles) was added, and the suspension was stirred for 5.5 h. Finally, the solid was filtered off and dried at vacuum.

Synthesis of solid S1-P.

A mixture of **S1** nanoparticles (20 mg) and **P** (20 mg) were suspended in a mixture of DMF-water 50:50 (v:v) (20 ml) followed by the addition of safranin O dye (20 mg) in order to avoid the delivery of the dye from the pores. Then, 18 µL of $CuSO_4$ 10^{-2} mol/L solution and 180 µL of sodium ascorbate 10^{-3} mol/L were added to the previous mixture. The final mixture was stirred at 90 °C for 3 days. The nanoparticles were centrifugated and washed thoroughly with water. The resulting solid **S_1-P** was dried under vacuum.

Synthesis of solid S2-P.

200 mg of calcined MCM-41 and 96 mg of (0.18 mmol) of doxorubicin hydrochloride chemotherapeutic were suspended in 15 ml of water. Then the mixture was stirred for 24 h at room temperature with the aim of achieving the maximum loading in the pores of the MCM-41 scaffolding. The solids were filtered and then an excess of 3-(azidopropyl)triethoxysilane (240 uL g, 0.96 mmoles) was added in 15 ml of acetonitrile and the suspension was stirred for 5.5 h. Finally, the solid was filtered off and dried at vacuum. In a second step these nanoparticles (20 mg) and **P** (20 mg) were suspended in a mixture of DMF-water 50:50 (v:v) (20 ml) followed by the addition of doxorubicin (10 mg) in order to avoid the delivery of the dye from the pores. Then 18 µL of $CuSO_4$ 10^{-2} mol/L solution and 180 µL of sodium ascorbate 10^{-3} mol/L were added to the previous mixture. The final mixture was stirred at 90 °C for 3 days. The nanoparticles were centrifugated and washed thoroughly with water. The resulting solid **S2-P** was dried under vacuum.

5.- Materials characterization.

Figure 1 (see manuscript) shows the X-ray diffraction (XRD) patterns of the nanoparticulated MCM-41 matrix as-synthesised, the MCM-41 calcined, **S1** solid (loaded with safranin O and functionalized with azide moieties) and the final material **S1-P** (with the peptide sequence **P** anchored on the outer surface). The MCM-41 as-synthesised displayed the four typical low-angle reflections of a hexagonal-ordered matrix indexed at (100), (110), (200) and (210) Bragg peaks. In curve of MCM-41 calcined, a significant shift of the (100) peak in the XRD is observed. These observations are in agreement with the condensation of silanols in the calcination step, which caused an approximate cell contraction of 6-8 Å. Finally, curves c and d shows the **S1** and **S1-P** solids XRD patterns. For both materials a broadening of the (100) and (200) peaks are observed due to a reduction in contrast related to the functionalisation process and to the filling of mesopores with safranin O. Nonetheless, the intensity of the (100) peak in this pattern strongly indicates that the loading process with the dye and the additional functionalisation with 3-(azidopropyl)triethoxysilane and the subsequent anchoring of peptide **P** did not modify the mesoporous MCM-41 scaffold.

In Figure SI-1 (curve a), the N_2 adsorption-desorption isotherms of the MCM-41 calcined nanoparticles is represented. This curve displays an adsorption step with a P/P_0 value of between 0.1 and 0.3, corresponding to a type IV isotherm, which is typical of mesoporous materials. This first step is due to nitrogen condensation in the mesopores. With the BJH model on the adsorption curve of the isotherm, the pore diameter and pore volume were calculated to be 3.23 nm and 0.85 cm^3g^{-1}, respectively. The absence of a hysteresis loop in this range and the low BJH pore distribution suggested a cylindrical uniformity of mesopores. The total specific area was 1028.05 m^2g^{-1}, calculated using the BET model. The a_0 cell parameter (4.43 nm), the pore diameter (3.23 nm) and the wall thickness (1.98 nm) were calculated by from XRD, porosimetry and TEM studies. A second remarkable feature of the curve is the characteristic H1 hysteresis loop that appears in the isotherm at a high relative pressure ($P/P_0 > 0.8$) and associated with a wide pore size distribution. This corresponds to the filling of the large pores among the nanoparticles (0.32 cm^3g^{-1} calculated by the BJH model) due to textural porosity. For the **S1** material, the N_2 adsorption-desorption isotherm is typical of mesoporous systems with filled mesopores (see Figure SI-1, curve b). In this case, and as expected, a lower N_2 adsorbed volume (0.10 cm^3g^{-1}) and surface area (90.7 m^2g^{-1}) were found when compared with the starting MCM-41 material. As observed, this solid presents a curve with no gaps at low relative pressure values if compared to the mother MCM-41 matrix (curve a). Table SI-1 shows the BET-specific surface values, pore volumes and pore sizes calculated from the N_2 adsorption-desorption isotherms for MCM-41 calcined and **S1** and **S2** solids.

The contents of grafted peptide and cargos in solids **S1**, **S1-P** and **S2-P** were determined by thermogravimetric and elemental analysis and are shown in Table SI-2.

TEM images for the MCM-41 calcined sample, **S1** and **S1-P** solids are depicted in Figure 2. In all cases, a detailed look to individual nanoparticles, showed the typical channels of the MCM-41 matrix visualized as alternate black-white lines.

Finally, a particle diameter of ~100 nm was determined. **S2-P** shows a similar XRD profile (see manuscript) and TEM images to that observed for **S1-P**. Dynamic light scattering (DLS) studies showed particles with a mean diameter of 94.1 nm for calcined MCM-41 and of 106.5 nm for **S1-P** solid (see Figure SI-2 and Table SI-3). Also, Figure SI-2 showed that calcined MCM-41 nanoparticles and the final material **S1-P** formed some aggregates of 534.7 and 421.4 nm of diameter, respectively.

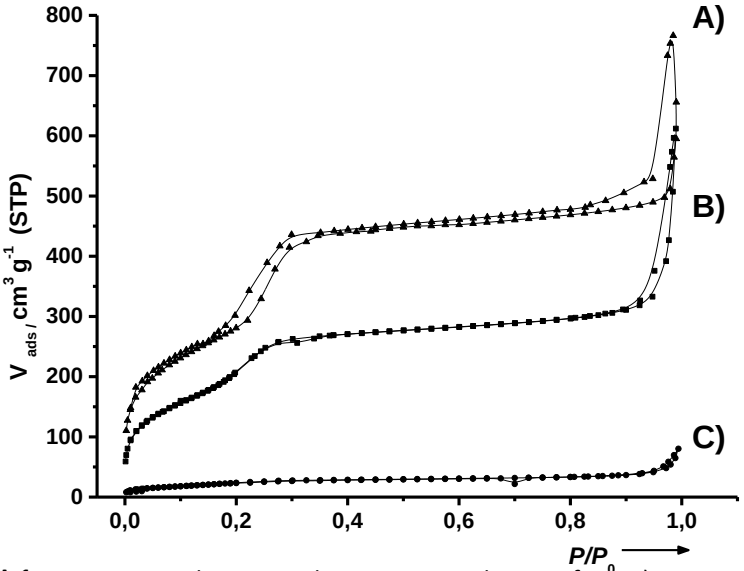

Figure SI-1. Nitrogen adsorption–desorption isotherms for: a) MCM-41 calcined mesoporous material and b) **S2** and c) **S1** material.

Table SI-1. BET-specific surface values, pore volumes and pore sizes calculated from the N_2 adsorption-desorption isotherms for selected materials.

	S_{BET} ($m^2\ g^{-1}$)	Total pore volume [a] ($cm^3\ g^{-1}$)	BHJ pore [b] (nm)
MCM-41	1028.05	3.23	0.85
S1	90.70	-	0.10
S2	167.10	-	0.56

[a] Pore volumes and pore sizes were associated with only intraparticle mesopores.

[b] Pore size estimated by the BJH model applied to the adsorption branch of the isotherm.

Table SI-2. Content (α) in gram of anchored molecules and cargo per gram of SiO_2 for the prepared solids.

	α_{azide} ($g \cdot g^{-1}$ SiO_2)	α_{cargo} ($g \cdot g^{-1}$ SiO_2)	$\alpha_{peptide}$ ($g \cdot g^{-1}$ SiO_2)
S1	0.033	0.370	-
S1-P	0.033	0.185	0.084
S2-P	0.033	0.085	0.068

Table SI-3. Diameter and zeta potential of calcined MCM-41and **S1-P** nanoparticles.

	Diameter (nm)	**% of nanoparticles**	**Zeta potential (mV)**
MCM-41	94.1	92.2	-26.3
	534.7	7.8	
S1-P	106.5	97.8	48.1
	421.5	2.2	

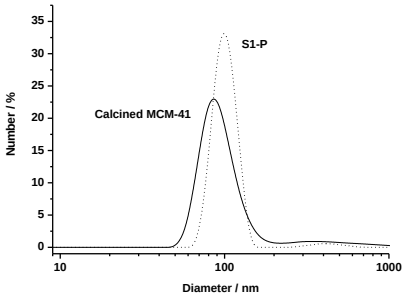

Figure SI-2. Size distribution by number of particles obtained by DLS studies for calcined MCM-41 and **S1-P**.

6.- Cargo release studies.

S1-P consists in mesoporous MCM-41-type nanoparticles containing safranin O in the pores and capped with peptide **P**. As part of the nanoparticles design, the grafted peptide H-GIVRAKEAEGIVRAK-OH was expected to cap the pores and inhibit cargo delivery. Subsequent action of cathepsin B is anticipated to cleave the amide bond from positively charged arginine (R) and alanine (A) amino acids

in the target GIVRAK sequence, thus allowing cargo release. In order to check this aperture mechanism release kinetics studies were carried out. In a typical experiment, 0.5 mg of solid **S1-P** were suspended in 2.8 mL of cathepsin B buffer (i.e. 50 mM AcNa, 1 mM EDTA, 8 mM DTT) at pH 5.4 (optimal conditions for enzyme activity as in the lysosomes) in both the absence and the presence of cathepsin B enzyme. The suspensions were stirred at 37 ^{o}C, at certain time aliquots were separated and centrifuged to eliminate the solid and dye delivery was determined by monitoring fluorescence of safranin O (λ_{exc} = 520 nm, λ_{em} = 585 nm) in the aqueous phase. Delivery results are shown in Figure SI-3. In the absence of cathepsin B a nearly flat baseline was observed indicating that the safranin O remains in the nanoparticles without release. In contrast, in the presence of cathepsin B, delivery of safranin O was observed as an increased dye emission in the solution. The safranin O release observed in the presence of cathepsin B is a consequence of the hydrolysis of the anchored peptide sequence **P**. The progressive hydrolysis of **P** significantly reduced its size with the subsequent pore opening and dye release. In order to prove the specificity of the molecular gate, similar kinetic release studies were carried out employing other enzymes such as amylases or ureases. No significant degradation and release of the cargo was observed with these enzymes (data not shown) proving the crucial role of cathepsin B in the aperture of the molecular gate.

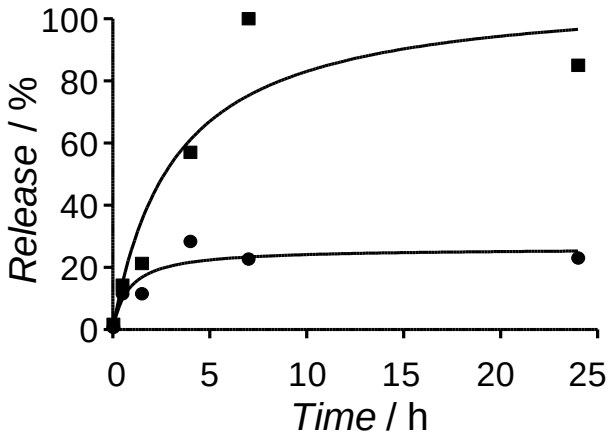

Figure SI-3. Release kinetics of safranin O from **S1-P** at 37ºC in the presence (■) or not (●) of recombinant cathepsin B enzyme.

In a second study, delivery studies from **S1-P** with a lysosomal extract of HeLa cells were carried out. The lysosomal extract is an optimal natural source of cathepsin B and would be useful to evaluate the correct behaviour of **S1-P** material in living cells. Previously to its use, the total protein amount in the lysosomal extract was determined (0.07 $mg \cdot mL^{-1}$). For the delivery studies, 0.5 mg of solid **S1**-**P** were suspended in 2.8 mL of cathepsin B buffer at pH 5.4 and 0.5 mL of lysosomal extract (0.035 mg) from HeLa cells was added. As a control, the same amount of solid **S1-P** was suspended in aqueous media at the same pH and, instead of lysosomal extract, a mixture of proteins with the same concentration than that measured for the lysosomal extract, was added (see Manuscript Figure 1). As seen, addition of lysosomal extract of HeLa cells to aqueous suspensions of solid **S1-P** induced a remarkable pore opening and a fast release (80% of maximum dye release after ca. 50 minutes). Moreover, in the absence of lysosomal extract the **S1-P** remains tightly capped.

7.- Cell line and primary cells experiments.

Cell culture conditions.

HeLa human cervix adenocarcinoma were purchased from the German Resource Centre for Biological Materials (DSMZ). Murine embryonic fibroblasts from wild-type (MEFs WT), cathepsin B–deficient (MEFs CatB -/-) were used for experiments at passages 5-9 and were kindly provided by J. A. Villadangos. Cells were grown in D-MEM supplemented with 10% FBS. Penicillin and streptomycin was added to the medium in case of MEFs. Cells were maintained at 37 °C in an atmosphere of 5% carbon dioxide and 95% air and underwent passage twice a week.

Lysosomal extract of HeLa cells.

Cells were plated in sterile ϕ 150 mm plates at 80% of confluence. Then, medium was removed, cells were washed with PBS before adding 10 mL of cytosolic extraction buffer (20 µg/mL digitonin, 250 mM sucrose, 20 mM Hepes, 10 mM KCl, 1.5 mM $MgCl_2$, 1 mM EDTA, 1 mM EGTA, 1 mM pefablock, pH 7.5) per

plate. Once the buffer was added, cells were incubated for 10 min on ice and submitted to continuous shaking. After this initial incubation, buffer was removed and 8-10 mL of lysosomal extraction buffer containing this time a concentration of 200 μg/mL of digitonin was put in the plate. Again, cells were incubated for 10 min on ice and submitted to continuous shaking. The digitonin concentration and treatment times were optimized to result in the total release of cytosolic LDH activity without disruption of lysosomes in the first step. To determine the proper obtention of the lysosomal extract, cathepsin activity was determined by mixing the cytosolic and lysosomal extracts with the cathepsin reaction buffer (50 mM sodium acetate, 4 mM EDTA, 8 mM DTT, 1 mM pefablock, pH 6.0) in the presence of a fluorogenic substrate of cathepsin B (Z-RR-AMC). The enzyme activities were estimated by adding one volume of 20 μM zRR-7-amino-4-methylcoumarin (AMC) (Calbiochem-Novabiochem) in the cathepsin reaction buffer (50 mM sodium acetate, 4 mM EDTA, 8 mM DTT, 1 mM pefablock, pH 6.0). Kinetic release of the AMC (λ_{exc} = 380 nm, λ_{em} = 442 nm) was followed over 20 min at 37 °C with a Wallac 1420 workstation. No cathepsin B activity was detected in the cytosolic extracts.

WST-1 cell viability assay.

Cells were seeded in sterile 24-well microtiter plates at a seeding density of 2 x 10^4 cells/well for HeLa and 4 x 10^4 for MEFs WT and they were allowed to settle for 24 h. **S1-P** in PBS was added to cells at a final concentration of 200, 150, 100 and 50 μg/mL. After 23 h, WST-1 (35 μL of a 5 mg/mL solution) was added to each well. Cells were further incubated for 1 h (a total of 24 h of incubation was therefore studied), and absorbance was measured at 595 nm (See Figure SI-4). In case of **S2-P**, the nanoparticles were suspended in PBS and added to cells at a final concentration of 50 μg/mL. WST-1 was added after 47 h to each well and further incubated for 1 h and then absorbance was measured.

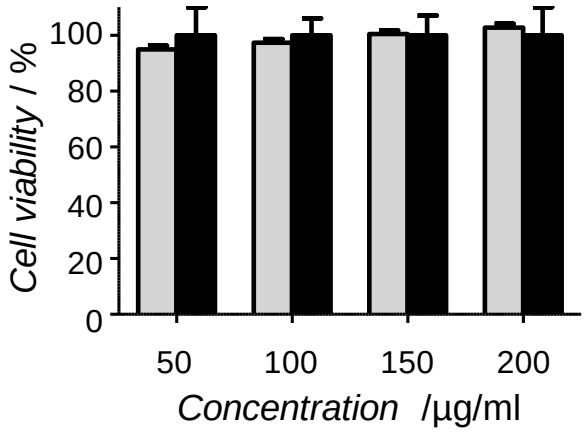

Figure SI-4. WST-1 cell viability assay. HeLa and MEFs WT cells were treated with **S1-P** at concentrations of 200, 150, 100 and 50 μg/mL and cell viability was measured 24 h later. Two independent experiments were developed including triplicates. Data are represented as mean ± s. e.

S1-P cellular internalization (flow cytometry studies).

HeLa cells were seeded at $2.5 \cdot 10^4$ cells per well and MEFs cell were seeded at $1.53 \cdot 10^4$ cells per well in a 24 well plate. After 24 h, cells were treated with MCM-41 and S1 at concentration of 100 $ug \cdot ml^{-1}$. Cells were incubated for 20 hours, then washed with PBS twice and detached from the plate. Quantification of Safranine O fluorescence was performed with the WinMDI program, version 2.9. Two independent experiments containing triplicates were performed with similar results.

S1-P cellular internalization (live confocal microscopy studies).

HeLa cells were seeded in ϕ 24 mm glass coverslips in six-well plates at a seeding density of 10^5 cells/well. After 24 h, cells were treated when indicated with 4 μl of cathepsin B inhibitor (4μM). 4 h later, cells were treated with **S1-P** or **S2-P** at a final concentration of 100 μg/mL (**S1-P**) or 50 μg/mL (**S2-P**). For **S1-P**, the medium was removed to eliminate compounds after 18 h of incubation and cells were stained with 10 ng/mL of Hoechst 33342 and 5 mg/mL wheat germ agglutinin (WGA) Alexa Fluor 647 for 30 min in PBS containing 10% FBS. Slides

were visualized under a confocal microscope employing Leica TCS SP2 AOBS (Leica Microsystems Heidelberg GmbH, Mannheim, Germany) inverted laser scanning confocal microscope using oil objectives: 63X Plan-Apochromat-Lambda Blue 1.4 N.A. Confocal microscopy studies were performed by Confocal Microscopy Service (CIPF). Two-dimensional pseudo colour images (255 colour levels) were gathered with a size of 1024 x 1024 pixels and Airy 1 pinhole diameter. All confocal images were acquired using the same settings and the distribution of fluorescence was analyzed using the Image J Software. MEFs WT and MEFs CatB -/- cells were seeded in ϕ 24 mm glass coverslips in six-well plates at a seeding density of 10^5 cells/well. After 24 h were incubated with **S1-P** following the same procedure than in HeLa cells.

Endosomal internalization and lysosomal localization of S1-P.

In order to check the supposed endosomal internalization and subsequent lysosomal localization of the nanoparticles, HeLa cells were electroporated with the lysosomal-associated membrane protein 1 (LAMP1) fused to the green fluorescent protein (GFP, LAMP1-GFP). LAMP1 is a glycoprotein located in the lysosomal membrane, which gives a dotted pattern distribution when fused to the GFP due to its lysosomal membrane association. After electroporation, HeLa cells were treated with **S1-P** at 50 μg/mL for 24 h. Subsequent analysis of the cells showed the existence certain colocalization among the dotted pattern associated to nanoparticles and the dotted pattern associated to LAMP1-GFP-associated vesicles, thus proving the lysosomal localization of the nanoparticles (see Figure SI-5).

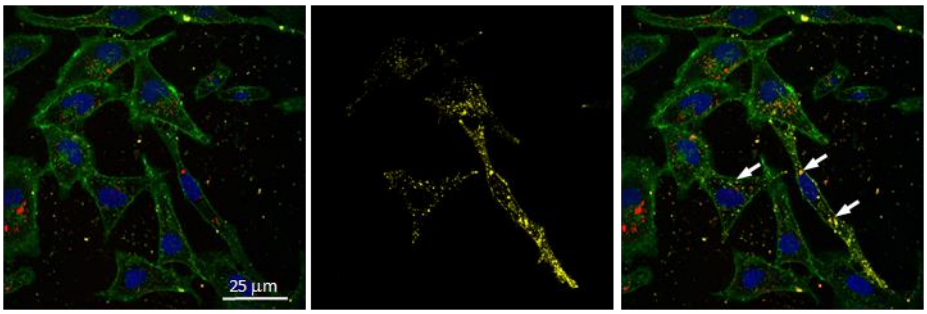

Figure SI-5. To determine the lysosomal localization of the nanoparticles, HeLa cells were electroporated with LAMP1–GFP and treated with **S1-P** at 50 μg/mL. The co-localization of the LAMP1–GFP lysosome-associated signal (yellow) and nanoparticle safranin O associated fluorescence (red) was observed in the presence of DNA marker Hoechst 33342 (blue) and plasma membrane marker WGA-Alexa-Fluor 647 (green), thus proving the lysosomal localization of the nanoparticles. White arrows indicate the co-localization of LAMP1–GFP with nanoparticles.

S2-P cellular internalization (live confocal microscopy studies).

For doxorubicin release studies, MEFs WT and MEFs CatB -/- cells were pre-treated or not in the presence of 4 μM of cathepsin B inhibitor, then incubated for 44 h with **S2-P** at concentration of 100 $\mu g/mL^{-1}$ and finally were analyzed by confocal microscopy. In this case, a TCS SL (Leica) confocal microscope was employed.

2.6. Caspase 3 targeted cargo delivery in apoptotic cells using capped mesoporous silica nanoparticles

Cristina de la Torre,[a,b,c+] Laura Mondragón,[a,b,c,d+] Carmen Coll,[a,b,c] Alba García-Fernández,[a,b,c] Félix Sancenón,[a,b,c] Ramón Martínez-Máñez,[*a,b,c] Pedro Amorós,[e] Enrique Pérez-Payá[f,g] and Mar Orzáez[*f]

[a] *Centro de Reconocimiento Molecular y Desarrollo Tecnológico (IDM), Unidad Mixta Universidad Politécnica de Valencia-Universidad de Valencia.*

[b] *Departamento de Química, Universidad Politécnica de Valencia, Camino de Vera s/n, 46022, Valencia, Spain.*

[c] *CIBER de Bioingeniería, Biomateriales y Nanomedicina (CIBER-BBN).*

[d] *Centre Méditerranéen de Médecine Moléculaire (C3M) - Equipe "Contrôle métabolique des morts cellulaires" – Université Nice Sophia Antipolis Institut national de la santé et de la recherche médicale (Inserm) U1065, BP 2 3194, 06204, Nice (France).*

[e] *Institut de Ciència del Materials (ICMUV), Universitat de València. P.O. Box 22085, E-46071 València, Spain.*

[f] *Centro de Investigación Príncipe Felipe, Laboratorio de Péptidos y Proteínas. Avda. Autopista del Saler 16, 46012 Valencia, Spain.*

[g] *Instituto de Biomedicina de Valencia, IBV-CSIC, Jaume Roig 11, 46010 Valencia, Spain.*

+ Both authors contributed equally to this work.

Received: ***June 2015***
Published online: ***Oct 2015***

Chem. Eur. J. 2015, 21, 15506

Excessive apoptotic cell death is at the origin of several pathologies, such as degenerative disorders, stroke or ischemia-reperfusion damage. In this context strategies to improve inhibition of apoptosis and other types of cell death are of interest and may represent a pharmacological opportunity for the treatment of cell death-related disorders. In this scenario new peptide-containing delivery systems (solids **S_1-P_1** and **S_1-P_2**) are described based on mesoporous silica nanoparticles (MSNs) loaded with a dye and capped with the KKGDEVDKKARDEVDK (**P_1**) peptide that contains two repeats of the DEVD target sequence which are selectively hydrolysed by caspase-3 (**C3**). This enzyme plays a central role in the execution-phase of apoptosis. HeLa cells electroporated with **S_1-P_1** are able to deliver the cargo in the presence of staurosporin (STS) which induces apoptosis with the consequent activation of the cytoplasmic **C3** enzyme. Moreover the nanoparticles **S_1-P_2**, containing both a cell-penetrating TAT peptide and P1 also entered in HeLa cells and delivered the cargo preferentially in cells treated with the apoptosis ***inducer cisplatin.***

Recently, the combination of new advances in nanotechnology and biomolecular chemistry resulted in the design of new nanodevices able to develop innovative biologically related functions in areas such as bioengineering, biosensing and bionanotechnology.[1] In this context, mesoporous silica nanoparticles (MSNs) have proved to be excellent containers for storage and delivery due to their unique mesoporous structure and large loading capacity.[2] Moreover mesoporous silica can be easily functionalized, and this has allowed the design of MSNs equipped with switchable molecular/supramolecular pore-capping ensembles able to be selectively opened with a number of different chemical, physical and biochemical stimuli.[3] This results in the design of stimuli-responsive hybrid gated materials showing zero release yet able to deliver the cargo at-will.[4]

In this scenario, biomolecules have been widely used in the design of gated MSNs.[5] Among them, the combination of peptides as caps and enzymes as triggers offers great potential. In fact, although not as popular as other stimuli,

the use of enzymes in gated materials is highly appealing as the use of tailor-made peptides and specific enzymes may induce remarkable selectivity to advanced gated devices for on-command delivery in realistic biological environments. Although certain examples have been reported using esterases,[6] glycosidases,[7] peptidases,[8] reductases,[9] ureases[10] and DNases[11] this subfield in the area of gated nanochemistry has not been fully explored. Moreover, the participation of enzymes in multiple biological steps makes this approach unique for the design of advanced delivery devices and there is still plenty of research to develop in this field. In particular, and as far as we know, there are not MSNs specifically designed to be selectively opened in the presence of caspase enzymes.

A number of gated materials have been designed for delivery of cytotoxics, with the main objective of reducing the secondary effects associated to classical chemotherapy due to the unspecific biodistribution of the drugs.[12] In contrast to this approach we have put our attention on the design of gated MSNs with the objective of decreasing unwanted cell death. Excessive cell death is at the origin of several pathologies, such as degenerative disorders, stroke or ischemia-reperfusion damage.[13] Therefore, controlled inhibition of cell death represents a pharmacological opportunity for the treatment of these disorders. Among the different existing types of cell death in this study we have focused on apoptosis,[14] a biological process in which the cell undergoes a series of biochemical and morphological changes that induce the destruction of the cell in a silent and ordered way. This process is initiated by a series of ligands that activate a family of cell death receptors located in the plasma membrane (extrinsic apoptosis) or after the induction of mitochondrial outer membrane permeabilization (MOMP) by internal cell death stimuli (intrinsic apoptosis).[15] No matter the origin, both pathways converge in the activation of a family of cysteine aspartyl proteases known as caspases. Once activated, these enzymes act as the executioner machinery of apoptosis cleaving essential substrates of the cell, causing the dismantling of the cells.[16] In this scenario we have focused on caspase-3 (**C3**). The **C3** cleavage site on protein substrates is highly conserved and consists of a four

amino acid target site (i.e. DEVD; Asp-Glu-Val-Asp) which is cleaved after the Asp residue.[17] This specificity allows **C3** to be highly selective.

A first approach to target apoptotic cells would be to develop selective-delivery carriers that are able to release their cargo in these particular cells. This will allow the development, in the near future, of nanoparticles with anti-apoptotic cargo, to stop cell death. In this context, and taking into account our previous experience in the development of gated nanoparticles containing peptides as molecular caps,[18] we report herein the preparation of gated MSNs capable of selectively deliver their cargo in the presence of activated **C3** enzyme in cells (Figure 1A), once apoptosis has been induced. We selected mesoporous MCM-41 nanoparticles (ca. 100 nm) as inorganic scaffold which was synthesized according to reported procedures.[19] The nanoparticles were loaded with safranin O dye and the external silica surface was functionalized with 3-(azidopropyl)triethoxysilane (solid $\mathbf{S_1}$). The initial MCM-41 and $\mathbf{S_1}$ support were subsequently characterized using standard techniques. The mesoporous structure of MCM-41 and $\mathbf{S_1}$ were confirmed by TEM and XRD studies (Figure 1B and 1C). The starting MCM-41 material and $\mathbf{S_1}$ showed a spherical shape of ca. 110 nm (see Supporting Information). Moreover the MCM-41 calcined starting material showed a typical adsorption-desorption isotherm of MSNs. The application of the BET model resulted in a value for the total specific surface of 1001 m^2g^{-1} and a pore volume of 0.79 cm^3g^{-1}. Additionally, a pore diameter of 2.52 nm was calculated. In contrast, the N_2 adsorption-desorption isotherm of $\mathbf{S_1}$ was typical of mesoporous systems with partially filled mesopores and a significant decrease in the N_2 volume adsorbed and in the surface area was found. In particular $\mathbf{S_1}$ showed a specific surface of 438 m^2g^{-1} and a pore volume of 0.31 cm^3g^{-1} (see Supporting Information for further details).

Finally $\mathbf{S_1}$ was capped with the peptidic sequence NH_2-KKGDEVDKKARDEVDK-alkyne, $\mathbf{P_1}$, (containing two repeats of the DEVD target sequence). $\mathbf{P_1}$ was attached to $\mathbf{S_1}$ by the copper(I)-catalyzed Huisgen azide/alkyne 1,3-dipolar cycloaddition "click" reaction,[20] which induces the formation of a 1,2,3-triazole heterocycle upon reaction of the azide group (on the solid) and the triple bond (on $\mathbf{P_1}$). A

scheme of the final material is depicted in Figure 1A. The $\mathbf{P_1}$-functionalized solid ($\mathbf{S_1}$-$\mathbf{P_1}$) was isolated by centrifugation and washed to eliminate both residual dye and free peptide. TEM analysis confirmed that $\mathbf{S_1}$-$\mathbf{P_1}$ retained the mesoporous structure (see Figure 1B and Figure SI-3). The safranine O and peptide contents in $\mathbf{S_1}$-$\mathbf{P_1}$ were determined by elemental analysis and thermogravimetric studies, and amounted to 0.130 and 0.034 mmol g^{-1} SiO_2, respectively (see Supporting Information).

To investigate the enzyme-responsive gating properties of $\mathbf{S_1}$-$\mathbf{P_1}$ in the presence of **C3** 0.5 mg of $\mathbf{S_1}$-$\mathbf{P_1}$ were suspended in PBS (10% glycerol, 1 mM DTT) and the suspension stirred at 37 ^{o}C in the absence and in the presence of **C3** enzyme. Uncapping and subsequent delivery of the dye was determined through the measurement of fluorescence emission at 585 nm (λ_{ex} = 520 nm) of the safranine O dye released. The delivery profile is displayed in Figure 1D. It shows values of safranine O release at each time normalized against total release. In the absence of caspase-3, solid $\mathbf{S_1}$-$\mathbf{P_1}$ showed a negligible dye release, indicating tight pore closure, whereas in the presence of **C3** enzyme a clear cargo release was observed due to the hydrolysis of the peptide sequence $\mathbf{P_1}$. After 400 minutes, ca. 80% of the total delivery was observed for $\mathbf{S_1}$-$\mathbf{P_1}$.

Proved the specific cargo release *in vitro*, the proper aperture of the gated $\mathbf{S_1}$-$\mathbf{P_1}$ material was studied *ex vitro* using HeLa cells. It is well know that when nanoparticles of ca 100 nm are in contact with cells these are usually internalized by endocytosis reaching lysosomes. However in this case due to the cytoplasmic localization of **C3** endocytosis of $\mathbf{S_1}$-$\mathbf{P_1}$ must be avoided. For that purpose, $\mathbf{S_1}$-$\mathbf{P_1}$ was introduced in HeLa cells by electroporation.

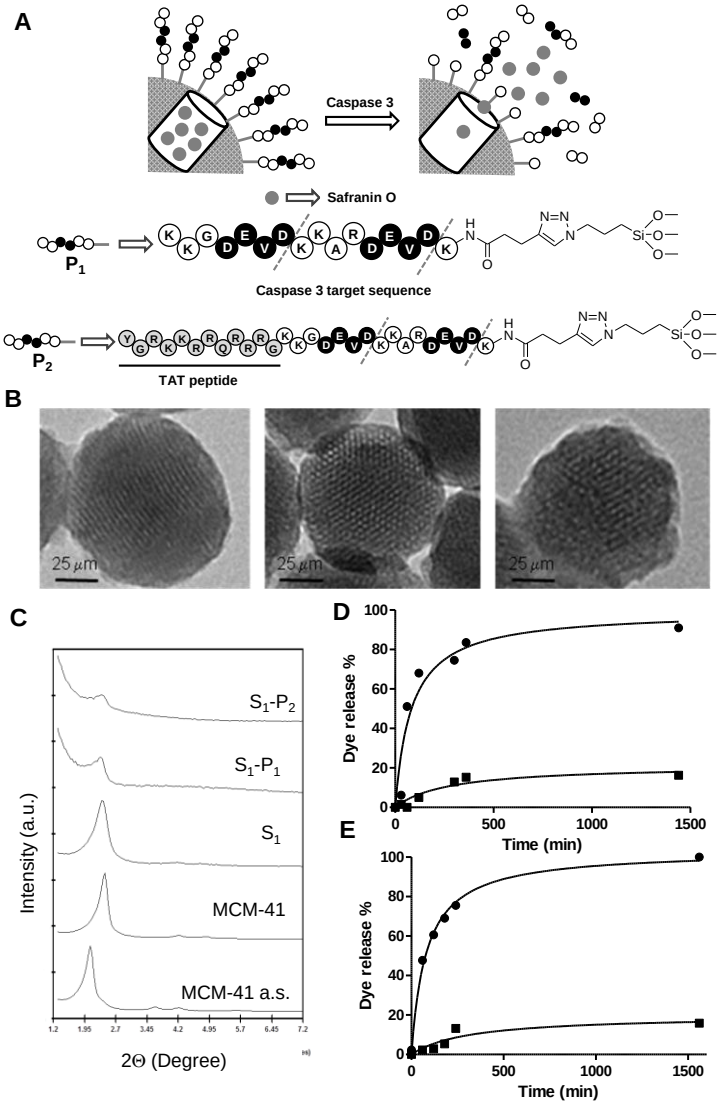

Figure 1. A) Schematic representation of the gated materials **S₁-P₁** and **S₁-P₂** capped with peptides **P₁** and **P₂**, dashed grey lines indicate the locations of caspase hydrolysis. B) From left to right, TEM images of calcined MCM-41, **S₁-P₁** and **S₁-P₂** showing the typical porosity associated to MCM-41 mesoporous matrix. C) Powder X-ray patterns of MCM-41 as synthesized, calcined MCM-41, **S₁**, **S₁-P₁** and **S₁-P₂**. D, E) *In vitro* release profiles of safranin O in the absence (■) and in the presence (●) of recombinant caspase-3 (**C3**) at 37 °C and pH 7.2 for **S₁-P₁** and **S₁-P₂**, respectively.

Staurosporin, a nonspecific protein kinase inhibitor that induces apoptosis with the consequent activation of **C3,** was used in HeLa cells [21]. Cleavage and aperture of the molecular gate of **S_1-P_1** by **C3** was assessed by confocal microscopy by means of safranin O associated fluorescence. For that purpose, cells were also stained with the DNA marker Hoechst 33342 and the cellular membrane marker Wheat Germ Agglutinin Alexa Fluor 647 (WGA). Results are shown in Figure 2A. HeLa cells electroporated with **S_1-P_1** in the absence of STS showed a poor cytoplasmic fluorescence associated to safranin O, whereas when similar experiments were carried out with cells treated with STS a clear safranin O fluorescence was observed. This difference was attributed to **C3** activation and the subsequent hydrolysis of the **P_1** peptide containing the DEVD target sequence that resulted in cargo delivery. Moreover, in order to further prove the specific **C3**-mediated aperture of **S_1-P_1**, HeLa cells were electroporated with **S_1-P_1** and treated with the **C3** inhibitor Q-VD-OPh[22] for 24 hours previous the addition of STS. The objective was to block **C3** activation. Under these conditions confocal microscopy images showed significant reduction of safranin O cytoplasmic signal, proving the major role of **C3** in the aperture of the molecular gate (Figure 2A). Quantification of the cytoplasmic fluorescence associated to safranin O was determined for the different treatments and it is shown in Figure 2B. In agreement with confocal images a significantly larger fluorescence was observed in cells electroporated with **S_1-P_1** in the presence of STS (**S_1-P_1**+STS) when compared with **S_1-P_1** and **S_1-P_1**+STS+Q-VD-OPh treatments. In order to discard toxicity associated with **S_1-P_1**, cell viability in the absence of apoptotic stimulus at different nanoparticle concentrations was evaluated by WST-1 (Figure 2C). No toxicity was found for **S_1-P_1** up to concentrations of 100 μg mL^{-1}.

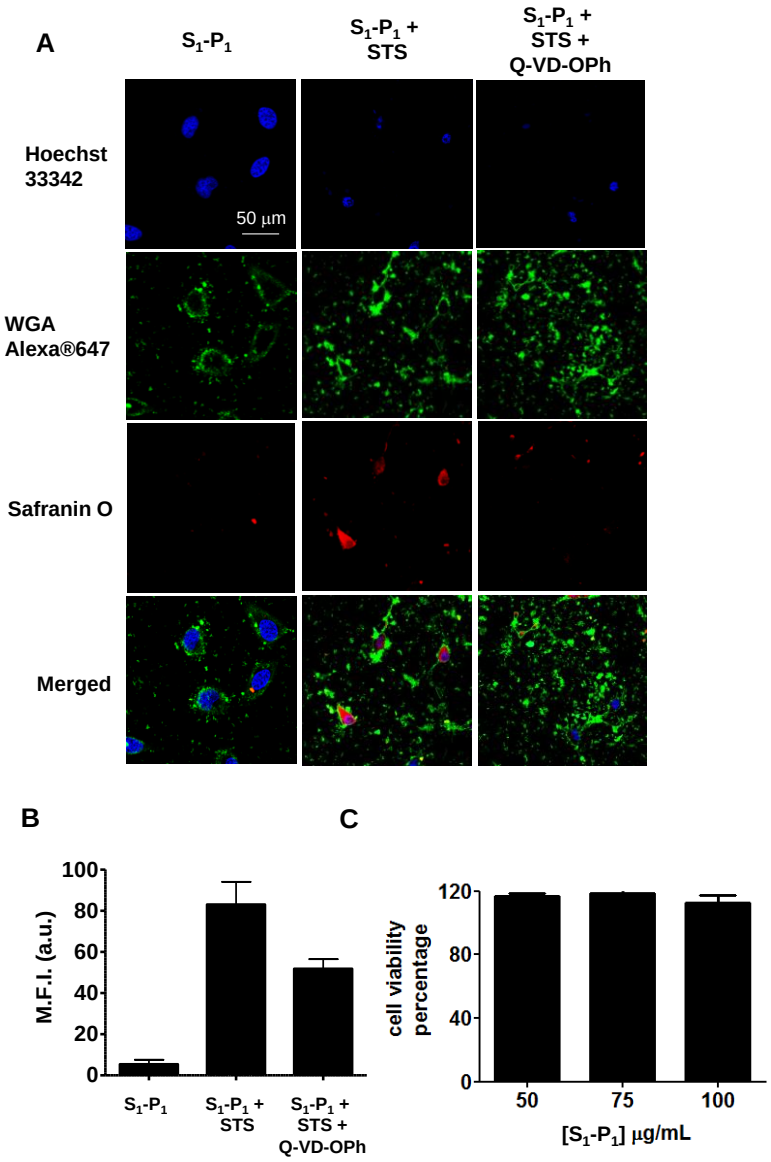

Figure 2. A) HeLa cells were electroporated in the presence of 100 μg/mL **S₁-P₁** and incubated for 24 hours, previous the addition of STS 1.5 μM when indicated for 4 hours. Inhibition of **C3** by Q-VD-OPh 20 μM was also performed 24 hours prior the addition of STS. The cellular uptake of **S₁-P₁** was followed by safranin O associated fluorescence (red) in the presence of DNA marker Hoechst 33342 (blue) and plasma membrane marker WGA Alexa Fluor®647 (green). B) Quantification of the safranin O associated fluorescence intensity for the different treatments. Three independent experiments were developed

obtaining similar results. Data are expressed as mean ± s. Statistically significant differences were found among the different treatments when paired t Student test were applied, C) Cell viability analyzed by WST-1 at different nanoparticle concentrations.

The experiments above demonstrated that MSNs were able to display cargo delivery in the presence of **C3** enzyme via hydrolysis of the $\mathbf{P_1}$ capping peptide. However *ex vivo* experiments were performed by electroporation in order to increase the permeability of the cell membrane allowing $\mathbf{S_1}$-$\mathbf{P_1}$ MSNs to be introduced in the cytosol where **C3** enzyme exists. In this context we also considered the fact that synthetic peptides can be designed containing both, amino acid sequences recognized by target-enzyme and amino acid sequences in charge of cell entry-control. In this scenario a new peptidic sequence based on the original $\mathbf{P_1}$ was synthesized but this time adding to the N-terminal the sequence corresponding to the cell penetrating peptide TAT (peptide $\mathbf{P_2}$, see Figure 1A).[23] The TAT peptide is known to facilitate cellular uptake of various molecular cargo from nanosize particles to small chemical molecules and large fragments of DNA.

Solid $\mathbf{S_1}$-$\mathbf{P_2}$ was synthesized following a similar procedure to that used for the preparation of $\mathbf{S_1}$-$\mathbf{P_1}$ (see Figure 1A). The mesoporous structure in $\mathbf{S_1}$-$\mathbf{P_2}$ was confirmed by TEM and XRD studies (see Figure 1B and 1C). The safranin O and peptide contents in $\mathbf{S_1}$-$\mathbf{P_2}$ were determined by elemental analysis and thermogravimetric studies, and amounted to 0.205 and 0.016 mmol g^{-1} SiO_2, respectively (see Supporting Information). $\mathbf{S_1}$-$\mathbf{P_2}$ nanoparticles were suspended in PBS (10% glycerol, 1 mM DTT) at 37 ^{o}C in the absence and in the presence of **C3** enzyme. The delivery kinetics profile is displayed in Figure 1E. $\mathbf{S_1}$-$\mathbf{P_2}$ showed a poor cargo delivery in the absence of recombinant **C3** whereas a clear cargo release was observed in the presence of this enzyme. Moreover studies in HeLa cells were performed following similar procedures than those used for $\mathbf{S_1}$-$\mathbf{P_1}$ but without the use of electroporation. In this case cisplatin (CDDP), which causes DNA crosslinkings, was employed as an apoptosis inducer able to activate **C3**.[24] In a typical experiment HeLa cells were seeded, and 24 hours later, were treated with $\mathbf{S_1}$-$\mathbf{P_2}$ for 6 hours and then CDDP was added when indicated. 24 hours later, cells

were stained with the DNA marker Hoechst 33342 and the cellular membrane marker WGA and cells were studied by confocal microscopy. Appearance of cytoplasmic associated safranin O fluorescence can be observed in case of the cells treated with **S_1-P_2** in the presence of CDDP (Figure 3A). By contrast, a very poor safranin O signal was detected in **S_1-P_2** treated cells in the absence of the apoptosis inducer. Subsequent quantification of safranin O cytoplasmic associated fluorescence showed a significant emission increase in cells treated with CDDP when compared to control cells (Figure 3B). Finally, to discard toxicity associated with **S_1-P_2** cell viability was evaluated by WST-1 in the absence of an apoptotic stimulus at different nanoparticle concentrations (Figure 3C). No important toxicity was found for **S_1-P_2** nanoparticles up to concentrations of 100 μg mL^{-1}.

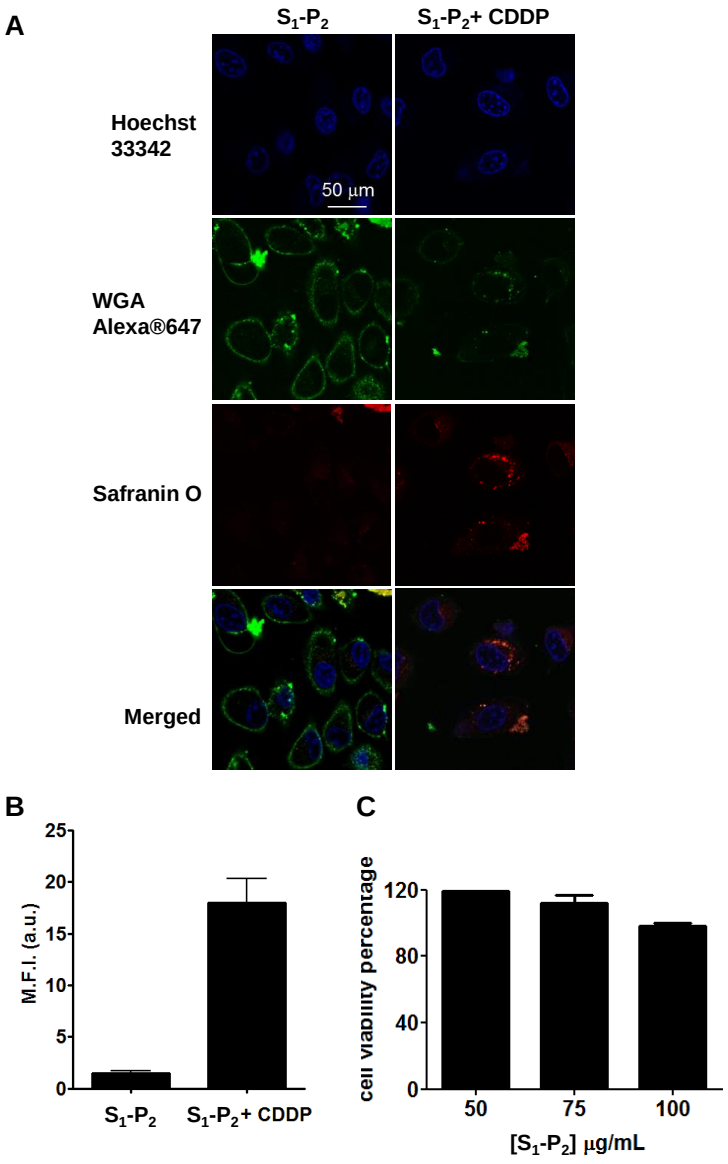

Figure 3. A) HeLa cells were treated with 100 μg/mL **S₁-P₂** and incubated for 4 hours previous the addition of CDDP 50 μM when indicated. After 24 hours of incubations confocal microscopy studies were performed. The cellular uptake of **S₁-P₂** was followed by safranin O associated fluorescence (red) in the presence of DNA marker Hoechst 33342 (blue) and plasma membrane marker WGA Alexa Fluor®647 (green). Cytoplasmic Safranin O associated fluorescence was observed in samples treated with **S₁-P₂** and CDDP, but not

in case of control samples treated only **S_1-P_2**. B) Quantification of the safranin O associated fluorescence intensity for the different treatments. Three independent experiments were developed obtaining similar results. Data are expressed as mean ± s. Statistically significant differences were found among the different treatments when paired t Student test were applied, C) Cell viability analyzed by WST-1 at different nanoparticle concentrations.

In summary, we have shown that it is possible to use capping peptide sequences on mesoporous silica supports in order to develop nanodevices showing nearly "zero" release yet specifically opened in the presence of the targeted proteolytic enzyme **C3** in cells. HeLa cells electroporated with **S_1-P_1** showed a poor cytoplasmic fluorescence associated to safranin O while a clear cargo release was observed in the presence of the apoptosis inducer STS. Moreover the nanoparticles **S_1-P_2**, containing both a cell-penetrating TAT peptide and **P_1**, entered in HeLa cells and delivered the cargo preferentially in cells treated with the apoptosis inducer cisplatin. These preliminary results can lead towards the adoption of new therapeutic strategies to inhibit apoptotic cell death. Based on the fact that the field of peptide-protease pair is well-known and offers advanced opportunities for on command delivery protocols, we believe that the synthetic strategy followed herein, which combines the use of mesoporous nanoparticles with highly specific targeting peptides, can have biomedical relevance to further design improved custom-made delivery systems for other particular diseases.

Acknowledgements

We thank the Spanish Government (Project MAT2012-38429-C04 and SAF2010-15512) and the Generalitat Valenciana (PROMETEOII/2014/061) for support. C.T. is grateful to the Spanish Ministry of Science and Innovation for her PhD fellowship. L.M. thanks the Generalitat Valenciana (VALI+D program), Nice city council ("Aides Individuelles aux Jeunes Chercheurs - 2011") and Fondation de la Recherche Médicale for her post-doctoral contracts. C.C. thanks the GeneralitatValenciana for their post-doctoral contract VALI+D. We thank the

confocal microscopy service, Alberto Hernández from CIPF confocal microscopy service for their technical support.

References

1. a) K. Ariga, Q. M. Ji, M. J. McShane, Y. M. Lvov, A. Vinu, J. P. Hill, *Chem. Mat.* **2012**, *24*, 728. b) L. Treccani, T. Y. Klein, F. Meder, K. Pardun, K. Rezwan, *Acta Biomater.* **2013**, *9*, 7115.

2. F. Hoffmann, M. Cornelius, J. Morell, M. Froba, *Angew. Chem. Int. Edit.* **2006**, *45*, 3216.

3. a) E. Aznar, R. Martínez-Máñez, F. Sancenón, *Exp. Opin. Drug Deliv. Rev.* **2009**, *6*, 643. b) C. Coll, A. Bernardos, R. Martínez-Máñez, F. Sancenón, *Acc. Chem. Res.* **2013**, *46*, 339.

4. a) P. Yang, S. Gai, J. Lin, *Chem. Soc. Rev.* **2012**, *41*, 3679-3698. b) Z. Li, J. C. Barnes, A. Bosoy, J. F. Stoddart, J. I. Zink, *Chem. Soc. Rev.* **2012**, *41*, 2590. c) B. W. Trewyn, I. I. Slowing, S. Giri, H. -T. Chen, V. S. –Y. Lin, *Acc. Chem. Res.* **2007**, *40*, 846.

5. a) D. Tarn, C. E. Ashley, M. Xue, E. C. Carnes, J. I. Zink, C. J. Brinker, *Acc. Chem. Res.* **2013**, *46*, 792. b) C. –H. Lu, B. Willner, I. Willner, *ACS Nano* **2013**, *7*, 8320. c) Q. He, J. Shi, *J. Mater. Chem.* **2011**, *21*, 5845.

6. a) K. Patel, S. Angelos, W. R. Dichtel, A. Coskun, Y. W. Yang, J. I. Zink, J. F. Stoddart, *J. Am. Chem. Soc.* **2008**, *130*, 2382. b) Y. –L. Sun, Y. Zhou, Q. –L. Li, Y. –W. Yang, *Chem.Commun.* **2013**, *49*, 9033. c) A. Bernardos, L. Mondragón, I. Javakhishvili, N. Mas, C. de la Torre, R. Martínez-Máñez, F. Sancenón, J. M: Barat, S. Hvilsted, M. Orzáez, E. Pérez-Payá, P. Amorós, *Chem. Eur. J.* **2012**, *18*, 13068.

7. a) A. Bernardos, E. Aznar, M. D. Marcos, R. Martínez-Máñez, F. Sancenón, J. Soto, J. M: Barat, P. Amorós, *Angew. Chem. Int. Ed.* **2009**, *48*, 5884-5887. b) A. Agostini, L. Mondragón, A. Bernardos, R. Martínez-Máñez, M. D. Marcos, F. Sancenón, J. Soto, A. Costero, C. Manguán-García, R. Perona, M. Moreno-Torres, R. Aparicio-Sanchís, J. R. Murguía, *Angew. Chem. Int. Ed.* **2012**, *51*, 10556. c) M. L. Yin, E. G. Ju, Z. W. Chen, Z. H. Li, J. S. Ren, X. G. Qu, *Chem. Eur. J.* **2014**, *20*, 14012.

8. a) A. Schlossbauer, J. Kecht, T. Bein, *Angew. Chem. Int. Ed.* **2009**, *48*, 3092-3095. b) P. D. Thornton, A. Heise, *J. Am. Chem. Soc.* **2010**, *132*, 2024. c) X. J. Yang, F. Pu, C. E. Chen, J. S. Ren, X. G. Qu, *Chem. Commun.* **2012**, *48*, 11133.

9. a) N. Mas, A. Agostini, L. Mondragón, A. Bernardos, F. Sancenón, M. D. Marcos, R. Martínez-Máñez, A. M. Costero, S. Gil, M. Merino-Sanjuan, P. Amorós, M. Orzáez,

E. Pérez-Payá, *Chem. Eur. J.* **2013**, *19*, 1346. b) X. Li, T. Tang, Y. Zhou, Y. Zhang, Y. Sun, *Micropor. Mesopor. Mater.* **2014**, *184*, 83.

10. A. Agostini, L. Mondragón, C. Coll, E. Aznar, M. D. Marcos, R. Martínez-Máñez, F. Sancenón, J. Soto, E. Pérez-Payá, P. Amorós, *ChemistryOpen* **2012**, *1,* 17.

11. a) Y. F. Zhu, W. J. Meng, N. Hanagata, Dalton Trans. **2011**, *40*, 10203. b) G. Zhang, M. Yang, D. Cai, K. Zheng, X. Zhang, L. Wu, Z. Wu, *ACS Appl. Mater. Inter.* **2014**, *6*, 8042.

12. L. M. Bimbo, L. Peltonen, J. Hirvonen, H. A. Santos, *Curr. Drug Metab.* **2012**, *13*, 1068.

13. D. R. Green, G. Kroemer, *J. Clin. Invest.* **2005**, *115*, 2610.

14. G. Kroemer, L. Galluzzi, P. Vandenabeele, J. Abrams, E. S. Alnemri, E. H. Baehrecke, M. V. Blagosklonny, W. S. El-Deiry, P. Golstein, D. R. Green, M. Hengartner, R. A. Knight, S. Kumar, S. A. Lipton, W. Malorni, G. Nunez, M. E. Peter, J. Tschopp, J. Yuan, M. Piacentini, B. Zhivotovsky, G. Melino, *Cell Death Differ.* **2009**, *16*, 3.

15. a) A. Jourdain, J. -C. Martinou, *Int. J. Biochem. Cell Biol.* **2009**, *41*, 1884. B) M. R. Sprick, H. Walczak, *BBA-Mol. Cell Res.* **2004**, *1644*, 125.

16. M. Poreba, A. Strozyk, G. S. Salvesen, M. Drag, *Cold Spring Harb. Perspect. Biol.* **2013**, *5*, a008680.

17. a) J. -B. Denault, G. S. Salvesen, *Methods Mol. Biol.* **2008**, *414*, 191. b) C. Pop, G. S. Salvesen, F. L. Scott, in *Programmed Cell Death, the Biology and Therapeutic Implications of Cell Death, Part B* **2008**, *446*, 351.

18. a) C. Coll, L. Mondragón, R. Martínez-Máñez, F. Sancenón, M. D. Marcos, J. Soto, P. Amorós, E. Pérez-Payá, *Angew. Chem. Int. Edit.* **2011**, *50*, 2138. b) C. de la Torre, L. Mondragón, C. Coll, F. Sancenón, M. D. Marcos, R. Martínez-Máñez, P. Amorós, E. Pérez-Payá, M. Orzáez, *Chem. Eur. J.* **2014**, *20*, 15309. c) C. de la Torre, A. Agostini, L. Mondragón, M. Orzáez, F. Sancenón, R. Martínez-Máñez, M. D. Marcos, P. Amorós, E. Pérez-Payá, *Chem. Commun.* **2014**, *50*, 3184. d) L. Mondragón, N. Mas, V. Ferragud, C. de la Torre, A. Agostini, R. Martínez-Máñez, F. Sancenón, P. Amorós, E. Pérez-Payá, M. Orzáez, *Chem. Eur. J.* **2014**, *20*, 5271. e) A. Agostini, L. Mondragón, C. Coll, E. Aznar, M. D. Marcos, R. Martínez-Máñez, F. Sancenón, J. Soto, E. Pérez-Payá, P. Amorós, *ChemistryOpen* **2012**, *1*, 17.

19. a) C. T. Kresge, M. E. Leonowicz, W. J. Roth, J. C. Vartuli, J. S. Beck, *Nature* **1992**, *359*, 710. b) N. K. Mal, M. Fujiwara, Y. Tanaka, *Nature* **2003**, *421*, 350.

20. a) V. V Rostovtsev, L. G. Green, V. V. Fokin, K. B. Sharpless, *Angew. Chem. Int. Ed.* **2002**, *41*, 2596. b) C. W. Tornoe, C. Christensen, M. Meldal, *J. Org. Chem.* **2002**, *67*,

3057. c) H. C. Kolb, M. G. Finn, K. B. Sharpless, *Angew. Chem. Int. Ed.* **2001**, *40*, 2004.

21. M. Andersson, J. Sjostrand, A. Petersen, A. K. S. Honarvar, J. O. Karlsson, *Invest. Ophthalmol. Vis. Sci.* **2000**, *41*, 2623.

22. T. L. Brown, in *Cell Volume and Signaling* **2004**, *559*, 293.

23. a) H. Brooks, B. Lebleu, E. Vives, *Advanced Drug Deliver. Rev.* **2005**, *57*, 559. b) S. M. Farkhani, A. Valizadeh, H. Karami, S. Mohammadi, N. Sohrabi, F. Badrzadeh, *Peptides* **2014**, *57*, 78. c) M. Orzaez, L. Mondragón, I. Marzo, G. Sanclimens, A. Messeguer, E. Pérez-Payá, M. J. Vicent, *Peptides* **2007**, *28*, 958.

24. L. Mondragón, L. Galluzzi, S. Mouhamad, M. Orzáez, J. M. Vicencio, I. Vitale, A. Moure, A. Messeguer, E. Pérez-Payá, G. Kroemer, *Apoptosis* **2009,** *14*, 182.

Chem. Eur. J. 2015, 21, 15506.

Caspase 3 targeted cargo delivery in apoptotic cells using capped mesoporous silica nanoparticles

Cristina de la Torre, Laura Mondragón, Carmen Coll, Alba García-Fernández, Félix Sancenón, Ramón Martínez-Máñez, Pedro Amorós , Enrique Pérez-Payá and Mar Orzáez.

Supporting Information

General methods

XRD, TGA, elemental analysis, TEM, N_2 adsorption-desorption, NMR, and fluorescence spectroscopy techniques were employed to characterize the synthesized materials. Powder X-ray measurements were performed on a Philips D8 Advance Diffractometer using CuKα radiation. Thermogravimetric analyses were carried out on a TGA/SDTA 851e Mettler Toledo balance, using an oxidant atmosphere (air, 80 mL/min) with a heating program consisting of a heating ramp of 10 °C per minute from 393 to 1273 K and an isothermal heating step at this temperature for 30 min. TEM images were obtained with a 100 JEOL JEM-1010 microscope. N_2 adsorption-desorption isotherms were recorded with a Micromeritics ASAP2010 automated sorption analyzer. The samples were degassed at 120 °C in vacuum overnight. The specific surface areas were calculated from the adsorption data in the low pressure range using the BET model. Pore size was determined following the BJH method. Live cellular internalization studies were performed in a confocal Leica microscope handled with a TCS SP2 system, equipped with an acoustic optical beam splitter (AOBS) and Leica microscope TCSSL. Cell viability measurements were carried out with a Wallac 1420 workstation. Peptides **P_1** was synthesized employing an automatic peptide synthesizer 422A from Applied Biosystems. Purification and analysis of the complete peptide sequence by HPLC were carried out by means of a Merck Hitachi L-2130 HPLC pump and a sample carrier L-2200 with a LiChospher 100 C18 (250 x 10 mm) column. The eluent was monitored at 220 nm employing a Merck Hitachi UV Detector L-2200 autosampler and employing a LiChrospher 100 C18 (150 x 3.9 mm) column, and as mobile phase different acetonitrile-aqueous TFA (0.1%) mixtures. Mass spectrometry analysis was performed employing a MALDI TOF/TOF 4700 Proteomics Analyzer from Applied Biosystems.

Chemicals

The chemicals tetraethylorthosilicate (TEOS), *n*-cetyltrimethylammonium bromide (CTABr), sodium hydroxide (NaOH), 3-(azidopropyl)triethoxysilane, tissue culture grade dimethylsulfoxide (DMSO), 4-pentynoic acid, anhydrous dimethylformamide (DMF), trifluoroacetic acid (TFA), triisobutylsilane (TIS) and

HPLC grade amino acids were purchased from Sigma-Aldrich Química S. A. (Madrid, Spain) and used without further purification. 3-(azidopropyl)triethoxysilane was provided by SelectLab Chemicals. Sodium ascorbate and cobalt (II) sulfate pentahydrate were from Scharlab (Barcelona, Spain). HPLC grade solvents, Fmol-Lys(Mtt)-Wang resin (90 µm, 0.4-1.00 mmol/g), (benzotriazol-1-yloxy)tripyrrolidinophosphonium hexafluorophosphate (PyBOP) and oxyma pure were obtained from Merck (Barcelona, Spain). All other reagents were of general laboratory grade and were purchased from Merck unless otherwise stated. Peptide **P_2** was purchased from China Peptides with more than 90% of purity. D-MEM with L-glutamine, fetal bovine serum (FBS), trypan blue solution (0.4%) cell culture grade, trypsin, wheat germ agglutinin Alexa Fluor 647, and Hoechst 33342 were provided by Gibco-Invitrogen. Staurosporine, *N*-(2-quinolyl)valyl-aspartyl-(2,6-difluorophenoxy)methyl ketone (q-VD-OPh non-O-methylated) and *cis*-platinum were purchased from Sigma-Aldrich. The cell proliferation reagent WST-1 was obtained from Roche Applied Science.

Synthesis of peptide sequence (P_1)

Peptide sequence Ac-KKGDEVDKKARDEVDK-OH was synthesized by Fmoc-based solid phase chemistry using a 433A Applied Biosystem Peptide Synthesizer. Before peptide was synthetized 4-pentinoic acid was added to the sequence at the *N*-terminal of the side chain of lysine in the Fmol-Lys(Mtt)-Wang's resin used through an amide bond using PyBOP, DIEA and oxyma pure. Then synthesis was performed and the peptide was cleaved from the resin by treatment with trifluoroacetic acid (TFA 94%, TIS 1% and H_2O 5%) during 4 hours and purified by preparative RP-HPLC (Lycrospher 100 C18, 10 mm) using acetonitrile-aqueous TFA (0.1%) mixtures. The identity and purity was confirmed by MALDI-TOF mass spectrometry (Figure SI-1) and HPLC (see Figure SI-2).

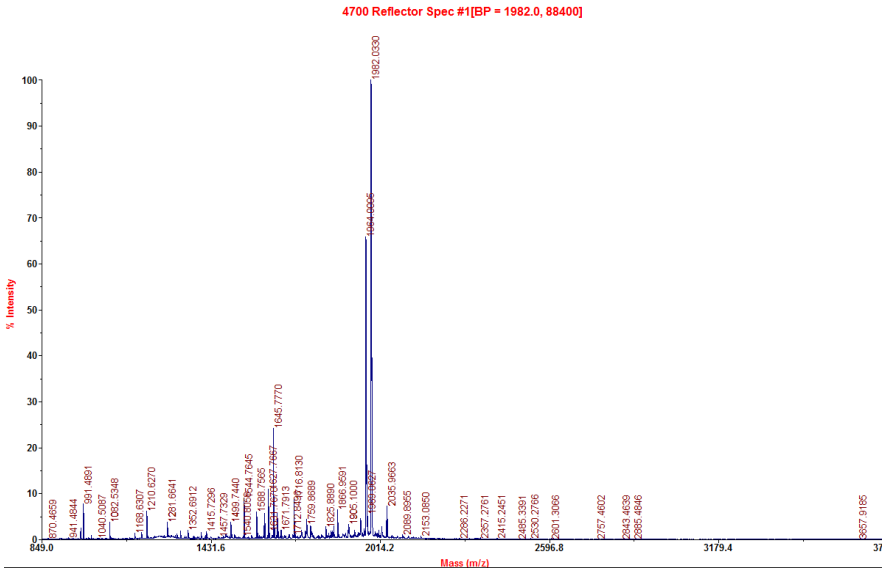

Figure SI-1. Mass spectra of **P$_1$** (mass of the peptide 1982.03).

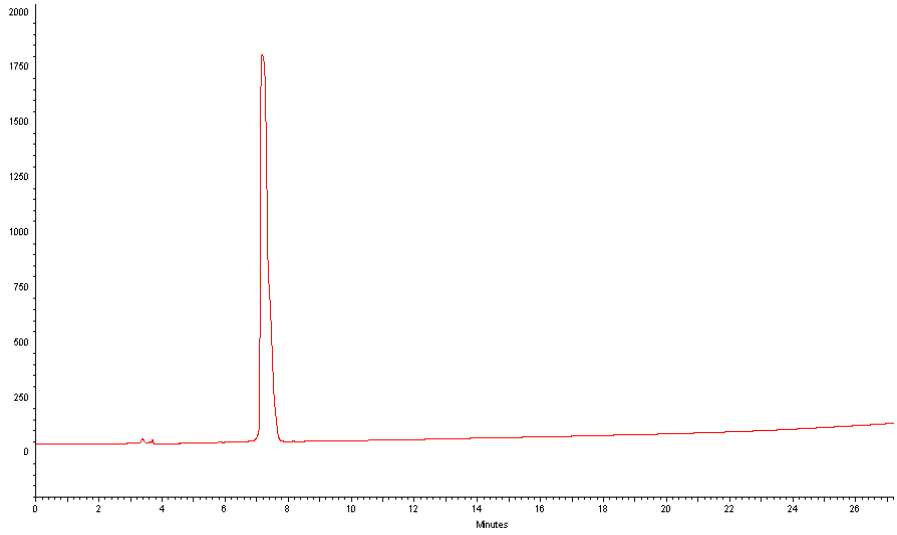

Figure SI-2. HPLC profile of purification of the peptide **P$_1$**.

Synthesis of mesoporous silica nanoparticles.

The MCM-41 mesoporous nanoparticles were synthesized by the following procedure: *n*-cetylmethylammoniumbromide (CTABr, 1.00 g, 2.74 mmol) was first dissolved in 480 mL of deionized water. Then 3.5 mL of NaOH 2.0 M in deionized water were added to the CTABr solution, followed by adjusting the solution temperature to 80 ^{o}C. TEOS (5.00 mL, 2.57 x 10^{-2} mol) was then added dropwise to

the surfactant solution. The mixture was allowed to stir for 2h to give a white precipitate. Finally the solid obtained was centrifuged at 9500 rpm for 10 minutes and washed with deionized water until neutral pH. Then, it was dried at 60 ^{o}C (MCM-41 as-synthesized). To prepare the final porous material (MCM-41), the as-synthesized solid was calcined at 550 ^{o}C using oxidant atmosphere for 5 h in order to remove the template phase.

Synthesis of solid S_1

Calcined MCM-41 (200 mg) and safranin O (57 mg, 0.16 mmol) were suspended in acetonitrile (12 mL). Then the suspension was stirred during 24 hours at room temperature with the aim of achieving the maximum loading in the pores of the MCM-41 scaffolding. Afterward an excess of 3-(azidopropyl)triethoxysilane (0.25 g, 1 mmol) was added, and the suspension was stirred for 5.5 h. Finally, the solid was filtered off, washed with 30 mL of acetonitrile and dried at vacuum.

Synthesis of solid S_1-P_1

For the preparation of the solid **S_1-P_1**, azide-functionalized nanoparticles **S_1** (30 mg) and the peptide **P_1** (30 mg) were suspended in a 50:50 v/v DMF-H_2O mixture (30 mL) in the presence of an excess of safranin O (200 mg, 0.8 mmol) in order to avoid the delivery of the dye from the pores to the bulk solution during the synthesis of the final solid. Then, 100 µL of a solution of $CuSO_4 \cdot 5H_2O$ (1.0×10^{-3} mol dm^{-3}) and 100 µL of sodium ascorbate (1.0×10^{-2} mol dm^{-3}) were added. The reaction mixture was stirred at 90 ^{o}C for 3 days. The nanoparticles were centrifuged and washed thoroughly with water (9500 rpm, 10 min) to remove the unreacted and absorbed molecules. Supernatant was discarded and the process was repeated till supernatant showed no fluorescence associated to safranin O (λ_{ex}= 520 nm, λ_{em}= 580 nm). Finally, nanoparticles were dried under vacuum.

Synthesis of solid S_1-P_2

For the preparation of the solid **S_1-P_2**, a mixture of azide-functionalized nanoparticles **S_1** (20 mg) and the peptide **P_2** (20 mg) were suspended in a 50:50

mixture of DMF and H_2O (16 mL) in the presence of an excess of safranin O (190 mg, 0.8 mmol) in order to avoid the delivery of the dye from the pores to the bulk solution during the synthesis of this solid. Then, 62.5 µL of a solution of $CuSO_4 \cdot 5H_2O$ (1.0×10^{-3} mol dm^{-3}) and 110 µL of sodium ascorbate (5.6×10^{-3} mol dm^{-3}) were added. The reaction mixture was stirred at 90 ºC for 3 days. The nanoparticles were centrifuged at 9500 rpm for 10 minutes and washed thoroughly with water to remove the unreacted and absorbed molecules. Washing procedure was the same than the followed for solid **S_1-P_1**.

Materials characterization

Solid **S_1** was characterized using standard procedures. Figure 1C in the paper shows powder X-ray patterns of the nanoparticulated MCM-41 support and the **S_1** functionalised material. The PXRD of siliceous nanoparticulated MCM-41 as-synthesized presents four low-angle reflections typical of a hexagonal array that can be indexed as (100), (110), (200) and (210) Bragg peaks. A significant displacement of the (100) peak in the XRD powder of the nanoparticulated MCM-41 calcined sample is clearly appreciated in the curve of MCM-41 calcined, corresponding to an approximate cell contraction of 4 Å. This displacement and the broadening of the (110) and (200) peaks are related to further condensation of the silanol groups during the calcinations step. In the curve of **S_1**, a slight intensity decrease and the disappearance of the (110) and (200) reflections were observed, most likely related to a loss of contrast due to the filling of the pore voids with the safranin O. Moreover the presence of the (100) peak in the XRD patterns of **S_1**, **S_1-P_1** and **S_1-P_2** strongly evidences that the loading process with the dye and the further functionalization with 3-(azidopropyl)triethoxysilane and peptides **P_1** and **P_2** have not damaged the mesoporous 3D MCM-41 scaffolding.

Preservation of the mesoporous structure in the final functionalized solids was also confirmed by means of TEM. Figure SI-3 shows the morphology of the MSN materials. As can be seen, MCM-41 scaffolding has been prepared as spherical particles with diameters of ca.100 nm, and the loaded and functionalized solids

(**S_1-P_1** and **S_1-P_2**) maintains the initial morphology of the MCM-41 matrix. The figure also shows the typical channels of the MCM-41 matrix either as alternate black and white stripes or as a pseudohexagonal array of pore voids. These channels are visualized not only in the calcined material but also in **S_1-P_1** and **S_1-P_2**.

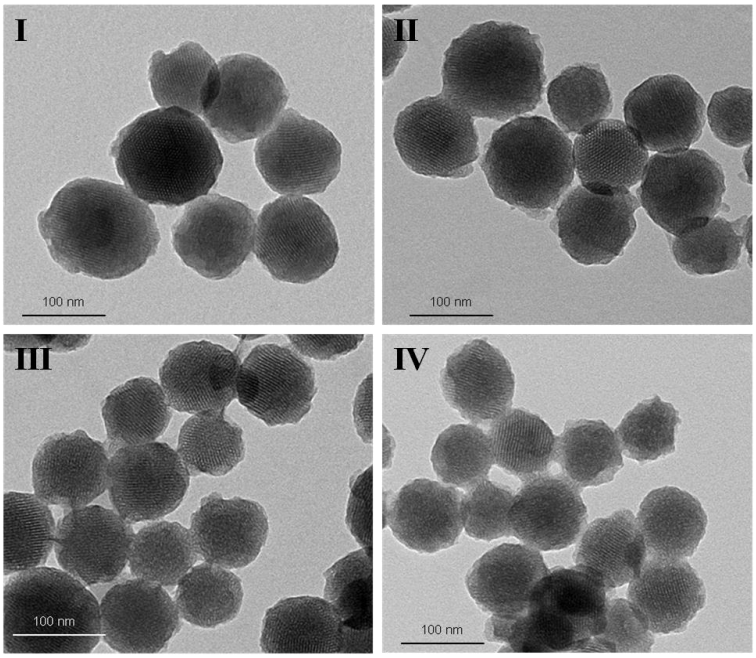

Figure SI-3. TEM images of MCM-41 calcined (I), solid **S_1** (II), solid **S_1-P_1** (III) and solid **S_1-P_2** (IV).

Further DLS (Dynamic Light Scattering) studies showed particles with a mean diameter of 151 nm for MCM-41, 112 nm for **S_1-P_1** and 133 nm for **S_1-P_2** (see Figure SI-4). Also, Figure SI-4 showed that calcined MCM-41 nanoparticles and the final materials formed aggregates of 586.36, 625.95 and 1006.25 nm of diameter, respectively. However, only about 4% of the total nanoparticles are aggregated.

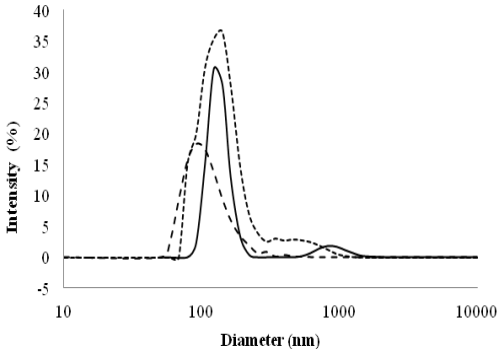

	Diameter (nm)	% of nanoparticles
MCM-41	151	91.3
	586	8.7
S_1P_1	112	98.8
	626	1.2
S_1P_2	133	92.7
	1006	7.3

Figure SI-4. Size distribution by intensity of particles obtained by DLS studies. The average size of nanoparticles of calcined MSN (dot), **S_1-P_1** (straight) and **S_1-P_2** (black line) was found to be ca. 110-150 nm.

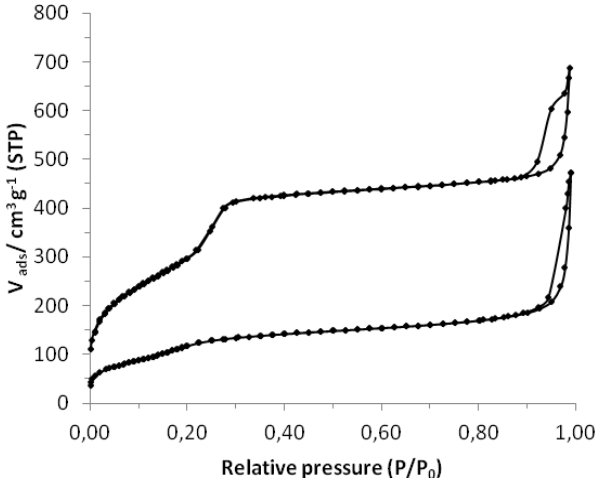

Figure SI-5. Nitrogen adsorption-desorption isotherms for MCM-41 mesoporous material and **S_1**.

The N_2 adsorption-desorption isotherms of the nanoparticulated MCM-41 calcined material shows an adsorption step at intermediate P/P_0 value (0.1-0.3) typical of this solids (see Figure SI-5). This step can be related to the nitrogen condensation inside the mesopores by capillarity. The absence of a hysteresis loop in this interval and the narrow BJH pore distribution suggest the existence of

uniform cylindrical mesopores. The application of the BET model resulted in a value for the total specific surface of 1001 m^2/g and a pore volume of 0.79 cm^3/g. From the XRD, porosimetry and TEM studies, the a_0 cell parameter (3.65 nm), the pore diameter (2.52 nm) and a value for the wall thickness (1.14 nm) were calculated. In addition to this adsorption step associated to the micelle generated mesopores, a second feature appears in the isotherm at a high relative pressure ($P/P_0 < 0.8$). This adsorption correspond to the filling of the large void among the particles and present a volume of 0.33 cm^3/g (calculating by using the BJH model) and then must be considered as a textural-like porosity. In this case, the curves show a characteristic H1 hysteresis loop and a wide pore size distribution.

The N_2 adsorption-desorption isotherm of **S_1** is typical of mesoporous systems with partially filled mesopores, and a significant decrease in the N_2 volume adsorbed and in the surface area (438 m^2/g) was observed (see Figure SI-5). In fact, this solid shows flat curves when compared (at the same scale) to those of the MCM-41 parent material. Additionally, a certain textural porosity is preserved. BET specific surface values, pore volumes and pore sizes calculated from the N_2 adsorption-desorption isotherms for MCM-41 and **S_1** are listed in Table SI-1.

Table SI-1. BET specific surface values, pore volumes and pore sizes calculated from the N_2 adsorption-desorption isotherms for selected materials.

	S_{BET} ($m^2\ g^{-1}$)	Total pore volume [a] ($cm^3\ g^{-1}$)	BHJ pore [b] (nm)
MCM-41	1001	0.79	2.52
S_1	438	0.31	-

[a] Pore size estimated by the BJH model applied to the adsorption branch of the isotherm.

[b] Pore volumes and pore size were associated with only intraparticle mesopores.

The content of 3-(azidopropyl)triethoxysilane, safranin O and peptide in **S_1**, **S_1-P_1** and **S_1-P_2** solids were determined by elemental, thermogravimetric analysis and

by UV measurements. As stated above mesoporous nanoparticles were first loaded with safranin O and then, the external surface functionalized with azidopropyl moieties (see above for details). The amount of safranine at the end of the reaction in the solution (after washing) was determined by UV in order to calculate the amount of dye loaded in the material. As the quantity of safranine O is then known, the amount of grafted azidopropyl was easily calculated by TGA analysis. A similar procedure was followed in order to measure the amount of the peptide anchored onto the external surface. Finally, elemental analysis was used to confirm the total amount of organic matter (the sum of saftanin O, azidopropyl and peptide contents) measured by TGA. Values of contents are detailed in Table SI-2.

Table SI-2. Content in mmol of anchored molecules and dye in mmol g^{-1} SiO_2 for solids **S_1**, **S_1-P_1** and **S_1-P_2**.

	Azide (mmol g^{-1} SiO_2)	Safranin O (mmol g^{-1} SiO_2)	Peptide (mmol g^{-1} SiO_2)
S1	0.039	0.389	-
S_1-P_1	0.039	0.130	0.034
S_1-P_2	0.039	0.205	0.016

Dye delivery studies

The controlled release behavior of **S_1-P_1** and **S_1-P_2** were studied in buffer media in the presence of 35 µL of caspase 3 enzyme (0.14 mg/mL) at pH 6. The selected pHs are those at which the enzyme presented their optimal activity. Buffer media was PBS with 10 % of glycerol and 1 mM of DTT. In a first experiment, solid **S_1-P_1** (0.5 mg) was suspended in 3 mL of the buffer solution containing caspase 3 enzyme and the final suspension was stirred in a bath at 37 ^{o}C. The uncapping and subsequent delivery of the dye was easily detected by monitoring the safranin O emission band (λ_{ex}= 520 nm, λ_{em}= 580 nm). As a control experiment, dye release

was also measured using suspensions of **S_1-P_1** and **S_1-P_2** under similar conditions, but in the absence of caspase 3 enzyme.

The difference in dye delivery in both experiments is displayed in Figure 1D and 1E in the paper. Each point in the figure was determined using the above-described protocol, the suspension was filtered at a certain time using TFA filters and the emission of safranin O in the solution was measured. In the absence of the caspase 3 enzyme, a flat baseline was found, indicating that the safranin O cargo remained in the nanoparticles without release. In contrast, in the presence of the enzyme, delivery of safranin O was observed as increased dye fluorescence in terms of time.

2.7. Gated Mesoporous Silica Nanoparticles Using a Double-Role Circular Peptide for the Controlled and Target-Preferential Release of Doxorubicin in CXCR4-expresing Lymphoma cells.

Cristina de la Torre,[a,b,c] Isolda Casanova,[c,d] Gerardo Acosta,[c,e] Carmen Coll,[a,b,c] María José Moreno,[c,d] Fernando Albericio,[c,e,g,h] Elena Aznar, [a,b,c] Ramón Mangues,[c,d] Miriam Royo,[c,f] Félix Sancenón [a,b,c] and Ramón Martínez-Máñez*[a,b,c]

[a] *Centro de Reconocimiento Molecular y Desarrollo Tecnológico (IDM), Unidad Mixta Universidad Politécnica de Valencia-Universidad de Valencia.*

[b] *Departamento de Química, Universidad Politécnica de Valencia. Camino de Vera s/n, 46022, Valenicia, Spain.*

[c] *CIBER de Bioingenieria, Biomateriales y Nanomedicina (CIBER-BBN)*

[d] *Grup d'Oncogènesi i Antitumorals*
Institut d'Investigacions Biomèdiques Sant Pau, Hospital de Sant Pau

[e] *Institute for Research in Biomedicine*
Barcelona Science Park–University of Barcelona, Baldiri Reixac 10, 08028 Barcelona

[f] *Combinatorial Chemistry Unit, Barcelona Science Park*
Baldiri Reixac 10, 08028 Barcelona, Spain

[g] *Department of Organic Chemistry, Universitat de Barcelona, 08028 Barcelona, Spain*

[h] *School of Chemistry Yachay Tech,Yachay City of Knowledge, Urcuqui, Ecuador*

Received: ***Oct 2014***
Published online: **Feb 2015**

Adv. Funct. Mater. 2015, 25, 687.

Abstract

B-cell non-Hodgkin's lymphoma (B-NHL) is the most frequent malignant lymphoid neoplasm, which has a high degree of relapse and chemoresistance. Thus, strategies to improve currently used therapies are needed. In this context, we describe herein a new CXCR4-targeted delivery system using mesoporous silica nanoparticles (MSNs) that were loaded with doxorubicin and capped with a derivative of the T22 peptide (**P**). This design makes full use of the great affinity of the T22 peptide to CXCR4 receptor which is overexpressed in lymphoma cells. The peptide was able to guide the gated nanoparticle to B-NHL cells to facilitate MSNs uptake via the CXCR4 receptor. The endocyted **P**-capped MSNs were also opened by endosomal proteolytic enzymes to allow intracellular doxorubicin delivery.

Introduction

In the last few years, nanotechnology has proved an innovative approach for drug-delivery therapies. The development of drug-release systems capable of delivering active molecules to certain cells in a controlled manner is a timely pursued goal. In this scenario, mesoporous silica nanoparticles (MSNs) have been demonstrated to be excellent reservoirs and vehicles for drug storage[1-5] because of their unique mesoporous structure, large specific volume, and easy functionalisation. MSNs are also considered biocompatible, can be uptaken by cells via endocytosis, and can be functionalised with a large collection of switchable molecular/supramolecular pore-capping ensembles to develop gated MSNs capable of retaining a cargo and delivering it upon the application of a specific chemical[6-12] (e.g., redox molecules, selected anions, pH changes), or physical[13-18] (e.g., light, temperature or magnetic fields) or biochemical (e.g., enzymes, antibodies, or DNA) stimuli.[19-24] Furthermore, thanks to the easy surface functionalisation in MSNs, the possibility of decorating them with additional functional elements as targeting ligands opens up new possibilities in the design of gated delivery nanodevices.[25]

In this context, the use of biomolecules in capped mesoporous nanostructures has proved useful in the design of delivery systems for applications in more

biological and realistic settings. Among biomolecules, the employment of peptides is especially appealing since their use in combination with MSNs is envisioned to offer great potential, and may provide exquisite selectivity in the design of advanced gate-opening devices for highly specific applications. In recent years, scientists have developed different exploratory works on the design of peptide-capped nanoparticles capable of being hydrolysed by proteases.[26-31] However many of these studies have focused on the mode of anchoring peptidic chains or in conformational changes to trigger the gating mechanism. In parallel, researchers have also explored the targeting functionality of short peptides to help gated nanoparticles reach their cellular target with satisfactory results.[32-37] However the use of peptides for a double role (e.g., targeting and gating) is scarce in MSNs.[38]

In this work, we paid attention to B-cell non-Hodgkin's lymphoma (B-NHL), the most frequent malignant lymphoid neoplasm. Its standard treatment combines chemotherapy (e.g., cyclophosphamide, doxorubicin, vincristine and prednisolone) with Rituximab, a monoclonal antibody that targets CD20.[39,40] Despite most B-NHL patients initially respond to chemotherapy, with about 40-50% complete responses, many of them undergo relapse.[41]

Drug resistance in relapsed lymphomas is partly acquired by homing lymphoma cells to bone marrow microenvironment where interaction with stromal cells stimulates their survival and confers chemoresistance.[42] This interaction is mainly regulated by chemokine receptor CXCR4, which is expressed in the membrane of lymphoma cells and is activated by the chemokine CXCL12. The CXCR4/CXCL12 axis is involved in the survival and trafficking of malignant B cells, and in their homing to lymph nodes.[43] CXCR4 overexpression has also been associated with poor prognosis in several B-cell malignancies.[44,45] Moreover, in diffuse large B-cell lymphoma, the most frequent B-NHL subtype, CXCR4 expression enhances cell dissemination and associates with shorter patient survival.[46] In this context, targeting chemotherapeutic agents to CXCR4-overexpressing lymphoma cells may be important to overcome chemoresistance.

A suitable approach to achieve this goal would be to develop delivery carriers that are able to selectively reach the CXCR4 receptor. However, as far as we know, such targeted release systems have not yet been described.

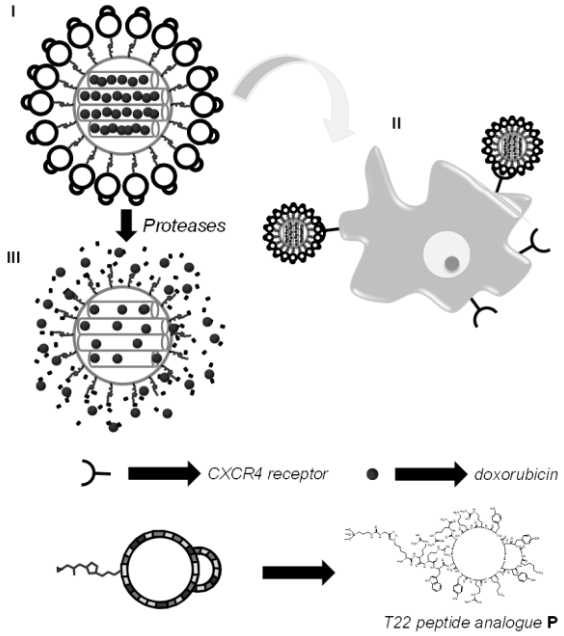

Scheme 1. Representation of the targeted and capped proposed system. (I) Solid **S2** is capped with targeting T22 peptide analogue **P**, which inhibits the release of entrapped doxorubicin. (II) The targeting gated system is recognised by the CXCR4 receptor and is endocyted. (III) Doxorubicin delivery from **S2** is triggered by proteases.

With this background, and taking into account the need to develop new delivery carriers to overcome usual side effects and chemoresistance in lymphoma, we were interested in attempting the design of a targeted delivery system to B-NHL cells. The controlled-release nanomaterial we prepared is shown in Scheme 1. It consists of mesoporous nanoparticles that were loaded with the cytotoxic drug doxorubicin. As the capping and targeting agent, we selected an engineered version polyphemusin II peptide from the horseshoe crab named T22. In the engineered peptide, three substitutions at residues Tyr5, Lys7 and Tyr12 dramatically enhanced the affinity of natural peptide T22 for the CXCR4 receptor.[47-49]

Results and Discussion

Design and synthesis of peptide-gated MSN

In the present work, MCM-41-based MSNs were selected as an inorganic scaffold. The nanoparticulated mesoporous support was prepared by using tetraethyl orthosilicate (TEOS) as a hydrolytic inorganic precursor and surfactant hexadecyltrimethylammonium bromide (CTABr) as the porogen species. After surfactant removal by calcination, bare MSNs were obtained. The inorganic support was then loaded with antitumoural drug doxorubicin, and the outer surface of the nanoparticles was functionalised with propargyl-containing linker 1-(3-(triethoxysilyl)propyl)-3-prop-2-ynyl-urea (1) (see the Experimental Section for details), obtained by the nucleophilic addition of propargylamine to 3-(triethoxysilyl)propylisocyanate. This procedure yielded solid **S1**.

An azide-containing analogue of peptide T22 with Lys(N_3) in the N-Terminal (**P**) was obtained by Fmoc solid-phase synthesis using a Rink amide ChemMatrix resin and all the Cys side chains protected with the Trt group. Having finished peptide elongation, the peptide was cleaved from the resin using the TFA-TIS-H_2O mixture at 25 ^{o}C for 1 h. This linear peptide was then oxidised for its cyclisation using DMSO as an oxidising agent and was purified by semipreparative HPLC-MS to obtain the final azide-T22 derivative (**P**), which is depicted in Scheme 2. The product was characterised by HRMS (Calc. For $C_{115}H_{178}N_{42}O_{23}S_4$ $[M^{+4}H]^{4+}$ 660.8227, found 660.8236) and a peptide content of 86% was obtained. The peptide was also studied by circular dichroism and the spectrum exhibited a strong negative band at 210 nm and a strong positive band near 200.6 nm, and was similar to that described for T22[50] (see Figure SI-3).

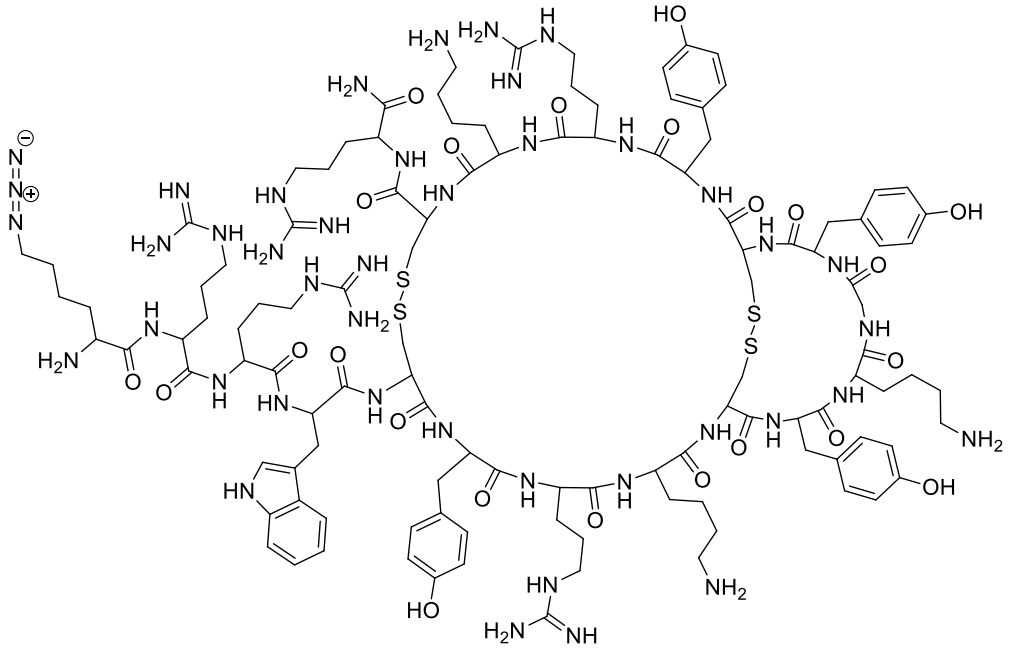

Scheme 2. Structure of the final azide-containing T22 analogue peptide (**P**).

Finally, the capped nanoparticles **S2** were prepared using a "click" reaction between **S1** and the azide-containing T22 analogue peptide **P**. The peptide was expected to form a dense targeting layer around the MSNs capable of retaining doxorubicin inside pores. Doxorubicin delivery was also expected to occur in the presence of proteases that were able to hydrolyse the amide bonds in the peptide.

Materials characterization

Once obtained, all the prepared solids were characterised by standard procedures for hybrid organic-inorganic mesoporous materials. Firstly, the ordered structure of the inorganic supports was carefully studied. The typical MCM-41 structure of the starting material was confirmed by powder X-Ray diffraction (PXRD) both before and after the calcination step to obtain an empty ordered framework of mesopores (see Figure 1a and b). As seen in Figure 1, the

PXRD pattern of the as-synthesised siliceous nano-particulated MCM-41 shows the typical low-angle reflections of a hexagonal array. After the calcination step, a significant displacement of the main peak (assigned to the (100) Brag reflection) was observed, which corresponded to an approximate cell contraction of 4 Å. This displacement and the broadening of the (110) and (200) peaks were related to the further condensation of the silanol groups in the calcination step. The PXRD pattern of solid **S1** was also recorded (Figure 1c). In this case, a slight intensity decrease of the (100) reflection and a broadening of the (110) and (200) reflections were observed, most likely due to loss of contrast in relation to the pore voids filling with doxorubicin. Nevertheless, the value and intensity of the (100) peak in this pattern strongly evidenced that the loading process with the dye and the further functionalisation did not damage the mesoporous 3D MCM-41 scaffolding.

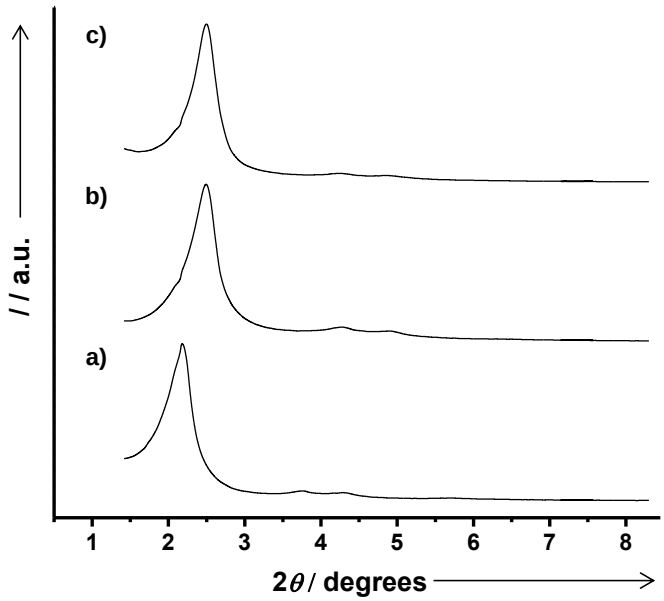

Figure 1. Powder X-ray diffraction patterns of solids (a) MCM-41 as-synthesised, (b) calcined MCM-41 and (c) **S1** containing the doxorubicin drug.

The morphology in solids **S1** and **S2** was also studied by TEM (Figure 2). In the obtained representative images, the spherical morphology of the particles with a

mean diameter of ca. 100 nm is seen. The typical channels of the MCM-41 matrix can be easily observed as either alternate black and white stripes or a pseudohexagonal array of the pore voids in the images of solids **S1** and **S2**.

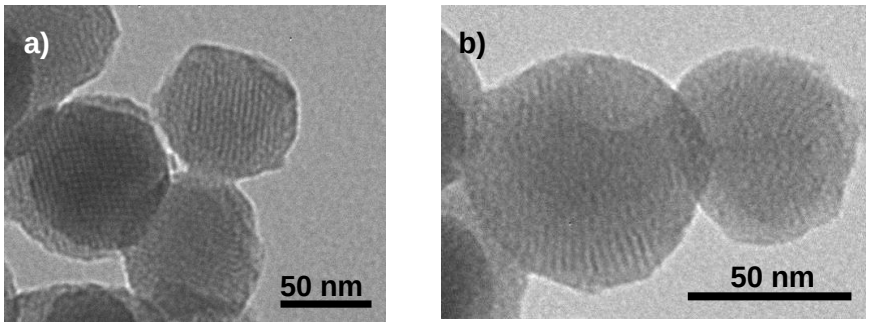

Figure 2. Representative TEM images of a) solid **S1** and b) solid **S2**.

DLS (Dynamic Light Scattering) studies were also conducted to estimate the hydrodynamic diameter of the particles. Thus for the calcined parent material, a narrow nanoparticle size distribution (Figure 3) with a mean diameter of 116 nm was obtained, while a value of 118 nm was recorded for solid **S1**.

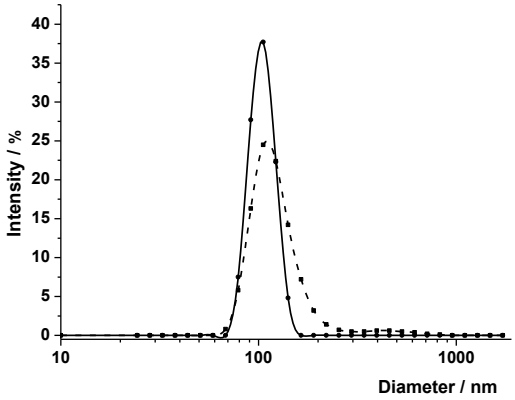

Figure 3. Size distribution by number of particles obtained in the DLS studies for calcined MCM-41 (solid line) and **S1** (dashed line).

Finally, a study of the mesopore system was conducted by recording the N_2 adsorption-desorption isotherms of the nano-particulated calcined MCM-41 material and solid **S1**. For the calcined nanoparticles, a sharp adsorption step at an intermediate P/P_0 value (0.1-0.3) was obtained, which is typical of these solids (see Figure 4). Following this first step, a second adsorption process was recorded at a high relative pressure (> 0.9). This adsorption profile is typical of mesoporous nanoparticles, where the first step was related to the nitrogen condensation inside the mesopores by capillarity, and the second one corresponded to the filling of the large voids among the particles, that must be considered a textural-like porosity. The application of the BET model resulted in a total specific surface value of 992.2 m^2/g and a pore volume of 0.78 cm^3/g. The application of the BJH model at the intermediate relative pressure also estimated a narrow pore distribution which centred at 2.54 nm (see the inset of Figure 4a). These data, together with the absence of a hysteresis loop in the intermediate pressure interval, suggest the existence of uniform cylindrical mesopores. By also taking into account the a_0 cell parameter calculated from PXRD (3.65 nm) and the obtained pore diameter (2.54 nm), it was possible to estimate a wall thickness value (1.11 nm).

In contrast, the N_2 adsorption-desorption isotherms of **S1** recorded a sharp drop in the N_2 volume adsorbed and in the specific surface area (753.6 m^2/g) (see Figure 4). This feature is typical of mesoporous systems with at least partially filled mesopores. On the curve, apart from the adsorption step associated with the micelle-generated mesopores, a second feature also appears in the isotherm at a high relative pressure due to the textural porosity.

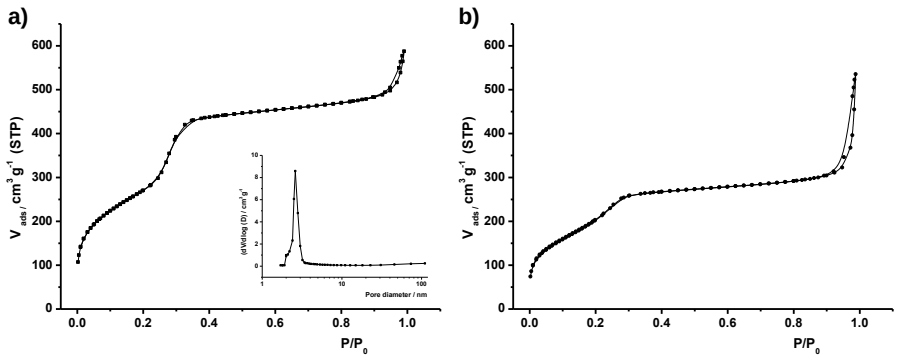

Figure 4. Nitrogen adsorption-desorption isotherms for a) MCM-41 mesoporous nanoparticles (inset: pore size distribution) and b) solid **S1**.

The BET-specific surface values, pore volumes and pore sizes calculated from the N_2 adsorption-desorption isotherms for MCM-41 and **S1** are listed in Table 1.

Table 1. The BET-specific surface values, pore volumes and pore sizes calculated from the N_2 adsorption-desorption isotherms for selected materials.

	S_{BET} (m^2 g^{-1})	Pore volume [a] (cm^3 g^{-1})	Pore Size [a,b] (nm)	Textural pore size (nm)
MCM-41	992.2	0.78	2.54	42.00
S1	753.6	0.52		43.11

[a]Pore volume and size associated with intraparticle mesopores.

[b] Pore size estimated by using the BJH model applied to the adsorption branch of the isotherm.

The isopropyltriethoxysilane and doxorubicin content in solid **S1** was determined by elemental and thermogravimetric analyses. In these studies, the amounts of 0.44 mmol/gSiO_2 of linker **1** and of 0.11 mmol/gSiO_2 of doxorubicin were estimated.

Doxorubicin delivery studies

The possibility of retaining the cargo inside a vehicle until its target is reached is a crucial, highly desirable feature in the drug delivery system to reduce side effects and increase efficiency. In this context, *in vitro* cargo release studies of **S2** in water, done in the presence and absence of a proteolytic enzyme obtained from *Streptomices griseus,* were performed. The prepared solid **S2** was suspended in 1 mL of water at pH 8 and then the suspension was fractionated into two parts. To one part, 4 mL of the solution containing the protease enzyme (*Streptomices griseus* enzyme; C_{enzyme} = 0.12 mg/mL, H_2O, pH 8) were added, and 4 mL of H_2O, pH 8, were added to the other part, but no enzyme was present. Both suspensions were stirred and aliquots were taken at the scheduled times. After centrifugation to eliminate the solid, the fluorescence of doxorubicin delivered to the solution was measured at 595 nm (λ_{ex} = 495 nm). The drug delivery profile in both experiments is displayed in Figure 5.

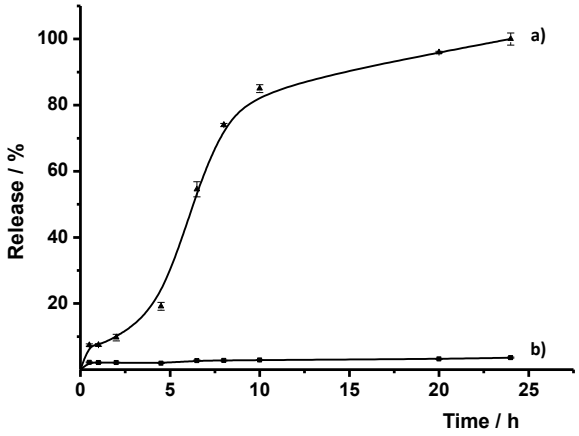

Figure 5. The release profile of **S2** a) in the presence and b) absence of the enzyme.

In the absence of the proteolytic enzyme, a remarkable flat baseline was obtained, which indicates that doxorubicin remained in the nanoparticles without release. In particular, cargo delivery was lower than 2%, even after 24 h. In contrast, a cargo release in the presence of protease was shown as an increase in doxorubicin fluorescence according to time. The observed behaviour was assigned

to the protease-induced hydrolysis of the peptidic bonds of the anchored peptide **P**, which resulted in the delivery of the entrapped cargo.

Evaluation of silica mesoporous nanoparticles in the Toledo-B-NHL cell line

Controlling cell targeting and penetrability of drugs is a major issue in emerging medicine. Thus after demonstrating the effective release of **S2**, we evaluated **S2**-induced CXCR4 internalisation and its antitumour effect on Toledo B-NHL cells, which express high levels of the CXCR4 receptor in the membrane. Interaction of CXCR4 with its natural ligand, SDF-1α, has been described to induce its rapid phosphorylation and internalisation.[51] In order to demonstrate the interaction of solid **S2** with CXCR4, followed by internalisation and cargo delivery, we evaluated the effect of the nanoparticle on CXCR4 membrane levels in Toledo cells. Toledo cells were exposed to **S2** for 1 h and the CXCR4 levels in the membrane were quantified by flow cytometry. As a positive control, we also evaluated the effect of AMD3100, an antagonist of the CXCR4 receptor that triggers its internalisation. Cells were also exposed to bare MSNs as a negative control. These nanoparticles contained neither doxorubicin nor gating peptide **P** and were used to see the effect of the inorganic support on the receptor expression. As shown in Figure 6A, Toledo cells treated with bare MSNs expressed high levels of CXCR4 in the membrane, which significantly decreased after exposure to the other tested compounds. These experiments allowed us to conclude that **S2**, like the AMD3100 antagonist, rapidly induced CXCR4 internalisation, while bare MSNs did not affect the receptor expression. This evidence clearly indicates the direct interaction between the gating and targeting peptide **P** in **S2** nanoparticles and the CXCR4 chemokine receptor.

In another step, we evaluated the antitumour activity of **S2** in Toledo cells. In order to corroborate the previously observed specific CXCR4 targeting of **S2**, we also performed competition assays with the CXCR4 antagonist AMD3100. In these experiments, the viability of Toledo cells significantly decreased after exposure to **S2** (75μg/mL) for 48 h, while cell exposure to bare MSNs had no effect on cell viability. The antitumoural effect of the **S2** nanoparticle was partially reversed

when cells were pre-incubated with AMD3100 (see Figure 6B). Finally, apoptosis induction by **S2** was evaluated by Hoescht nuclear staining. The cells treated with the nanoparticle **S2** for 48 h showed many apoptotic bodies, which were identified by their chromatin condensation and fragmentation, as seen in Figure 6C. All these data indicated that **S2** triggers cell death in the Toledo B-NHL cells by induction of apoptosis, which is accomplished through CXCR4-dependent internalisation.

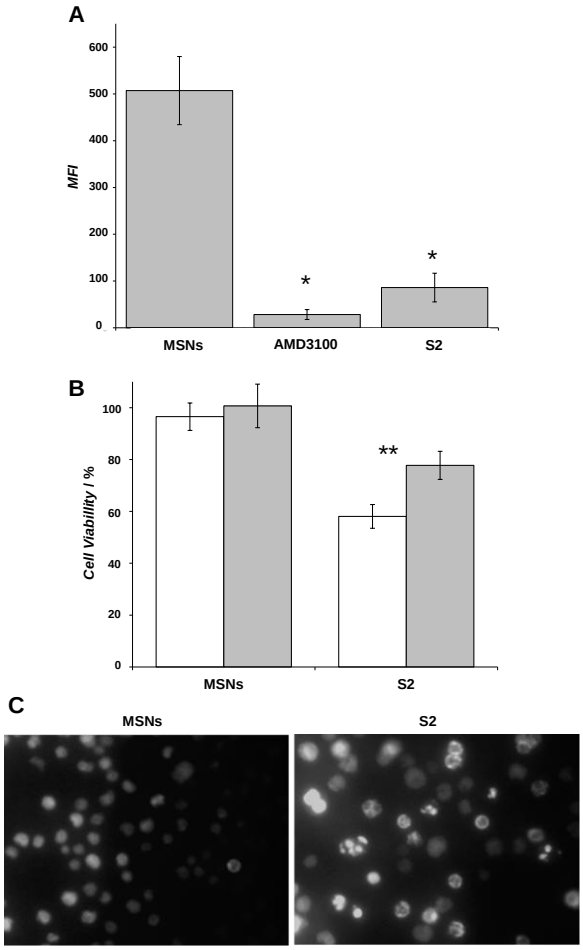

Figure 6. a) Flow cytometry analysis of the CXCR4 surface expression in Toledo cells exposed to bare MSNs (75 µg/mL), AMD3100 (10 µg/mL) and **S2** (75 µg/mL) for 1 h. b) Evaluation of cell viability inhibition by **S2** (75µg/mL) in Toledo cells for 48 h. White bars:

no pre-treatment with antagonist AMD3100 (10μg/mL). Grey bars: after a 1h pre-treatment with antagonist AMD3100 (10 μg/mL). c) Apoptosis induction after 48 h of exposure of Toledo cells to **S2** (75 μg/mL). * P value<0.05, ** P value <0.01.

The performed cellular studies indicate that **S2** selectively induces cell death in the Toledo CXCR4-expressing cells. First of all, we observed that **S2** induces CXCR4 internalisation in lymphoma cells, which suggests a direct interaction between T22 peptide **P** in the nanoparticle and the chemokine receptor. Consistently, internalisation of CXCR4 by the interaction with its ligand, CXCL12, has been previously described in lymphoma cells that come into contact with stromal cells,[43] and also in multiple myeloma cells.[52]

Moreover, the antitumour activity of the nanoparticle was partially reversed by the pre-treatment with a CXCR4 antagonist, AMD3100, which demonstrates that its effect is, at least in part, mediated by CXCR4. The specific targeting of nanoparticles to CXCR4 by the T22 ligand has previously been described in colorectal cancer cells using a protein-only nanoparticle.[49] However, this is the first time that a chemotherapeutic drug has been specifically targeted to cells expressing this receptor. CXCR4 neutralisation by different molecules has been previously reported to show a strong antilymphoma effect, thus killing CXCR4-expressing lymphoma cells by a specifically designed nanosystem like **S2** can be an effective approach to reverse drug-resistance and to induce antitumour activity in B-NHL. As the CXCR4 receptor is overexpressed in other haematologic malignancies, e.g., acute myeloid leukaemia, chronic lymphocytic leukaemia or acute lymphoblastic leukaemia[44,45,53], in which the CXCL12/CXCR4 axis mediates cell survival and drug resistance,[54,55] the specific targeting of chemotherapeutic agents to the CXCR4 receptor could be also an effective strategy to treat different types of haematologic malignancies.

Finally, the specific targeting of doxorubicin to CXCR4-expressing cells would not only enhance its antitumour effect, but would also diminish toxicity in normal cells. Doxorubicin is an anthracycline that intercalates DNA and is commonly used to treat many types of cancers, including several haematological malignancies.

However, severe adverse effects, of which cardiotoxicity is the most relevant, are frequently associated with high cumulative doses of this drug.[56] For this reason, different approaches have been developed as drug delivery systems to enhance the antitumour effect of doxorubicin, while also reducing its toxicity in normal cells. Thus entrapment of doxorubicin into liposomes, hydrogels and nanoparticles has been evaluated in different cancer types.[57] However, none of these formulations include the specific targeting of the drug to tumour cells. In contrast, the new delivery system **S2** proposed herein is able to conduct the delivery of a chemotherapeutic drug to CXCR4-expressing cells. Specificity of delivery would enhance the antitumour effect in tumour cells, which overexpress CXCR4, and would diminish toxicity in normal cells.

Conclusions

In summary, we have developed a CXCR4-targeted delivery system using MSN containing T22 analogue peptide **P** as a dual functional element. In the prepared nanosystem, peptide **P** was able to cap the pores in MSN to block the release of the doxorubicin drug. Anchored peptide **P** also guides the capped nanoparticle to B-NHL cells and facilitates MSN uptake via the CXCR4 receptor. The endocyted capped MSN were opened thanks to the proteolytic enzymes present in the lysosomes, which degrade peptide **P** and allow doxorubicin delivery. These can be considered a preliminary result towards adopting new therapeutic strategies to kill CXCR4-expressing lymphoma cells. This is also one of the few examples that use peptides as a targeting and capping element in MSNs. We believe that the synthetic strategy followed herein, which combines the use of mesoporous nanoparticles with highly specific targeting peptides, can contribute to further design improved delivery systems for other specific diseases.

Experimental Section

Chemicals: The chemicals tetraethylorthosilicate (TEOS), n-cetyltrimethylammonium bromide (CTABr), sodium hydroxide (NaOH), protease from *Streptomyces griseus*, fluorescein and CXCR4 inhibitor AMD3100 were

acquired from Sigma-Aldrich and were used without further purification. Copper (II) sulphate pentahydrate ($CuSO_4 \cdot 5H_2O$) and sodium ascorbate were purchased from Scharlab. Doxorubicin hydrochloride was obtained from Sequoia. The H-Rink amide ChemMatrix resin was provided by PCAS BioMatrix Quebec, Canada. Solvents MeOH, DMF, DCM, tert-butylmethyl ether, ACN, DMSO and the reactives TFA, DIEA, HBTU, piperidine, DIPCDI, HOAt, TIS were supplied by Sigma-Aldrich, Carlo Erba SDS and Panreac. The amino acid C-terminal, Fmoc-Arg(Pbf)-OH, was purchased from Iris Biotech.

General techniques: The T22 peptide analogue was synthesised using instrumentation in the CIBER BBN Synthesis of Peptide Unit.

UV spectroscopy, HPLC and HPLC-MS were used for the analysis and purification of the azide-containing T22 peptide. UV measurements were taken on a UV-Vis Recording Spectrophotometer UV-2501PC at 290 nm.

Analytical RP-HPLC was carried out in a Waters instrument comprising a XBridge™ BEH130 C18 reversed-phase HPLC analytical column (4.6 x 100 mm, 3.5 µm; Waters), a separation module (Waters 2695), an automatic injector (Waters 717 autosampler), and a photodiode array detector (Waters 2298). Data were processed with the Empower 2 software. UV detection was performed at 220 nm, and the linear gradients from 5%B to 100%B were run at a flow rate of 1.0 mL/min for 8 min. The elution solvent system was: A: H_2O (+0.045% TFA) and B: ACN (+0.036% TFA).

The HPLC-MS analyses of peptide samples were carried out in a Waters instrument comprising a Sunfire™ C18 reversed-phase analytical column (2.1 mm x 100 mm, 5 µm; Waters), a separation module (Waters 2695), an automatic injector (Water 717 autosampler), a photodiode array detector (Waters 2298), and a Waters micromass ZQ spectrometer unit. Data were processed with the MassLynx V4.1 software (Waters). UV detection was performed at 220 nm, and

the linear gradients of ACN (+0.07% formic acid) in H_2O (+0.1% formic acid) were run at a flow rate of 0.3 mL/min for 8 min.

HPLC purification was carried out by semipreparative RP-HPLC in a Waters instrument comprising a Sunfire™ C18 reversed-phase semipreparative column, 5.0 µm, 19 x 100 mm, a separation module (Waters Delta 600), a Waters 600 controller, an automatic injector (Waters 2700), a dual absorbance detector (Waters 2487) and a fraction collector II (Waters). UV detection was performed at 220 nm, and the linear gradients from 5%B to 100%B were run at a flow rate of 15.0 mL/min over 20 min. The elution solvent system was: A: H_2O (+0.1% TFA) and B: CH_3CN (+0.05% TFA).

Powder X-ray diffraction (PXRD), the thermogravimetric analysis (TGA), elemental analysis, transmission electron microscopy TEM) and N_2 adsorption-desorption were employed to characterise the prepared materials. PXRD measurements were taken with a Philips D8 Advance diffractometer using CuK_α radiation. The TGA analyses were carried out on a TGA/SDTA 851e Mettler Toledo balance using an oxidant atmosphere (air, 80 mL/min) with a heating programme consisting in a heating ramp of 10 ^oC per minute from 393 to 1273 K, and an isothermal heating step at this temperature lasting 30 minutes. Fluorescence spectroscopy was carried out on a JASCO FP-8300 fluorimeter. TEM images were obtained with a 100 kV Philips CM10 microscope.

Synthesis of the propargyl-containing linker 1: 1.28 mL (5 mmol) of 3-(triethoxysilyl)propylisocyanate with 320 µL (5 mmol) of propargylamine were reacted in 15 mL of CH_2Cl_2 overnight. Then the solvent was evaporated to obtain the final propargyl-containing product 1-(3-(triethoxysilyl)propyl)-3-prop-2-ynyl-urea (**1**), as depicted in Scheme SI-1. The obtained product was characterised by ^1H NMR (400 MHz, $CDCl_3$): δ 0.53 (t, 2H), 1.11 (t, 3H), 1.50 (qt,2H), 2.12 (t, 1H), 3.06 (qd, 2H), 3.70 (qd, 2H), 3.85 (qd,2H), 5.85(dt, 1H) ppm; ^{13}C NMR (101 MHz, $CDCl_3$) δ 158.40, 80.91, 70.24, 57.58, 42.53, 29.36, 23.22, 17.72, 7.32; HRMS-EI

m/z: calcd for $C_{13}H_{26}N_2O_4Si$ 302.1662; found: 302.1683; FT-IR typical urea bands were found (see Supporting Information for more details).

Solid-Phase Synthesis of the T22 analogue ([$Tyr^{5,12}Lys^7$]Polyphemusin II)[1]: An azide-containing analogue of T22 (**P**) with Lys(N_3) in the N-Terminal was obtained using all the Cys side chains protected with Trt. For this purpose, 200 mg of the H-Rink amide ChemMatrix resin (0.114 mmol; loading 0.57 mmol/g) were washed with MeOH, DMF, DCM and TFA/DCM 1%, DMF, DCM and DIEA 5%/DCM, DMF and DCM. The amino acid C-terminal Fmoc-Arg(Pbf)-OH (0.220 mg; 0.3 mmol) was introduced into the resin using as a coupling system HBTU (0.130 mg; 0.3mmol) and DIEA (0.078 mL; 0.4 mmol) in DMF, and the mixture was shaken for 1 h. Then the Fmoc-Arg(Pbf)-Rink amide resin was filtered and washed with DMF (5 x 1 min) and DCM (5 x 1 min). The Fmoc group was eliminated by treatments with piperidine-DMF (1:4; 25 mL/g resin; 2 x 5 min). Filtrates were collected and quantified by UV (290 nm) to obtain a loading of 0.50 mmol/g. Based on this loading, the following protected amino acids were incorporated (3 equiv each) using HBTU (3 equiv) and DIEA (4 equiv) into the DMFas coupling system with 60-s preactivation, except for Fmoc-Cys(Trt)-OH (3 equiv). This was incorporated using DIPCDI (3 equiv) and HOAt (3 equiv) into DMF by a 3-minute preactivation to avoid epimerisation. Washes between couplings and the Fmoc group elimination steps were performed using DMF (5 x 1 min) and DCM (5 x 1 min). Having finished peptide elongation, the peptide was cleaved from the resin using the mixture TFA-TIS-H_2O (95:2.5:2.5, 30 mL) at 25 ^oC for 1 h. Were separated by filtration from the resin and were partially evaporated and then precipitated by addition of cold tert-butylmethyl ether. The suspension was centrifuged, the supernatant was discarded, and the solid was dissolved in H_2O-ACN (1:1) and lyophilised to obtain 250 mg of the linear peptide crude depicted in Scheme SI-2 (yield: 83%; purity: 85%).

T22 analogue cyclisation ([$Tyr^{5,12}Lys^7$]Polyphemusin II): The obtained peptide was oxidised for its cyclisation. To this end, the linear peptide precursor (100 mg, 3.78 x 10^{-5} mol) was dissolved in water-acetonitrile (1:1; 126 mL, 3 x 10^{-4} M) and

pH was adjusted to 8 with aqueous ammonia. DMSO was added (5% of the total volume) as the oxidising agent. The reaction was stirred for 12 h at room temperature and monitored by HPLC. After reaction completion, the solvent was removed by lyophilisation to obtain 96 mg of the cyclic peptide crude (yield: 96%). The crude was purified by semipreparative HPLC-MS (Figure SI-2) and fractions were collected to obtain the final azide-T22 analogue (**P**), which is seen in Scheme 2.

Synthesis of mesoporous silica nanoparticles: MCM-41 mesoporous nanoparticles were synthesised by the following procedure: n-cetyltrimethylammonium bromide (CTABr, 1.00 g, 2.74 mmol) was first dissolved in 480 mL of deionised water. Then 3.5 mL of NaOH 2.00 M in deionised water were added to the CTABr solution, and then the solution temperature was adjusted to 80 ^{o}C. At that time, TEOS (5.00 mL, 2.57 x 10^{-2} mol) was added drop-wise to the surfactant solution. The mixture was allowed to stir for 2 h to give a white precipitate. After this time, the solid product was centrifuged, washed with deionised water and ethanol, and dried at 60 ^{o}C to give MCM-41 as-synthesised mesostructured nanoparticles. To obtain the final porous nanoparticulated material (MSNs), the as-synthesised solid was calcined at 550 ^{o}C in an oxidant atmosphere for 5 h to remove the template phase.

Synthesis of solid S1: MSNs solid support (190 mg) and doxorubicin hydrochloride (96 mg, 0.17 mmol) were suspended in Milli-Q water (7.5 mL) and stirred for 24 h at room temperature to achieve maximum loading in the pores of the MCM-41-type scaffolding. Then the solid was filtered and dried under vacuum. In another step, 192 mg of the doxorubicin loaded solid were suspended in 30 mL of acetonitrile and 0.96 mmol of the propargyl-containing linker **1** were added. The mixture was stirred for 5.5 h, then filtered, washed with acetonitrile and dried under vacuum to yield red-pink solid **S1**.

Synthesis of solid S2: To prepare solid **S2**, previously functionalised nanoparticles **S1** (12 mg) and azide-containing T22 peptide **P** (15 mg) were

suspended in a 50:50 v/v DMF-H_2O mixture (10 mL) in the presence of excess doxorubicin (5 mg, 0.008 mmol) to avoid the delivery of the drug from pores to the bulk solution during synthesis. Then 5.7 μL of a solution of $CuSO_4 \cdot 5H_2O$ (10^{-3} $mol \cdot L^{-1}$) and 5.7 μL of sodium ascorbate (10^{-2} $mol \cdot L^{-1}$) were added. The reaction mixture was stirred at room temperature for 3 days. Then the nanoparticles were centrifuged and washed thoroughly with water to remove unreacted and absorbed molecules. The resulting red-pink nanoparticles were dried under vacuum to yield capped solid **S2**. This solid contained doxorubicin in the pore voids and the T22 analogue peptide **P** was anchored in the pore outlets, as depicted in Scheme SI-3.

Cell lines and culture conditions: Toledo is a human non-Hodgkin's lymphoma cell line obtained from the American Type Culture Collection. Toledo cells were cultured with RPMI 1640 supplemented with 10% fetal bovine serum, 1% glutamine, 100 U/mL penicillin/streptomycin (Life Technologies) and incubated at 37 ^{o}C in a humidified atmosphere containing 5% CO_2.

FACS analysis: A fluorescence-activated cell sorting (FACS) analysis was performed to evaluate CXCR4 membrane expression in the Toledo cells exposed to calcined MCM-41 nanoparticles, solid **S2** (75 μg/mL) or AMD3100 (10 μg/mL) for 1 h. For each sample, $3x10^6$ cells were washed in phosphate-buffered saline (PBS) and incubated for 30 min at 4ºC with the PE-Cy5 mouse anti-human CXCR4 monoclonal antibody or PE-Cy5 mouse IgG2a (BD Pharmingen) as an isotype control. Cells were washed twice with PBS and the cell surface expression of CXCR4 was detected by flow cytometry (FACS Calibur, BD). Data were analysed with the Cell Quest Pro software. The results are expressed as the mean fluorescence intensity (MFI) ± SD.

Cytotoxicity assays: The antitumour activity of solid **S2** was evaluated by measuring cell metabolic capacity (viability) using the Cell Proliferation Kit II (XTT) (Roche Diagnostics) and following the manufacturer's recommendations. Briefly, Toledo cells were seeded into 96-well plates ($30x10^4$ cells/well) and exposed to

calcined MCM-41 nanoparticles (PBS) or solid **S2** (75 μg/mL), with or without a 1 h pre-treatment with AMD3100. After a 48 h exposure at 37 ^{o}C, XTT detection solution was added to the wells and absorbance was measured at the 450 nm wavelength with a spectrophotometer. Growth inhibitory activity was expressed as a percentage of cell viability, as compared with the untreated controls. Values are the averages of the replicates performed in at least two independent experiments.

Apoptotic detection and DNA fragmentation: To evaluate the induction of apoptosis, nuclear staining was performed with Hoescht 3342 dye (Sigma) in the cells exposed to calcined MCM-41 nanoparticles (PBS) or solid **S2** (75 μg/mL) for 48 h. During exposure, 2 μl/mL of Hoescht dye were added to the cell culture and live cells were observed under a fluorescence microscope (Zeiss).

Acknowledgements

Financial support from the Spanish Government (MAT2012-38429-C04 and PIB2010BZ-00563), Generalitat Valenciana (PROMETEOII/2014/047), Generalitat de Catalunya (2009-SGR-1437), Instituto de Salud Carlos III (FI10/00758 and FIS PII2/01861), MaratóTV3 416/C/2013-2030, CIBER-BBN (Nanomets), and Institut de Recerca Josep Carreras Sant Pau is gratefully acknowledged. C.T. is grateful to the Spanish MEC for her grant. We also acknowledge Cristina Suárez for her technical support and the use of the CIBER-BBN Nanotoxicology and Synthesis of Peptides platforms

References

1. M. Vallet-Regí, F. Balas, D. Arcos, *Angew. Chem.* **2007**, *119*, 7692 ; *Angew. Chem. Int. Ed.* **2007**, *46*, 7548.

2. K. M. L. Taylor-Pashow, J. Della Rocca, R. C. Huxford, W. Lin, *Chem. Commun*. **2010**, *46*, 5832.

3. P. Yang, S. Gai, J. Lin, *Chem. Soc. Rev*. **2012**, *41*, 3679; d) Z. Li, J. Barnes, A. Bosoy, J. F. Stoddart, J. I. Zink*, Chem. Soc. Rev*. **2012**, *41*, 2590.

4. M. Colilla, B. González, M. Vallet-Regí, *Biomat. Sci*. **2013**, *1*, 114.

5. Q. He, J. Shi, *J. Mater. Chem*. **2011**, *21*, 5845.

6. C.-Y Lai, B.G. Trewyn, D.M. Jeftinija, K. Jeftinija, S. Xu, S. Jeftinija, V. S. –Y. Lin, *J. Am. Chem. Soc.* **2003**, *125*, 4451.

7. C. Park, K. Oh, S.C. Lee, C. Kim, *Angew. Chem. Int. Ed.* **2007**, *46*, 1455.

8. R. Liu, X. Zhao, T. Wu, P. Feng, *J. Am. Chem. Soc.*, **2008**, *130*, 14418.

9. Z. Luo, K. Cai, Y. -Hu, L. Zhao, P. Liu, L. Duan, W. Yang, Angew. Chem. **2011**, *123*, 666; *Angew. Chem. Int. Ed.* **2011**, *50*, 640.

10. C. Wang, Z. Li, D. Cao, Y.-L. Zhao, J. W. Gaines, O. A. Bozdemir, M.W. Ambrogio,M. Frasconi, Y. Y. Botros, J. I. Zink, J. F. Stoddart, *Angew. Chem*. **2012**, *124*, 5556; Angew. *Chem. Int. Ed*. **2012**, *51*, 5460.

11. Y. Zhang, Q. Yuan, T. Chen, X. Zhang, Y. Chen, W. Tan, *Anal. Chem.* **2012**, *84*, 1956.

12. D. Tarn, M. Xue, J. I. Zink, *Inorg. Chem.* **2013**, *52*, 2044.

13. N. K. Mal, M. Fujiwara, Y. Tanaka, *Nature*, **2003**, *421*, 350.

14. A. Schlossbauer, S. Warncke, P. M. E. Gramlich, J. Kecht, A. Manetto, T. Carell, T. Bein, *Angew. Chem*. **2010**, *122*, 4842; *Angew. Chem. Int. Ed.* **2010**, *49*, 4734.

15. E. Ruiz-Hernández, A. Baeza, M. Vallet-Regi, *ACS Nano* **2011**, *5*, 1259.

16. D. He, X. He, K.Wang, J. Cao, Y. Zhao, *Adv. Funct. Mater.* **2012**, *22*, 4704.

17. E. Aznar, L. Mondragón, J.V. Ros-Lis, F. Sancenón, M.D. Marcos, R. Martínez-Máñez, J. Soto, E. Pérez-Payá, P. Amorós, *Angew. Chem. Int. Ed.* **2011**, *50*, 11172.

18. A. Baeza, E. Guisasola, E. Ruiz-Hernández, M. Vallet-Regi, *Chem. Mater.* **2012**, *24*, 517.

19. A. Schlossbauer, J. Kecht, T. Bein, *Angew. Chem*. **2009**, *121*, 3138 ; *Angew. Chem. Int. Ed.* **2009**, *48*, 3092.

20. C. Park, H. Kim, S. Kim, C. Kim, *J. Am. Chem. Soc***. 2009**, *131*, 16614 – 16615.

21. A. Bernardos, L. Mondragón, E. Aznar, M.D. Marcos, R. Martínez-Máñez, F. Sancenón, J. Soto, J. M. Barat, E. Pérez-Payá, C. Guillem, P. Amorós, *ACS Nano* **2010**, *4*, 6353.

22. P. D. Thornton, A. Heise, *J. Am. Chem. Soc.*, **2010**, *132*, 2024-2028.

23. A. Popat, B. P. Ross, J. Liu, S. Jambhrunkar, F. Kleitz, S. Z. Qiao, *Angew. Chem.* **2012**, *124*, 12654; *Angew. Chem. Int. Ed*. **2012**, *51*, 12486.

24. Z. Chen, Z. Li, Y. Lin, M. Yin, J. Ren, X. Qu, *Chem. Eur. J.* **2013**, *19*, 1778.

25. C.E. Ashley, E.C. Carnes, G.K. Phillips, D. Padilla, P.N. Durfee, P.A. Brown, T.N. Hanna, J. Liu, B. Phillips, M.B. Carter, N.J. Carroll, X. Jiang, D.R. Dunphy, C.L Willman, D.N. Petsev, D.G. Evans, A.N. Parikh, B. Chackerian, W. Wharton, D.S. Peabody, *Nat.Mat.* **2011**, *10*, 389.

26. C. Coll, L. Mondragón, R. Martínez-Máñez, F. Sancenón, M.D. Marcos, J. Soto, P. Amorós E. Pérez-Payá, *Angew. Chem.* **2011**, *123*, 2186; *Angew. Chem. Int. Ed.* **2011**, *50*, 2138.

27. K. Radhakrishnan , S. Gupta , D. Gnanadhas , P.C. Ramamurthy, D. Chakravortty , A.M. Raichur, *Part. Part. Syst. Charact.* **2014**, *31*, 449.

28. C. de la Torre C, A. Agostini, L. Mondragón, M. Orzáez, F. Sancenón, R. Martínez-Máñez, M.D. Marcos, P. Amorós, E. Pérez-Payá, *Chem Commun*, **2014**, *50*, 24, 3184.

29. L. Mondragón, N. Mas, V. Ferragud, C. de la Torre, A. Agostini, R. Martínez-Máñez, F. Sancenón, P. Amorós, E. Pérez-Payá, M. Orzáez, *Chem. Eur. J.* **2014**, *20*, 5271.

30. J. Zhenga, X. Tiana, Y. Sunb, D. Lub, W. Yanga, *Int. J. Pharmaceutics* **2013**, *450*, 296.

31. K. Murai, M. Higuchi, T. Kinoshita, K. Nagataa, K. Kato, *Phys.Chem. Chem. Phys.*, **2013**, *15*, 11454.

32. D.M. Copolovici, K. Langel, E. Eriste, U. lo Langel, *ACSNano*, **2014**, *8*, 1972.

33. Q. Zhang, X. Wang, P.-Z. Li, K.T. Nguyen, X.-J. Wang, Z. Luo, H. Zhang, N. S. Tan, Y. Zhao, *Adv. Funct. Mater.* **2014**, *24*, 2450.

34. C.E. Ashley, E.C. Carnes, K.E. Epler, D.P. Padilla, G.K. Phillips, R.E. Castillo, D.C. Wilkinson, B.S. Wilkinson, C.A. Burgard, R.M. Kalinich, J.L. Townson, B. Chackerian, C.L. Willman, D.S. Peabody, W. Wharton, C.J. Brinker, *ACSNano* **2012**, *6*, 2174.

35. Q. Zhang, F. Liu, K.T. Nguyen, X. Ma, X. Wang, B. Xing, Y. Zhao, *Adv. Funct. Mater.* **2012**, *22*, 5144.

36. Z. Luo, K. Cai, Y. Hu, L. Zhao, P. Liu, L. Duan, W. Yang, *Angew. Chem. Int. Ed.* **2011**, *50*, 640.

37. J. Zhang, Z.-F. Yuan, Y. Wang, W.-H. Chen, G.-F. Luo, S.-X. Cheng, R.-X. Zhuo, X.-Z. Zhang, *J. Am. Chem. Soc.* **2013**, *135*, 5068.

38. Z. Zhao, H. Meng, N. Wang, M.J. Donovan, T. Fu, M. You, Z. Chen, X. Zhang, W. Tan, *Angew. Chem. Int. Ed.* **2013**, *52*, 7487.

39. P. Feugier, A. Van Hoof, C. Sebban, P. Solal-Celigny, R. Bouabdallah, C. Fermé, B. Christian, E. Lepage, H. Tilly, F. Morschhauser, P. Gaulard, G. Salles, A. Bosly, C. Gisselbrecht, F. Reyes, B. Coiffier *J. Clin. Oncol.* **2005**, *23*, 4117.

40. M. Pfreundschuh, E. Kuhnt, L. Trümper, A. Österborg, M. Trneny, L. Shepherd, D.S. Gill, J. Walewski, R. Pettengell, U. Jaeger, P.-L. Zinzani, O. Shpilberg, S. Kvaloy,

P.N. Brown, R. Stahel, N. Milpied, A. López-Guillermo, V. Poeschel, S. Grass, M Loeffler, N. Murawski, *Lancet Oncology* **2011**, *12*, 1013.

41. S. Cultrera, S. Dalia, *Cancer Control,* 2012, *19*, 204.

42. J. Linderoth J, P.Edén , M. Ehinger, J. Valcich ,M. Jerkeman , O. Bendahl, M.Berglund, G.Enblad, M.Erlanson, G.Roos, E.Cavallin-Ståhl, *British Journal of Haematology*, **2008**,*141*,423.

43. J. Arai, M. Yasukawa, Y. Yakushijin, T. Miyazaki, S. Fujita, Eur J Haematol. **2000**, *64*, 323.

44. N. Ishibe, M. Albitar, I. Jilani, L.R. Goldin, G.E. Marti, N.E. Caporaso, *Blood* **2002**, *100*, 1100.

45. S.-Y. Ko, C.-J. Park, S.-H. Park, Y.-U. Cho, S. Jang, E.-J. Seo, N. Kim, D.-Y. Kim, K.N. Koh, H.J. Im, J.-J. Seo, H.-S. Chi, *Leuk Res*. **2014**, *38*, 65.

46. M.J. Moreno, R. Dieguez-Gonzalez, S. Novelli, A. Mozos, A. Gallardo, M.A. Pavón, M.V. Céspedes, A. Grañena, M. Alcoceba, O. Blanco, M. Gonzalez-Díaz, J. Sierra, R. Mangues, I. Casanova, *J. Pathol.* **2014**, DOI: 10.1002/path.4446

47. X. Liang, *Chem. Biol. Drug Des.* **2008**,*72*, 97.

48. T. Murakami, T.-Y. Zhang, Y. Koyanagi, Y. Tanaka, J. Kim, Y. Suzuki, S. Minoguchi, H. Tamamura, M. Waki, A. Matsumoto, N. Fujii, H. Shida, J.A. Hoxie, S.C. Peiper, N. Yamamoto *J. Virol.* **1999**, *73*, 7489.

49. U.Unzueta, M.V. Céspedes, N.Ferrer-Miralles, I. Casanova, J. Cedano, J.L. Corchero, J.Domingo-Espín, A.Villaverde, R.Mangues, E. Vázquez, *Int J Nanomedicine*. **2012**, *7*, 4533.

50. H. Tamamura, M. Imai, T. Ishihara, M. Masuda, H. Funakoshi, H. Oyake, T. Murakami, R. Arakaki, H. Nakashima, A. Otaka, T. Ibuka, M. Waki, A. Matsumoto, N. Yamamoto, N. Fujii, *Bioorg. Med. Chem.* **1998**, *6*, 1033.

51. J.M. Busillo, J.L. Benovic, *Biochim. Biophys. Acta*, **2007**, *1768*, 952.

52. Y. Alsayed, H. Ngo, J. Runnels, X. Leleu, U.K. Singha, C.M. Pitsillides, J.A. Spencer, T. Kimlinger, J. M. Ghobrial, X. Jia, G. Lu, M. Timm, A. Kumar, D. Côté, I Veilleux, K.E. Hedin, G.D. Roodman, T.E. Witzig, A.L. Kung, T. Hideshima, K.C. Anderson, C.P. Lin, I.M. Ghobrial, *Blood* **2007**, *109*, 2708.

53. A.C. Spoo, M. Lu¨bbert, W.G. Wierda, J.A. Burger, *Blood* **2007**, *109*, 786.

54. M.B. Meads, L.A. Hazlehurst, W.S. Dalton, *Clin. Cancer. Res*. **2008**,*14*, 2519.

55. S. López-Giral, N.E. Quintana, M. Cabrerizo, M. Alfonso-Pérez, M. Sala-Valdés, V.G. De Soria, J.M. Fernández-Rañada, E. Fernández-Ruiz, C. Muñoz, *J. Leukoc. Biol.* **2004**, *76*, 462.

56. Y. Shi, M. Moon, S. Dawood, B. McManus, P.P. Liu, *Herz.* **2011**, *36*, 296.

57. O. Tacar, P. Sriamornsak, C.R. Dass, *J. Pharm. Pharmacol.* **2013**, *65*, 157.

Adv. Funct. Mater., 2015, 25, 687

Gated Mesoporous Silica Nanoparticles Using a Double-Role Circular Peptide for the Controlled and Target-Preferential Release of Doxorubicin in CXCR4-expresing Lymphoma cells.

Cristina de la Torre, Isolda Casanova, Gerardo Acosta, Carmen Coll, María José Moreno, Fernando Albericio, Elena Aznar, Ramón Mangues, Miriam Royo,* Félix Sancenón and Ramón Martínez-Máñez**

Supporting Information

Propargyl-containing linker 1

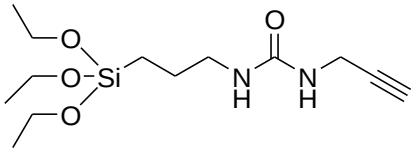

Scheme SI-1. Structure of propargyl-containing linker **1.**

The FT-IR spectroscopy analysis confirmed binding between propargylamine and 3-(triethoxysilyl)propylisocyanate to give *propargyl-containing linker **1***. Figure SI-1 shows the FT-IR spectra of the product. The existence of the urea bond was confirmed by the presence of wide stretching bands which centred at 2928 and 2885 cm^{-1} and the C=O stretching vibration at 1623 cm^{-1}. The absorption band due to the C-H stretching vibration of the alquinyl group can be seen at around 3319 cm^{-1}.

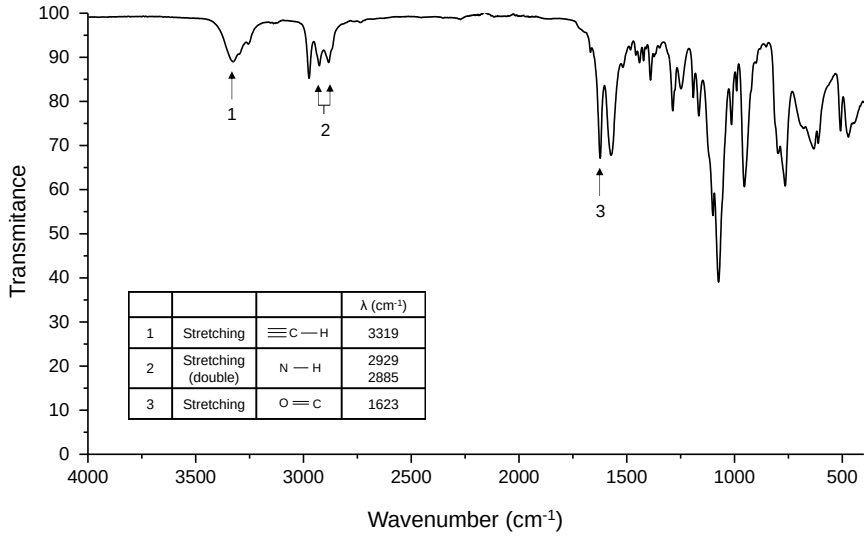

Figure SI-1. FT-IR spectra of the *propargyl-containing linker.*

Synthesis of the linear precursor of peptide P

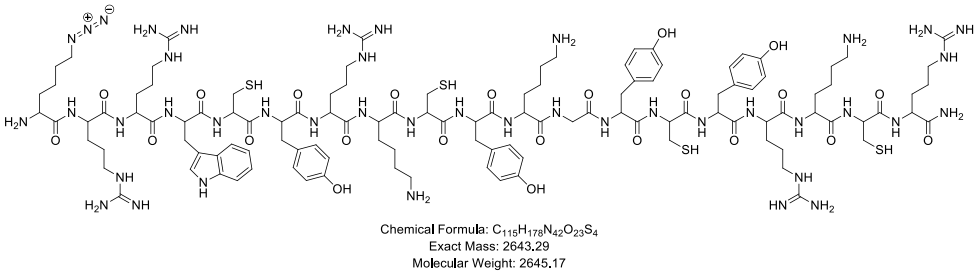

Scheme SI-2. The T22 peptide linear precursor with Lys(N_3) at the N-Terminal.

Characterisation of peptide P

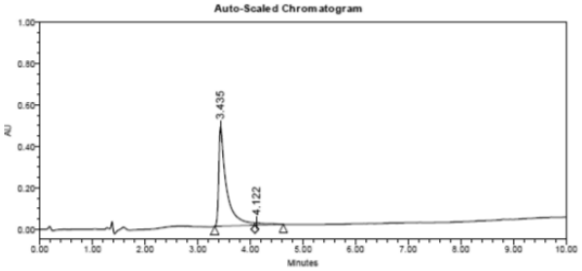

HPLC Cyclic Compound

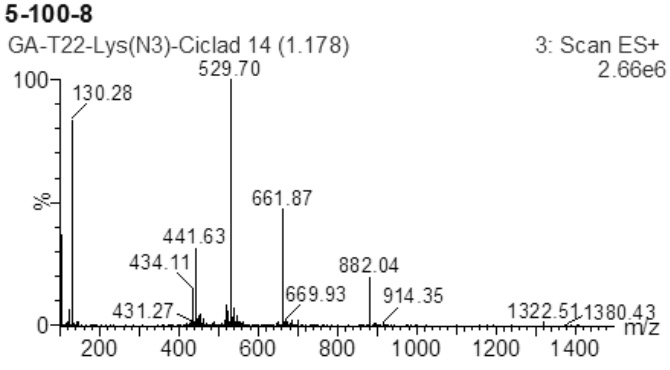

HPLC-MS Cyclic Compound ion fragments +2/2; +3/3; +4/4; +5/5

Figure SI-2. HPLC and HPLC-MS of cyclic peptide **P**.

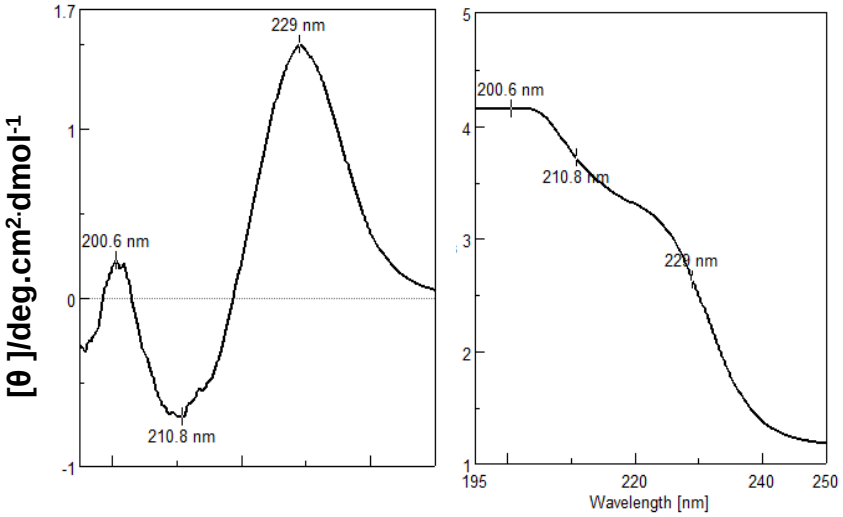

Figure SI-3. Circular dichroism of cyclic peptide **P**.

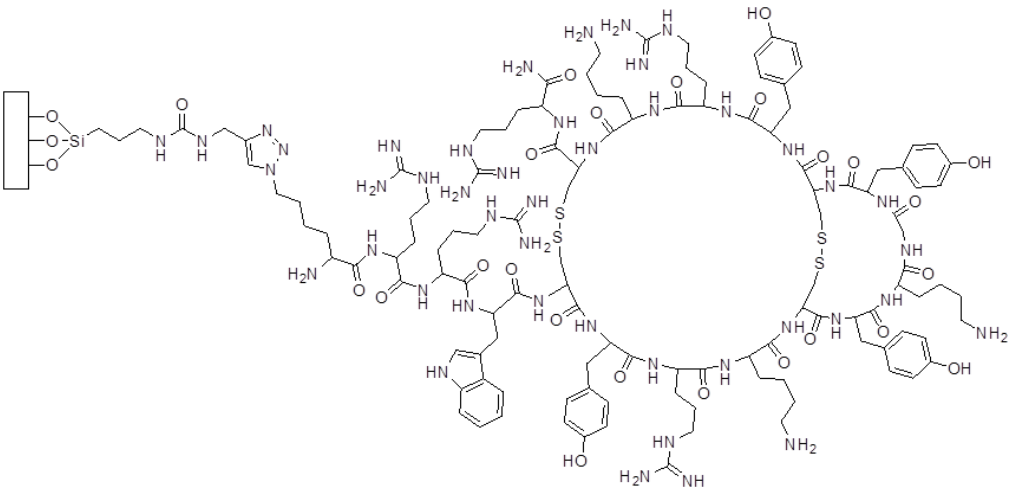

Scheme SI-3. Representation of analogue T22 peptide **P** anchored in the pore outlets of MSN.

2.8. C9h peptide delivered from ε-polylysine-capped mesoporous silica nanoparticles induced apoptosis in cancer cells

Cristina de la Torre,[b,c,d] Leticia Domínguez-Berrocal,[a] José R. Murguía,[b,c] Ramón Martínez-Máñez,[b,c,d]* Jerónimo Bravo,[a]* and Félix Sancenón[b,c,d]

a Departamento de Genómica y Proteómica, Instituto de Biomedicina de Valencia c/ Jaime Roig 11, 46010, Valencia (Spain)

b Centro de Reconocimiento Molecular y Desarrollo Tecnológico (IDM), Centro Mixto Universidad Politécnica de Valencia, Universidad de Valencia, Valencia (Spain) Camino de Vera s/n, 46022, Valencia (Spain).

[c] CIBER de Bioingeniería, Biomateriales y Nanomedicina, Madrid (Spain).

[d] Departamento de Química, Universidad Politécnica de Valencia, Camino de Vera s/n, 46022, Valencia (Spain).

Submitted to "Chemistry: A European Journal."

Abstract

Apoptotic signalling pathways are altered in numerous pathologies such as cancer. In this scenario, caspase-9/PP2Acα interaction constitutes a key target with pharmacological interest to re-establish apoptosis in tumour cells. Very recently a short peptide (C9h) known to disrupt caspase-9/PP2Acα interaction with subsequent apoptosis induction was described. Here we prepared two sets of mesoporous silica nanoparticles loaded with safranin O (**S2**) or with C9h peptide (**S4**) and functionalized with ε-polylysine as capping unit. Aqueous suspensions of both nanoparticles showed negligible cargo release whereas in the presence of pronase a marked delivery of safranin O or C9h was observed. Confocal microscopy studies carried out with HeLa cells indicated that both materials were internalized and released their entrapped cargos. Besides, a marked decrease in HeLa cell viability (ca. 50%) was observed when treated with C9h-loaded **S4** nanoparticles. Moreover, **S4** provides peptide protection from degradation additionally allowing a dose reduction to observe an apoptotic effect when compared with C9h alone or in combination with a cell-penetrating peptide (i.e. Mut3DPT-C9h). Flow cytometry studies, by means of Annexin V-FITC staining, showed the activation of apoptotic pathways in HeLa as a consequence of **S4** internalization, release of C9h peptide and disruption of caspase-9/PP2Acα interaction

Introduction

Apoptosis is a genetically programmed cell death that when deregulated is associated with cancers. Recently, several phosphatases have become attractive targets for the treatment of a variety of diseases, including cancers. [1-4] However, the only clinical drugs targeting phosphatases are the immunosuppressive cyclosporin A and FK506, which inhibit serine/threonine phosphatase 2B (calcineurin) and NFAT activation.[5-9] Nevertheless, long-term usage of these drugs can lead to undesirable side effects.[10]

Some of us previously generated a new bifunctional peptide that specifically binds PP2Acα (human DPT-C9h or mouse DPT-C9), composed by the cell-

penetrating peptide (CPP) DPT-sh1 followed by a caspase-9-derived sequence (C9h).[11] The resulting sychnologic peptide targets caspase-9/PP2Acα interaction, leading to caspase-9 activation, mitochondrial membrane permeabilization, cytochrome c release and apoptosis in a variety of human and mouse cancer cell lines. The mouse-specific peptide DPT-C9 also induced tumor growth inhibition in lung (K-RasLA-1) and breast cancer (PolyomaMiddleT, PyMT) mouse models showing neither toxicity nor immunogenic response.[11] DPT-C9h had a specific effect on transformed B cells isolated from chronic lymphocytic leukemia patients without any effect on T-cells, NK-cells and monocytes, but did not show any effect on primary B cells from healthy donors.[12]

A major concern when using peptides as therapeutics is the potential effects of serum proteases on peptide degradation prior to cellular internalization. Several approaches have been used to stabilize CPPs for in vivo applications, such as the incubation with SDS or polysialic acid, substitution of L-aminoacids by D-isomers containing peptides, retroinversion, the use of non-natural aminoacids, modification of peptide backbones, cyclization, disulfide bond formation, constrained peptides and stapled peptides among others. [13] DPT-C9h serum proteolysis resistance was improved by mutating a serum protease cleavage site comprised within the CPP sequence. The peptide Mut3DPT-C9h with an arginine to alanine mutation at the eighth residue of the DPT sequence showed enhanced peptide stability and a better pharmacokinetic profile, also maintaining the same apoptotic effect as the original DPT-C9h. [14] However this and other reported techniques to stabilize peptides are complex and time consuming. In this scenario, we decided to explore alternative methods for delivering the caspase-9 derived sequence C9h in the cell in a CPP independent manner *(vide infra)*.

From another point of view, the administration of certain drugs is hindered by their low water solubility, rapid degradation, decreased bioavailability and lack of specificity, which is responsible for severe side effects.[15,16] Such features highlight the limitations of certain drugs used nowadays in the clinic, since there are constraints relative to the maximum dose and number of treatments that can be

administered to each patient.[17] In fact, such dose restriction in conjugation with a decreased bioavailability usually results in a lower therapeutic outcome and can trigger the development of resistance to these therapies.[18]

Therefore, it is crucial to develop carriers capable of protecting drugs and delivering them in temporally controlled fashion, improving their therapeutic outcome as a result. Controlled release of drugs at will and at site is an expanding research field in biotechnology and biomedicine. [19]

In this scenario, the use of mesoporous silica nanoparticles (MSNs) as inorganic nanocarriers of selected cargo molecules (including drugs) has been extensively explored in the last decade due to favorable characteristics of MSNs such as large load capacity, biocompatibility, high thermal stability, homogeneous porosity, inertness and tunable pore sizes. [20-22] When compared to organic nanocarriers,[23] MSNs are more resistant to pH, temperature variations and to mechanical stress, which renders them an improved ability to protect the cargo when in contact with body fluids. [24] Drugs, genes or proteins are usually loaded in MSNs by submerging the nanoparticles in solutions containing the therapeutic molecules.[25] In this process, payloads are encapsulated in MSNs matrix by adsorption, a process that involves the formation of hydrogen bonds or electrostatic interactions between cargo molecules and MSNs. Besides, the external surface of the MSNs can be functionalized with certain molecular or supramolecular entities that controlled the release of the cargo at will upon the application of an external trigger.[26-28] These “gated” materials released the entrapped cargo in response to a local or external stimulus, such as pH, temperature, the presence of enzymes, electromagnetic field, near infrared (NIR) radiation, changes in redox potential, ultrasound and the presence of small molecules or biomolecules.[29] Gated materials have been extensively used in controlled release,[29a] in sensing/recognition protocols[30] and in complex communication networks.[31,32] Furthermore, MSNs have shown to preferentially accumulate in tumors in bio-distribution studies performed in human cancer

xenograft models and effectively deliver drugs in tumors and suppress tumor growth, presenting a satisfactory biocompatibility.[33-35]

Several organic and inorganic carriers have been used to protect (from enzymatic degradation) and to deliver proteins and peptides. Several types of organic biocompatible polymers (in the forms of micro or nanoparticles), liposomes, micelles and carbon nanotubes have been used for this application.[36,37] In this scenario, MSNs have been used to encapsulate and deliver proteins[38-40] but its use as inorganic carriers for the controlled release of small peptides has been barely explored.[41]

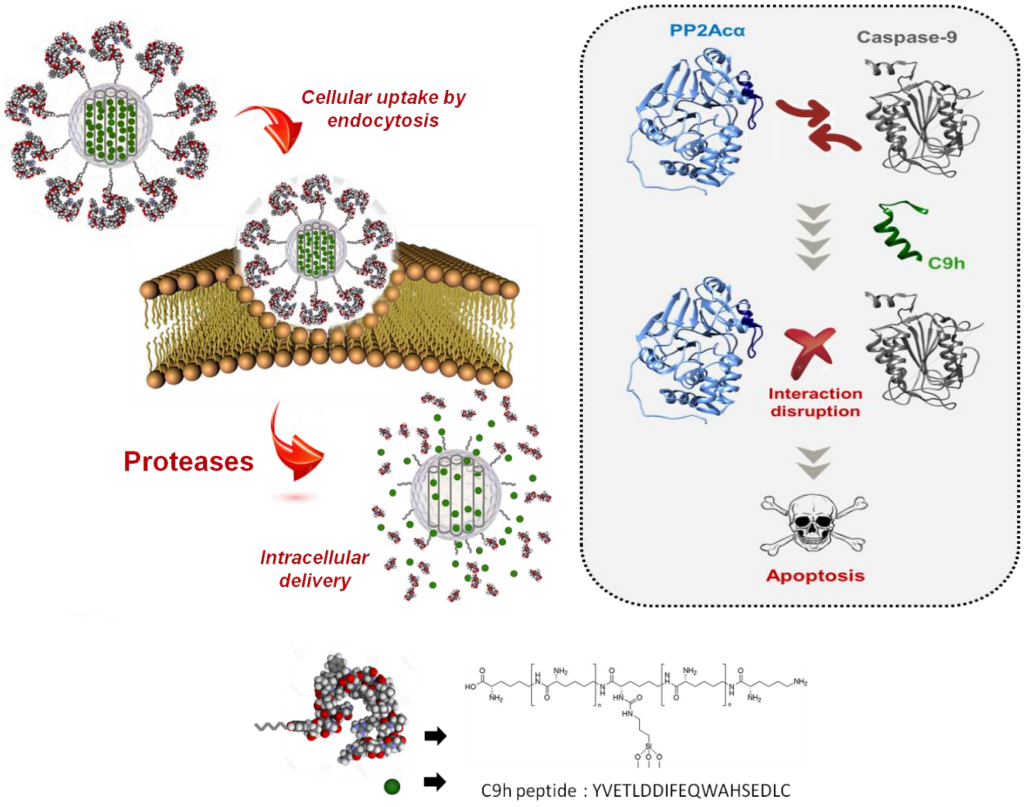

Scheme 1. Representation of the design and mechanism of action of MSNs S4 loaded with C9h peptide in the presence of intracellular proteases (up) and mechanism of action of C9h blocking PP2Acα-caspase 9 interaction (down).

Based in these concepts, we report herein the use of gated MSNs as nanocarriers to protect C9h from degradation and deliver the therapeutic peptide in cancer cells moreover allowing a dose reduction to observe an apoptotic effect.

Results and Discussion

Synthesis and characterization of gated nanoparticles.

Synthesis and characterization of gated nanoparticles. A schematic representation of the designed nanoparticles is shown in Scheme 1. MSNs of ca. 100 nm diameter were selected as carriers. The support was loaded with safranin O or C9h peptide and the pores capped by the covalent grafting of ε-polylysine onto the external surface of the nanoparticles through the formation of urea bonds. In the presence of proteases, the ε-polylysine coating is expected to be hydrolyzed allowing cargo release in cells (see Scheme 1). Moreover, the intracellular release of the entrapped C9h peptide is expected to disrupt PP2Acα-caspase 9 interaction inducing apoptosis.

The ε-polylysine selected consists of 25–35 repeated units of the L-Lysine amino acid. Unlike normal peptide bonds, in which amino acids are linked through the amino group of the α-carbon, the lysine amino acids in ε-polylysine are molecularly linked by the amino moiety located in the ε carbon. This polymer is obtained by natural fermentation of *Streptomyces* bacterial strains.[42] ε-polylysine has been used as a drug-delivery and gene-delivery carrier in the development of hydrogels, and also as an antimicrobial agent.[43] In addition, it has been reported to be nontoxic for humans, even at high doses, and biodegradable by amidases.[44]

MSNs were synthesized using CTAB as a template and TEOS as a hydrolytic inorganic precursor.[45] Calcination of the mesostructured phase resulted in the starting porous scaffold (solid S0). Then the pores of S0 were loaded with safranin O by suspending nanoparticles in an acetonitrile solution of the dye for 24h and the external surface was functionalized with (3-isocyanatopropyl)triethoxysilane yielding solid **S1**. Finally, ε-polylysine was covalently anchored onto the external surface through the formation of urea bonds to cap the pores (solid **S2**).[46]

Another set of nanoparticles were prepared, employing a similar procedure to that describe above, but using C9h peptide (YVETLDDIFEQWAHSEDLK) as cargo instead of safranin O. In a first step, the size of the C9h peptide was assessed using the data extracted from the Protein Data Bank (PDB), code 1JXQ in order to determine if C9h can be loaded in the pores of **S0**.[12] Scheme 2 shows the ε-helix structure of the sequence corresponding to C9h in the caspase-9 crystallographic structure. As could be seen from the crystallographic data, the C9h peptide adopts a quasi-cylindrical shape with a diameter of ca. 1.7 nm and a length of ca. 2.25 nm. Taking into account that pore diameter of **S0** is 3.32 nm (see Table 1) it was expected that C9h could be loaded efficiently into the nanoparticles. However, it is known that peptide structure can vary as a function of the solvent used. Therefore, in a second study, a structure analysis of C9h peptide was performed by circular dichroism in PBS buffer. As could be seen in Figure 1, C9h peptide adopted a non-structured conformation in PBS, which was different than that shown by the same sequence in caspase 9. However, it was found that C9h adopted a helical conformation upon addition of increasing quantities of trifluoroethanol (TFE). When TFE content reached 40%, C9h showed two troughs of molar ellipticity at 208 and 222 nm, characteristics of a high content of α helix in the sample.[47]

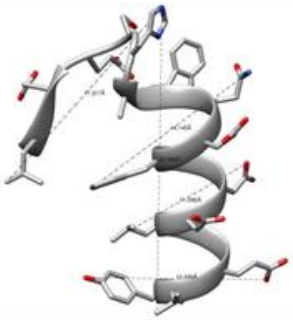

Scheme 2. Minimized structure of the peptide fragment, corresponding to C9h, inside caspase-9 protein.

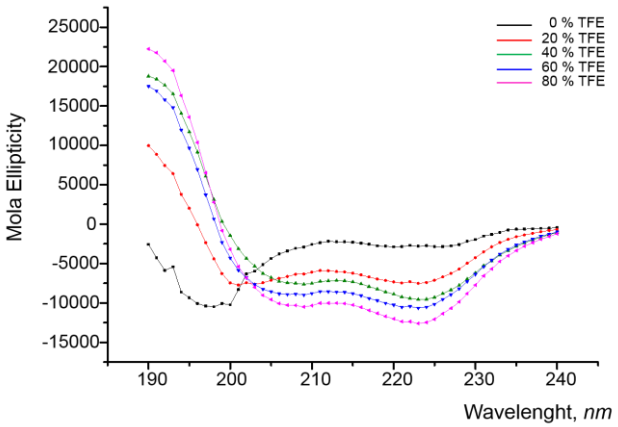

Figure 1. Circular dichroism spectra of C9h peptide in PBS buffer and in the presence of increasing quantities of TFE.

For the preparation of peptide loaded nanoparticles, solid **S0** was suspended in a solution containing C9h and the suspension was stirred for 24 h. The external surface of the C9h-loaded nanoparticles was then functionalized with 3-isocyanatopropyl)triethoxysilane yielding solid **S3** and afterwards, the pores were capped by the grafting of ε-polylysine through the formation of urea bonds (solid **S4**). Besides, we also prepared solid **S5** that is a similar solid to S4 but loaded with C9h peptide labelled with rhodamine B (YVETLDDIFEQWAHSEDLK-RhB).

Solids **S0**, **S1** and **S2** were fully characterized by powder X-ray diffraction (PXRD), transmission electron microscopy (TEM), N_2 adsorption-desorption isotherms, thermogravimetric measurements, elemental analyses and dynamic light scattering (DLS). The X-ray pattern of as-made MSNs showed four mesoporous characteristic low-angle reflections of a hexagonal-ordered array indexed as (100), (110), (200) and (210) Bragg peaks (see Supporting Information, Figure SI-1, curve a). Calcination of MCM-41 (solid S0) induced a significant shift of the (100) reflection (Figure SI-1, curve b). Finally, the subsequent loading steps with safranin O and further functionalization with ε-polylysine resulted in the loss of the (110) and (200) reflections, given the reduced contrast after loading/functionalization (Figure SI-1, curves c and d). However, the permanence

of the (100) peak still indicated that the mesoporous structure was maintained in **S1** and **S2** nanoparticles. TEM images of **S0**, **S1**, **S2** and **S4** showed that solids were obtained as spherical nanoparticles with diameters in the 80-100 nm range (see Figure 2 and Supporting Information Figure SI-2).TEM images confirmed the preservation of the mesoporous structure in all prepared solids. Besides, the size of the nanoparticles was determined by DLS. As shown in Figure 3, diameters of 96.2, 115.8, 146.9 and 169.3 were determined for **S0**, **S1**, **S2** and **S4** nanoparticles, respectively.

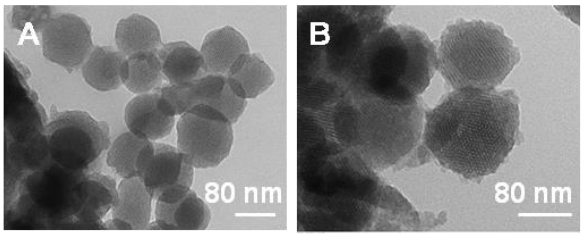

Figure 2. TEM images of (a) **S0** and(b) **S4**.

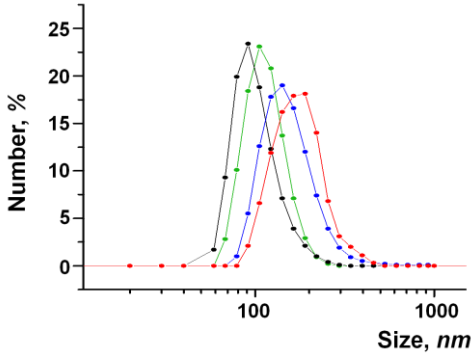

Figure 3. Size distribution by number of particles obtained by DLS studies for **S0** (black), **S1**(green), **S2** (blue) and **S4** (red) solids.

The N_2 adsorption-desorption isotherms of **S0** showed an adsorption step at intermediate P/P_0 value (0.1-0.3) which is related to the nitrogen condensation inside the mesopores by capillarity (see Supporting Information Figure SI-3). The application of the BET model resulted in a value for the total specific surface of 1101.2 $m^2\ g^{-1}$ and a pore volume of 1.17 $cm^3\ g^{-1}$. From the PXRD, porosimetry and

TEM studies, the a_0 cell parameter (4.50 nm), the pore diameter (3.32 nm) and the value for the wall thickness (1.18 nm) were calculated. The N_2 adsorption-desorption isotherms of **S1** and **S2** nanoparticles were typical of mesoporous systems with filled mesopores (see Figure SI-3), and a significant decrease in the N_2 volume adsorbed and in the specific surface area was observed (278.7 $m^2\ g^{-1}$ and 111.4 $m^2\ g^{-1}$ for S1 and S2, respectively). BET specific surface values, pore volumes and pore sizes calculated from the N_2 adsorption-desorption isotherms for **S0**, **S1** and **S2** are listed in Table 1.

Table 1. BET specific surface values, pore volumes and pore sizes calculated.

	S_{BET} ($m^2\ g^{-1}$)	Pore volume [a] ($cm^3\ g^{-1}$)	Pore Size [a,b] (nm)
S0	1101.2	1.17	3.32
S1	278.7	0.41	-
S2	111.4	0.24	-

[a] Pore volumes and pore sizes are only associated with intraparticlemesopores.

[b] Pore size estimated by using the BJH model applied on the adsorption branch of the isotherm.

Safranin O and C9h peptide contents in **S2** and **S4** nanoparticles were determined by elemental analysis and thermogravimetric studies and amounted to 0.08 and 0.02 mmol g^{-1} SiO_2, respectively (Table 2).

Table 2. Content of the molecular gate and guest molecules in grams per gram of SiO_2 for **S2** and **S4** nanoparticles.

	α guest molecule ($g\cdot g^{-1}$ SiO_2)	α gate ($mmol\cdot g^{-1}$ SiO_2)
S1	0.02	0.08
S_1-P_1	0.02	0.02

Cargo release studies of the capped nanoparticles. Cargo delivery from **S2** and **S4** was tested in the absence and in the presence of pronase from *Streptomyces griseus*. In a typical experiment, **S2** and **S4** nanoparticles were suspended in water at pH 8.0 at a final concentration of 0.5 mg mL^{-1}. The suspensions were stirred at 37 °C in the absence and in the presence of pronase. Uncapping and subsequent delivery of the dye from **S2** was determined through the measurement of fluorescence emission at 585 nm (λ_{ex} = 525 nm) of released safranin O at scheduled times. For solid **S4**, C9h peptide delivery was quantified through its absorbance at 280 nm. The obtained delivery profiles from **S2** and **S4** are shown in Figure 4. A negligible safranin O release from **S2** in the absence of pronase was observed (ca. 5% of the maximum dye delivered after 24 h). In contrast, a marked dye delivery was found in the presence of enzyme. A similar trend was observed for solid **S4** loaded with C9h peptide (Figure 4B); i.e. payload delivery was only found in the presence of pronase whereas a poor cargo release was observed in the absence of the enzyme. These results demonstrated that both rhodamine B dye and C9h peptide can be encapsulated in MSNs and delivered on-command in the presence of pronase

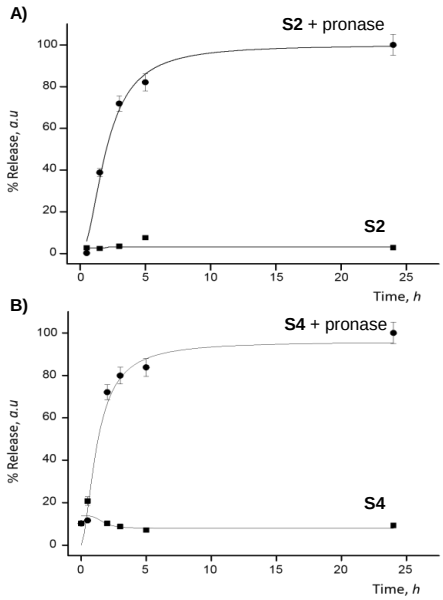

Figure 4. Release profiles of safranin O (A) and C9h peptide (B) from solids **S2** and **S4** in the absence and in the presence of pronase enzyme.

In vivo studies of cargo release. *In vivo* studies. Once the specific cargo release was proven *in vitro*, controlled payload delivery of **S2**, **S4** and **S5** nanoparticles was tested *ex vivo* using HeLa cells. In a first step, **S2** and **S5** uptake and cargo release in HeLa cells was studied by confocal microscopy. Cells were also stained with the DNA marker Hoechst 33342. The obtained results are shown in Figure 5. As could be seen, a marked cytoplasmic fluorescence associated with safranin O was observed for HeLa cells treated with **S2** nanoparticles. This observed fluorescence was ascribed to a proper uptake of **S2** nanoparticles by cells with subsequent hydrolysis of the ε-polylysine caps in lysosomes and safranin O intracellular delivery. Nearly the same results were obtained using **S5** nanoparticles. This solid was also successfully uptake by HeLa cells and the rhodamine B-labelled C9h peptide intracellularly delivered (Figure 5).

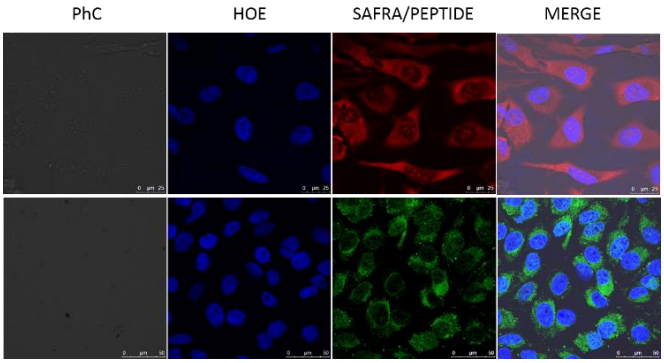

Figure 5. Confocal microscopy images of HeLa cells treated with 50 μg mL^{-1} of **S2** and **S5** nanoparticles. The cellular uptake was followed by safranin O associated fluorescence (red) or rhodamine B-peptide associated fluorescence (green) in the presence of DNA marker Hoescht 33342 (blue).

In a second step, and in order to discard any toxicity associated with the mesoporous scaffold or the ε-polylysine coating shell, cell viability assays using the safranin O-loaded solid **S2** at different concentrations were evaluated by the WST-1 test (see Figure 6). As could be seen **S2** nanoparticles were non-toxic for HeLa cells at concentration up to 500 μg mL^{-1} after 24 h of incubation.

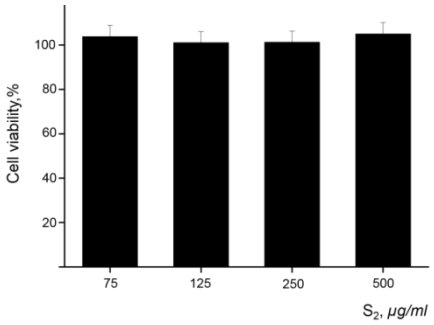

Figure 6. WST-1 viability assays carried out with different concentrations of **S2** nanoparticles incubated 24 h with HeLa cells.

After demonstrating that the MSNs are not toxic the apoptotic effect of C9h peptide delivered by **S4** in HeLa cells was studied. For this purpose HeLa cells were treated with three different concentrations of **S4** nanoparticles (75, 125 and 250 μg mL^{-1}) and cell viability was determined at 24, 48 and 72 h of incubation. Moreover, equivalent concentrations of Mut3DPT-C9h (1.35, 2.70 and 5.40 μM) to the concentrations of peptide delivered by **S4** were also analyzed in the same experimental conditions as controls. The obtained results are shown in Figure 7. From the data it can be concluded that C9h peptide delivered from **S4** nanoparticles after 72 h of incubation induced a sharp decrease in cell viability at 125 and 250 μg mL^{-1}. Also, cell viability reduction induced by C9h delivered from **S4** showed to be higher than that obtained using Mut3DPT-C9h at equivalent amounts (5.40 μM and 2.70 μM of peptide). At these concentrations, Mut3DPT-C9h was able to induce only a 10-20% decrease in cell viability, whereas when encapsulated in **S4** a marked 50% reduction was observed

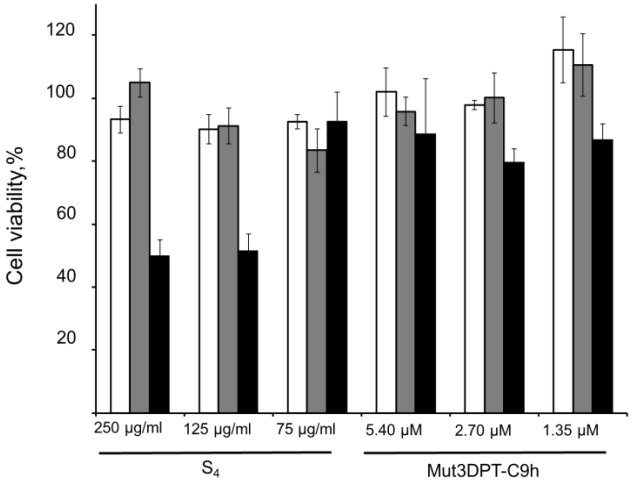

Fi**igure 7**. WST-1 cell viability assay of HeLa cells treated with S4(75, 125 and 250 µg mL^{-1})and with Mut3DPT-C9h (1.35, 2.70 and 5.40 µM) for 24 (white bars), 48 (grey bars) and 72h (black bars). 250, 125 and 75µgmL^{-1} of **S4** corresponds to 5.40, 2.70 and 1.35µM of Mut3DPT-C9h, respectively.

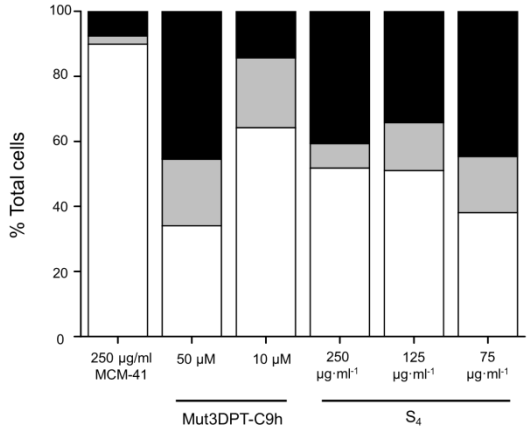

Figure 8. Quantification of cell viability and cell death was performed by flow cytometry by means of Annexin V-FITC staining. The percentage of dead cells (black), cells undergoing cell death (gray), and healthy cells (white) are shown for a 75, 125 and 250 µg mL^{-1} concentration of S4 and as positive control were used Mut3DPT-C9h peptide at 10 µM and 50 µM.

Finally, in order to get a better characterization of the apoptotic effect of C9h delivered from **S4**, apoptosis induction was measured using AnnexinV-FITC detection kit and analyzed by flow cytometry. For this purpose, HeLa cells were incubated with **S4** (at concentrations of 75, 125 and 250 μg mL^{-1} that corresponds to 1.35, 2.70 and 5.40 μM of free Mut3DPT-C9h, respectively) and Mut3DPT-C9h (10 and 50 μM). Cells treated with 50 μM of Mut3DPT-C9h were used as positive control. As could be seen in Figure 8, treatment of HeLa cells with 10 μM Mut3DPT-C9h induced a 36% of apoptosis, while a peptide concentration of 1.35 μM encapsulated in S4 (75 μg mL^{-1} of S4) induced ca. 55 % of cell death. A similar cell death was found for 50 μM of Mut3DPT-C9h and 75, 125 and 250 μg mL^{-1} of **S4**. Therefore, nanoformulation of DPT-C9h enhanced 37-fold the apoptotic effect of the peptide free in solution.

Mut3DPT-C9h is an improved variant of the original DPT-C9h CPP that has increased stability in mouse serum while keeping the same pro-apoptotic properties.[2] However, cancer cells treated with the therapeutic peptide C9h without being coupled to a delivery system at concentrations as high as 100 μM showed the same apoptosis levels as non-treated cells, since this peptide is not capable of being internalized in the cells without a vehicle.[1] Despite the reported advantages for cargo delivery into the cells, CPPs suffer some shortcomings as pharmaceutical products such as short duration of action caused by proteolysis and rapid renal clearance.[48] The results obtained with **S4** nanoparticles are remarkable because (i) allow the use of the C9h peptide without any modification and (ii) permit a peptide dose reduction up to 37 times to induce apoptosis in cancer cells.

Frequently, high biodegradability and low bioavailability have been limiting obstacles for the therapeutic use of peptides. Blood plasma contains more than 120 proteins, among which are present numerous proteolytic enzymes involved in peptide degradation. Our approach, i.e. peptide encapsulation in gated MSNs, could be of general application to deliver peptides. This may be of importance taking into account that a large number of peptide therapeutics has not obtained

FDA approval as they have been considered poor drug candidates because of their low bioavailability and instability.

Conclusions

In summary, we report herein the synthesis and characterization of two gated nanoparticles loaded with safranin O and with C9h peptide. Both materials are based in the use of MSNs as carriers and capped with ε-poylysine as a pronase-triggered biomolecular gate. Both nanoparticles showed negligible cargo release in the absence of pronase, whereas in the presence of enzyme a remarkable payload delivery was observed due the enzyme-induced ε-poylysine hydrolysis. Confocal microscopy studies revealed that HeLa cells were able to uptake both nanoparticles with subsequent cargo delivery. Moreover, **S4** nanoparticles (loaded with C9h) induced a marked reduction in HeLa cells viability as the peptide delivered promoted cell apoptosis. **S4**, or similar nanodevices based on MSNs, could be an alternative for C9h delivery inside cells without any sequence modification (such as the use of CPPs). Moreover, **S4** provides peptide protection from degradation additionally allowing a dose reduction of up to ten times to observe an apoptotic effect when compared with C9h alone or in combination with a CPP (i.e.Mut3DPT-C9h).

Experimental Section

Chemicals: Tetraethylorthosilicate (TEOS), *n*-cetyltrimethylammonium bromide (CTAB), sodium hydroxide, safranin O, 3-(triethoxysilyl)propyl isocyanate and the protease enzyme from *S. griseus* were purchased from Sigma–Aldrich Quimica S.A. (Madrid, Spain) and were used without further purification. ε-Poly-L-lysine was purchased from Chengdu Jinkai Biology Engineering Co., Ltd. All the other reagents were of a general laboratory grade and were purchased from Merck, unless otherwise specified. For cell culture studies, DMEM with high glucose, phosphate buffer, foetal bovine serum (FBS), trypsin and Hoescht 33342 were provided by Gibco. Cell proliferation reagent (WST-1) was obtained from Roche Applied Science. Annexin V-FITC was supplied by BD.

General techniques: PXRD, TG analysis, elemental analysis, EDX microscopy, N_2 adsorption-desorption isotherms were used to characterize the prepared materials. Power X-ray measurements were performed on a Philips D8 Advance diffractometers using CuKα radiation. Thermogravimetric analysis were carried out on a TGA/SDTA 851e Mettler Toledo balance, using an oxidant atmosphere (air, 80 ml/min) with a heating program consisting on a heating ramp of 10ºC per minute from 393 to 1273 K and an isothermal heating step at this temperature during 30 minutes. Elemental analysis was performed in a CE instrument EA-1110 CHN Elemental Analyzer. TEM images were obtained with a 100 kV JEOL JEM-1010 microscope. Nitrogen adsorption-desorption isotherms were recorded on a Micromeritics ASAP2010 automated sorption analyzer. Samples were degassed at 120 °C in a vacuum system overnight. Specific surface areas were calculated from the adsorption data in the low pressure range using the Brunauer-Emmett-Teller (BET) theory model. Pore size was determined following the Barrett-Joyner-Halenda (BJH) method. Fluorescence spectroscopy was carried out on a Felix 32 Analysis 1.2.

Synthesis of S0: CTAB (1.00 g, 2.74 mmol) was first dissolved in 480 mL of deionized water. After that, NaOH (3.5 mL, 2 M) in deionized water was added to the CTAB solution and the temperature was adjusted to 80ºC. TEOS (5 mL, 2.57 x 10^{-2} mol) was then added dropwise to the surfactant solution. The mixture was stirred for 2 h to yield a white precipitate. Finally the solid product was centrifuged, washed with deionized water and ethanol and dried at 60ºC. To prepare the final porous scaffold (S0), the as-made solid was calcined at 550ºC using an oxidant atmosphere for 5 h to remove the template phase (CTAB).

Peptide synthesis: Peptide C9h was synthesized by Synpeptide, adding an extra cysteine residue at the C-terminal to allow quantification. Peptide C9h-rhodamine B was synthesized by Synpeptide labeled with rhodamine B at the C-terminal.

Synthesis of S1, S2, S3 and S4: **S0** nanoparticles (30 mg) were suspended in a solution of acetonitrile (5 mL) containing safranin O (20 mg) or in a solution of DMSO (5 mL) containing C9h peptide (18 mg). Both mixtures were stirred overnight at room temperature. Afterward, excess of 3-(triethoxysilyl)propylisocyanate (60 µL, 0.2 mmol) was added and the final crudes stirred for 5.5 h at room temperature. By this procedure we obtained **S1** (loaded with safranin O) and **S3** (loaded with C9h peptide). Then, ε-polylysine (30 mg, 6.0 x 10^{-3} mmol of polymer) dissolved in acetonitrile (5 mL) was added to the previous suspensions and stirred for 2 h. Finally, the solids were filtered off. Once dried, both solids were washed with methanol to remove the unreacted ε-polylysine and then with PBS to remove the cargo remaining outside the pores. Finally, the solids were filtered and dried at vacuum. This experimental procedure yielded the final solids **S2** (loaded with safranin O) and **S4** (loaded with C9h peptide).

Synthesis of S5: Solid **S5** was prepared following the same procedure described above for **S2** and **S4** but loading nanoparticles with C9h peptide derivatized with rhodamine B (YVETLDDIFEQWAHSEDLK-RhB).

Circular dichroism: 50 µM of C9h peptide was dissolved in 10 mM sodium phosphate buffer pH 7.65. Samples were prepared in a final volume of 300 µL of 10 mM sodium phosphate buffer pH 7.65 with increasing concentrations of trifluoroethanol (20%, 40%, 60% and 80%). Samples were introduced in the spectropolarimeter in a quartz Suprasil Precission cell 0.1 cm cuvette (Hellma), using 300 µL of buffer solution as blank. Measurements were performed at 20 °C and repeated 10 times for each sample and 5 times for each blank. Spectropolarimeter raw data were generated in millidegrees and further corrected by substracting blank value to sample value and further converted to molar ellipticity units with Jasco software.

Cell culture: HeLa cells were cultured in DMEM supplemented with 10% FBS at 37ºC with 5% CO_2 and underwent passage twice a week.

WST-1 cell viability assay: Cells were cultured in 24-well microtiter plates at a density of 25 x 10^3 cells/well and allowed to attach for 24 h. **S2** was added to the cells at a final concentration from 75 to 500 μg mL^{-1}. After 24h of incubation, 10 μL of WST-1 were added to each well and incubated for 90 minutes. **S4** was added to the cells at a final concentration of 250, 125 and 75 μg mL^{-1} and incubated for 24, 48 and 72 h. Cell viability was measured with WST-1 reagent and absorbance at 450 and 690 nm as reference wavelength was measured with a Wallac 1420 workstation.

Confocal microscopy cellular internalization assays: HeLa cells were seeded in six-well microtiter plates at a density of 1.5 x 10^5 cells/well. After 24 h, cells were treated with 50 μg mL^{-1} of **S2**. After 30 min, medium was removed and cells were washed with PBS. Then, cells were incubated for 20 h at 37 °C and visualized under a confocal microscope.

FACS Annexin V apoptosis measurements: 25000 HeLa cells in 1 mL of DMEM supplemented with 10% FBS per well were seeded in 24-well plates and incubated for 24h at 37 °C with 5% CO_2 before being treated with different concentrations of **S4** and the equivalent concentration of Mut3DPT-C9h. Cells treated with 1% DMSO were used as negative control. After 24 h of incubation, AnnexinV – FITC apoptosis detection kit was added to the samples following the manufacturer's protocol and samples were analyzed with a FACS Canto (BD) flow cytometer.

Acknowledgements

The authors wish to express their gratitude to the Spanish government (Projects MAT2015-64139-C4-1, SAF2012-31405, SAF2015-67077-R, AGL2015-70235-C2-2-R (MINECO/FEDER)), the Generalitat Valencia (Projects PROMETEOII/2014/047, PROMETEO/2012/061) and the CIBER-BBN for their support. C.T. is grateful to the Spanish Ministry of Science and Innovation for her PhD fellowship.

References

1. M. A. Lyon, A. P. Ducrue, P. Wipf, J. S. Lazo, *Nat. Rev. Drug. Discov.* **2002**, *1*, 9612.
2. F. Ducret, C. Turc-Baron, P. Pointet, G. Vernin, O. Skowron, B. Mc Gregor, J. M. Gasc, G. Beaune, M. Vincent, *Nephrol. Ther.* **2005**, *1*, 52.
3. D. F. Lazar, A. R. Saltiel, *Nat. Rev. Drug Discov.* **2006**, *5*, 333.
4. N. K. Tonks, *Nat. Rev. Mol. Cell. Biol.* **2006,** *7*, 833**.**
5. J. Liu, J. D. Farmer, W. S. Lane, J. Friedman, I. Weissman, S. L.Schreiber, *Cell.* **1991**, *66*, 807**.**
6. Y. M. Li, J. E. Casida, *Proc. Natl. Acad. Sci. U.S.A.* **1992**, *89*, 11867**.**
7. R. E. Honkanen, *FEBS Lett*. **1993**, *330*, 283.
8. A. H. Walsh, A. Cheng, R. E. Honkanen, *FEBS Lett.* **1997**, *416*, 230**.**
9. H. Medyouf, H.Alcalde, C. Berthier, M. C. Guillemin, N. R. dos Santos, A. Janin, D. Decaudin, H. De Thé, J.Ghysdael, *Nat. Med.* **2007**, *6*, 736.
10. S. Martinez-Martinez, J. M. Redondo, *Curr. Med. Chem*. **2004**, *11*, 9972.
11. I. Arrouss, F. Nemati, F. Roncal, M. Wislez, K. Dorgham, D. Vallerand, N. Rabbe, N. Karboul, F. Carlotti, J. Bravo, D. Mazier, D. Decaudin, A. Rebollo, *PLoS One* **2013**, *8*, e60816.
12. I. Arrouss, D. Decaudin, S. Choquet, N. Azar, C. Parizot, J. M. Zini, F. Nemati, A. Rebollo, *Protein Pept. Lett.* **2015**, *22*, 539**.**
13. J. Fominaya, J. Bravo, A. Rebollo, *Ther. Deliv.* **2015**, *6*, 1171.
14. J. Fominaya, J. Bravo, D. Decaudin, J. Y. Brossa, F. Nemati, A. Rebollo, *Ther. Deliv.* **2015**, *6*, 139**.**
15. A. J. Primeau, A. Rendon, D. Hedley, L. Lilge, I. F. Tannock, *Clin. Cancer Res.* **2005**, *11*, 8782.
16. M. A. Izquierdo, R. H. Shoemaker, M. J. Flens, G. L. Scheffer, L. Wu, T. R. Prather, R. J. Scheper, *Int. J. Cancer* **1996**, *65*, 230**.**
17. X. J. Liang, C. Chen, Y. Zhao, P. C. Wang, *Methods Mol. Biol***. 2010,** *596*, 467.
18. Q. He, J. Shi, *Adv. Mater.* **2013**, *26*, 391.
19. (a) C. Ding, Z. Li, *Mat. Eng. Sci. C.* **2017**, *76*, 1440; (b) A. Llopis-Lorente, B. Lozano-Torres, A. Bernardos, R. Martínez-Máñez, F. Sancenón, *J. Mater. Chem. B* **2017**, *5*, 3069; (c) M. W. Tibbitt, J. E. Dahlman, R. Langer, *J. Am. Chem. Soc.* **2016**, *138*, 704.
20. W. X. Mai, H. Meng, *Integr. Biol.*, **2013**, *5*, 19.
21. A. L. Doadrio, A. J. Salinas, J. M. Sánchez-Montero, M. Vallet-Regí, *Curr. Pharm. Des.* **2015**, *21*, 6213.
22. C. Argyo, V. Weiss, C. Braüchle, T. Bein, *Chem. Mater*. **2014**, *26*, 435.

23. (a) M. Gagliardi, C. Borri, *Curr. Pharm. Des.* **2017**, *23*, 393; (b) R. X. Zhang, T. Ahmed, L. Li, L. Yi, A. A. Z. Jason, X. Y. Wu, *Nanoscale* **2017**, *9*, 1334; (c) X. Guo, L. Wang, X. Wei, S. Zhou, *J. Polym. Sci. A Polym. Chem.* **2016**, *54*, 3525.

24. Z. Li, J. C. Barnes, A. Bosoy, J. F. Stoddart, J. I. Zink, *Chem. Soc. Rev.* **2012**, *41*, 2590.

25. Y. Wang, Q. F. Zhao, N. Han, L. Bai, J. Li, J. Liu, E. X. Che, L. Hu, Q. Zhang, T. Y. Jiang, S. L. Wang, *Nanomed.* **2015**, *11*, 313.

26. R. Sun, W. Wang, Y. Wen, X. Zhang, *Nanomat.* **2015**, *5*, 2019.

27. S. Mura, J. Nicolas, P. Couvreur, *Nat. Mat.* **2013**, *12*, 991.

28. D. Tarn, C. E. Ashley, M. Xue, E. C. Carnes, J. I. Zink, C. J. Brinker, *Acc. Chem. Res.* **2013**, *46*, 792.

29. (a) E. Aznar, M. Oroval, Ll. Pascual, J. R. Muguía, R. Martínez-Máñez, F. Sancenón, *Chem. Rev.* **2016**, *116*, 561; (b) A. Agostini, L. Modragón, A. Bernardos, R. Martínez-Máñez, M. D. Marcos, F. Sancenón, J. Soto, A. Costero, C. Manguan-García, R. Perona, M. Moreno-Torres, R. Aparicio-Sanchis, J. R. Murguía, *Angew. Chem. Int.* Ed. **2012**, *51*, 10556; (c) A. Agostini, L. Mondragón, C. Coll, E. Aznar, M. D. Marcos, R. Martínez-Máñez, F. Sancenón, J. Soto, E. Pérez-Payá, P. Amorós, *ChemOpen* **2012**, *1*, 17; (d) E. Aznar, R. Villalonga, C. Giménez, F. Sancenón, M. D. Marcos, R. Martínez-Máñez, P. Díez, J. M. Pingarrón, P. Amorós, *Chem. Commun.* **2013**, *49*, 6391; (e) C. Giméenz, C. de la Torre, M. Gorbe, E. Aznar, F. Sancenón, J. R. Murguía, R. Martínez-Máñez, M. D. Marcos, P. Amorós, *Langmuir* **2015**, *31*, 3758; (f) C. de la Torre, I. Casanova, G. Acosta, C. Coll, M. J. Moreno, F. Albericio, E. Aznar, R. Mangues, M. Royo, F. Sancenón, R. Martínez-Máñez, *Adv. Func. Mater.* **2015**, *25*, 687; (g) C. de la Torre, A. Agostini, L. Mondragón, M. Orzáez, F. Sancenón, R. Martínez-Máñez, M. D. Marcos, P. Amorós, E. Pérez-Payá, *Chem. Commun*. **2014**, *50*, 3184.

30. **(**a) F. Sancenón, Ll. Pascual, M. Oroval, E. Aznar, R. Martínez-Máñez, *ChemOpen* **2015,** *4*, 418; (b) M. Oroval, E. Climent, C. Coll, R. Eritja, A. Aviñó, M. D. Marcos, F. Sancenón, R. Martínez-Máñez, P. Amorós, *Chem. Commun*. **2013**, *49*, 5480; (c) Ll. Pascual, I. Baroja, E. Aznar, F. Sancenón, M. D. Marcos, J. R. Murguía, P. Amorós, K. Rurack, R. Martínez-Máñez, *Chem. Commun*. **2015,** *51*, 1414.

31. C. Giménez, E. Climent, E. Aznar, R. Martínez-Máñez, F. Sancenón, M. D. Marcos, P. Amorós, K. Rurack, *Angew. Chem. Int. Ed.* **2014**, *53*, 12629.

32. A. Llopis-Lorente, P. Diez, A. Sánchez, M. D. Marcos, F. Sancenón, P. Martínez-Ruíz, R. Villalonga, R. Martínez-Máñez, *Nat. Commun.* **2017**, *8*, 15511.

33. J. Lu, M. Liong, Z. Li, J. I. Zink, F. Tamanoi, *Small* **2010**, *6*, 1794.

34. A. Baeza, M. Manzano, M. Colilla, M. Vallet-Regí, *Biomater. Sci.* **2016**, *4*, 803.

35. J. M. Rosenholm, C. Sahlgren, M. Lindén, *Nanoscale* **2010**, *2*, 1870.

36. S. Poh, J. B. Lin, A. Panitch, *Biomacromolecules* **2015**, *16*, 1191.

37. A. Patel, K. Cholkar, A. K. Mitra, *Ther. Deliv.* **2014**, *5*, 337.

38. B. Sung, C. Kim, M. H. Kim, *J. Colloid Interface Sci.* **2015**, *450*, 26.

39. M. Witting, M. Molina, K. Obst, R. Plank, K. M. Eckl, H. C. Hennies, M. Calderón, W. Frieß, S. Hedtrich, *Nanomedicine.* **2015**, *11*, 1179.

40. E. Yu. I. Galiana, R. Martínez-Máñez, P. Stroeve, M. D. Marcos, E. Aznar, F. Sancenón, J. R. Murguía, P. Amorós, *Colloids Surf. B* **2015**, *135*, 652.

41. K. Braun, A. Pochert, M. Lindén, M. Davoudi, A. Schimdtchen, R. Nordström, M. Malsmsten, *J. Colloid Interface Sci.* **2016**, *475*, 161.

42. S. Shima, H. Sakai, *Agric. Biol. Chem.* **1977**, *41*, 1807.

43. C. Zhou, P. Li, X. Qi, A. R. M. Sharif, Y. F. Poon, Y. Cao, M. W. Chang, S. Su Jan Leong, M. B. Chan-Park, *Biomaterials* **2011**, *32*, 2704.

44. I. L. Shih, M. H. Shen, Y. T. Van, *Bioresour. Technol.* **2006**, *97*, 1148.

45. S. Cabrera, J. El Haskouri, C. Guillem, J. Latorre, A. Beltrán, D. Beltrán, M. D. Marcos, P. Amorós, *Solid State Sci.* **2000**, *2*, 405.

46. L. Mondragón, N. Mas, V. Ferragud, C. de la Torre, A. Agostini, R. Martínez-Máñez, F. Sancenón, P. Amorós, E. Pérez-Payá, M. Orzáez*, Chem. Eur. J.* **2014**, *20*, 5271.

47. N. J. Greenfield, *Nat. Protoc.* **2007**,*1*, 2876.

48. A. Mickan, D. Sarko, U. Haberkorn, W. Mier, *Curr. Pharm. Biotechnol.* **2014**, *15*, 200.

3. Detection of Carbon Monoxide for biomedical applications

3.1. Introduction

3.1.1 Carbon monoxide

Carbon monoxide (CO), consisting of one carbon and one oxygen atoms, has a molar mass of 28.0, which makes it slightly lighter (ρ = 1.145 kg/m^3 at 25 °C, 1 atm) than air. The bond length between the carbon and the oxygen atom is 112.8 pm, which is consistent with a triple bond that consists of two covalent ones as well as one dative covalent bond. The bond dissociation energy of 1072 kJ/mol represents the strongest chemical linkage known. With a boiling point of −191.5 °C and a melting point of −205.02 °C it is a gas at normal conditions. The ground electronic state of carbon monoxide is a singlet state 2 since there are no unpaired electrons.

Carbon monoxide is known as "*the silent killer*", because is a poisonous gas that has no odour, colour or taste. Carbon monoxide is produced from the partial oxidation of carbon-containing compounds; this is when there is not enough oxygen to produce carbon dioxide (CO_2), such as when operating a stove or an internal combustion engine in an enclosed space. Coal gas (which was widely used before the 1960s for domestic lighting, cooking, and heating) had carbon monoxide as a significant fuel constituent. Some processes in modern technology, such as iron smelting, still produce carbon monoxide as a byproduct. The combustion of excess of carbon in air at high temperature is a major industrial source of CO. In this process air is passed through a bed of coke heated in oven. The initially produced CO_2 equilibrates with the remaining hot carbon to give CO. Above 800 °C, CO is the predominant product.

Furthermore, carbon monoxide is a reactive gas which takes part in the synthesis of multiple organic compounds. From an inorganic point of view, carbon monoxide is involved in the industrial preparation of methane (natural gas). Carbon monoxide is also used as industrial reductor in the extraction of metals from the corresponding metal oxide ores.

A long time ago, Paracelsus (1493-1541) remarked that *"All substances are poisonous. Only the dose differentiates a poison from a remedy."* His observation very aptly describes the components of the heme degradation pathway. Carbon monoxide, like bilirubin, has had a long-standing reputation as a biological villain. It is an odorless, tasteless, and invisible poison, lethal to humans through its interference with oxygen delivery and use. A telltale rosy hue of a victim's skin and mucous membranes belies the fatal truth that CO has surreptitiously replaced oxygen on the hemoglobin molecule, rendering its circulation, not only a futile, but also fatal, exercise. Recently, however, CO has been credited with beneficial biochemical and physiologic properties similar to those of its companion gas, nitric oxide (NO) which, when bound to soluble guanylyl cyclase (sGC), stimulates the production of cyclic GMP.[1]

In humans, the production rate of CO per kg body weight is 2 to 3 times higher in newborns than in adults.[2] Under pathologic conditions, however, such as hemolysis, increased ineffective erythropoiesis, or increased hemoprotein turnover, the rate of CO production can increase many fold in the adult male from 18-160 µmol/hr.[3]

The non-enzymatic production of CO is one of the more intriguing phenomena recently confirmed in biological systems devoid of heme. Originally reported in 1968,[4] lipid peroxidation was suggested as a source of CO again in 1976 and 1978.[5,6] A role for CO-derived from *in vivo* lipid peroxidation in tissues, like the brain, remains speculative, but worthy of serious consideration as potential CO-mediated processes are investigated. Photooxidation, mediated by natural (riboflavin and BR) or synthetic photosensitizers (some metalloporphyrins), may be another potential source of CO, especially in more translucent subjects, such as premature infants receiving phototherapy. As animals have become dependent upon bacteria, for example intestinal colonization, CO produced by bacteria may also turn out to be relevant to the understanding of not only intestinal physiology but also dysfunction.[7]

3.1.1.1 Pollutant role

The annual global emissions of carbon monoxide into the atmosphere have been estimated to be as high as 2600 million tones, of which about 60% are from human activities and about 40% from natural processes.[8] Anthropogenic emissions of carbon monoxide originate mainly from incomplete combustion of carbonaceous materials. The largest proportion of these emissions is produced by exhausts of internal combustion engines, especially by motor vehicles with petrol engines. Other common sources include various industrial processes, power plants using coal, and waste incinerators. Some widespread natural non-biological and biological sources, such as plants, oceans and oxidation of hydrocarbons, give rise to the background concentrations outside urban areas. Indoor levels of CO range from 0.5 to 5 parts per million (ppm) but may reach much higher values (e.g. 100 ppm) with inefficient heating or ventilation, or in the presence of environmental tobacco smoke.[9] In urban areas, ambient levels are typically 20 to 40 ppm, but may peak at much higher levels in heavily congested areas or alongside highways.

After reaching the lungs, carbon monoxide diffuses rapidly across the alveolar and capillary membranes. It also readily crosses the placental membranes. Carbon monoxide binds reversibly to one of the haem proteins. Approximately 80–90% of the absorbed carbon monoxide binds with haemoglobin, which causes a reduction in the oxygen-carrying capacity of the blood. The affinity of haemoglobin for carbon monoxide is 200–250 times than for oxygen, while the relative affinities of other haem proteins (e.g. myoglobin), cytochrome oxidase and cytochrome P-450 for carbon monoxide are much lower. The carbon monoxide affinity for haemoglobin displaces oxygen from oxyhaemoglobin and, at the same time, changes the allosteric structure of haemoglobin in such a way that the afinity of the remaining sites for bound oxygen increases. As a consequence, the oxygen carrying capacity of the blood is reduced and the release of oxygen (and therefore its delivery) to the tissues is inhibited, leading to progressive asphyxia (See **Figure 3.1**).

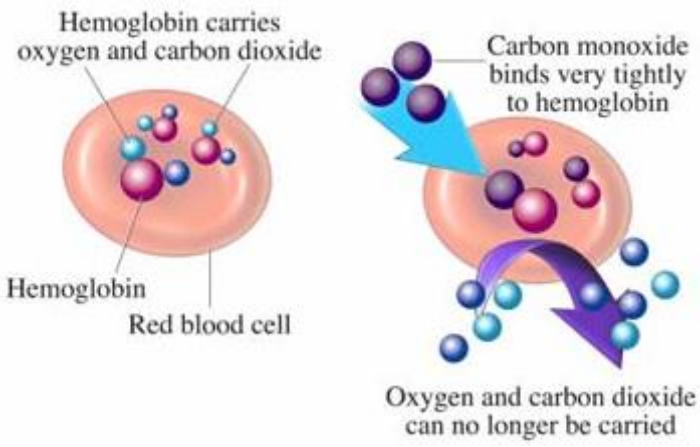

Figure 3.1. Scheme of carbon monoxide poisoning interfering with the proper binding of hemoglobin with oxygen.

Areas of high metabolic activity (heart, brain) are particularly susceptible to the resulting cellular hypoxia. Carbon monoxide is also a cellular poison in its own right as it competes with oxygen for other haemoproteins such as myoglobin, peroxidase, catalases and the cytochromes, although as the affinity of oxygen for cytochrome oxidase is high the effect on this system may be quite small.[10] Binding of carbon monoxide to cardiac muscle myoglobin can result in myocardial depression and hypotension leading to ischemia, which exacerbates the hypoxia induced by the impaired oxygen delivery.[11,14] The main features of acute carbon monoxide poisoning are headache, nausea, confusion, stupor and coma. [12] (**See Table 3.1**) Headache, nausea and fatigue are also signs of chronic poisoning, but there is also an insidious deterioration in intellectual capacity, with difficulties in concentration and decreased cognitive function.[13]

Table 3.1. Symptoms derived from exposure to different levels of CO.

Level of CO (ppm)	Health Effects and other information
0	Normal, fresh air.
9	Maximum recommended indoor CO level (ASHRAE).
10-24	Possible health effects with long-term exposure.
25	Max TWA exposure for 8 hour work-day (ACGIH).
50	Maxium permissible exposure in workplace (OSHA).
100	Sligh headache after 1-2 hours.
200	Dizziness, naseau, fagitue, headache after 2-3 hours of exposure.
400	Headache and nausea after 1-2 hours of exposure. Life threatening in 3 hours.
800	Headache, nausea, and dizziness after 45 minutes; collapse and unconsciousness after 1 hour of exposure. Death within 2-3 hours.
1000	Loss of consciousness after 1 hour of exposure.
1600	Headache, nausea and dizziness after 20 minutes of exposure. Death within 1-2 hour.
3200	Headache, nausea and dizziness after 5-10 minutes; collapse and unconsciousness after 30 minutes of exposure. Death within 1 hour.
6400	Death within 30 minutes.
12800	Immediate physiological effects, unconsciousness. Death within 1-3 minutes of exposure.

Taking into account the prominent roles played by carbon monoxide in the environment, remarkable efforts in its accurate detection has been carried out. When reviewing the existing methods for CO detection one has to go back in 1911, when canaries were traditionally used in coal mines to early detect life threatening gases, including CO. First analytical detectors were issued by the

Bureau of Mines, for the first time in 1938 and extended in following publications.[14]

Most of the techniques used for carbon monoxide measurement in the environment employ spectroscopic methods or gas chromatography (GC). At this respect, non-dispersive infrared (NDIR) spectroscopy and GC using flame ionization detection (FID) are the two most common methods used to analyze carbon monoxide in environmental samples. Commercial instruments are capable of achieve limits of detection in the ppb range.

In NDIR spectroscopy, air is pumped into samples cells and the absorption is measured at a carbon monoxide vibrational band at 2,174 cm^{-1} (4.7 μm). An optical filter is employed before the sample to remove light of other frequencies. Most NDIR spectrometers use gas filter correlation (GFC) methodology to improve sensitivity and reduce interferences by other gasses (EPA, Air quality criteria for carbon monoxide. Washington, DC: U.S. Environmental Protection Agency; 2000. EPA600P66001F).

In GC analysis of carbon monoxide, air samples are pumped through a silica gel or alumina pre-column followed by an analytical column composed of a molecular sieve. The pre-column captures CO_2, non-methane hydrocarbons, and water, and the molecular sieve effectively separates carbon monoxide from hydrogen and methane. Since the sensitivity for carbon monoxide by FID is low, a hydrogen-rich carrier gas is used to reduce carbon monoxide to methane using heated nickel as a catalyst prior to FID analysis. Electron capture detection (ECD) can also be used in conjunction with GC to measure atmospheric levels of carbon monoxide. In addition, GC/mass spectrometry, GC with mercury reduction gas detection, Fourier transform infrared (FTIR) spectroscopy, tunable diode laser spectroscopy (TDLS), and resonance fluorescence spectroscopy have also been used to measure carbon monoxide levels in air.[15]

Commercially available electrochemical carbon monoxide detectors for home use can be purchased. These detectors use electrodes that reside in an electrolyte

solution such as dilute sulfuric acid. Carbon monoxide is oxidized at one electrode to CO_2 and O_2 is consumed at the other electrode.[16] Measurement of the current in the cell provides the concentration of carbon monoxide in the atmosphere.

In spite of the above mentioned facts, established methods for CO detection have still some drawbacks to be solved. Most of them cannot measure CO directly, require several time-consuming intermediate steps (> 15 min) involving chemical reactions and/or are likely to generate false alarms in the presence of other chemicals or interfering gases. As an alternative to these classical methods, the use of chromo-fluorogenic probes for CO detection and sensing has been explored in the last years. Most of the chromo-fluorogenic probes for CO detection are based on metal transition complexes and on organic fluorophores functionalized with CO-reacting moieties. A brief overview of selected chromo-fluorogenic probes for CO detection is given in **section 3.1.2**.

3.1.1.2 Therapeutic role

CO, a diatomic low molecular weight gas, shares similarities with NO in terms of molecular size and structure. CO however, is a relatively stable non-radical gas that typically reacts in biological systems with metal centers of hemoproteins.[17] The endogenous production of CO as the natural product of hemoglobin turnover has been recognized since the middle of the twentieth century. However the production of CO in biological systems was previously regarded by the scientific community as a metabolic elimination product. In 1968, the heme oxygenase (HO) enzyme system responsible for the catalytic turnover of heme, was characterized and identified as a major source of CO in the body.[18] The inducible form of this enzyme, HO-1, was identified as identical to the major 32 to 34 kDa stress protein responsive to xenobiotic stress. Importantly, further studies established an association between the heme metabolic pathway and the cellular stress response involving HO-1, which contributes to cellular adaptation to toxic environmental challenges.[19] Subsequent research sought to determine the physiological function of endogenously produced CO, as well as its role as a

mediator of the cytoprotective properties of HO-1.[20] Although several studies have employed exogenous CO at low concentration, they revealed an impact of this gas on intracellular signaling pathways.[21] These studies identified new roles of CO on the regulation of several fundamental biological processes, including vascular tone, inflammation, neurotransmission, cell proliferation, programmed cell death, mitochondrial biogenesis, and autophagy.[22]

CO is naturally produced in the human body, primarily as the product of the turnover of hemoglobin and cellular hemoproteins. Heme, which is used as a prosthetic cofactor for hemoproteins, is degraded by HO enzyme system. HO catalyzes the rate limiting step in heme degradation, to generate biliverdin-IXα, CO, and ferrous iron (Fe(II)), and requires molecular oxygen and nicotinamide adenine dinucleotide phosphate (NADPH). Non-heme sources may make a minor contribution to exogenous CO production. In the blood, CO binds hemoglobin to form carboxyhemoglobin (COHb). CO may also be inhaled with ambient air, in the context of smoking, accidental or occupational exposure, or as a component of certain therapy. (See **Figure 3.2**)

Inhalation of CO has been viewed as a novel therapeutic approach for certain diseases. At this respect, Fujimoto and co-workers applied inhaled CO to rats to examine whether cardiac ischemia-reperfusion injury *in vivo* could be ameliorated.[23] Rats inhaled CO (250, 500, or 1000 ppm) for 24 h in a chamber, and myocardial ischemia/reperfusion damage was induced by occluding the left anterior descending coronary artery for 30 min. Although no protective effects were observed with low levels of inhaled CO, 1000 ppm significantly reduced the ratio of infarct areas to risk areas and suppressed the migration of macrophages and monocytes into infarct areas and the expression of tumour necrosis factor (TNF)-α in the heart. There were no visible side effects with this CO inhalation therapy, as no alterations in the arterial blood pressure, pulse rate, and body temperature were detected in the treated animals.

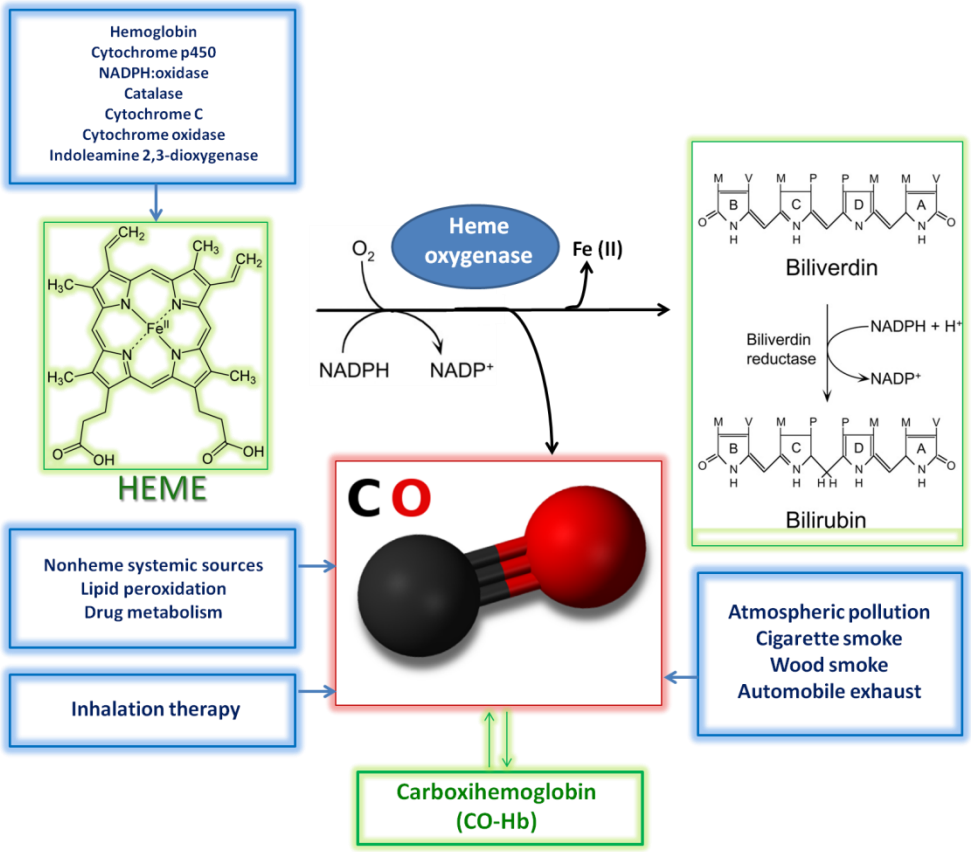

Figure 3.2. Sources of biological carbon monoxide (CO). Adapted from J.Korean, *Intern Med* **2013**, *28*, 123.

On the one hand, no deleterious effects were found for chronic exposure of the rodents to 500 ppm continuously for up to 2 years.[24] It has also been claimed that the exposure level of CO at 100 ppm can be harmless if the exposure duration is limited to a few hours. On the other hand, exposing rats for 20 h/day to CO (200 ppm) for 14 consecutive days induced a 21% increase in right ventricular hypertrophy and a 7% increase in left ventricular hypertrophy.[25]

Based on the capability of certain transition metal carbonyls to release CO in biological fluids, a series of CO-releasing molecules (CORM) were designed by Motterlini's research team. The first generation of CORM, such as tricarbonyldichlororuthenium(II) dimer (CORM-2), are soluble only in organic

solvents, such as DMSO, which calls into question the safety of these compounds when used in vivo. Furthermore, the release of CO from these compounds usually requires physical (e.g., irradiating light) or chemical (e.g., strong ligands, such as DMSO) stimuli.[26]

By coordinating glycine onto the metal center, water-soluble and less toxic CORMs (such as CORM-3) were prepared. CORM-3 was able to release CO *in vitro*, *ex vivo* and *in vivo*. Besides, CORM-3 has several advantages over the first generation of CORMs such as water solubility (ca. 1 mol of CO per mole of CORM-3 is liberated within 10 min after dissolved in water), and its ease to control the concentration and release rate of CO.[27] Both physiological pH and strong ligands present in the biological environment ar enough to dissociate CO from the metal center.[28]

Several prototypical CORMs have been extensively tested in experimental models, including the original Mn_2CO_{10} (CORM-1), CORM-2 and CORM-3.[29] A water-soluble boron containing CORM (CORM-A1) has also been developed, which slowly releases CO ($t_{1/2}$ = 21 min) in a pH and temperature-dependent fashion.[30] Besides, a new CORM based on iron and cysteamine (CORM-S1) has recently been synthesized, which is also soluble in water and releases CO under irradiation with visible light, while it is stable in the dark.[31] (See **Figure 3.3**)

CORMs have demonstrated vasoactive effects. In particular, CORM-3 has shown to produce a rapid vasodilatory response.[32] This compound has been shown to alleviate damage in ischemia/reperfusion injury, inhibit allograft rejection, suppress nitric oxide production from macrophages and attenuate cardiovascular inflammation and thrombin-induced neuroinflammation. While CORM-3 has been shown to prevent reoccurrence of sepsis and to reduce liver injury after cecal ligation and puncture (CLP), CORM-2 prolongs survival and reduces inflammation.

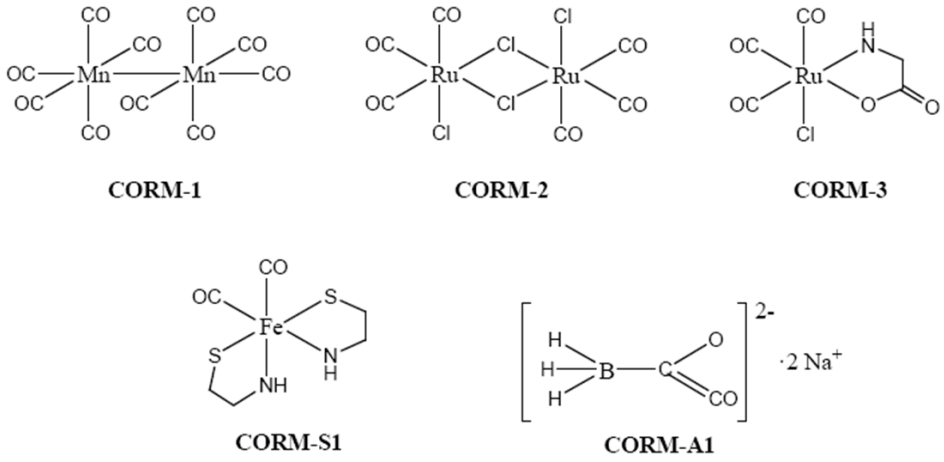

Figure 3.3. Structure of most common CORMs.

3.1.2 Chemosensors to detect carbon monoxide

Symptoms as confusion and tiredness as well as migraine and dizziness can arise from long term exposures even at low levels of CO (30–50 ppm). It is a concern that these symptoms are often misdiagnosed as those of common viral infections. Due to the interest in detecting this gas at subtoxic concentrations (lower than 50 ppm) is therefore becoming important to avoid harm from its presence as a chronic poison. The majority of sensors used for the detection of CO in air are based on electrochemical cells and on semiconducting metal oxides (typically tin dioxide). However, significant progress has been made recently towards the development of new CO sensors using different technologies.

In this context, chemosensors for carbon monoxide, that exhibit striking optical changes visible to the 'naked eye' at low concentrations of the analyte, are seen as a powerful alternative to the established systems. Moreover since the discovery of the benign role of carbon monoxide, a whole new research field, focused on the real-time detection of CO in living cells and tissues, has emerged. This coincides with interest in the therapeutic potential of CORMs that are able to

release CO in a controlled manner via hydrolysis or photoactivation. The growth of these fields has led to attempts to develop luminescent chemosensors capable of quantifying the production of endogenous CO or the generation of CO by CORMs in cells. However, despite these facts, few systems capable of the fluorogenic detection of CO in cells and tissues have been reported.

Most of the probes developed for the optical sensing of CO, both for detection in air or in cells, are based on metal complexes, as they possess many promising attributes suited to the design of chromo- or fluorogenic probes.[33] The possibility of tuning the steric and/or electronic features of metal complexes enables a subtle control to be exerted over the selectivity and reactivity of the metal towards CO.[34] In terms of CO detection, the sensing mechanism is intrinsically related with the reactivity of the metal centre towards carbon monoxide and in most cases the detection is often unsurprisingly related to the direct coordination of CO to the metal. The binding of CO with the metal centre can occur at a vacant coordination site or through the displacement of a labile ligand. When using metal complexes the optical response can be triggered in two different ways. It can arise from (a) the OFF–ON switching of the optical response from the metal complex, which acts as both receptor and signalling unit; or (b) via the revival of the optical signal of a displaced ligand, which was previously quenched by its close proximity to the metal centre. Alternatively, transition-metal catalysed carbonylation, hydrocarboxylation and azidocarbonylation reactions in the presence of CO have also proved to be useful in generating highly fluorescent derivatives from poorly emissive organic precursors.[35] Ideally, such reactions should be immediate and need to take place under mild temperatures and at atmospheric pressure.

For example, selective and sensitive detection of CO was achieved using the binuclear rhodium complex *cis*-$[Rh_2(C_6H_4PPh_2)_2(O_2CCH_3)_2](HAc)_2$.[36] This complex contains two cyclometalated phosphine ligands and undergoes a colour change from violet to orange via replacement of an acetic acid molecule by CO (see **Figure 3.4**). In addition, replacement of the second acetic acid molecule by CO induces a color change to yellow. A collection of binuclear rhodium complexes displayed

high CO selectivity with remarkable detection limits. For example, ([Rh_2{(*m*-$CH_3C_6H_3$)P(*m*-$CH_3C_6H_4$)$_2$}$_2$(O_2CCH_3)$_2$](HAc)$_2$), adsorbed on silica gel, is capable of CO detection by the "naked eye" at concentrations as low as 0.2 ppm in air. Furthermore, the binding of CO in all rhodium complexes was fully reversible.

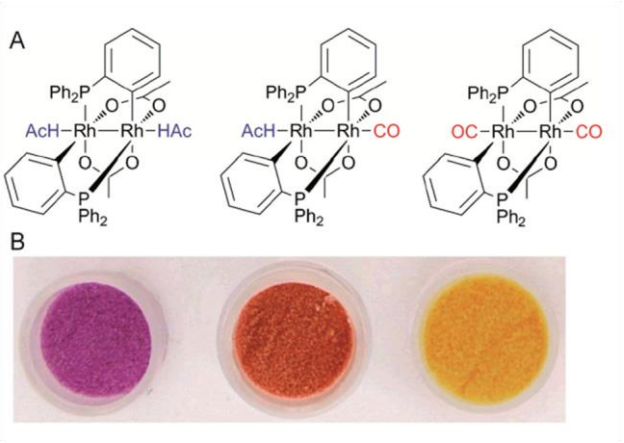

Figure 3.4. Colorimetric detection of CO via binuclear rhodium complexes. (A) Basic structure of the complexes (HAc = CH_3CO_2H). (B) The photograph shows ([Rh_2{(*m*-$CH_3C_6H_3$)P(*m*- $CH_3C_6H_4$)$_2$}$_2$(O_2CCH_3)$_2$]·(CH_3CO_2H)$_2$) adsorbed on silica gel in the absence (left) and presence of 8 ppm (middle) and 2000 ppm (right) of CO in air. *Adapted with permission from) M.E. Moragues, J. Esteban, J.V. Ros-Lis, R. Martínez-Máñez , M.D. Marcos, J. Soto, F.Sancenón, J. Am. Chem. Soc.* ***2011****, 133, 15762. Copyright ©* ***2011*** *American Chemical Society.*

Unfortunately, these organometallic complexes are only soluble in organic solvents or in mixed aqueous solutions. Thus, these complexes are not useful for the real-time detection of physiological levels of CO inside living cells. In this context, fluorescence sensing and imaging has emerged as one of the most powerful techniques to monitor the concentration, localization and even movements of biomolecules in living systems. In fact a variety of fluorescent probes for other small signalling molecules, such as NO and hydrogen sulfide, has been already used in biology.[37]

However, the construction of fluorescent sensors for CO is still at a very early stage and the reported probes are very limited.

Recently, Feng and co-workers reported two readily available allyl fluorescein probes, which were found to be highly selective and sensitive to CO in the presence of $PdCl_2$.[38] These probes has good stability, are water soluble, and presented rapid and distinct colorimetric and fluorescent turn-on signal changes in the presence of CO. Moreover, a very low dose of these two probes can be used to detect and track CO in HeLa living cells (see **Figure 3.5**).

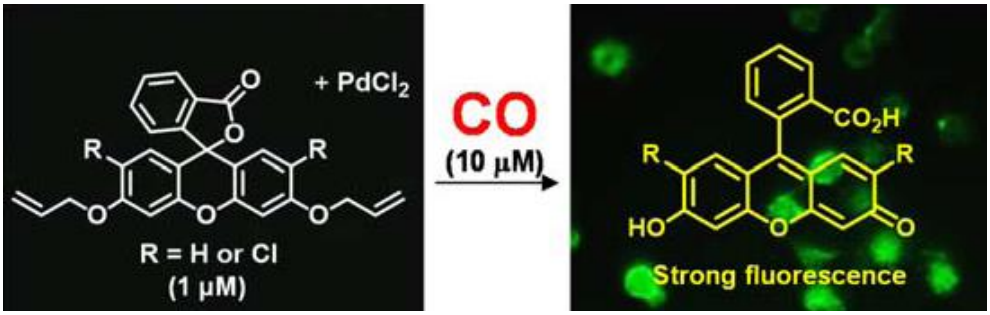

Figure 3.5. Fluorescent detection of CO in living cells using an allyl fluorescein ether. The probe have good stability, good water-solubility, and rapid and distinct colorimetric and remarkable fluorescent turn-on signal changes for CO in presence of $PdCl_2$. *Reprinted with permission from S. Feng, D, Liu, W.Feng, G. Feng,* Anal. Chem. ***2017**, 89, 3754. Copyright ©**2017** American Chemical Society.*

Using a similar approach, Zhang and co-workers prepared a first example of colorimetric and NIR fluorescent dual probe.[39] This probe consists of a naphthofluorescein fluorophore functionalized with two allylchloroformate moieties. Naphthofluorescein was chosen as a signaling fluorophore due to its long excitation and emission wavelengths (> 600 nm), relatively large Stokes shift and easy availability.[40] Allyl chloroformate was linked to the hydroxyl groups of naphthofluorescein as the response site to trap Pd^0 according to the Tsuji–Trost reaction. The derivatization of the hydroxy groups of naphthofluorescein in

position 4 and 9 with allyl chloroformates yielded a colorless and non-fluorescent closed lactone form. However, in the presence of CO and Pd(II) the free naphthofluorescein moiety is released with subsequent generation of a strong NIR fluorescence emission. Moreover, confocal fluorescence images of HeLa living cells demonstrated that probe was suitable for tracking intracellular CO (see **Figure 3.6**).

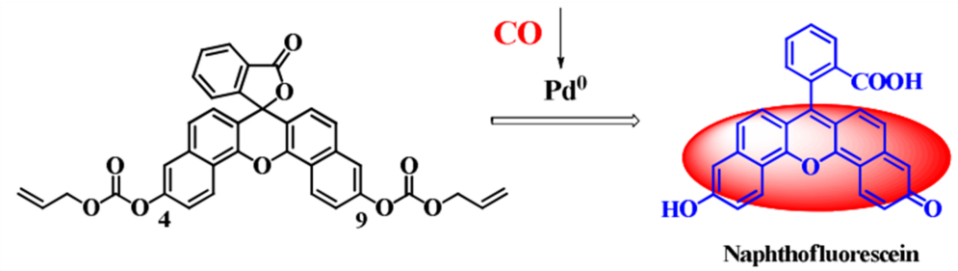

Figure 3.6. Proposed sensing mechanism of naphthofluorescein probe for CO detection based on *in-situ* generation of Pd^0. *Reproduced from J. Yan, J. Zhu, Q. Tan, L. Zhou,P. Yao, Y. Lu, J. Tan and L. Zhang, RSC Adv.* ***2016****, 6, 65373, with permission of the Royal Society of Chemistry.*

The biological detection of carbon monoxide is still in its infancy and urgently needs probes with an improved fluorescence response over a shorter timeframe in order to monitor the role of endogenous CO in cells and tissues. However, the sensing systems reported so far show substantial promise, suggesting that an understanding of this fascinating role of carbon monoxide will soon be aided by further improvements in probe design.

3.2. References

1. (a) R. Wang, *J Physiol Pharmacol* **1998**, 76, 1-15. (b) T.M. Dawson,S.H. Snyder, *J Neurosci* **1994**, *14*, 5147.

2. L. Wranne*, Acta Paediatr Scand* **1967**, *56*, 381.

3. R.F. Coburn, W.S. Blakemore, R.E. Forster*, J Clin Invest* **1963**, *42*, 1172.

4. H. Nishibayashi, T. Tomura, R. Soto, R.W. Estabrook, *Baltimore, MD: University Park Press;* **1968.**

5. D.G. Wolff, W.K. Bidlack, *Biochem Biophys Res Commun* **1976**, 73, 850-857

6. A.D. Lindstrom, M.W. Anders, *Toxicol Lett* **1978,** *1*, 307.

7. C.B. Kim, S.R. Hintz, H.J. Vreman, D.K. Stevenson, *Dev Pharmacol Ther* **1988**, *11*, 166.

8. Air quality criteria for carbon monoxide. Washington, DC. *US Environmental Protection Agency, Office of Research and Development,* **1991** (publication no. EPA-600/B-90/045F)

9. D. Penney, V. Benignus, S. Kephalopoulos, D. Kotzias, M. Kleinman, A. Verrier, *WHO Guidelines for Indoor Air Quality: Selected Pollutants, Copenhagen*, **2010**, 55.

10. R.F. Coburn, *Prev Med* **1979**, *8*, 310.

11. I.Blumenthal, *J. R. Soc. Med* **2001**, *94*, 270.

12. W.R. Harvey, P. Hutton, *Curr Anaesth Crit Care* **1999**, *10*, 158.

13. R.A.M Myers, A. Defazio, M.P. Kelly, *J Clin Psychol* **1998**, *54*, 555.

14. J. J. Forbes, G. W. Grove, *Bureau of Mines Miners' Circ*., **1954**, *33,*3.

15. P.C. Novelli, *Chemosphere Global Change Sci.* **1999,** *1*, 115.

16. H.J. Vreman, D.K. Stevenson, W. Oh, *Clin Chem*. **1994**, *40*, 1927.

17. T. Sjostrand*, Acta Physiol. Scand*. **1952**, *26*, 338.

18. R. Tenhumen, H. S. Marver, R. Schmid, *Proc. Natl. Acad. Sci. USA*, **1968**, *61*, 748.

19. L.A. Applegate, P. Luscher, R.M. Tyrrell, *Cancer Res* **1991**, *51*, 974.

20. S.W. Ryter, J. Alam, A.M. Choi, *Physiol Rev* **2006**, *86*, 583.

21. H.P. Kim, S.W. Ryter, A.M. Choi, *Annu. Rev. Pharmacol. Toxicol.* **2006**, *46*, 411.

22. S.W. Ryter, A.M.K. Choi, *Korean J Intern Med* **2013**, *28*, 123.

23. H. Fujimoto, M. Ohno, S. Ayabe, H. Kobayashi, N. Ishizaka, H. Kimura, K.-I Yoshida, R. Nagai, *Arterioscler Thromb Vasc Biol*. **2004**, *24*, 1848.

24. L.E. Otterbein, A.M. Choi., *Am J Physiol Lung Cell Mol Physio*l. **2000**, 279, L1029.

25. J.P. Loennechen, O.G. Nilsen, I. Arbo, P. Aadahl , T. Nilsen, H.L. Waldum, A.K. Sandvik, O. Ellingsen, *Toxicol Appl Pharmacol*. **2002,** *178*, 8.

26. R. Motterlini, J. E. Clark, R. Foresti, P. Sarathchandra, B. E. Mann, C. J. Green, *Circ. Res.,* **2002**, *90*, E17.

27. J.E. Clark, P. Naughton, S. Shurey, C.J. Green, T.R. Johnson, B.E. Mann, R. Foresti, R. Motterlini, *Circ Res **2003**, 93*, e2.

28. R. Foresti, J. Hammad, J.E Clark, T.R. Johnson, B.E. Mann, A. Friebe, C.J. Green, R. Motterlini, *Br. J. Pharmacol. **2004**, 142*, 453.

29. B. Arregui, B. Lopez, M. G. Salom, F. Valero, C. Navarro, F. J. Fenoy, *Kidney Int.* **2004**, *65*, 564.

30. A. Sandouka, B. J. Fuller, B. E. Mann, C. J. Green, R. Foresti, R. Motterlini*, Kidney Int.* **2006**, *69*, 239.

31. R. Kretschmer, G. Gessner Guido, H. Gorls, S. Heinemann, M. Westerhausen, *J. Inorg. Biochem*. **2011**, *1005*, 6.

32. R. Foresti, J. Hammad, J. E. Clark, *Br. J. Pharmacol.* **2004**, *142*, 453.

33. K. K.-W. Lo and S. P.-Y. Li, *RSC Adv.* **2014**, *4*, 10560.

34. C. W. Rogers, ÑM. O. Wolf, *Coord. Chem. Rev.* **2002**, *233–234*, 341.

35. C. Marín-Hernández, A. Toscani, F. Sancenón, J. Wilton-Ely, R. Martínez-Máñez, *Chem. Commun*. **2016**, *52*, 5891.

36. (a) J. Esteban, J.V. Ros-Lis, R. Martínez-Máñez, M. Marcos, M. Moragues, J. Soto, F. Sancenón, *Angew Chem Int Ed*. **2010**, *49*, 4934; (b) M.E. Moragues, J. Esteban, J.V. Ros-Lis, R. Martínez-Máñez, M.D. Marcos, J. Soto, F.Sancenón, *J Am Chem Soc.* **2011**, *133*, 15762.

37. S. H. Heinemann, T. Hoshi, M. Westerhausen, A. Schiller, *Chem Commun* **2014**, *50*, 3644

38. S. Feng, D, Liu, W.Feng, G. Feng, *Anal. Chem.* **2017**, *89*, 3754.

39. J-W. Yan, J.-Y Zhu, Q.-F Tan, L .F. Zhou, P.-F. Yao, Y.T. Lu, J.-H Tan ,L. ZHang, *RSC Adv.* **2016,** 6, 65373.

40. Z. Xu, J. Yan, J. Li, P. Yao, J. Tan, L. Zhang, *Tetrahedron Lett*. **2016**, *57*, 2927.

3.3. Objectives

Taking into account the growing current interest in the development of chemosensors for carbon monoxide detection, the small quantity of described probes capable of tracking CO in living cells and our interest in the development of new chromo-fluorogenic systems we decided to prepare a new optical chemosensor for the sensitive, selective and rapid detection of CO both *in vitro* and *in vivo*.

In particular our main aims are:

- To design a fluorescent probe for CO detection based on a water-soluble Ru(II) complex.
- To evaluate the fluorogenic behavior of probe toward CO in aqueous environments.
- To evaluate the sensitivity and selective of the probe.
- To test the fluorogenic ability of the probe for the recognition of endogenous CO in living cells.
- To test the fluorogenic ability of the probe for the recognition of endogenous CO in an *in vivo* model.

3.4. *Ex-vivo tracking of endogenous CO with a ruthenium(II) complex*

Cristina de la Torre,[†,‡,§,+] Anita Toscani,[||,+] Cristina Marín-Hernández,[†,‡,§] Jonathan Robson,[||] Carmen Terencio,[§,Δ] Andrew White,[||] María José Alcaraz,[§,Δ] James D. E. T. Wilton-Ely,*[||] Ramón Martínez-Máñez,*[†,‡,§] and Félix Sancenón[†,‡,§]

[†] *Instituto Interuniversitario de Investigación de Reconocimiento Molecular y Desarrollo Tecnológico (IDM), UniversitatPolitècnica de València, Universitat de València.*

[‡] *Departamento de Química, UniversitatPolitècnica de València, Camino de Vera s/n, 46022, Valencia, Spain.*

[§] *CIBER de Bioingeniería, Biomateriales y Nanomedicina (CIBER-BBN).*

[||] *Department of Chemistry, Imperial College London, South Kensington Campus, London SW7 2AZ, UK.*

[Δ] *Department of Pharmacology, Universitat de València, Valencia, Spain.*

Submitted to Journal of the American Chemical Society

A two-photon fluorescent probe based on a ruthenium(II) vinyl complex is capable of selectively detecting carbon monoxide in cells (treated with CORM-3 or hemin) and ex vivo using mice with a subcutaneous air pouch as a model for inflammation. This is the first probe reported for the selective and sensitive detection of ex vivo CO in a realistic model.

Under ambient conditions, carbon monoxide (CO) is a colorless, odorless gas associated with incomplete combustion and widely known for its toxic effect on humans. Vivid descriptions of deaths attributed to 'fuel gas' leaks were common in the 19th century, since it contained between 5 to 40 % of CO.[1]Human toxicity is due to the high affinity of CO for iron, reducing the oxygen transport capacity of hemoglobin and the fact that the gas is broadly inhibitory for heme proteins and non-heme iron enzymes including hydrogenase[2] and nitrogenase.[3] Paradoxically, more than half a century ago it was found that CO is routinely formed endogenously in humans in small quantities, and that under certain pathophysiological conditions, CO production increases.[4]

In the body, it is known that CO serves many functions, including anti-inflammatory, antiproliferative, anti-apoptotic and anticoagulative roles. It is also an intrinsic metal ligand in enzymes and acts as a gaseous signaling molecule in mammals.[5] The discovery that hemoglobin is required as a substrate for the production of CO in vivo, and the identification of the role of heme oxygenases (HO-1 and HO-2) in the generation of this gas in mammals, framed the early investigations into this unexpected biological role of CO. Moreover, emerging evidence reveals that an increased generation of HO-derived CO plays a critical role in the resolution of inflammatory processes and alleviation of cardiovascular disorders.[6]

Although CO can be administered medically by inhalation, CO-releasing molecules (CORMs) are capable of exerting a variety of pharmacological action via the liberation of controlled amounts of CO in biological systems.[7a] CORMs are

currently being investigated in order to tailor therapeutic approaches to the prevention of vascular dysfunction, inflammation, tissue ischemia and organ rejection.[7b] Due to these benign roles, CO has garnered considerable attention recently and there is a great interest in gaining further understanding of its functions in biological systems.

One of the major obstacles limiting progress in this research area is the lack of real-time methods to selectively track CO in biological systems as established techniques are unsuitable for real-time tracking of intracellular CO in a non-invasive manner.8 There is therefore a need to develop convenient, sensitive and selective sensing methods for rapid detection of CO in living systems for biological research. Recently, fluorescence sensing and imaging with emissive probes has emerged as one of the most powerful techniques to detect biologically important molecules.[8,9] However, the development of fluorescent probes for monitoring CO at the cellular level still remains a challenge. Until very recently, the most significant breakthroughs came from the groups of He10 and Chang,[11] which reported two different types of fluorescent CO probes for the imaging of CO in living cells. Following those pioneering contributions, other similar probes have been developed and applied for cell imaging of CO.[12] However these probes are either complicated, difficult to synthesize, need to be excited by photodamaging UV light, have delayed fluorescence response times (commonly between 10 and 60 mins in the palladium-based systems), use cytotoxic non-ligated heavy metal salts (as carbonylation catalysts or Tsuji-Trost reaction mediators) or the addition of high concentrations of organic co-solvents[.12] For these reasons there is a lack of CO chemosensors for tracking this gas within an in vivo model. The development of a simple and reliable fluorogenic probe with improved features capable of detecting CO in living systems is a particularly timely area of research.

Two-photon fluorescence microscopy is an important biological imaging technique, which offers many advantages over conventional confocal microscopy. It allows the study of biological samples in three dimensions with submicrometer resolution and, due to the near-IR light used, has remarkable advantages over

other techniques. These include reduced specimen photodamage and greater penetration, allowing higher contrast imaging. Given these properties, the design of new two-photon fluorophores for biological sensing is therefore a nascent field of interest.[13]

The indicator displacement assay (IDA) is one of the most widely used approaches for the detection of anions and neutral molecules. This paradigm was extensively developed by Anslyn and uses a sensing ensemble formed by an abiotic receptor (designed in such a way that presented a high degree of complementarity with the target analyte) and an indicator (dye or fluorophore).[14] Coordination of the analyte with the receptor disrupts the sensing ensemble, releasing the indicator. Since the optical properties (color or fluorescence) of the free indicator differ from those of the sensing ensemble, the presence of the analyte is confirmed by the measurable macroscopic signal obtained.

In view of the aspects mentioned above, we report herein a novel molecular probe for the fluorogenic detection of CO in biological environments using the IDA paradigm. The probe (complex 6 in Scheme 1) takes inspiration from the ruthenium(II) vinyl complexes, which display exceptional results for the detection of CO in air.[15] However, a crucial difference is the use of a new fluorophore, 5-(3-thienyl)-2,1,3-benzothiadiazole (TBTD), as a signaling unit, which is coordinated directly to the metal center rather than as a substituent on the vinyl ligand. The design of probe 6 thus incorporates many of the desired characteristics needed for the sensing of carbon monoxide in cells. The immediate fluorogenic response, the outstanding emission enhancement and the exceptional sensitivity and selectivity make these complexes unique candidates for this application. However, the very low solubility of these complexes in water prevented them being applied directly to the sensing of CO in aqueous systems. A common approach to overcome such limitations is the modification of the ancillary ligands coordinated to the metal center. The replacement of triarylphosphine ligands with sulfonated triphenylphosphine ligands can achieve solubility in water and this has been applied extensively in catalysis.[16] However, this was found to lead to undesired

effects on the sensing behavior due to the concomitant changes in electronic, steric and coordination properties of the phosphines. An alternative strategy was thus employed to introduce hydrophilic groups to the vinyl substituent. Probe 6 was successfully synthesized using a terminal alkyne with an oligoethylene glycol moiety (HC≡CL in Scheme 1).

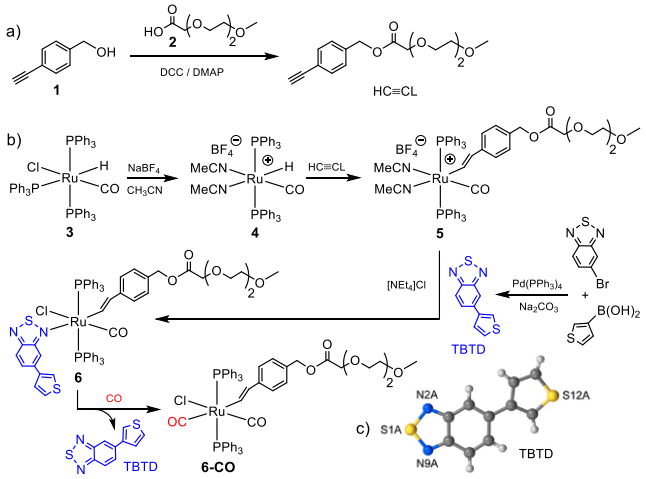

Scheme 1. (a) Synthesis of HC≡CL; (b) preparation of 6 and reaction of 6 with CO; c) crystal structure of TBTD (see Supporting Information).

Inexpensive 4-ethynylbenzyl alcohol (**1** in Scheme 1a) was treated with an oligoethylene glycol (PEG) derivative (**2**) in a simple esterification reaction using DCC/DMAP as coupling agents. After column chromatography, the HC≡CL ligand was characterized using NMR and IR spectroscopy, as well as mass spectrometry and elemental analysis. The new TBTD ligand was prepared through the Suzuki coupling of 5-bromo-2,1,3-benzothiadiazole and 3-thienylboronic acid (Supporting Information).

The synthesis of probe **6** (Scheme 1b) commences with commercially-available **3**, which was transformed to **4** using sodium tetrafluoroborate in acetonitrile. Complex **5** was generated from **4** by addition of HC≡CL. Finally, **5** was treated with a chloride source and the TBTD ligand to yield probe **6** in high yield (84%). Perhaps

due to the oligoethylene glycol chain, compound **6** failed to yield crystals suitable for a structural determination. In order to unequivocally determine the bonding mode and orientation of the coordinated TBTD ligand, the 9-phenanthrenyl analogue [Ru(CH=CHPhen-9)Cl(CO)(TBTD)$(PPh_3)_2$] (**7**) was prepared (Supporting Information). Single crystals of **7** allowed structural information to be obtained by X-ray diffraction (**Figure 1**). The addition of carbon monoxide to **7** led to quantitative conversion to **7 CO**, the structure of which was also determined.

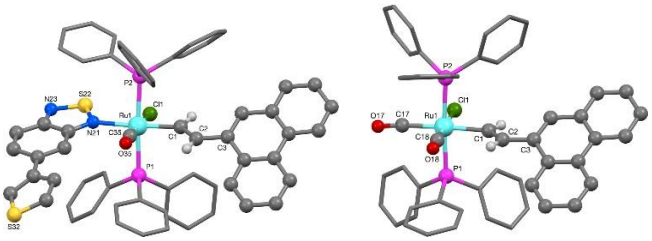

Figure 1. Crystal structures of compound **7** (left) and **7 CO** (right) .

The fluorogenic behavior of probe **6** in aqueous environments was first investigated in the absence and in the presence of CO. Analysis of a PBS (pH 7.4)-acetone 99.9:0.1 v/v solution of probe **6** (1.0×10^{-5} mol L^{-1}) revealed a very weak emission band centered at ca. 500 nm (upon excitation at 355 nm). This weak emission was ascribed to quenching of the TBTD fluorescence by the Ru(II) center (heavy atom effect). Passing increasing quantities of CO gas into the aqueous solution of probe **6** induced a progressive enhancement of the emission at 500 nm as shown in Figure 2. The observed emission enhancement was attributed to the dissociation of TBTD from the complex upon CO binding and this displacement was confirmed experimentally (Figure S2-17). The replacement of the labile TBTD ligand by the CO was found to disrupt the heavy-atom quenching effect of the Ru(II) center and accounted for the emission enhancement observed (see Scheme 1b). From the titration profile, a limit of detection as low as 1 ppb of CO was determined. The product formed, [Ru(CH=CHL)Cl$(CO)_2(PPh_3)_2$] (**6 CO**), was fully

characterized (Supporting Information) and analogous **7 CO** was also structurally characterized (**Figure 2**).

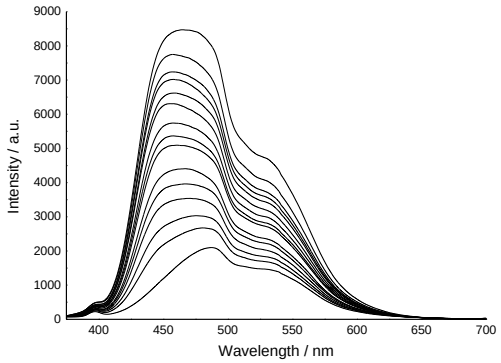

Figure 2. Turn-on fluorescence response (excitation at 355 nm) of a 1.0 x 10-5 mol L-1 of PBS (pH 7.4)-acetone 99.9:0.1 v/v solution of probe 6 upon addition of increasing quantities of CO (0-100 ppm).

In order to confirm that the fluorescence enhancement observed resulted from the displacement of TBTD by CO rather than the instability of complex 6 in aqueous solution, the fluorescence spectra were recorded every 5 minutes in the presence and absence of CO over a 1 hour period. As no emission enhancement was observed in the absence of CO, it can be concluded that the fluorescence response results from the presence of this gas in solution and not due to spontaneous release of the TBTD ligand in aqueous environments (e.g., through displacement by coordinated water). Although the cellular matrix is difficult to reproduce, 100 µM concentrations of reactive nitrogen and oxygen species, such as tryptophan, cysteine, BSA, imidazole, NOx, hydroxide, peroxide, were also added to aqueous solutions of probe 6, whilst the emission intensity was monitored. This experiment confirmed the selectivity of the probe towards CO as no significant increase in the TBTD emission was observed on addition of these compounds (Figure S4-1). Further tests confirmed the solution and photostability of probe 6 (Figures S4-3, S4-4 in Supporting Information).

These experiments successfully demonstrated the potential of probe 6 for sensing CO in cells as the probe is (i) sufficiently soluble in water, (ii) selective for CO, producing a remarkable fluorescence enhancement, (iii) emissive at higher wavelengths than the range typical of protein emissions (250-400 nm) and (iv) two-photon active (*vide infra*). These design properties are vitally important for single-molecule imaging in cells.

On the basis of the encouraging results described above, the imaging of CO in living cells was investigated using probe 6. The mouse macrophage RAW 264.7 cell line was selected as it can induce HO-1 and generate CO under different physiological conditions.[17] Viability assays (MTT) were carried out with RAW 264.7 cells and showed the non-toxicity of probe 6 after 1, 3, 24 and 72 h (Figure S5-1). Following this favorable toxicity assessment, the ability of probe 6 to visualize changes in CO levels in cells was tested. For this purpose, RAW 264.7 cells were incubated with probe 6 (10 µM) for 30 min. As can be seen in **Figure 3A**, this led to no discernible emission. However, when the cells were pre-incubated with the CO source, CORM-3, and then treated with probe 6 (10 µM), a dose-dependent intracellular two-photon fluorescence response was clearly observed. (**Figures 3B and 3C).**

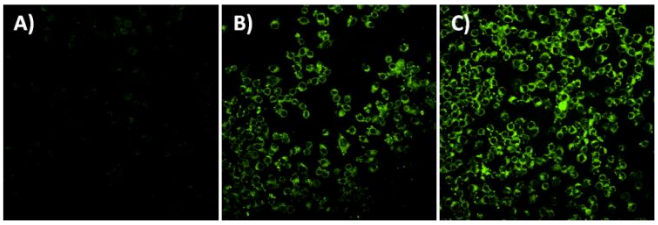

Figure 3. Two-photon excitation microscopy images of RAW 264.7 cells treated for 30 min with (A) 0 µM, (B) 10 µM and (C) 50 µM of CORM-3 followed by 10 µM of probe **6** in PBS (pH 7.4)-acetone 99.9:0.1 v/v. Images acquired upon excitation at 715 nm.

Another procedure to stimulate intracellular CO production is the use of heme cofactor. Carbon monoxide is naturally generated by the action of HO on heme

produced by the rupture of hemoglobin. Besides, heme administration is known to increase HO-1 expression and activity leading to subsequent CO generation.[18] Accordingly, RAW 264.7 cells were treated with hemin chloride in order to enhance intracellular CO levels, and so to further examine the ability of probe **6** to detect CO. Again, MTT viability assays were carried out to assess the toxicity of the hemin/probe **6** treatment in RAW 264.7 cells. For this purpose, cells were treated with hemin (100 μM) for 0.5, 3 and 6 h and then probe **6** (10 μM) was added for 30 min before imaging. Two controls were used; (i) cells without any treatment and (ii) cells treated only with probe **6** (10 μM) for 30 min. The viability experiments showed no toxicity of probe **6** in the presence of hemin (Figure S5-1).

RAW 264.7 cells were incubated with hemin (100 μM) for 3 h, then with probe **6** (10 μM) for 5, 10, 20 and 30 min prior to imaging. The two-photon excitation microscopy images obtained are shown in Figure S5-2. The RAW 264.7 cells treated with hemin and probe **6** showed a marked green emission that was again ascribed to the TBTD fluorophore released from probe **6** upon reaction with the CO generated. Moreover, a dose dependent response was observed when cells were treated with different hemin concentrations during the same time period (**Figure 4**). This showed a 10-fold enhancement when 100 μM hemin was used.

The response time for CO detection in the above experiments was rapid with the maximum emission being reached after only 10 minutes of probe incubation (Figure S5-2). For example, this compares favorably with the much slower response (after 60 min) of the ground-breaking molecular probe reported by Chang.[11] The only previously reported two-photon system for CO detection in cells is the elegant cyclopalladated carbazole-coumarin scaffold reported by Lin et al.[12i] However, its drawbacks include the synthetic route (7 steps in <1% yield from commercially-available reagents), the high CORM-2 concentration used (200 μM), the long response time (40 min) and the need for 10% DMSO solutions. These results clearly indicate that probe **6** can be used as an effective probe for monitoring changes in intracellular CO.

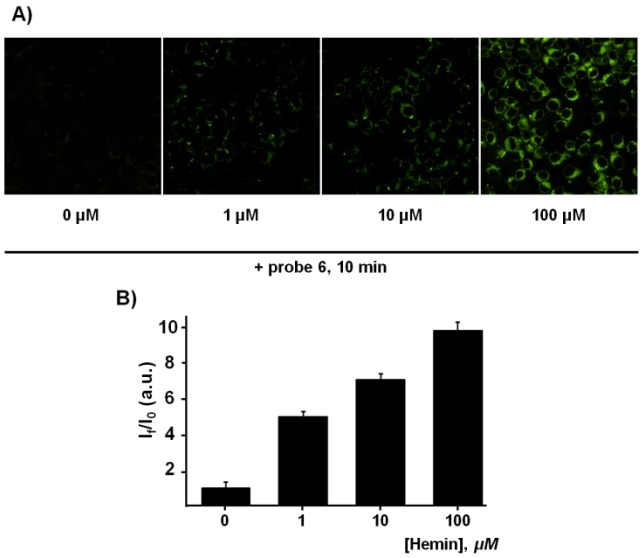

Figure 4. (A) Two-photon excitation microscopy images of RAW 264.7 cells treated with 0, 1, 10 or 100 µM of hemin for 3 h before incubation with probe **6** (10 µM) for 10 min. (B) Ratio of mean fluorescence intensity of cells at different conditions with control cells (0 µM hemin) using ImageJ software. Data are expressed as mean ± SEM of at least three independent experiments. Excitation at 715 nm.

Previous leading studies on CO detection in cells have typically employed incubation with CORMs or hemin to generate CO within the cellular environment.[12] However, applications of CO detection in more realistic models have not been reported previously. In order to address this important avenue of development, the remarkable *in vitro* results shown above with probe **6** were expanded in order to further test the potential and versatility of probe **6** for *ex vivo* CO detection. For this purpose, a subcutaneous air pouch inflammation mouse model was employed.

The cellular stress protein HO-1 serves a vital metabolic function for limiting the rate of degradation of heme to generate carbon monoxide, iron and biliverdin-IX_α (BV), the latter then being converted to bilirubin-IX_α.[6] Previous studies have

demonstrated that lipopolysaccharides (LPS) from many bacterial species initiate acute inflammatory responses in mammals that are typical of the host reaction to tissue injury or infection. In this scenario, it has been reported that LPS administration into a mouse air pouch induces an inflammatory reaction characterized by plasmatic exudation and migration of leukocytes to the cavity.[19] It was anticipated that administration of LPS would induce HO-1 protein expression in leukocytes migrating to the air pouch exudates, causing them to exhibit higher levels of CO than would be expected in the absence of LPS. Air pouches were produced in female Swiss mice by subcutaneous injections of 10 mL sterile air into the back. After 3 days, 5 mL of sterile air were injected into the same cavity. Six days after the formation of air pouches, inflammation was induced by injection of 1 mL of LPS (1 μg/mL) in saline. A control group was only injected with 1 mL of saline. After 18 hours, 3 mL of probe **6** (50 μM) was injected into the air pouch. After 30 minutes, mice were culled by cervical dislocation and the exudates in the pouch were collected. Cells were visualized using two-photon microscopy (excitation at 715 nm). As shown in Figure 4, cells from mice treated with LPS and probe **6,** showed a remarkable increase in fluorescence (**Figure 5D**) compared to cells from mice treated with only saline and probe. (**Figure 5C**). Moreover, as expected, a very low level of fluorescence was observed in cells from mice treated with LPS without probe **6** (Figure 5B) or only treated with saline (**Figure 5A**). These results clearly indicate that the Ru(II) vinyl complex **6** is able to fluorogenically detect CO *ex vivo* in a model of inflammation.

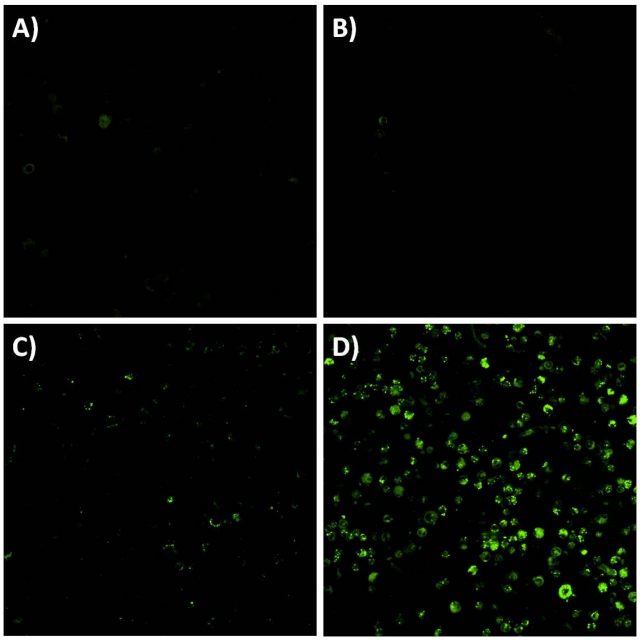

	A	B	C	D
LPS	-	+	-	+
Probe 6	-	-	+	+

Figure 5. Two-photon excitation microscopy images of cells from mice exudates after 18 h of saline or LPS treatment and 30 min with or without probe **6** in the air pouch. (A) mice treated with saline, (B) mice treated with LPS, (C) mice treated with saline and 50 µM of probe **6** (D), mice treated with LPS and 50 µM of probe **6**. Images were acquired upon excitation at 715 nm using a multiphoton microscope. See Figure S5-3 for larger version.

In summary, we have described the design of a Ru(II) vinyl complex capable of selectively detecting CO through a remarkable OFF-ON emission enhancement with a limit of detection as low as 1 ppb in PBS (pH 7.4)-acetone 99.9:0.1 v/v. Emission enhancement is attributed to the dissociation of TBTD from complex **6** upon CO binding. Probe **6** is selective for CO even in the presence of RNS and ROS, which all induced no response. Probe **6** proved to be non-toxic to cells and can be used in low doses for the two-photon fluorescence *in vitro* imaging of CO in RAW 264.7 cells in the presence of CORM-3 or hemin. Even more significantly, the

probe was successfully used for the two-photon fluorescence detection of CO *ex vivo* in cells, which were collected from the exudates of an air pouch inflammation mouse model. The combination of selectivity, sensitivity and inexpensive, straightforward synthesis make the system described here a very attractive and efficient probe for the facile fluorogenic detection of this gas in realistic environments. Moreover, we believe that our study could inspire the design of other chemosensors for the detection of other important analytes in realistic *in vivo* models.

ACKNOWLEDGMENTS

The authors wish to thank the Spanish government (Project MAT2015-64139-C4-1), the Generalitat Valencia (Project PROMETEOII/2014/047), CIBER-BBN, IC Global Engagements fund and the Santander Mobility Award Scheme. C.T. is grateful to the Spanish Ministry of Science and Innovation, A.T. thanks the Leverhulme Trust (RPG-2012-634) and J.A.R. thanks the EPSRC, all for PhD studentships. We thank the UV Microscopy service and E. Navarro Raga for multiphoton microscopy.

REFERENCES

1. Roberts, G. P.; Youn, H.; Kerby, R. L. *Mol. Biol. Rev.* **2004**, *68*, 453.
2. Rees, D. C. *Annu. Rev. Biochem.* **2002**, *71*, 221.
3. a) Christiansen, J.; Seefeldt, L. C.; Dean, D. R. *J. Biol. Chem.* **2000**, *275*, 36104; b) Lee, H. I.; Cameron, L. M.; Hales B. J.; Hoffman, B. M. *J. Am. Chem. Soc.* **1997**, *119*, 10121.
4. Sjoestrand, T. *Nature* **1949**, *164*, 580.
5. Szabo, C. *Nat. Rev. Drug Discov.* **2016**, *15*, 185.
6. Motterlini, R.; Otterbein, L. E. *Nat. Rev. Drug Discov.* **2010**, *9*, 728.
7. a) Kautz, A. C.; Kunz, P. C.; Janiak, J. *Dalton Trans.* **2016**, *45*, 18045; b) Motterlini, R.; Mann, B. E.; Foresti, R. *Expert Opin. Investig. Drugs* **2005**, *14*, 1305.
8. Marín-Hernández, C.; Toscani, A.; Sancenón, F.; Wilton–Ely, J. D. E. T.; Martínez-Mañez, R. *Chem. Commun.* **2016**, *52*, 5902.
9. Rogers, C. W.; Wolf, M. O. *Angew. Chem. Int. Ed.* **2002**, *41*, 1898.
10. Wang, J.; Karpus, J.; Zhao, B. S.; Luo, Z.; Chen, P. R.; He, C. *Angew. Chem. Int. Ed.* **2012**, *51*, 9652.

11. Michel, B. W.; Lippert, A. R.; Chang, C. J. *J. Am. Chem. Soc.* **2012**, *134*, 15668.

12. (a) Feng, W.; Liu, D.; Zhai, Q.; Feng, G. *Sens. Act. B* **2017**, *240*, 625; (b) Xu, Z.; Yan, J.; Li, J.; Yao, P.; Tan. J.; Zhang, L. *Tetrahedron Lett.* **2016**, *57*, 2927; (c) Yan, J. –W.; Zhu, J. –Y.; Tang, Q. –F.; Zhou, L. –F.; Yao, P. –F.; Lu, Y. –T.; Tan, J. –H.; Zhang, L. *RSC Adv.* **2016**, *6*, 65373; (d) Li, Y.; Wang, X.; Yang, J.; Xie, X.; Li, M.; Niu, J.; Tong, L.; Tang, B. *Anal. Chem.* **2016**, *88*, 11154; (e) Feng, W.; Liu, D.; Feng, S.; Feng, G. *Anal. Chem.* **2016**, *88*, 10648; (f) Feng, W.; Liu, D.; Feng, S.; Feng, G. *Anal. Chem.* **2016**, *88*, 10648; (g) Pal, S.; Mukherjee, M.; Sen, B.; Mandal, S. K.; Lohar, S.; Chattopadhyay, P.; Dhara, K. *Chem. Commun.* **2015**, *51*, 4410; (h) Cao, Y.; Li, D. –W.; Zhao, L. –J.; Liu, X. –Y.; Cao, X. –M.; Long, Y. –T. *Anal. Chem.* **2015**, *87*, 9696; (i) Zheng, K.; Lin, W.; Tan, L.; Chen, H.; Cui, H. *Chem. Sci.* **2014**, *5*, 3439.

13. Kim, H. M.; Cho, B. R. *Chem. Rev.* **2015**, *115*, 5014.

14. (a) Wiskur, S. L.; Ait-Haddou, H.; Lavigne, J. J.; Anslyn, E. V. *Acc. Chem. Res.* **2001**, *34*, 963. (b) Nguyen, B. T.; Anslyn, E. V. *Coord. Chem. Rev.* **2006**, *250*, 3118.

15. (a) Toscani, A.; Marín-Hernández, C.; Moragues, M. E.; Sancenón, F.; Dingwall, P.; Brown, N. J.; Martínez-Máñez, R.; White, A. J. P.; Wilton-Ely, J. D. E. T. *Chem. Eur. J.* **2015**, *21*, 14529; (b)Moragues, M. E.; Toscani, A.; Sancenón, F.; Martínez-Máñez, R.; White, A. J. P.; Wilton-Ely, J. D. E. T. *J. Am. Chem. Soc.* **2014**, *136*, 11930.

16. Pinault, P.; Bruce, D. W. *Coord. Chem. Rev.* **2003**, *241*, 1.

17. Alcaraz, M. J.; Vicente, A. M.; Araico, A.; Dominguez, J. N.; Terencio, M. C.; Ferrándiz, M. L. *Br. J. Pharmacol.* **2004**, *142*, 1191.

18. (a) Wu, L.; Wang, R. *Pharmacol. Rev.* 2005, *57*, 585; (b) Vicente, A. M.; Guillén, M. I.; Alcaraz, M. J. *Exp. Biol. Med.* **2003**, *228*, 514.

19. García-Fernández, A.; García-Laínez, G.; Ferrándiz, M. L.; Aznar, E.; Sancenón, F.; Alcaraz, M. J.; Murguía, J. R.; Marcos, M. D.; Martínez-Máñez, R.; Costero, A. M.; Orzáez, M. *J. Control. Release* **2017**, *248*, 60.

Ex-vivo tracking of endogenous CO with a ruthenium(II) complex

Cristina de la Torre, Anita Toscani, Cristina Marín-Hernández, Jonathan Robson, Carmen Terencio, Andrew White, María José Alcaraz, James D. E. T. Wilton-Ely, Ramón Martínez-Máñez, Félix Sancenón.

Supplementary Information

S1 General considerations regarding starting materials and equipment

Chemicals and solvents were purchased from Alfa-Aesar, Sigma-Aldrich and VWR and were used without further purification, unless otherwise stated. $[RuH(CO)(NCMe)_2(PPh_3)_2]BF_4$ was prepared using the literature method,[S1] replacing $AgClO_4$ with $NaBF_4$ under reflux[S2] in order to avoid the use of both perchlorate and silver salts. The synthesis of $[Ru(CH{=}CHPhen\text{-}9)Cl(CO)_2(PPh_3)_2]$ (**7·CO**) has been reported previously.[S3] Solvents used for UV-vis and fluorescence measurements were thoroughly degassed with nitrogen before use. All experiments and manipulations were conducted in air, unless otherwise specified. The commercially-available carbon monoxide lecture bottle (N3.7, purity 99.97%, with a CONCOA 302 – 2322 – CGA180 single-stage regulator) was purchased from CK Special Gases Limited (UK) and was used for the titration experiments. Standard Schlenk line and cannula techniques were used for the preparation of some of the compounds, where stated. Solvent mixtures are volume/volume mixtures. Solvents used in the reactions of oxygen and moisture sensitive compounds were dried and degassed according to standard techniques. Toluene was dried by passage through a column containing 3 Å molecular sieves. Triethylamine was distilled under nitrogen over calcium hydride after passing through 4 Å molecular sieves.

Waters LCT Premier ES-ToF (ESI) and a Micromass Autospec Premier (LSIMS) spectrometers were used for electrospray and high-resolution mass spectra (accurate mass mode). Further mass spectra analyses were performed at the Servei d'Espectrometria de Masses of the Universitat de València, Spain, on a Quadrupole time of flight (QqTOF) 5600 system (Applied Biosystems-MDS Sciex) spectrometer for high resolution mass spectra. The HRMS was operated in positive mode under the following conditions: Gas1 35 psi, GS2 35, CUR 25, temperature 450 ºC, ion spray, voltage 5500 V. Standard FTIR spectra were measured using a Perkin Elmer Spectrum GX spectrometer.

UV-vis spectra were recorded using a Perkin Elmer Lambda-20 (Imperial College) and a Jasco V-650 (Universitat Politècnica de València) spectrophotometer. Fluorescence measurements in solution were carried out

using Jasco FP-8500 (Universitat Politècnica de València) and Agilent (Varian) Cary Eclipse (Imperial College London) spectrofluorimeters.

For the experiments with gases, a gas mixer was connected to carbon monoxide and argon cylinders to afford CO/Ar mixtures at different ratios. The gases were purged at different flow rates (0 – 200 mL min^{-1}). Carbon monoxide concentrations were measured using an ambient carbon monoxide analyzer (Testo 315-2 model 0632 0317), properly validated with an ISO calibration certificate issued by Instrumentos Testo, Cabrils (Spain). NMR spectroscopy was performed at 25 °C using Bruker AV400 or 500MHz spectrometer at room temperature in $CDCl_3$ unless otherwise stated. ^{1}H NMR and $^{13}C\{^{1}H\}$ NMR chemical shifts (δ) were referenced to the residual non-deuterated solvent signal and the ^{13}C signal of the deuterated solvent respectively. The deuterated solvents were all purchased from Sigma Aldrich. $^{31}P\{^{1}H\}$ NMR chemical shifts were referenced externally to H_3PO_4 85% in H_2O respectively and were all proton decoupled. NMR spectra for air sensitive compounds were recorded under a nitrogen atmosphere with a suitable Young's tap NMR tube.

Cell images were taken using a multiphoton microscope Olympus FVB1000MPE, mounted on a vertical BX61WI motor and equipped with a water immersion objective XPLN25Xwmp with a numerical aperture of 1.05 and a working distance of 2 mm. The microscope was equipped with a tunable pulsed laser (Spectra Physics) in the range of 690 to 1040 nm with an average power of 2.0 W (Microscopy Service of Universitat de València).

Single crystals of **TBTD** were grown via vapor diffusion of hexane onto a solution of the compound in chloroform, while single crystals of **7** and **7·CO** were grown by slow diffusion of ethanol into a dichloromethane solution of the complexes. The crystals were mounted on fibers before data was collected using an Agilent Xcalibur 3 E diffractometer. For further details, see Section S3.

S2 Experimental details for new molecular compounds. Under nitrogen, 5-Bromo-2,1,3-Benzothiadiazole (300 mg, 1.395 mmol) and [Pd(PPh3)4] (240 mg, 0.208 mmol) were dissolved in dry, degassed 1,4-dioxane (25 mL) and the resulting yellow solution was stirred at room temperature for 15 min. A degassed, aqueous solution of Na_2CO_3 (10 mL, 2.0 mol L^{-1}) was then added, and the resulting orange suspension was heated at reflux for 10 min. After the addition of 3-thienylboronic acid (210 mg, 1.640 mmol) in 1,4-dioxane (10 mL), the mixture was left to stir at reflux for 24 h. The resulting brown solution was cooled and washed with deionized water (3 x 30 mL), dried over Na_2SO_4 and filtered. The pale brown solution was freed of volatiles under vacuum. Silica gel column chromatography (98% petroleum ether, 2% ethyl acetate) was then performed to purify the oily brown crude product to afford a bright yellow solid (140 mg, 46%). IR (ν_{max}/cm^{-1}): 3095, 2958, 1723, 1607, 1515, 1270, 1187, 1148, 1072, 890, 847. ^{1}H NMR ($CDCl_3$): δ_H 7.50 (dd, J_{HH} = 5.1, 2.9 Hz, 1H, thienyl-CH), 7.55 (dd, J_{HH} = 5.1, 1.4 Hz, 1H, thienyl-CH), 7.68 (m, 1H, thienyl-CH), 7.94 (dd, J_{HH} = 9.1, 1.7 Hz, 1H, C_6H_3-CH), 8.05 (d, J_{HH} = 9.1 Hz, 1H, C_6H_3-CH), 8.20 (m, 1H, C_6H_3-CH) ppm. $^{13}C\{^1H\}$ NMR ($CDCl_3$): δ_C 155.5, 154.1, 140.7, 136.9 (s x 4, C-quaternary), 129.7, 127.1, 126.3, 122.4, 121.6, 117.3 (s x 6, C-H) ppm. MS (ES +ve) m/z (abundance): 218 (100) $[M]^+$. Calculated for $C_{10}H_6N_2S_2$: C 55.0, H 2.8, N 12.8%. Found: C 55.2, H 2.7, N 12.7%.

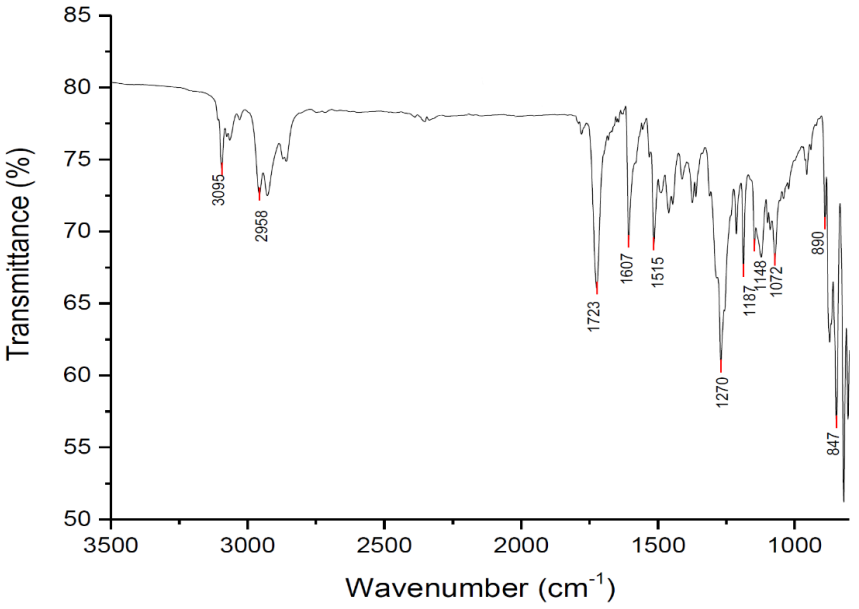

Figure S2-1. Solid state IR spectrum of TBTD.

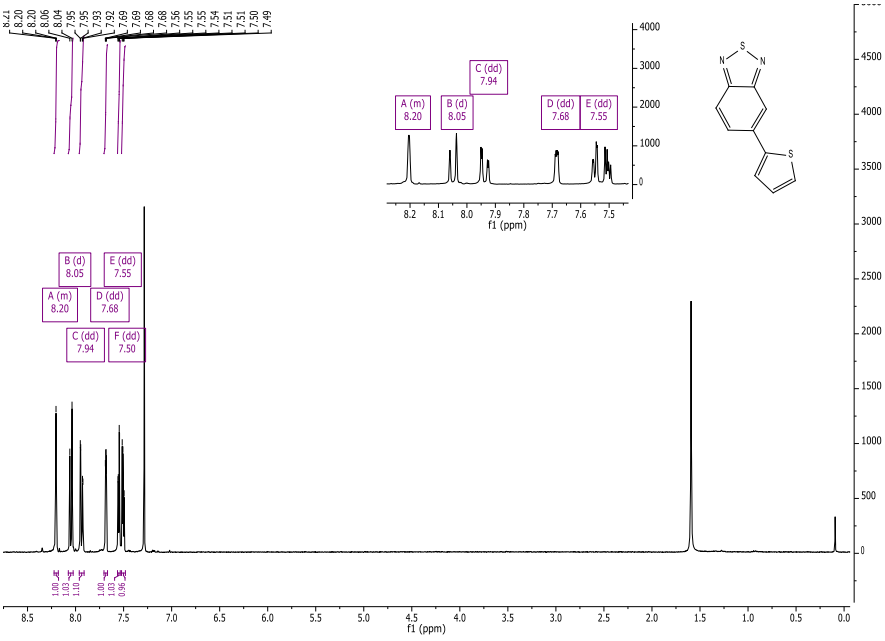

Figure S2-2. ^{1}H NMR spectrum ($CDCl_3$) of TBTD.

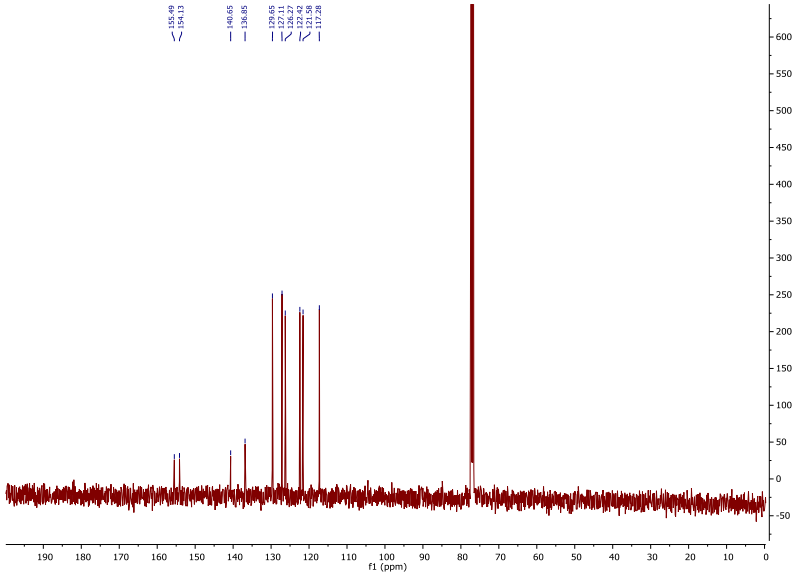

Figure S2-3. $^{13}C\{^{1}H\}$ NMR spectrum ($CDCl_3$) or TBTD.·

4-ethynylbenzyl-O-[2-(2-Methoxyethoxy)ethoxy]ethanoate (HC≡CL)

Under a nitrogen atmosphere, 2-[2-(2-methoxyethoxy)ethoxy]acetic acid (**2**, 623 µL, 723 mg, 4.06 mmol) was dissolved in dry, degassed dichloromethane (25 mL) and the solution was cooled to 0 °C with an ice bath. *N,N'*-dicyclohexylcarbodiimide [DCC] (838 mg, 4.06 mmol) was added as a dichloromethane solution (10 mL). A second dichloromethane (25 mL) solution of 4-ethynylbenzyl alcohol (**1**, 537 mg, 4.06 mmol) and 4-dimethylaminopyridine [DMAP] (94 mg, 0.77 mmol) was slowly added dropwise via a cannula, resulting in a cloudy yellow mixture. After the addition, the reaction mixture was stirred for 1 hour at 0 °C and then at room temperature overnight. Successively, the mixture was filtered through Celite in order to remove the resulting insoluble salts and the yellow filtrate was freed of volatiles under vacuum to provide the desired product as a pale yellow oil (405 mg, 34%). IR (ν_{max}/cm^{-1}): 1752 (C=O), 1196, 1104, 847, 821. ^{1}H NMR ($CDCl_3$): δ_H 3.11 (s, C≡CH), 3.39 (s, 3H, OMe), 3.56, 3.66, 3.71, 3.77 (m x 4, 4 x 2H, OCH_2), 4.23 (s, 2H, $OC\underline{H}_2C_6H_4$), 5.20 (s, 2H, $C(=O)CH_2$), 7.33, 7.50 (AB, J_{AB} = 8.0 Hz, 4H, C_6H_4) ppm. $^{13}C\{^{1}H\}$ NMR ($CDCl_3$): δ_C 170.3 (s, C=O), 136.1 (s, $C^{1/4}$-

C_6H_4) 132.3, 128.2 (s x 2, $C^{2/3}$-C_6H_4), 122.2 (s, $C^{1/4}$-C_6H_4), 83.2 (s, HC≡*C*), 77.8 (s, H*C*≡C), 71.9, 70.9, 70.7, 70.6 (s x 4, OCH_2), 68.7 (C(=O)*C*H_2), 65.9 (s, O*C*$H_2C_6H_4$), 59.1 (OCH_3) ppm. MS (ES +ve) *m/z* (abundance): 293 (10) $[M + H]^+$, 310 (70) $[M + H_2O]^+$, 315 (100) $[M + Na]^+$. HRMS: 315.1208 (calculated), 312.1200 (found) corresponding to $C_{16}H_{20}O_5Na$. Calculated for $C_{16}H_{20}O_5$: C 65.7, H 6.9%. Found: C 65.8, H 6.7%.

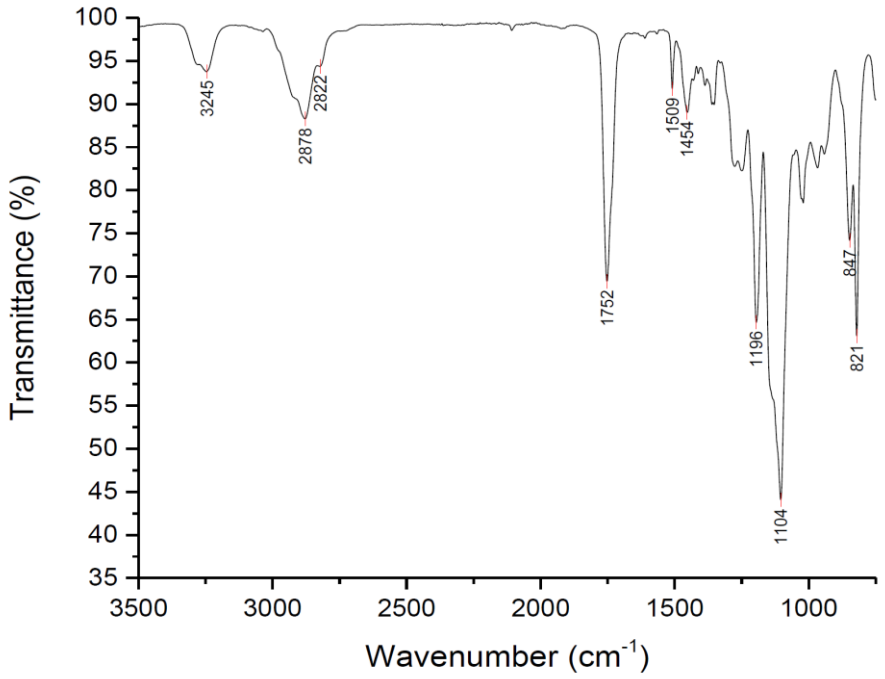

Figure S2-4. IR spectrum of HC≡Cl.

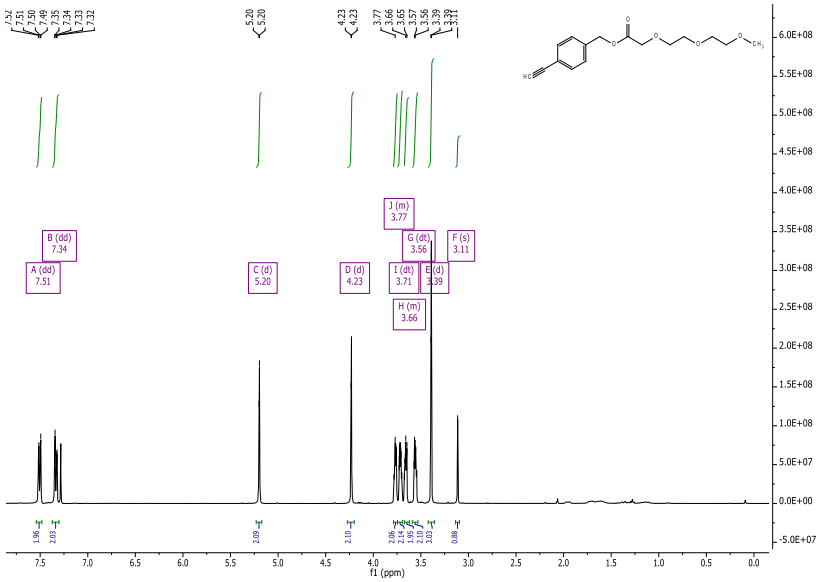

Figure S2-5. ^{1}H NMR spectrum ($CDCl_3$) of HC≡Cl.

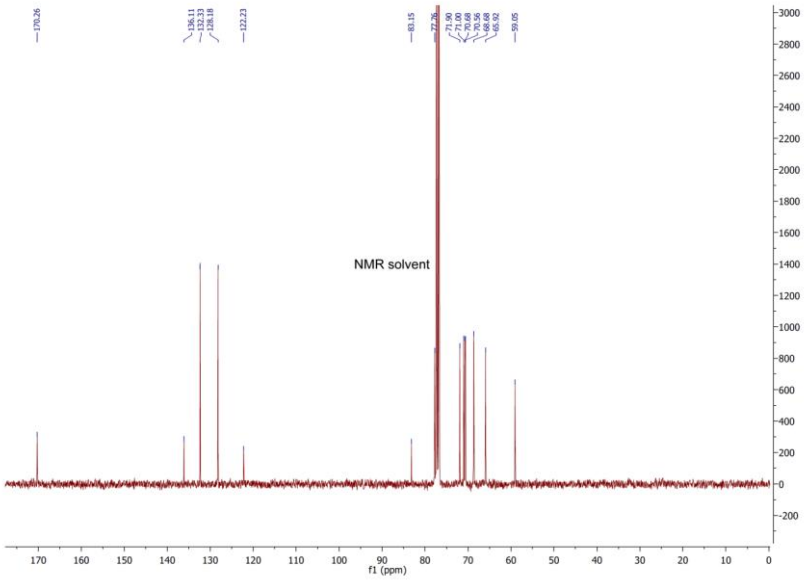

Figure S2-6. $^{13}C\{^{1}H\}$ NMR spectrum ($CDCl_3$) of HC□CL.

[Ru(CH=CHL)Cl(CO)(TBTD)(PPh_3)$_2$] (6)

Under nitrogen, [RuH(CO)($NCMe$)$_2$(PPh_3)$_2$]BF_4 (**4**, 120 mg, 0.146 mmol) was dissolved in dry, degassed dichloromethane (10 mL). To this was added HC≡CL (54 µL, 50 mg, 0.17 mmol) and the resulting pale yellow solution was stirred for 10 min. Then, [Et_4N]Cl (37 mg, 0.22 mmol) was added as a methanolic solution (3 mL) and the mixture was vigorously stirred for 15 minutes at 40 °C. All solvent was removed under reduced pressure (vacuum line) and dry, degassed dichloromethane (5 mL) was then added to dissolve the orange solid. In order to remove insoluble inorganic salts, the bright orange solution was filtered by cannula and a dry, degassed dichloromethane (5 mL) solution of TBTD (37 mg, 0.17 mmol) was added to afford a dark red solution, which was stirred for 15 min. at room temperature. The solvent was removed under vacuum and the red solid was recrystallized from a mixture of diethyl ether (3 mL) and petroleum ether (4 mL), filtered and dried (148 mg, 84%). The use of nitrogen in this procedure is as a precaution. Neither **4** nor **6** are unstable to air or moisture as solids or in solution, however the product obtained under anaerobic conditions is slightly more pure than when prepared in air. IR (ν_{max}/cm^{-1}): 1919 (CO), 1748 (C=O), 1545, 1481, 1433, 1194, 1082, 855. ^{1}H NMR (acetone-d_6): δ_H 3.29 (s, 3H, OMe), 3.49, 3.57, 3.63, 3.69 (m x 4, 4 x 2H, OCH_2), 4.18 (s, 2H, $OC\underline{H}_2C_6H_4$), 5.07 (s, 2H, $C(=O)CH_2O$), 5.96 (d, J_{HH} = 16.3 Hz, 1H, Hβ), 6.90 (d, J_{HH} = 7.8 Hz, 2H, C_6H_4), 7.18 (m, 12H, C_6H_5), 7.30 (m, 6H + 2H, C_6H_5 + C_6H_4), 7.54 (m, 12H, C_6H_5), 7.71 − 7.77 (m, 2H, TBTD), 7.95 (s(br), 1H, TBTD), 8.07 – 8.13 (m, 2H, TBTD), 8.38 (s(br), 1H, TBTD), 8.88 (dt, J_{HH} = 16.3 Hz, J_{HP} = 3.3 Hz, 1H, Hα) ppm. $^{31}P\{^1H\}$ NMR (Acetone-d_6): δ_P 25.4 (s, PPh_3) ppm. MS (ES +ve) *m/z* (abundance): 1218 (3) $[M + H_2O]^+$, 988 (100) $[M – TBTD]^+$. Calculated for $C_{63}H_{57}ClN_2O_6P_2RuS_2$: C 63.0, H 4.8, N 2.3%. Found: C 62.9, H 4.7, N 2.4%.

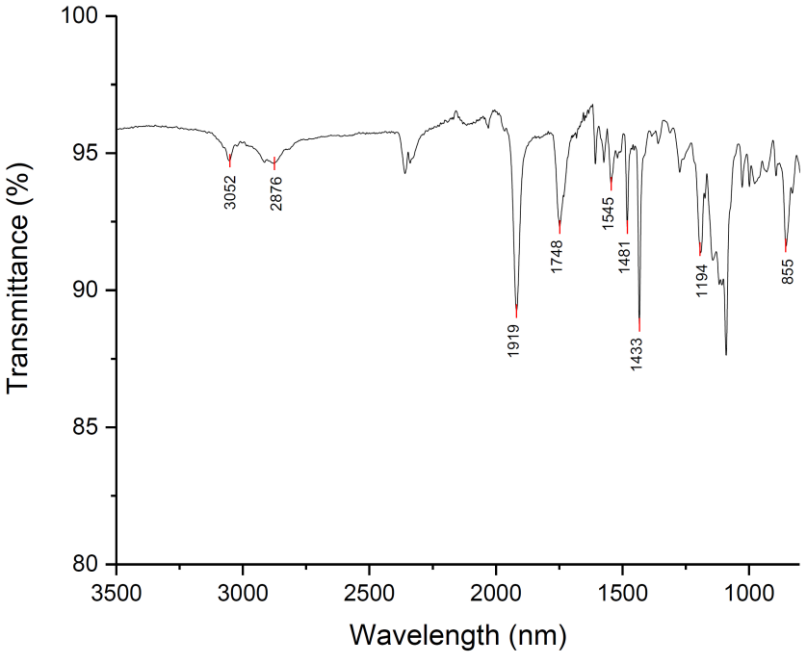

Figure S2-7. Solid state IR spectrum of compound **6**.

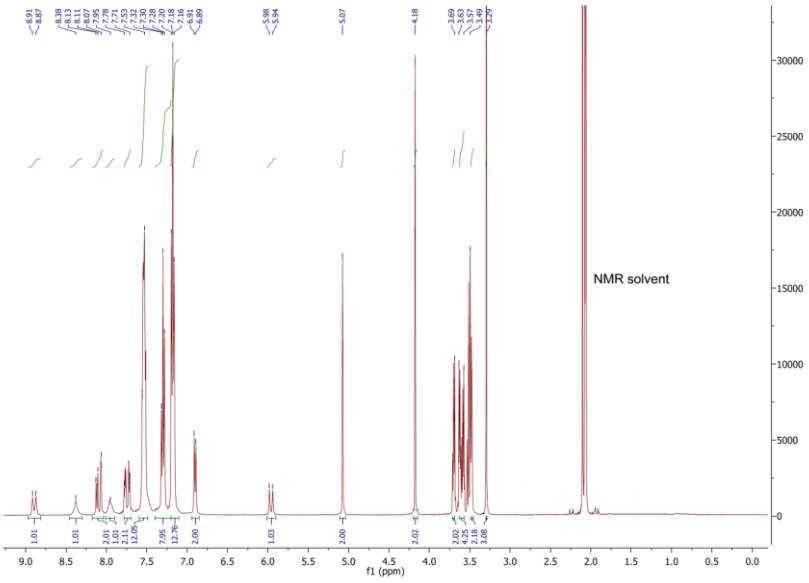

Figure S2-8. ^{1}H NMR spectrum (d_6-acetone) of compound **6**.

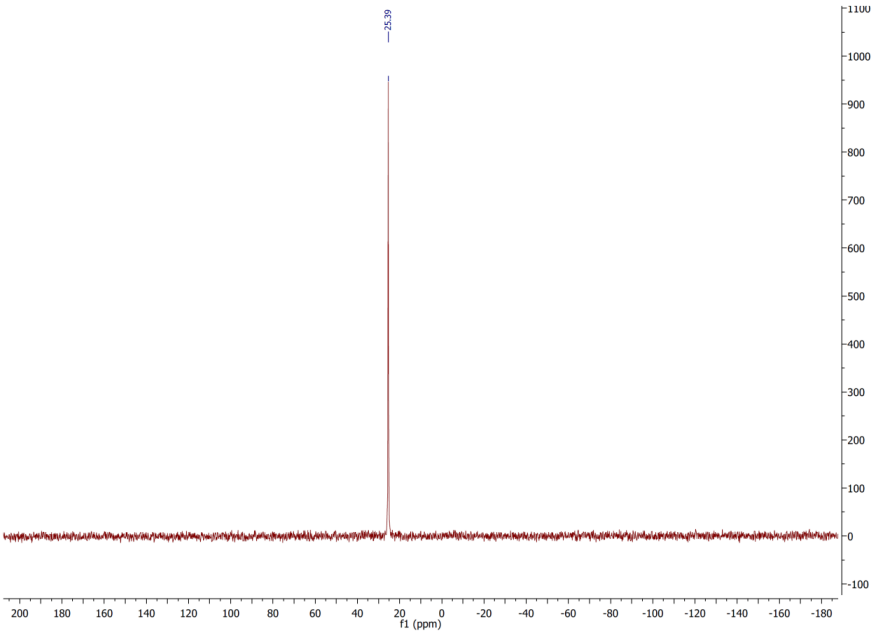

Figure S2-9. $^{31}P\{^{1}H\}$ NMR spectrum (d_6-acetone) of compound **6**.

[Ru(CH=CHL)Cl(CO)$_2$(PPh$_3$)$_2$] (6·CO)

Compound **6·CO** was prepared by treating an acetone solution (5 mL) of **6** (20.0 mg, 0.017 mmol) with carbon monoxide until the dark red solution became pale yellow. After the complete removal of the solvent under vacuum, the compound was dissolved in the minimum amount of acetone, followed by the addition of a diethyl ether (1 mL) and petroleum ether (4 mL) which resulted in the precipitation of an off-white solid, which was washed with cold petroleum ether (5 mL) and dried. Yield: 15.7 mg (93%). IR (ν_{max}/cm^{-1}): 2029 (CO), 1967 (CO), 1750 (C=O), 1482, 1434, 1193, 1091. ^{1}H NMR (acetone-d_6): δ_H 3.29 (s, 3H, OMe), 3.48, 3.58, 3.63, 3.71 (m x 4, 4 x 2H, OCH_2), 4.19 (s, 2H, $OC\underline{H}_2C_6H_4$), 5.10 (s, 2H, $C(=O)CH_2O$), 5.96 (d, J_{HH} = 18.0 Hz, 1H, Hβ), 6.86, 7.19 (AB, J_{AB} = 7.9 Hz, 4H, C_6H_4), 7.40 – 7.49 (m, 18H, C_6H_5), 7.74 – 7.79 (m, 12H, C_6H_5), 7.80 (dt, J_{HH} = 18.0 Hz, J_{HP} = 3.5 Hz, 1H, Hα) ppm. $^{31}P\{^{1}H\}$ NMR (acetone-d_6): δ_P 23.0 (s, PPh_3) ppm. MS (ES +ve) *m/z* (abundance): 1016 (100) $[M - Cl + MeCN]^+$. Calculated for $C_{54}H_{51}ClO_7RuP_2$: C 64.2, H 5.1%. Found: C 64.3, H 5.2%.

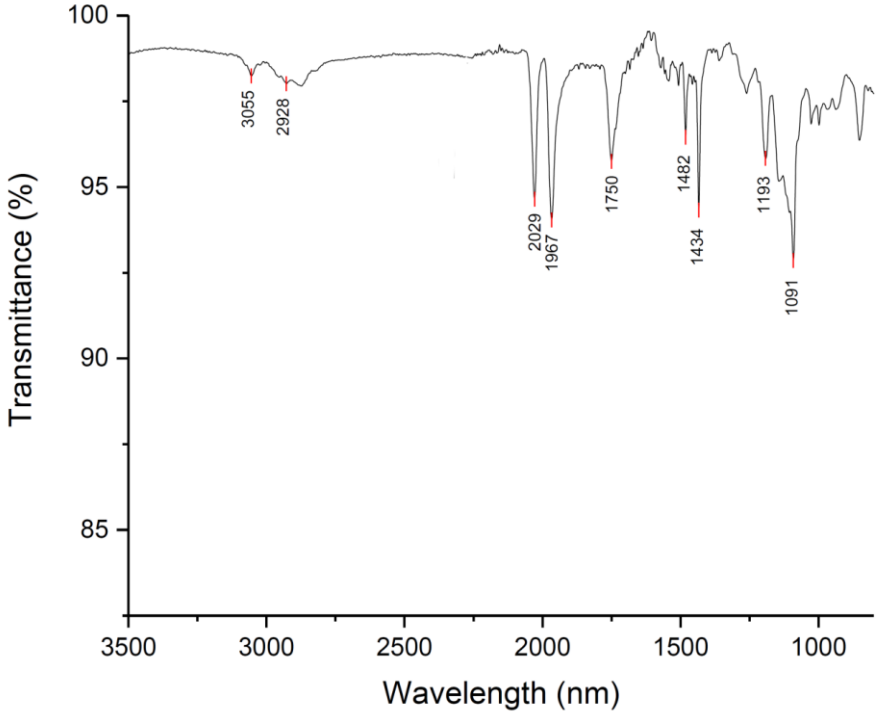

Figure S2-10. Solid state IR spectrum of compound **6·CO**.

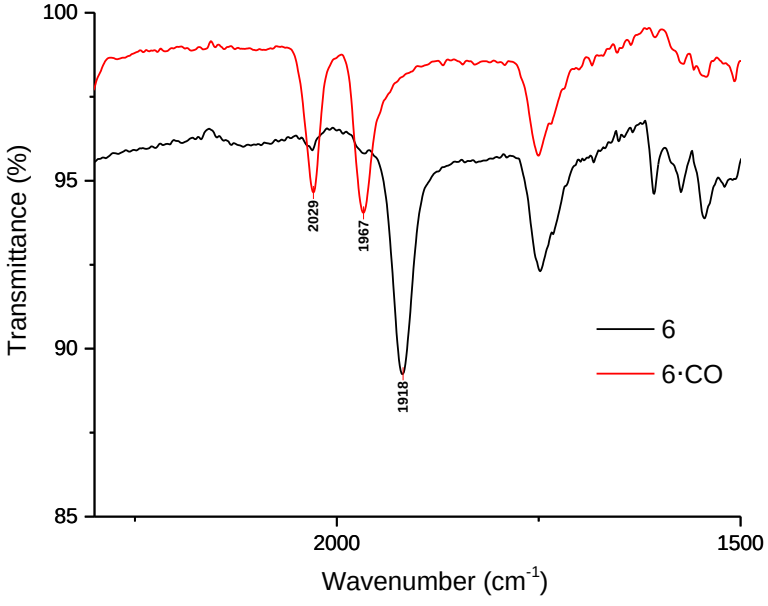

Figure S2-11. Solid state IR spectra of compounds **6** and **6·CO**.

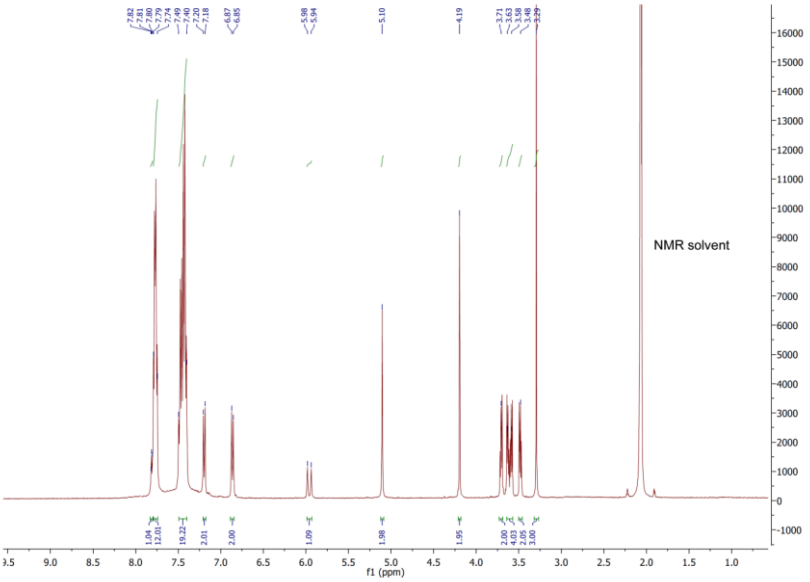

Figure S2-12. ^{1}H NMR spectrum (d_6-acetone) of compound **6·CO**.

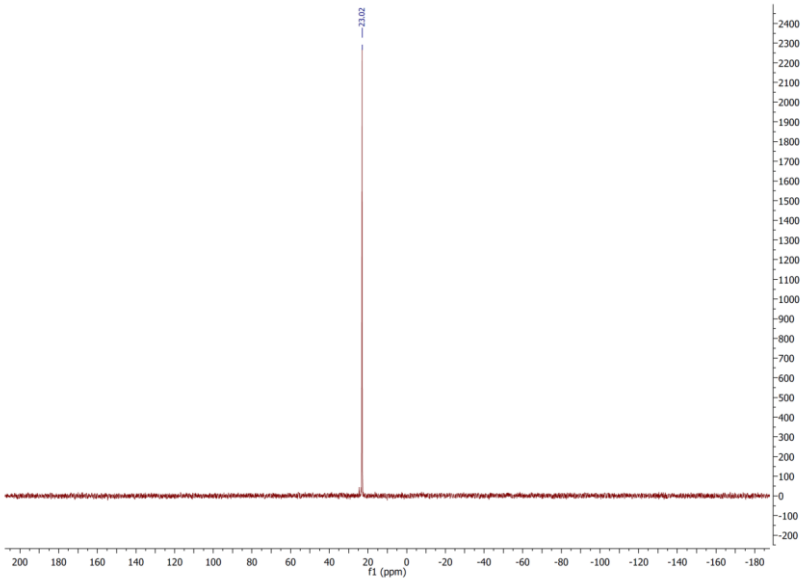

Figure S2-13. $^{31}P\{^{1}H\}$ NMR spectrum (d_6-acetone) of compound **6·CO**.

[Ru(CH=CHPhen-9)Cl(CO)(TBTD)(PPh_3)$_2$] (7)

A dichloromethane solution (10 mL) of [Ru(CH=CHPhen-9)Cl(CO)(PPh_3)$_2$] (50.0 mg, 0.056 mmol) was treated with a slight excess of TBTD (13.4 mg, 0.061 mmol). The reaction mixture was then stirred at room temperature for 30 min. The solvent was removed under vacuum and diethyl ether (10 mL) was added to the crude product. The resulting red solid was triturated for 10 min. and then filtered and dried (41.0 mg, 66%). IR (ν_{max}/cm^{-1}): 1912 (CO), 1609, 1544 (C=C), 1481, 1432, 1089. ^{1}H NMR (CD_2Cl_2): δ_H 6.85 (d, J_{HH} = 15.5 Hz, 1H, Hβ), 7.15 (s, 1H, phenanthrenyl), 7.18 – 7.22, 7.31 – 7.35 (m x 2, 18H, PPh_3), 7.45 (m, 1H, phenanthrenyl), 7.54 – 7.67 (m, 12H + 4H + 2H, PPh_3 + phenanthrenyl + TBTD), 7.76 (m, 1H, TBTD), 7.89 (m, 2H, TBTD), 8.30 (s(br), 1H, TBTD), 8.61 (m, 1H, phenanthrenyl), 8.68 (d, J_{HH} = 7.9 Hz, 1H, phenanthrenyl), 8.93 (dt, J_{HH} = 15.5 Hz, J_{HP} = 3.1 Hz, 1H, Hα) ppm. ^{31}P{^{1}H} NMR (CD_2Cl_2): δ_P 26.6 (s, PPh_3) ppm. MS (ES +ve) *m/z* (abundance): 1111 (5) [M]$^+$. Calculated for $C_{63}H_{47}ClN_2OP_2RuS_2 \cdot 0.25CH_2Cl_2$: C 67.1, H 4.2, N 2.5%. Found: C 67.2, H 4.1, N 2.9%.

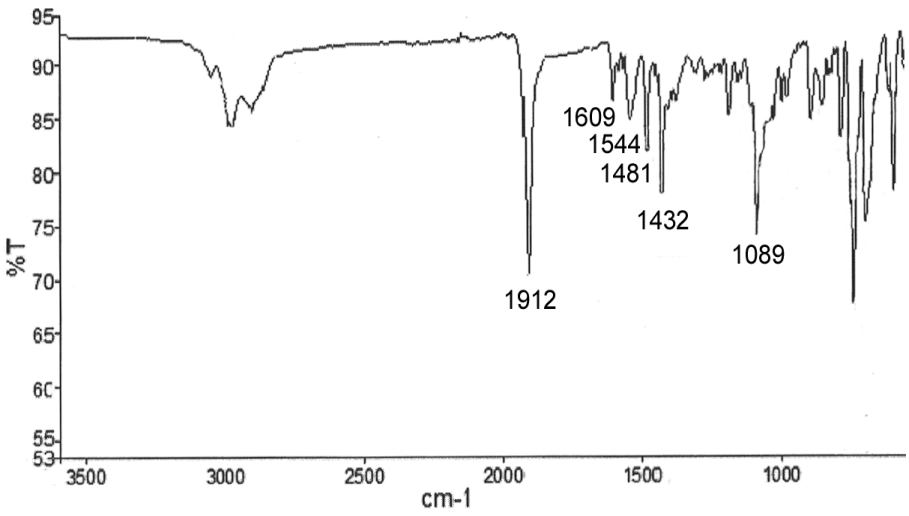

Figure S2-14. Solid state IR spectrum of compound **7**.

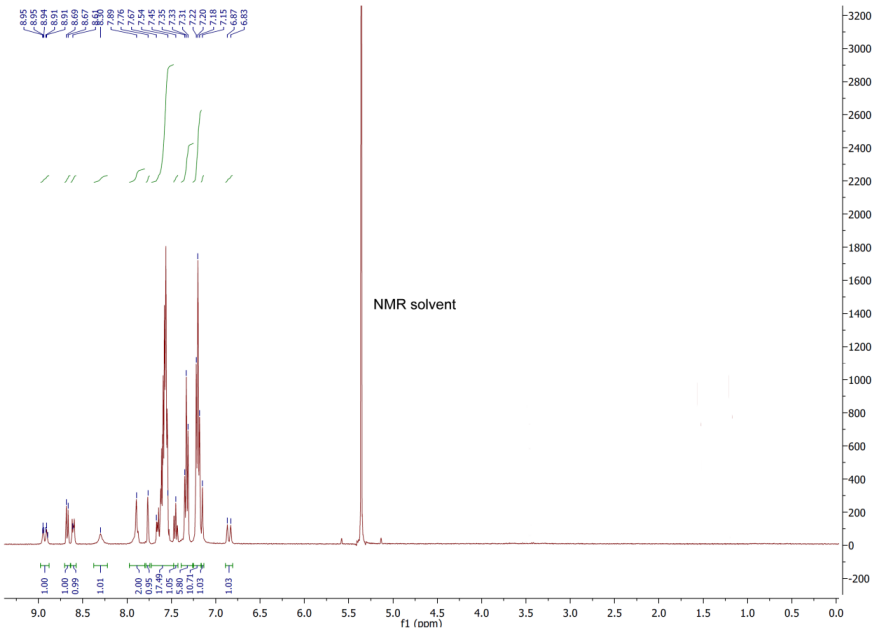

Figure S2-15. ^{1}H NMR spectrum (CD_2Cl_2) of compound **7**.

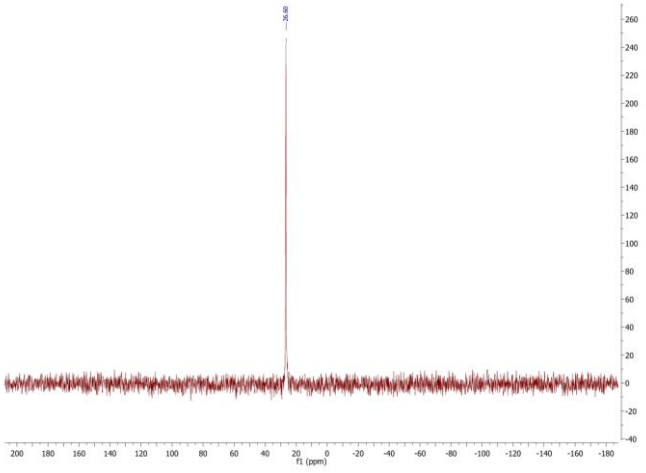

Figure S2-16. $^{31}P\{^{1}H\}$ NMR spectrum (CD_2Cl_2) of compound **7**.

Isolation of TBTD from probe 6

In order to further confirm that CO displaces the TBTD ligand, carbon monoxide gas CO gas was bubbled through a solution of probe **6** (30 mg in 2 mL of DCM) for

30 seconds. The solvent was then removed and the orange residue was then triturated with methanol and then filtered. This produced TBTD as a light yellow powder (4 mg, 73% yield).

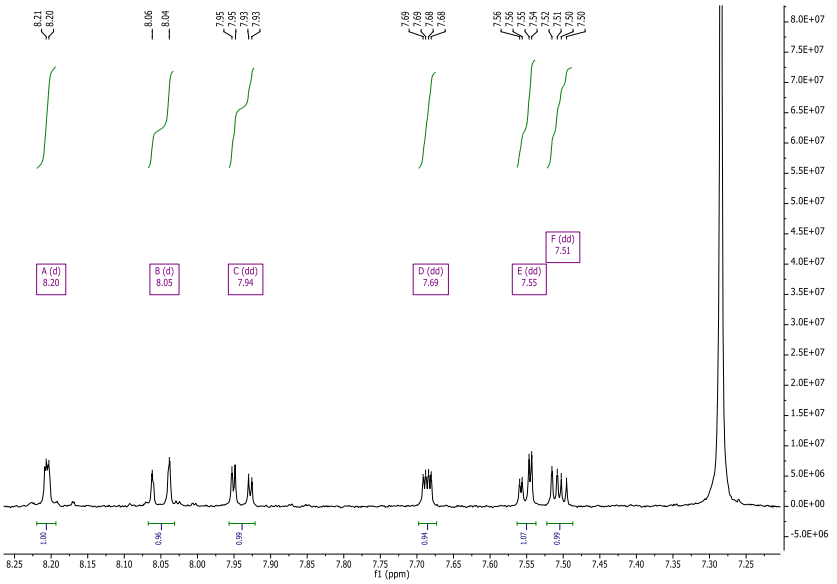

Figure S2-17. ^{1}H NMR spectrum of **TBTD** isolated on passing CO through a solution of compound **6**.

S3 Crystallography

The X-ray crystal structure of TBTD

Crystal data for **TBTD**: $C_{10}H_6N_2S_2$, M = 218.29, monoclinic, $P2_1/c$ (no. 14), a = 11.3068(9), b = 7.0845(5), c = 23.268(2) Å, β = 96.544(8)°, V = 1851.7(3) Å^3, Z = 8 (two independent molecules), D_c = 1.566 g cm^{-3}, μ(Mo-Kα) = 0.528 mm^{-1}, T = 173 K, pale yellow blocky needles, Agilent Xcalibur 3 E diffractometer; 3736 independent measured reflections (R_{int} = 0.0236), F^2 refinement,[S14] R_1(obs) = 0.0513, wR_2(all) = 0.1283, 2900 independent observed absorption-corrected reflections [$|F_o| > 4\sigma(|F_o|)$, $2\theta_{max}$ = 56°], 295 parameters. CCDC 1498392.

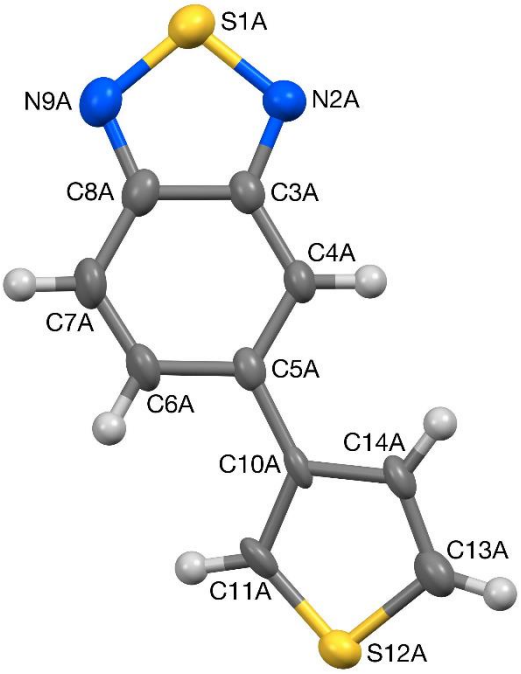

Figure S3-1. The structure of one (**TBTD-A**) of the two independent molecules present in the crystal of **TBTD** (50% probability ellipsoids). Selected bond lengths (Å), bond angles (°) and torsion angles (°): S(1A)-N(2A) 1.612(3), S(1A)-N(9A) 1.617(3), N(2A)-C(3A) 1.356(4), C(8A)-N(9A) 1.348(4), C(4A)-C(5A) 1.378(4), C(6A)-C(7A) 1.348(4), N(2A)-S(1A)-N(9A) 101.17(14), C4A-C5A-C10A-C14A 22.00.

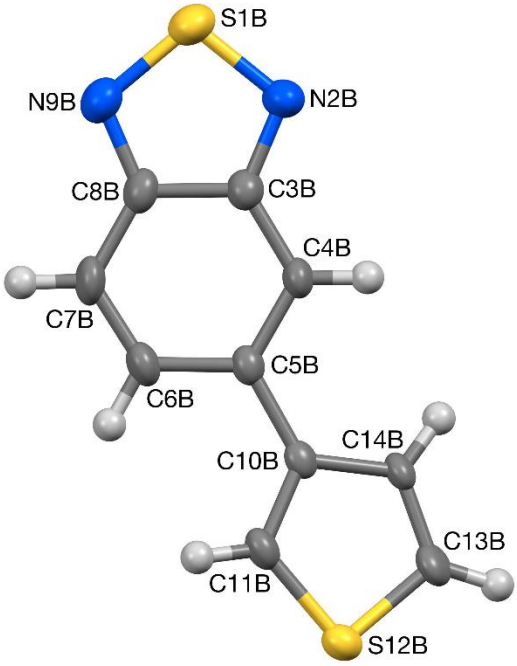

Figure S3-2. The structure of one (**TBTD-B**) of the two independent molecules present in the crystal of **TBTD** (50% probability ellipsoids). Selected bond lengths (Å), bond angles (°) and torsion angles (°): S(1B)-N(9B) 1.612(3), S(1B)-N(2B) 1.613(3), N(2B)-C(3B) 1.352(4), C(8B)-N(9B) 1.352(4), C(4B)-C(5B) 1.375(4), C(6B)-C(7B) 1.352(4), N(9B)-S(1B)-N(2B) 101.16(13), C4B-C5B-C10B-C14B 20.86.

The crystal structure of **TBTD** was found to contain two independent molecules (**TBTD-A** and **TBTD-B**), and in each molecule the C10-based thiophene unit was found to be disordered. In both instances two orientations were identified, of *ca*. 64:36 and 88:12% occupancy for molecules **A** and **B** respectively. The geometries of all four orientations were optimized, the thermal parameters of adjacent atoms were restrained to be similar, and only the non-hydrogen atoms of the major occupancy orientations were refined anisotropically (those of the minor occupancy orientations were refined isotropically).

The X-ray crystal structure of Compound 7

Crystal data for **7**: $C_{63}H_{47}ClN_2OP_2RuS_2 \cdot 3(CH_2Cl_2)$, M = 1365.38, triclinic, P-1 (no. 2), a = 12.1009(4), b = 14.7925(6), c = 17.7731(5) Å, α = 76.557(3), β = 82.335(2), γ = 85.440(3)°, V = 3062.73(18) Å^3, Z = 2, D_c = 1.481 g cm^{-3}, μ(Cu-Kα) = 6.367 mm^{-1}, T = 173 K, red blocks, Agilent Xcalibur PX Ultra A diffractometer; 11722 independent measured reflections (R_{int} = 0.0248), F^2 refinement, [S14] R_1(obs) = 0.0433, wR_2(all) = 0.1210, 10263 independent observed absorption-corrected reflections [$|F_o| > 4\sigma(|F_o|)$, $2\theta_{max}$ = 148°], 770 parameters. CCDC 1498393.

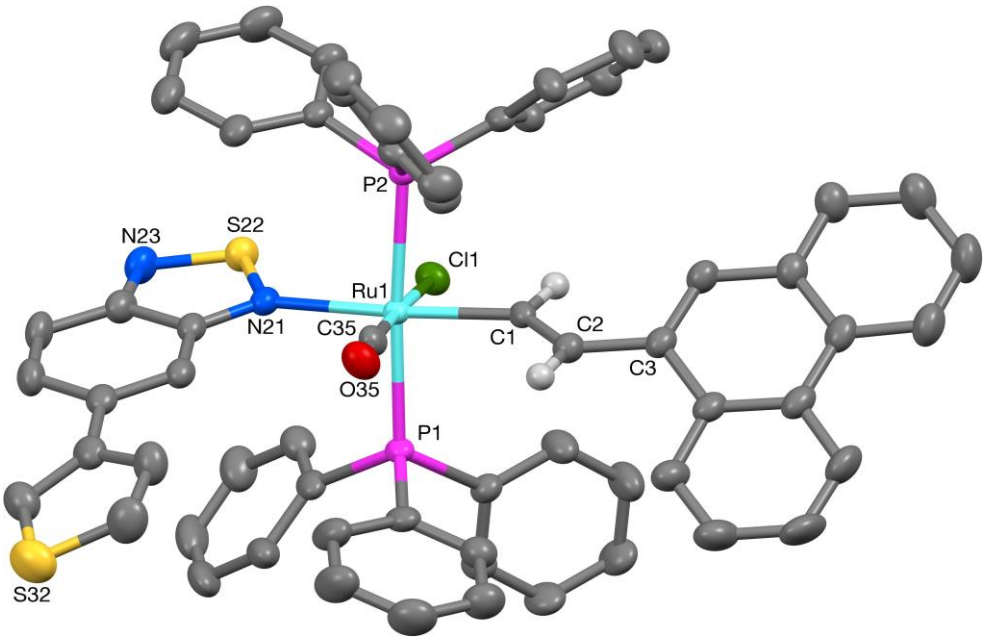

Figure S3-3. The crystal structure of **7** (50% probability ellipsoids). Selected bond lengths (Å), bond angles (°) and torsion angles (°): Ru(1)-C(35) 1.824(3), Ru(1)-C(1) 2.055(3), Ru(1)-N(21) 2.235(3), Ru(1)-(P1) 2.3998(8), Ru(1)-P(2) 2.4204(8), Ru(1)-Cl(1) 2.4657(8), C(1)-C(2) 1.335(5); P(1)-Ru(1)-P(2) 176.25(3), Ru(1)-C(1)-C(2) 134.2(2).

The C80- and C90-based dichloromethane solvent molecules in the structure of **7** were both found to be disordered; for the former, two orientations were identified of *ca*. 78 and 22% occupancy, whilst for the latter, three orientations

were identified of *ca*. 68, 19 and 13% occupancy. The geometries of all five orientations were optimized, the thermal parameters of adjacent atoms were restrained to be similar, and only the non-hydrogen atoms of the major occupancy orientations were refined anisotropically (those of the minor occupancy orientations were refined isotropically).

The X-ray crystal structure of compound 7·CO

Crystal data for **7·CO**: $C_{54}H_{41}ClO_2P_2Ru{\cdot}CH_2Cl_2$, M = 1005.25, triclinic, P-1 (no. 2), a = 10.4363(5), b = 14.9450(8), c = 15.1451(8) Å, α = 82.763(4), β = 77.136(4), γ = 88.273(4)°, V = 2284.6(2) Å^3, Z = 2, D_c = 1.461 g cm^{-3}, μ(Mo-Kα) = 0.632 mm^{-1}, T = 173 K, colorless tabular needles, Agilent Xcalibur 3 E diffractometer; 8946 independent measured reflections (R_{int} = 0.0275), F^2 refinement,[S14] R_1(obs) = 0.0348, wR_2(all) = 0.0780, 7592 independent observed absorption-corrected reflections [$|F_o| > 4\sigma(|F_o|)$, $2\theta_{max}$ = 56°], 569 parameters. CCDC 1498394.

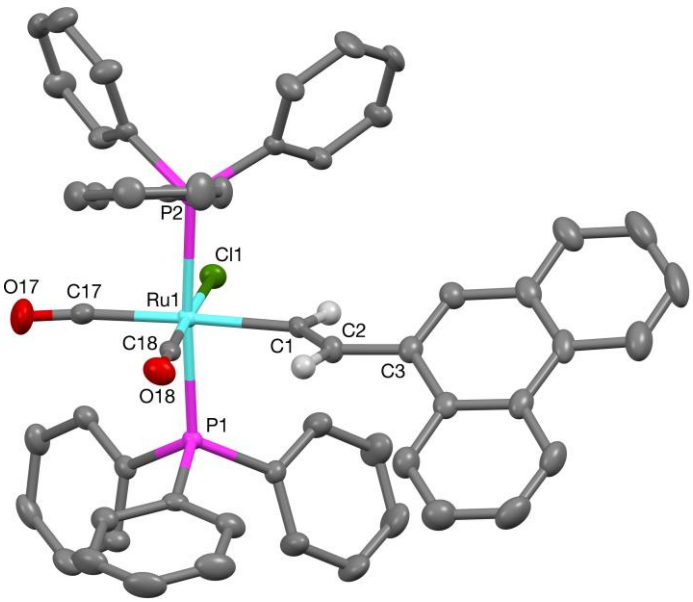

Figure S**3-4.** The crystal structure of **7·CO** (50% probability ellipsoids). Selected bond lengths (Å), bond angles (°) and torsion angles (°): Ru(1)-C(18) 1.849(3), Ru(1)-C(17)

1.965(3), Ru(1)-C(1) 2.120(3), Ru(1)-P(1) 2.4011(6), Ru(1)-P(2) 2.4112(6), Ru(1)-Cl(1) 2.4703(6), C(1)-C(2) 1.334(3), P(1)-Ru(1)-P(2) 175.83(2), C(2)-C(1)-Ru(1) 130.76(19).

S4 *Selectivity and stability studies*

S4.1 Carbon monoxide selectivity studies

The fluorescence emission of probe **6** (10^{-4} M solution in 0.1% acetone/PBS solution, PBS = phosphate-buffered saline) in the presence of tryptophan (10^{-4} M) imidazole (10^{-4} M), NO_x (50 ppm) and CO (200 ppm) was measured. The experiments were performed by adding 20 µL of 0.15 M solutions of tryptophan and imidazole in PBS buffer to a 10^{-4} M solution of probe **6.** In the case of NO_x, the gas was generated *in situ* and then bubbled through a solution of the complex without any further purification. The results obtained after addition of 50 ppm NO_x, 200 ppm CO and 100 µM of tryptophan and imidazole are shown in Figure S4-1 (left).

The fluorescence emission response (at 500 nm) of probe **6** (10^{-4} M solution in 0.1% acetone/PBS solution) was then determined in the presence of further range of small molecules and biologically relevant species (ROS and RNS) at a concentration of 100 µM. Figure S4-1 (right) shows data for (1) $OH^{\cdot}$; (2) $MeO^{\cdot}$; (3) $O_2^{\bullet-}$; (4) H_2O_2; (5) ClO^{-}; (6) SO_3^{2-}; (7) citric acid; (8) citrate; (9) ascorbic acid; (10) glutathione; (11) cysteine; (12) bovine serum albumin (BSA); (13) tryptophan; (14) imidazole; (15) NO_x; (16) CO.

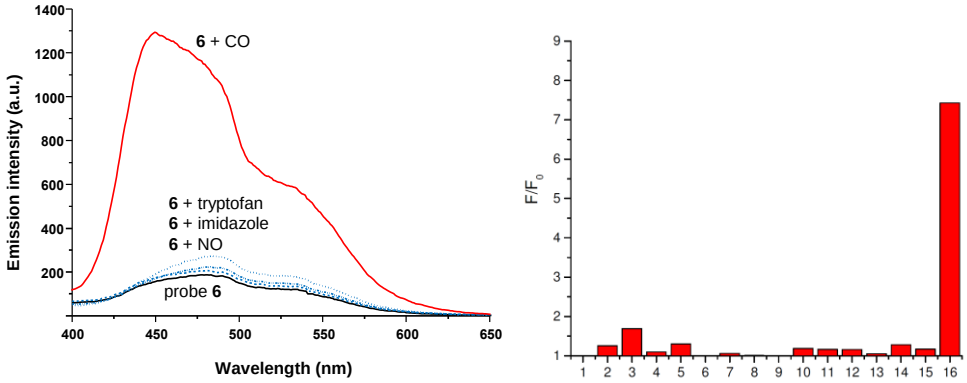

Figure S4-1. Fluorescence emission spectra (above) of complex **6** alone and in the presence of tryptophan, imidazole, nitric oxide, CO and (below) the fluorescence response of complex **6** in the presence of the interferents listed above.

S4.2 Solution and UV stability profiles for Probe 6

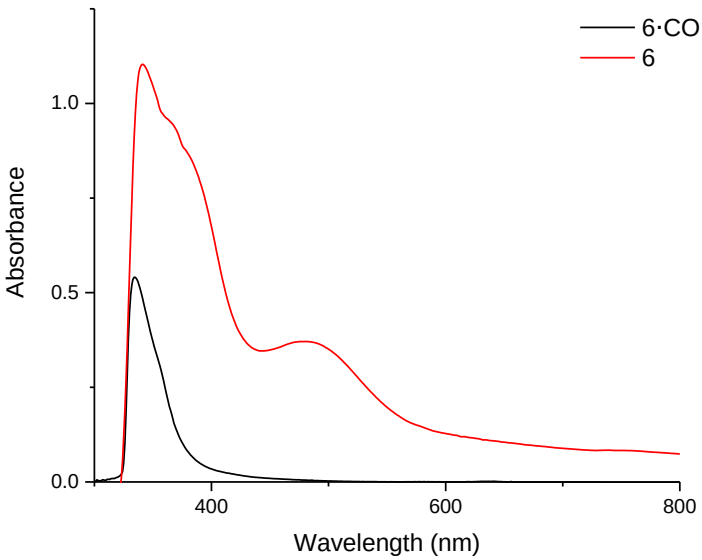

Figure S4-2. Absorption Spectra of **6** and **6·CO**.

The solution stability and photostability of probe **6** (10^{-4} M solution in 0.1% acetone/PBS solution PBS = phosphate buffered saline) were explored by

measuring the fluorescence intensities at 500 nm every 2 minutes for 60 minutes in the absence [■] or presence of UV-irradiation (●) (365 nm). Data are presented in Figure S4-4.

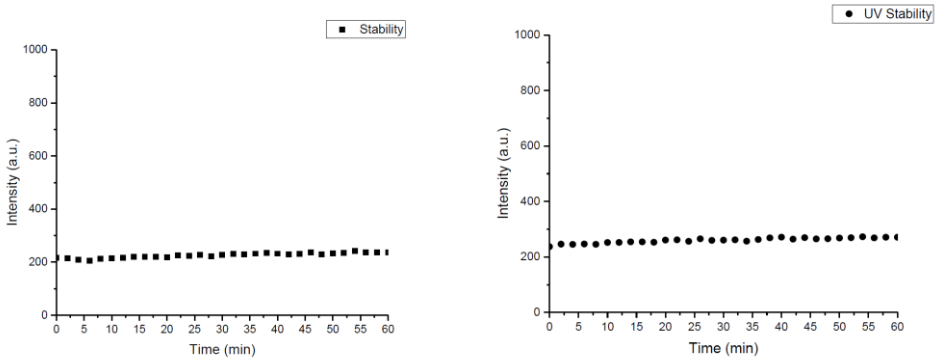

Figure S4-3. Solution stability (left) and photostability in the presence of UV irradiation (right) of probe **6**.

S4.3 Stability of probe 6 in the presence of BSA, cysteine and peroxide

Stability profiles of probe **6** (10^{-4} M solution in 0.1% acetone/PBS solution) in the presence of bovine serum albumin (BSA) (100 μM) [■], in the presence of cysteine (100 μM) (●) and in the presence of H_2O_2 (100 μM) (▲) were measured. The probe was excited at 365 nm and fluorescence intensities at 500 nm were monitored in 5 minute intervals for 60 minutes to generate the data shown in Figure S4-4 below.

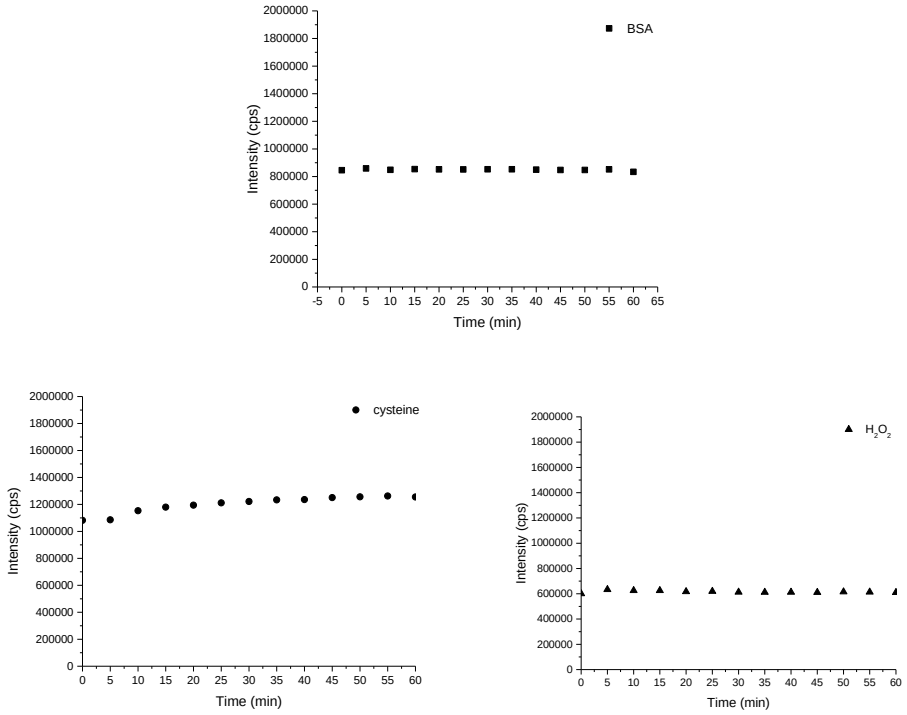

Figure S4-4. Stability of probe 6 in the presence of BSA (top), cysteine (bottom, left) and hydrogen peroxide (bottom, right) measured through the fluorescence intensity at 500 nm.

S5 Cytotoxicity and confocal microscopy studies

S5.1 MTT assay

The MTT assay is a colorimetric test that assesses the reduction of the cell viability (balance between living and dead cells) over time, when the cells are incubated with the tetrazolium salt 3-(4,5-dimethylthiazolyl-2)-2,5-diphenyltetrazolium bromide (MTT). This assay involves the reduction of MTT by mitochondrial dehydrogenase. During this process, the yellow MTT is reduced to the purple formazan by metabolically active cells (living cells), whereas it is not internalized and metabolized by death cells. The resulting intracellular purple product, which can be spectrophotometrically quantified, indicates the degree of

cell viability in the presence of different concentrations of the compounds. The viability test was performed in 96-well plates where RAW 264.7 cells were placed at a density of 250,000 cells per well. The cells were incubated with hemin at 100 µM at different times and with probe **6** for the final 30 minutes.

The RAW 264.7 murine macrophages cells were routinely grown in the Pharmacology Department (Faculty of Pharmacy) at the Universitat de València in a DMEM (Dulbecco's Modified Eagle's Medium)/Nutrient Mixture F-12 Ham containing 10% fetal calf serum (FCS), and 1% penicillin/streptomycin purchased from Sigma Aldrich. The maintenance of the cell culture was carried out according to standard protocols provided by the European Collection of Authenticated Cell Cultures (ECACC). Cells were incubated with hemin solution at a final concentration of 100 µM for 30 min, 3 or 6 h. Then, the medium was gently aspirated and cells washed with PBS. Fresh medium was added and cells were treated with 10 µM of probe **6** for 30 minutes. After further washing, 200 µL of a solution of MTT (0.1 mg mL^{-1}) in fresh medium were added and the cells were incubated for 45 min at 37 ° C. Finally, the medium was aspirated and 200 µL of DMSO were added to measure the absorbance of each well at 492 nm using a 96-well multiwell-plate reader Wallac 1420 VICTOR2^{TM} (Perkin Elmer).

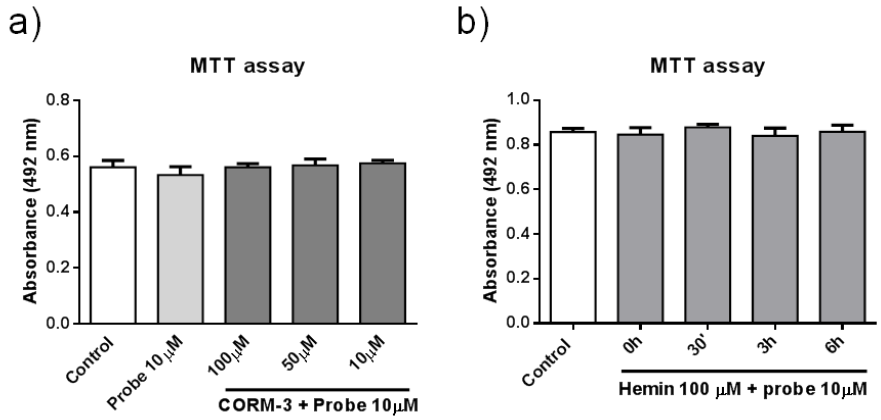

Figure S5-1. Cell viability determined in RAW 264.7 mouse macrophages after (a) CORM-3 treatment at 100 µM, 50 µM and 10 µM for 30 minutes with the addition of probe **6** (10 uM) for 30 minutes. (b) Hemin treatment at 100 µM for 30 min, 3 h or 6 h, with the addition of probe 6 (10 uM) for 30 minutes. (b) Hemin treatment at 100 µM for

30 min, 3 h or 6 h, with the addition of probe **6** (10 μM) for 30 min. Data are expressed as mean ± SEM (n = 6). Control = non-treated blank cells.

Cell conditions for CO detection with probe **6** using CORM-3 as the CO source were tested by MTT assay. First, cells were incubated with CORM-3 at a final concentration of 0, 10, 50 or 100 μM for 30 min. Then probe **6** (10 □M) was added and cells were incubated for 30 min before MTT addition. After the addition of the MTT salt, cells were further incubated for another 45 min before taking absorbance measurements (Figure S5-1). The same procedure was followed using hemin to generate CO. Cells were incubated for 3 hours with hemin at 100 μM concentration (the highest concentration probed for confocal studies). Then probe **6** was added at 10 μM for 30 minutes. Finally, MTT was added and, after 1 h of incubation, the absorbance at 492 nm was measured.

S5.2 Cellular internalization kinetics of probe 6

Cellular internalization studies were performed using a confocal Olympus FV1000MPE instrument with a water immersion objective XPLN25xWMP with a numeric aperture of 1.05 and a working distance of 2 mm. The fluorescence of the images was quantified using Image J software (see Figure S5-2).

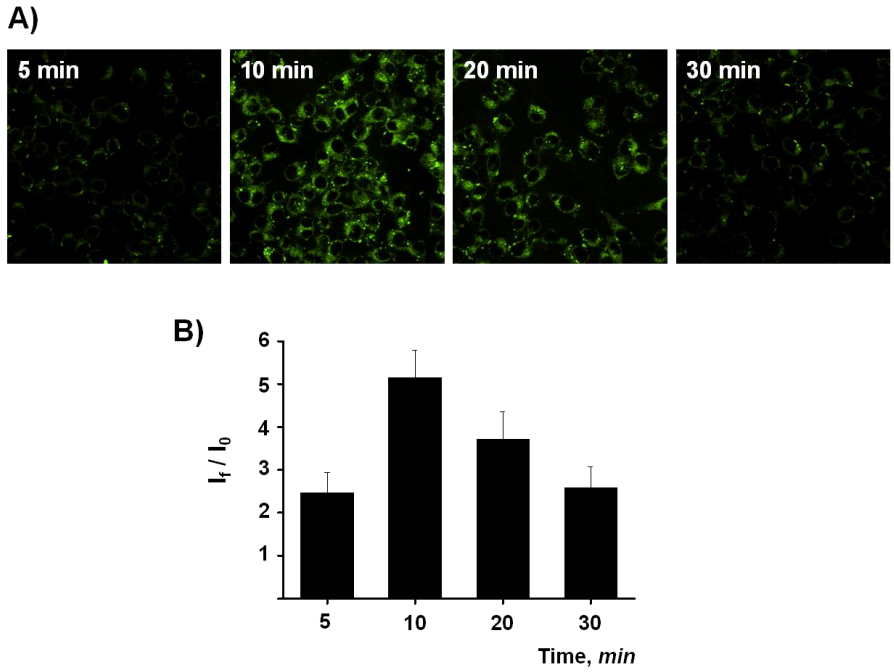

Figure S5-2. Sensor kinetics in RAW 264.7 cells. (A) Confocal images of cells incubated with Hemin solution at 100 µM for 3 h and after this, cells were incubated during 5, 10, 20, or 30 min with probe **6** at 10 µM prior to imaging. This resulted in the green emission of the TBTD ligand becoming visible as the CO generated triggers the release of the fluorescent ligand and the formation of the dicarbonyl complex (**6 CO**). (B) Mean fluorescence intensity of cells incubated at different times with probe **6** after induced CO generation, referenced to mean fluorescence intensity of non-treated cells (due to autofluorescence). Four images of each condition were quantified using Image J software. Data are expressed as mean ± SEM.

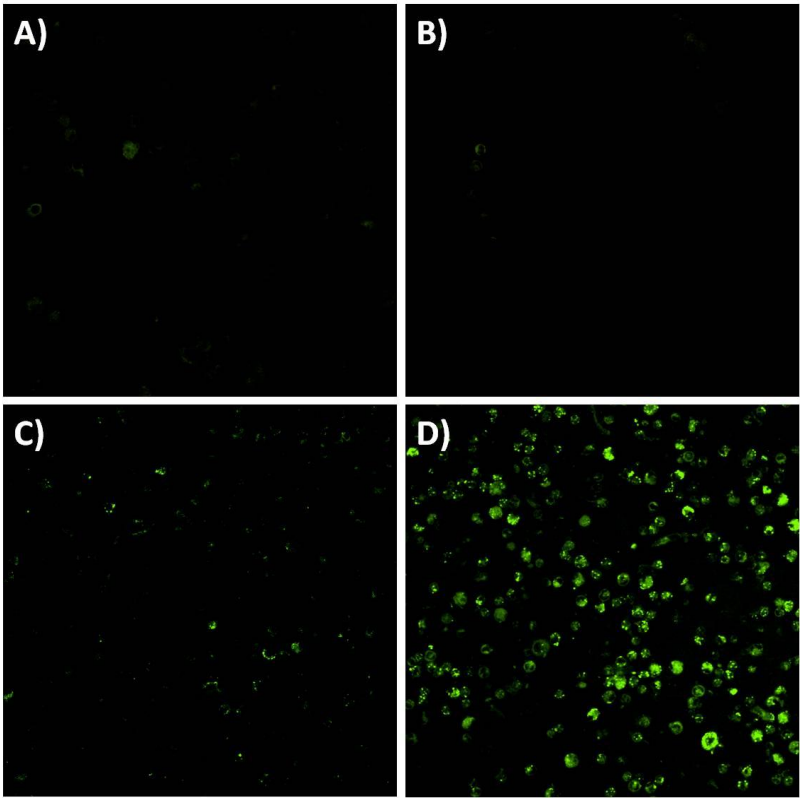

	A	B	C	D
LPS	-	+	-	+
Probe 6	-	-	+	+

Figure S5-3. Two-photon excitation microscopy images of cells from mice exudates after 18 h of saline or LPS treatment and 30 min with or without probe **6** in the air pouch. (A) mice treated with saline, (B) mice treated with LPS, (C) mice treated with saline and 50 µM of probe **6** (D), mice treated with LPS and 50 µM of probe **6**. Images were acquired upon excitation at 715 nm using a multiphoton microscope.

S5.3 Animal preparation - mouse air pouch model

Animals were obtained from Janvier (Le Genest St Isle, France). All studies were conducted in accordance with European Union regulations for the handling and use of laboratory animals. Animal protocols were approved by the Institutional Animal Care and Use Committee of the Universitat de València. Three mice were used for each sample.

The air pouch was generated in female Swiss mice (25–30 g) as described previously.[S4,S5] Air pouches were produced by subcutaneous injections of 10 mL of sterile air into the back of Female Swiss CD-1 mice (25–30 g). Three days later, 5 mL of sterile air were injected into the same cavity. Six days after the formation of air pouches, inflammation was induced by an injection of 1 mL of lipopolysaccharide (LPS, 1 μg/mL) in saline.[S6-S8]

At the indicated time point, 3 mL of 50 μM of probe **6** was injected into the air pouch and, after 30 min, the mice were culled by cervical dislocation and the exudate from the pouch was collected. Cells present in the exudates were measured using a Coulter counter. After centrifuging the exudates, the supernatants were removed and the remaining pellets were re-suspended at a final concentration of 3.0 x 10^5 cell mL^{-1} and introduced to a culture plate with a coverglass. Cells were fixed into the coverglass using paraformaldehyde at 4% for 15 min, washed twice with PBS and visualized under the multiphoton microscope. Separate sets of experiments were performed for the above-mentioned assays. Mice injected only with LPS and then with 3 mL of saline were used as a control. Furthermore, another experiment was carried out in mice without LPS, but with probe **6** to check the selective response of the probe to CO.

S6 References

S1. Cavit, B. E.; Grundy, K. R.; Roper, W. R. *J. Chem. Soc., Chem. Commun.* **1972***,* 60.

S2. Hill, A. F.; Tocher, D. A.; White, A. J. P.; Williams, D. J.; Wilton-Ely, J. D. E. T. *Organometallics* **2005**, *24*, 5342.

S3. Toscani, A.; Marín-Hernández, C.; Moragues, M. E.; Sancenón, F.; Dingwall, P.; Brown, N. J.; Martínez-Máñez, R.; White, A. J. P.; Wilton-Ely, J. D. E. T. *Chem. Eur. J.*, **2015**, *21*, 14529.

S4. Edwards, J. C.; Sedgwick, A. D.; Willoughby, D. A. *J. Pathol*. **1981**, *134*, 147.

S5. Posadas, I.; Terencio, M. C.; Guillén, I.; Ferrándiz, M. L.; Coloma, J.; Payá, M.; Alcaraz, M. J. *Naunyn-Schmiedeberg's Arch. Pharmacol*. **2000**, *361*, 98.

S6. Duarte, D. B.; Vasko, M. R.; Fehrenbacher, J. C. *Curr Protoc Pharmacol*, **2012**, Chapter 5, Unit 5.6.

S7. Escrig, V.; Ubeda, A.; Ferrándiz, M. L.; Darias, J.; Sanchez, J. M.; Alcaraz, M. J.; Paya, M. *J. Pharmacol. Exp. Ther.* **1997**, *282*, 123.

S8. Araico, A.; Terencio, M. C.; Alcaraz, M. J.; Domínguez, J. N.; León, C.; Ferrándiz, M. L. *Life Sci.* **2007**, *80*, 2108.

4. Conclusions and perspectives

Among the different types of inorganic nanomaterials, mesoporous silica nanoparticles have emerged as promising multifunctional platforms. Since their introduction in the drug delivery landscape, mesoporous materials for drug delivery are receiving growing scientific interest for their potential applications in the biotechnology and nanomedicine fields.

The application of nanotechnology in cancer treatment and diagnostics raises high expectations for millions of patients for better, more efficient, safe and affordable healthcare. Nanotechnology will likely contribute to overcoming many of the current limitations of cancer treatments in terms of more specific delivery of therapeutics to molecular targets within tumors and limiting toxic side effects.

The present thesis has attempted to contribue to this field. In fact, all hybrid materials here presentesd have been designed in orderto respond to several biomedical needs and have been developed as proof of concept for posible future therapeutic applications.

First of all, a general introduction has been included in the first chapter of this thesis. The main aspects of nanotechnology and the development of hybrid organic-inorganic mesoporous materials have been reported. In particular, the application of stimuli-responsive hybrid materials as controlled drug delivery systems was emphasized. Moreover, a brief description of some significant examples of gated nanodevices based on mesoporous silica supports for controlled delivery applications has been presented. Furthermore, biochemical aspects about cellular uptake and intracellular drug delivery have been discussed. The fundaments of supramolecular chemistry, especially about molecular recognition chemistry are also presented in chapter one.

In the second chapter of this work, biocompatible systems for the controlled release of bioactive molecules into cells using peptides as molecular gates have been developed. Five different organic-inorganic hybrid materials have been presented. In all cases the same inorganic nanoscopic silica matrix (MCM-41) was employed to store the cargo to be released yet different capping moieties were

anchored onto the surface. The first example was a mesoporous hybrid material capped with a peptide sequence capable of releasing an entrapped dye by changes in temperature. Cargo delivery correlated well with the change of the peptide conformation from α-helix to a random coil. The material was designed taking into account that the conformation transformation is a reversible process, so the funtionalized support can be reloaded and reused.

The second example was developed paying attention to the fact that cathepsins enzymes are highly associated to cancer development and metastasis. Then, new capped silica mesoporous nanopartices for intracellular controlled cargo release within Cathepsin B expressing cells was described. Nanoparticles were capped with a peptide which is able to be hydrolyzed highly specifically by Cathepsin B and highly selective for this enzyme among lysosomal cysteine proteases. The in vitro and cellular results showed a enzyme-dependent cargo release. In the third example were presented another system using peptides as molecular gate. The objective was to develop a selective-delivery carrier that is able to relase their cargo in apoptotic cells in order to develop nanoparticles with anti-apoptotitc cargo, to stop cell death. We reported the preparation of gated MSNs capable of selectively deliver their cargo in the presence of Caspase 3 enzyme in cells once apoptosis has been induced. In this example, a cell penetrating peptide was used in order to achieve the directly release of nanoparticles into cytosol of cells.

The fourth example included in the second chapter, was focused on the design of a new system to improve used therapies in B-cell non-Hodgkin's lymphoma. Was described a CXCR4-targeted delivery system using mesoporous silica nanoparticles capped with a derivative of the T22 peptide. This peptide show great affinity to CXCR4 receptor, which is overexpressed in lymphoma cells. We described here a new system able to guide the gated nanoparticles to B-NHL cells to facilitate MSNs uptake via receptor and then release their cargo by endosomal proteolytic enzymes.

Finally, the last example included in this chapter was focused on the design, synthesis, characterization and application of a protease-responsive nanodevice for intracellular-controlled release of a peptide. When peptides are used as therapeutics, the potential effects of serum proteases on peptide degradation, sometimes is prior to cellular internalization. In this scenario we decided to explore alternative methods for delivering the caspase-9 derived sequence C9h in the cell in a CPP independent manner. It has been demonstrated that C9h peptide disrupts caspase-9/PP2Acα interaction with the subsequent apoptosis induction. Herein, we developed ε-poly-L-lysine capped nanoparticles as suitable intracellular delivery device of peptide C9h in cancer cells, observing an apoptotic effect.

Finally, the third chapter has been devoted to the introduction of carbon monoxide and its different roles as pollutant and as therapeutic agent. Existing methods for CO detection and existing medical therapies involving CO used as regulator of neurotransmission, vascular tone, inflammation, cell proliferation, apoptosis, mitochondrial biogenesis and autophagy have been detailed. Encouraged to keep the biological importance of CO in mind and considering the potential use of carbon monoxide for therapeutic applications, in this chapter the study was focused on the development of water-soluble transition metal complex able to detect and determine CO in biological and cellular media. In this chapter is reported the design of a two-photon fluorescent probe based on a Ru(II) vinyl complex that is capable of selectively detecting carbon monoxide in cells (treated with CORM-3 or hemin) and *in vivo* using mice with a subcutaneous air pouch as a model for inflammation.

Although *in vitro* proofs of concept have been reported for a number of stimuli-responsive systems, only a few have been tested in in vivo preclinical models, and very few (thermosensitive liposomes and iron oxide nanoparticles) have reached the clinical stage. For most of these systems, the complexity of their architectural design and difficulties in the scaling-up of their synthesis are likely to hamper their translation from the bench to the bedside. There are critical issues

that need to be addressed to facilitate the development of MSNs for biomedicine. The success rely on developments on both the material and the biological side in order to understand the cellular functions of the population to be targeted, the physiological restrictions that need to be overcome for successful delivery and the behavior of the drug carriers in an biological environment. Protocols for reproducible synthesis and functionalizations and adequate systems for in vitro testing of toxicity, targetability and drug delivery are critical components for this process. Detailed understanding on how ‘‘biobehaviour’’ is influenced by surface modifications, size, charge, roughness (porosity), protein adsorption and conjugated molecules will be a critical aim. Furthermore, biocompatibility and biodistribution and biodegradability in vivo are burning topics. Future research efforts addressing these primordial topics.

On the oher hand, the biological detection of carbon monoxide is still in its infancy and urgently needs probes with an improved fluorescence response over a shorter timeframe in order to monitor the role of endogenous CO in cells and tissues. However, the sensing system reported so far show substantial promise, suggesting that an understanding of this fascinating role of carbon monoxide will soon be aided by further improvements in probe design. More real *in vivo* assays and the sensor response needs to be investigated.

List of publications

Results of this PhD Thesis and other contributions have resulted in the following scientific publications:

Cristina de la Torre, Leticia Domínguez-Berrocal, José R. Murguía, Ramón Martínez-Mañez, Jerónimo Bravo, Félix Sancenón, *C9h peptide delivered from ε-polylisine-capped mesoporous silica nanoparticles induced apoptosis in cancer cells*, Chemistry: A European Journal **2017, Submitted**.

Cristina de la Torre, Anita Toscani, Cristina Marin-Hernández, Carmen Terencio, Maria José Alcaraz, James D.E.T. Wilton-Ely, Ramón Martínez-Mañez, Félix Sancenón, *Tracking CO in vivo with a Ru (II) complex*, Nature Communications **2017, Submitted.**

Antoni Llopis-Lorente, PaulaDiez, Cristina de la Torre, Alfredo Sanchez, Félix Sancenón, M. Dolores Marcos, Ramón Martínez-Mañez, Paloma Martinez-Ruíz, Reynaldo Villalonga, *Enzyme-Controlled Nanodevice for Acetylcholine-Triggered Cargo Delivery Based on Janus Au-Mesoporous Silica Nanoparticles, Chemistry: A European Journal* ***2017****, 23, 4276-4281.*

Roberto Montes-Robles , Andy Hernández, Javier Ibáñez, Rafael Masot-Peris, Cristina de la Torre, Ramón Martínez-Máñez, Eduardo García-Breijo, Rubén Fraile, *Design of a low-cost equipment for optical hyperthermia*, Sensors and Actuators A: Physical, **2017**, *255*, 61–70.

Paula Díez, Alfredo Sánchez, Cristina de la Torre, María Gamella, Paloma Martínez-Ruíz, Elena Aznar, Ramón Martínez-Máñez, José M. Pingarrón, Reynaldo Villalonga**,** *Neoglycoenzyme-Gated Mesoporous Silica Nanoparticles: Toward the*

Design of Nanodevices for Pulsatile Programmed Sequential Delivery, ACS Appl. Mater. Interfaces, **2016**, *8*, 7657–7665.

Asha Tukappa, Amelia Ultimo, Cristina de la Torre, Teresa Pardo, Félix Sancenón, Ramón Martínez-Máñez, Polyglutamic Acid-Gated Mesoporous Silica Nanoparticles for Enzyme-Controlled Drug Delivery, *Langmuir*, **2016**, *32*, 8507–8515.

Édgar Pérez-Estevea, María Ruiz-Ricoa, Cristina de la Torre, Empar Llorca, Félix Sancenón, María D. Marcos, Pedro Amoróse, Carmen Guilleme, Ramón Martínez-Máñez, José Manuel Barat, *Stability of different mesoporous silica particles during anin vitro digestion*, Microporous and Mesoporous Materials **2016**, *230*, 196–207.

Édgar Pérez-Esteve**,** María Ruiz-Ricoa, Cristina de la Torre, Empar Llorca, Luis A. Villaescusa, Félix Sancenón, María D. Marcos, Pedro Amoróse, Ramón Martínez-Máñez, José Manuel Barat**,** *Encapsulation of folic acid in different silica porous supports: A comparative study*, Food Chemistry **2016**, *196*, 66–75.

Sameh Elsayed, Cristina de la Torre, Luis E. Santos-Figueroa, Cristina Marín-Hernández, Ramón Martínez-Máñez , Félix Sancenón , Ana M. Costero , Salvador Gil, Margarita Parra, *Azide and sulfonylazide functionalized fluorophores for the selective and sensitive detection of hydrogen sulfide*, Sensors and Actuators B: Chemical **2015**, *207*, 987–994.

Cristina de la Torre, Laura Mondragón, Carmen Coll, Alba García-Fernández, Félix Sancenón, Ramón Martínez-Máñez, Pedro Amorós, Enrique Pérez-Payá, Mar Orzáez, *Caspase 3 Targeted Cargo Delivery in Apoptotic Cells Using Capped Mesoporous Silica Nanoparticles,* Chem. Eur. J. **2015**, *21,* 15506–15510.

Cristina Giménez, Cristina de la Torre, Mónica Gorbe, Elena Aznar, Félix Sancenón, Jose R. Murguía, Ramón Martínez-Máñez, M. Dolores Marcos,

and Pedro Amorós, *Gated Mesoporous Silica Nanoparticles for the Controlled Delivery of Drugs in Cancer Cells*, Langmuir **2015**, 31, 3753–3762.

Cristina de la Torre, Isolda Casanova, Gerardo Acosta, Carmen Coll, María José Moreno, Fernando Albericio, Elena Aznar, Ramón Mangues, Miriam Royo, Félix Sancenón, Ramón Martínez-Máñez, *Gated Mesoporous Silica Nanoparticles Using a Double-Role Circular Peptide for the Controlled and Target-Preferential Release of Doxorubicin in CXCR4-Expresing Lymphoma Cells,* Adv. Funct. Mater. **2015**, *25*, 687–695.

Mónica Gorbe, Andrea Barba-Bon, Cristina de la Torre, Salvador Gil, Ana María Costero, Félix Sancenón, Jose Ramón Murguía, Ramón Martínez-Máñez, *Synthesis and In Vitro Evaluation of a Photosensitizer-BODIPY Derivative for Potential Photodynamic Therapy Applications,* Chem. Asian J. **2015**, *10*, 2121**.**

Sameh El Sayed, Cristina de la Torre, Luis E. Santos-Figueroa, Ramón Martínez-Máñez, Félix Sancenón, Mar Orzáez, Ana M. Costero, Margarita Parra & Salvador Gil, *2,4-dinitrophenyl ether-containing chemodosimeters for the selective and sensitive 'in vitro' and 'in vivo' detection of hydrogen sulfide*, Supramolecular Chemistry **2015**, *27*, 244-254.

Luis Enrique Santos-Figueroa, Cristina de la Torre, Sameh El Sayed, Félix Sancenón, Ramón Martínez-Máñez, Ana María Costero, Salvador Gil, Margarita Parra, *A Chemosensor Bearing Sulfonyl Azide Moieties for Selective Chromo-Fluorogenic Hydrogen Sulfide Recognition in Aqueous Media and in Living Cells*., Eur. J. Org. Chem. **2014**,1848–1854.

Cristina de la Torre, Laura Mondragón, Carmen Coll, Félix Sancenón, M. Dolores Marcos, Ramón Martínez-Máñez, Pedro Amorós, Enrique Pérez-Payá, Mar Orzáez, *Cathepsin-B Induced Controlled Release from Peptide-Capped Mesoporous Silica Nanoparticles*, Chem. Eur. J. **2014**, *20*,15309–15314.

Luis Enrique Santos-Figueroa, Cristina de la Torre, Sameh El Sayed, Félix Sancenón, Ramón Martínez-Máñez, Ana María Costero, Salvador Gil, Margarita Parra, *Highly Selective Fluorescence Detection of Hydrogen Sulfide by Using an Anthracene-Functionalized Cyclam–Cu^{II} Complex.,* Eur. J. Inorg. Chem. **2014**, 41–45.

Laura Mondragón, Núria Mas, Vicente Ferragud, Cristina de la Torre, Alessandro Agostini, Ramón Martínez-Mañez, Félix Sancenón, Pedro Amorós, Enrique Pérez-Payá, Mar Orzaez. *Enzyme-responsive intracellular-controlled release using silica mesoporous nanoparticles capped with ε-poly-L-lysine*, Chemistry **2014** , 20, 5271-5281.